Università di Pisa

School of Graduate Studies G. Galilei

PhD Thesis in Chemical Sciences

Nanometric and sub-nanometric structural properties of complex functional materials by means of solid-state NMR techniques

Francesca Martini

Supervisor

Marco Geppi

Advisors

Prof. Jeremy J. Titman

Dr. Jïri Brus

Pisa, January 2014

Introduction

In the last decades, the rapid technological development in many different fields, from information and computer technology to biomedical and clean energy storage or production, raised the interest in the research for materials combining low-costs and good chemico-mechanical properties with the ability of executing specific functions to be exploited in the final applications. Although it is difficult to collect such a wide variety of systems, differing for both chemical composition and functional properties, in a single class of materials, the definition of functional materials is commonly used to refer to systems that possess the native ability of performing specific functions. Even if the chemical composition of functional materials can vary form organic, to inorganic, to hybrid organic-inorganic, there is an increasing tendency, common to the different application fields, to use polymeric materials. Indeed, the latter combine low costs with advantageous properties such as easy processability and high flexibility, which make easier their use also in miniaturized devices, in line with the latest technological tendencies. Among functional materials there are semiconductors, superconductors, light emitting systems, energy materials, magnetic materials, etc., which possess different functional properties, such as ionic or electronic conductivity, energy storage and production, piezoelectricity, magnetism, etc.. An important class of functional materials is that of smart materials, which includes systems able to give specific responses to external solicitations. To make some examples, the so-called actively moving polymers can change their shape under the effect of external stimuli of different nature, such as thermal or mechanical. Chromogenic materials give an optical response, which is commonly a change of their emission/absorption properties, to specific thermal, mechanical or electrical solicitations. Photoactive materials employed in solar cell devices are able of transducing solar into electric energy.

A common feature of this wide variety of materials is that their functional behaviour has its origin in their structural and dynamic properties on a molecular and supramolecular scale. For example, in polymeric proton or anion exchange membranes the ion conductivity is strongly influenced by the extent of phase separation between the hydrophobic and hydrophilic domains responsible for the ion transport. Again, the ability of shape memory polymers to pass from their temporary to their permanent shape is related to the phase properties of the polymeric domains (switches), as well as to the number of cross-links (netpoints) in the polymer network. Finally, the degree of mixing between donor and acceptor domains in polymeric photoactive materials plays a fundamental role in determining the power conversion efficiency of the final solar cell. Despite the large research efforts dedicated to unravel the complicated relationships between 'microscopic" and macroscopic behaviour, the structural and dynamic properties of functional materials, and their correlation with the functional behaviour, are often unknown or not completely understood. Indeed, many different features on a molecular and supramolecular scale, such as chemical composition, phase and morphological properties, degree of mobility or interfacial interactions, can interplay to influence the performance of a material in its designed function. Moreover, these properties are extremely sensitive to the synthesis and processing procedures, as well as to the post-treatment processes eventually used.

Solid-State NMR (SSNMR) is one of the most powerful techniques for the study of the structural and dynamic properties of solid materials, on wide spatial (1-1000 Å) and motional frequency (Hz-GHz) ranges. Indeed, in contrast to liquid-state NMR, in the solid state both the spectral and the relaxation properties of the nucleus under observation are affected by the anisotropic contributions of the internal Hamiltonians, such as chemical shift anisotropy, dipolar and quadrupolar couplings, which can contain detailed information on chemical, structural, and dynamic properties of the system. Even isotropic chemical shifts are determined not only by chemical features, as it is mostly the case in the liquid state, but they also reflect structural and conformational properties typical of the solid-state. An important advantage of SSNMR with respect to other techniques, such as X-ray diffraction, is the possibility of studying almost every kind of

solid systems, either crystalline or amorphous, either mono- or poly-phasic, containing either single or multiple organic and/or inorganic components. Particularly, in multi-component materials information on the different organic and/or inorganic domains, as well as on the interface between different components, can be selectively obtained also thanks to the possibility of observing different nuclei.

Because of the capability of investigating numerous structural and/or dynamic properties, SSNMR can give an important contribution in understanding the complex correlations between "microscopic" and macroscopic properties in functional materials. In this thesis, systems belonging to different classes of functional materials (anion exchange membranes for fuel cells, chromogenic polymeric materials, and polymeric photoactive materials for solar cells) were extensively studied by using SSNMR. Depending on the system investigated, different SSNMR techniques were combined to obtain different and complementary information on the structural and dynamic features of interest, aiming at shedding light on the molecular and supramolecular origin of the observed functional behaviour. ^{19}F and ^{1}H chemical shift and dipolar interactions were measured by means of one- and two- dimensional experiments for obtaining crystallographic information on crystalline compounds. The observation and analysis of ^{13}C spectral features was used to investigate structural and phase properties of organic domains. Detailed information on the phase properties of polymeric domains, as well as on their mobility in the Hz-kHz regime, were obtained by measuring ^{1}H T_2. Dynamic properties in the MHz regime of polymeric materials were investigated exploiting ^{1}H and ^{13}C T_1. At last, the observation of proton spin diffusion was useful to investigate morphological properties on larger spatial scales, such as the distribution and the degree of mixing of different domains and/or components in polyphasic and/or multi-components systems.

This thesis is articulated in seven chapters.

Chapter 1 introduces the SSNMR framework, presenting the theoretical background necessary to the comprehension of the SSNMR studies described in Chapters 3-7. Chapter 2 contains an introduction to functional materials, particularly focusing on the correlations between "microscopic" properties and functional behaviour, and on the role of SSNMR in the study of these systems. Then, in the remaining Chapters, the most impor-

tant SSNMR studies that I carried out during my PhD on different classes of functional materials are presented. Each chapter starts with a presentation of the materials investigated, along with the results obtained by other experimental techniques, if present. The presentation of the SSNMR results is supported by descriptions of the employed SSNMR techniques and methodologies, which were different for the different studies. Chapter 3 presents an example of the application of SSNMR to the study of a novel anion exchange membrane based on polymeric materials. The combination of ^{13}C CP/MAS experiments with ^{1}H T_1 and $T_{1\rho}$ measurements allowed information on the phase and structural properties of both the polymeric matrix and the conductive functional groups to be obtained, so contributing a complete and detailed picture of the properties of the material to be achieved. In the study reported in Chapter 4, the phase and dynamic behaviour of polymeric luminescent indicators were investigated, with the final aim of identifying the processes, occurring at a molecular and/or supramolecular level, responsible for the luminescent response of these materials under heating. In this case, the analyses of on resonance ^{1}H FIDs acquired at increasing temperatures was found to be a very powerful tool for investigating the phase transformations occurring in polymeric domains, providing both structural and dynamic information. In Chapter 5 a detailed characterization of the dynamic properties in polymeric photoactive materials for solar cells is presented. In particular, the simultaneous analysis of ^{1}H and ^{13}C T_1 curves as functions of temperature through suitable theoretical models was used to achieve a detailed characterization of the motional processes occurring in the MHz regime. Chapters 6 and 7 deal with the application of advanced high-resolution SSNMR techniques to the measurements of ^{19}F and ^{1}H chemical shift anisotropies in crystalline materials containing both organic and inorganic components. In Chapter 6, a methodological approach for the measurement of ^{19}F chemical shift anisotropy based on both the analysis of spinning sideband profiles and the use of two-dimensional recoupling experiments is presented, along with the results obtained on two reference samples. Finally, Chapter 7 contains the applications of the methods described in Chapter 6 to the structural chararacterization of different zirconium phosphonates.

Contents

Chapter 1

Fundaments of NMR

1.1 The Zeeman interaction

Nuclear Magnetic Resonance spectroscopy (NMR) [1–3] is based on the interactions among nuclear spins and magnetic fields, which can be internal or external to the considered spin system. The most important interaction is that between the nuclear spins and the external magnetic field ($\mathbf{B_0}$); this is called the Zeeman interaction, and it is described by the Hamiltonian:

$$\hat{\mathcal{H}}_0 = -\hat{\boldsymbol{\mu}} \cdot \mathbf{B_0} \tag{1.1}$$

where $\hat{\boldsymbol{\mu}}$ is the magnetic moment operator of the nuclear spin, related to the spin angular momentum operator $\hat{\mathbf{I}} = (\hat{I}_x, \quad \hat{I}_y, \quad \hat{I}_z)$ by the equation:

$$\hat{\boldsymbol{\mu}} = \hbar\gamma\hat{\mathbf{I}} \tag{1.2}$$

Since $\mathbf{B_0}$ is generally assumed orientated along the z axis of the laboratory frame, the Hamiltonian in 1.1 becomes:

$$\hat{\mathcal{H}}_0 = -\hbar\gamma B_0 \hat{I}_z \tag{1.3}$$

where γ is a constant characteristic of the nuclear species, called the gyromagnetic ratio, which can have positive or negative values. In 1.3 γ is expressed in (Hz $\cdot$ T^{-1}). The Hamiltonian in 1.3 has $2I + 1$ eigenfunctions, commonly known as Zeeman states,

which correspond to the eigenfunctions of the $\hat{I}_z$ operator. The Zeeman states are usually indicated with the notation $|I, m\rangle$, with the quantum number $m = I, I-1, \cdots -I$ related to the orientation of the projection of the spin magnetic moment along z. For example, when $I = \frac{1}{2}$, as in the case the nucleus ^{1}H, the equation 1.3 has two eigenfunctions $|I, m\rangle$, with $m = \frac{1}{2}$ and $-\frac{1}{2}$, commonly known as $|\alpha\rangle$ and $|\beta\rangle$ states, respectively. When γ is positive, in the state $|\alpha\rangle$ the z component of the spin magnetic moment is parallel to $\mathbf{B_0}$, while in the state $|\beta\rangle$ is antiparallel. In the following discussion, γ is always assumed to be positive. In these experimental conditions, the Zeeman states are stationary states, meaning that the expectation value of any observable $\hat{O}$, given by the equation $\langle I, m| \hat{O} |I, m\rangle$, is not time-dependent. It is worth to mention the expectation values of the components of the angular momentum operator $\hat{\mathbf{I}}$, which are zero for the $\hat{I}_x$ and $\hat{I}_y$ components, and equal to m for the $\hat{I}_z$ one. These results show that, when the sole magnetic field $\mathbf{B_0}$ is present, the axis z, which corresponds to the orientation of the magnetic field, constitutes the quantization axis of the spin system. The energies of the Zeeman states are given by the eigenvalues of 1.3, and follow the equation:

$$E_m = -\hbar\gamma B_0 m \tag{1.4}$$

Eq. 1.4 shows a dependence of the energy of the states $|I, m\rangle$, which are degenerate in absence of $\mathbf{B_0}$, on the quantum number m, with lower energy values for the Zeeman states with the $\hat{I}_z$ component oriented in the same direction of the external magnetic field. The latter, for positive values of γ, correspond to the states $|I, m\rangle$ with $m > 0$. For example, in the case of $I = \frac{1}{2}$, the state at lower energy is $|\alpha\rangle$. The difference between the energies of two consecutive Zeeman states is:

$$\Delta E_{m+1,m} = -\hbar\gamma B_0 = -\hbar\omega_0 \tag{1.5}$$

where the frequency $\omega_0 = \gamma B_0$ is the Larmor frequency of the observed nucleus, here expressed as angular frequency in rad/sec. At the thermal equilibrium the nuclear spins populate the Zeeman states following the Boltzmann distribution:

$$\frac{N_{m+1}}{N_m} = e^{-\frac{\Delta E_{m+1,m}}{k_b T}} \tag{1.6}$$

where N_{m+1}, and N_m are the numbers of spins in the Zeeman states $|I, m+1\rangle$ and $|I, m\rangle$, k_b is the Boltzmann constant, and T is the temperature in Kelvin. In particular, at room temperature the states at lower energies (in the case of $I = \frac{1}{2}$ the $|\alpha\rangle$ state) are slightly more populated than the higher energy ones (in the case of $I = \frac{1}{2}$ the $|\beta\rangle$ state). This corresponds to a condition in which the sum of the spin magnetic moments is parallel to $\mathbf{B_0}$. It is worth to notice that $\Delta E_{m+1,m}$ is usually very small, of the order of 10^{-26}-10^{-25}J for the nucleus ^1H at Larmor frequencies of the order of hundreds of MHz. This implies that the difference in populations between the Zeeman states is very small, except at very low temperatures, causing problems of low sensitivity in the NMR experiments.

1.2 The NMR phenomenon: the case of one isolated spin

Let's consider an isolated nuclear spin in the magnetic field $\mathbf{B_0}$. This spin could be in any of the physical acceptable states, $|\psi\rangle$, which can be written as linear combinations of the Zeeman states, according to the equation:

$$|\psi\rangle = \sum_{m=-I}^{I} c_m |I, m\rangle \tag{1.7}$$

The states $|\psi\rangle$ are not stationary, but are characterized by a spin polarization along the z axis, being the spin polarization the direction in which the spin magnetic moment is well defined. In other words, this means that the expectation value of the $\hat{I}_z$ operator, $\left\langle \hat{I}_z \right\rangle = \langle\psi| \hat{I}_z |\psi\rangle$, is not time-dependent. On the other hand, from the time-dependent Shrödinger equation it can be demonstrated that the states $|\psi\rangle$ evolve under the effect

of $\mathbf{B}_0$, according to the equation:

$$|\psi\rangle\,(t) = \hat{R}_z(\omega_0 t)\,|\psi\rangle\,(0) \tag{1.8}$$

where ω_0 is the Larmor frequency, and $\hat{R}_z(-\omega_0 t)$ is the rotation operator $e^{-i(-\omega_0 t\hat{I}_z)}$. By using a classic interpretation, Eq. 1.8 describes the clockwise precession of the magnetic moment vector around the axis of $\mathbf{B_0}$, the z axis, at the angular frequency ω_0. From a quantum-mechanical point of view, this implies the mixing over time of the components $\hat{I}_x$ and $\hat{I}_y$ of the spin angular momentum operator, related to the components $\hat{\mu}_x$ and $\hat{\mu}_y$ of the spin magnetic moment, so that the corresponding expectation values are subjected to an oscillatory evolution in time at the same angular frequency ω_0. Considering a delay τ such as $\omega_0\tau = \frac{\pi}{2}$, the evolution of the spin polarization in the xy plane is:

$$\begin{array}{ccccccc} & & \tau & & \tau & & \tau & \\ |+x\rangle & \longrightarrow & |-y\rangle & \longrightarrow & |-x\rangle & \longrightarrow & |+y\rangle \end{array} \tag{1.9}$$

where the notation $|\pm i\rangle$ indicates a spin polarization oriented along the positive $(+)$ or negative $(-)$ direction of the axis i.

Another important aspect of the NMR phenomenon is the effect of an oscillating field $\mathbf{B_{rf}(t)}$, perpendicular to the main field $\mathbf{B_0}$. In these conditions, the spin Hamiltonian becomes:

$$\hat{\mathcal{H}} = -\hat{\boldsymbol{\mu}}(\mathbf{B_0} + \mathbf{B_{rf}}(t)) \tag{1.10}$$

To simplify the discussion, it is very useful to change the reference frame from the Laboratory frame to a frame, called rotating frame, whose z axis corresponds to that of the Laboratory frame, and whose xy plane rotates around $\mathbf{B_0}$ at the Larmor frequency ω_0. It can be demonstrated that, when the oscillation frequency of $\mathbf{B_{rf}}(t)$ field coincides with the Larmor frequency ω_0, the spin Hamiltonian in the rotating frame is:

$$\hat{\mathcal{H}}^R = -\hat{\boldsymbol{\mu}} \cdot \mathbf{B_{rf}^R} \tag{1.11}$$

with $\mathbf{B_{rf}}^R$ conventionally orientated along the negative x axis of the rotating frame. Analogously to what seen for $\mathbf{B_0}$ in the Laboratory frame, the evolution of the spin states $|\psi\rangle$ under the effect of 1.11 can be classically represented by the precession of the spin magnetic moment around $\mathbf{B_{rf}^R}$ at the angular frequency $\omega_{rf} = \gamma B_{rf}^R$, which implies a mixing of the $\hat{I}_y$ and $\hat{I}_z$ components. Similar to the case of precession around $\mathbf{B_0}$, considering a delay τ for which $\omega_{rf}\tau = \frac{\pi}{2}$, the evolution of the spin polarization in the xy plane is:

$$|+z\rangle \xrightarrow{\tau} |-y\rangle \xrightarrow{\tau} |-z\rangle \xrightarrow{\tau} |+y\rangle \tag{1.12}$$

A radiofrequency pulse determining the anticlockwise (clockwise) precession of the spin polarization around the axis $+i$ is usually indicated with the notation $(\Omega)_i$ ($(\Omega)_{-i}$), where Ω is the angle, in radians or degrees, described by the spin polarization.

1.3 The NMR phenomenon: the case of a multiple spins system

In real samples the number of nuclei is so large that is not possible to know exactly the state of a single nuclear spin, but we can obtain information only on the average properties of the spins in the ensemble. The concept of spin polarization is substituted by that of magnetization, which, in a vectorial representation, can be defined as the result of the vectorial sum of the magnetic moments of all the spins. In order to describe the properties and the evolution of an ensemble of spins, assumed to be identical to each other, it is convenient to use the density operator $\hat{\rho}$, defined by the expression:

$$\hat{\rho} = \frac{1}{N}\sum_{i=1}^{N} |\psi\rangle \langle\psi| \tag{1.13}$$

where ψ is a generic spin state, as defined in 1.7, and N is the number of spins in the spin system. The expectation value of a generic operator $\hat{Q}$ for the spin system can be extracted from the density operator through the equation [3]:

$$\left\langle \hat{Q} \right\rangle = Tr\{\hat{\rho}\hat{Q}\} \tag{1.14}$$

Moreover, the evolution of the properties of the spin system under the effect of a perturbation $\mathcal{H}(t)$ can be described by the time-dependent Liouville-von Neuman equation [4]:

$$\frac{\partial \hat{\rho}(t)}{\partial t} = -i[\hat{\mathcal{H}}(t), \hat{\rho}(t)] \tag{1.15}$$

where $\hat{\mathcal{H}}(t)$ and $\hat{\rho}(t)$ are the Hamiltonian and the spin density operators at the time t, respectively.

In order to understand the physical meaning of the density operator, it is useful to consider its matrix representation, that is known as the density matrix. For simplicity, the case of spins with $I = \frac{1}{2}$ is considered, so that each state ψ is given by a linear combination of the $|\alpha\rangle$ and $|\beta\rangle$ Zeeman states:

$$\psi = c_\alpha |\alpha\rangle + c_\beta |\beta\rangle \tag{1.16}$$

In this case, the density matrix assumes the form:

$$\boldsymbol{\rho} = \begin{pmatrix} \rho_{\alpha\alpha} & \rho_{\alpha\beta} \\ \rho_{\beta\alpha} & \rho_{\beta\beta} \end{pmatrix} = \begin{pmatrix} \overline{c_\alpha c_\alpha^*} & \overline{c_\alpha c_\beta^*} \\ \overline{c_\beta c_\alpha^*} & \overline{c_\beta c_\beta^*} \end{pmatrix} \tag{1.17}$$

where each element is obtained by the following equation:

$$\rho_{mm'} = \langle I, m| \hat{\rho} |I, m'\rangle \tag{1.18}$$

In 1.17 the diagonal elements are called populations, while the off-diagonal ones are called coherences. The populations, in the case considered here $\rho_{\alpha\alpha}$ and $\rho_{\beta\beta}$, are related to the spin populations of the Zeeman states $|\alpha\rangle$ and $|\beta\rangle$, and the difference between

the two is proportional to the net spin magnetization along the z axis. The latter is defined *longitudinal* magnetization. On the other hand, the coherences $\rho_{\alpha\beta}$ and $\rho_{\beta\alpha}$ are related to the presence of a net spin magnetization perpendicular to the z axis, which is defined *transverse* magnetization. In particular, the coherences are complex numbers, whose phase ϕ is equal to the phase of the *transverse* spin magnetization with respect to the x axis.

Coming to the NMR phenomenon, let's consider a multiple spin systems in the presence of the external magnetic field $\mathbf{B_0}$, at thermal equilibrium. In these conditions the populations in 1.17 follow the Boltzmann distribution, and the density matrix $\boldsymbol{\rho}$ assumes the form:

$$\boldsymbol{\rho} = \begin{pmatrix} \frac{1}{2} + \frac{1}{4}\mathbb{B} & 0 \\ 0 & \frac{1}{2} - \frac{1}{4}\mathbb{B} \end{pmatrix} \tag{1.19}$$

where $\mathbb{B}$ is the Boltzmann factor:

$$\mathbb{B} = \frac{\hbar\gamma B_0}{k_B T} \tag{1.20}$$

The fact that the coherences have zero value means that there is not transverse magnetization. On the other hand the presence of a non-zero difference between the populations $\rho_{\alpha\alpha}$ and $\rho_{\beta\beta}$, that is:

$$\rho_{\alpha\alpha} - \rho_{\beta\beta} = \frac{1}{2}\frac{\hbar\gamma B_0}{k_B T} \tag{1.21}$$

indicates that there is a net *longitudinal* magnetization, whose absolute value increases with $\mathbf{B_0}$, and decreases with temperature. Moreover, the fact that the difference $\rho_{\alpha\alpha} - \rho_{\beta\beta}$ is positive, meaning that the state $|\alpha\rangle$ is more populated than the state $|\beta\rangle$, indicates that the orientation of the longitudinal magnetization is parallel to the magnetic field $\mathbf{B_0}$.

When a transverse field, $\mathbf{B_{rf}}$, oscillating at the Larmor frequency ω_0 is applied, it is useful to pass to the rotating frame described in section 1.2. The density operator in the rotating frame can be obtained by the transformation:

$$\hat{\tilde{\rho}} = \hat{R}_z(-\omega_0 t)\hat{\rho}\hat{R}_z(\omega_0 t) \tag{1.22}$$

The evolution of $\hat{\tilde{\rho}}$ under the effect of $\mathbf{B_{rf}^R}$ is determined by the equation 1.15. In particular, at time t, it is given by the equation:

$$\hat{\tilde{\rho}} = \hat{R}_x(-\omega_{rf}t)\hat{\rho}\hat{R}_x(\omega_{rf}t) \tag{1.23}$$

that, in a vectorial representation, describes the precession of the spin magnetization around $\mathbf{B_{rf}^R}$ at the angular frequency ω_{rf}. For example, when $\omega_{rf}t = \frac{\pi}{2}$, the density matrix assumes the form:

$$\tilde{\boldsymbol{\rho}} = \begin{pmatrix} \frac{1}{2} & -\frac{1}{i4}\mathbb{B} \\ \frac{1}{i4}\mathbb{B} & \frac{1}{2} \end{pmatrix} \tag{1.24}$$

Eq 1.24 shows that the effect of B_{rf} was to equalize the populations $\rho_{\alpha\alpha}$ and $\rho_{\beta\beta}$, that means there is no more net spin magnetization along z, and to convert their difference into coherences, that means a non-zero transverse spin magnetization. Since $\mathbf{B_{rf}}$ was assumed to be directed along the $-\hat{x}$ direction, the orientation of the obtained transverse magnetization is $-y$. If, at this point, the field B_{rf} is switched off, and if we ignore the relaxation processes, the density operator will evolve under the effect of the magnetic field along z (B_z), which, due to the presence of other interactions, is slightly different from B_0. The latter aspect will be treated in more details in the following sections. The evolution of $\hat{\tilde{\rho}}$ in the rotating frame is described by the equation:

$$\hat{\tilde{\rho}} = \hat{R}_z(-\omega t)\hat{\rho}\hat{R}_z(\omega t) \tag{1.25}$$

Physically, using the vectorial representation, this corresponds to the precession of the magnetization vector around B_z at the frequency ω, that represents the off-set with respect to the Larmor frequency ω_0 ($\omega = \omega_z - \omega_0 = \gamma B_z - \gamma B_0$).

1.4 The NMR experiment

In NMR the sample is subjected to a fixed external magnetic field, $\mathbf{B_0}$, so that at the equilibrium there is a net spin magnetizizeation along z. In a generic NMR experiment the equilibrium longitudinal magnetization is converted into transverse magnetization,

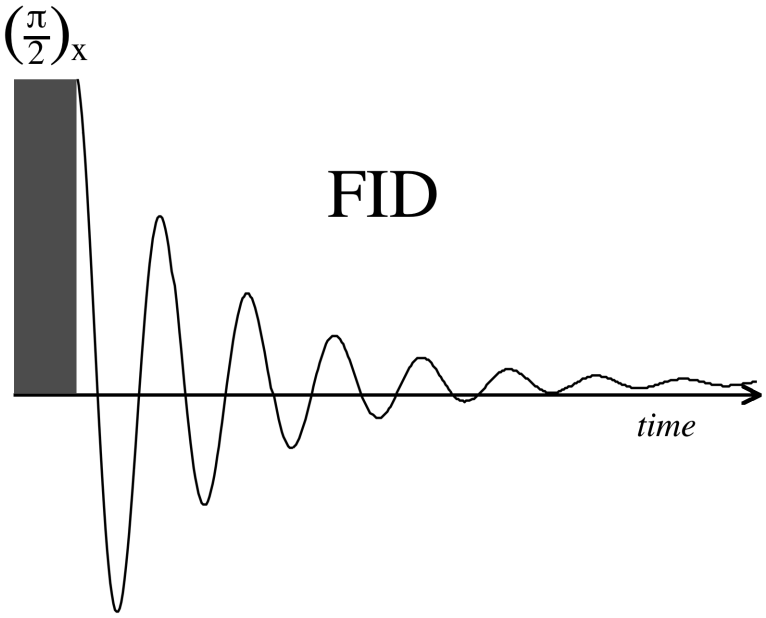

Figure 1.1: Direct excitation experiment. A radiofrequency pulse converts the longitudinal to the transverse magnetization ($\frac{\pi}{2}$ pulse); the time evolution of the transverse magnetization, which is usually described by an oscillating decaying function (Free Induction Decay, FID), is observed.

through the application of a suitable sequence of radiofrequency pulses (the $\mathbf{B_{rf}}$ field), and then the time evolution of the transverse magnetization, the NMR signal, is observed. The raw signal is an oscillating function decaying over time, called the Free Induction Decay (FID), which is usually Fourier transformed to obtain the NMR spectrum in the frequency domain. In Figure 1.1 the most simple NMR experiment, that is the direct excitation experiment, is shown. The transverse magnetization is created by means of a $(\frac{\pi}{2})_x$ radiofrequency pulse along the x axis, where $\frac{\pi}{2}$ is the angle described by the magnetization under the effect of $\mathbf{B_{rf}}$, followed by the acquisition of the FID.

1.5 The interactions internal to the spin system

In the previous paragraphs the interaction of the nuclear spins with an external magnetic field $\mathbf{B_0}$, the Zeeman interaction, was considered. However, in a real sample, each nuclear spin is subjected also to other weaker interactions with magnetic and electric fields deriving form the surrounding electrons and nuclei. These interactions, which occur

within the spin system itself, are known as internal interactions, and need to be taken into account for a complete description of the NMR phenomenon. The Hamiltonian of each internal interaction $\hat{\mathcal{H}}_i$ assumes the general form:

$$\hat{\mathcal{H}}_i = -\gamma\hbar\hat{\mathbf{I}} \cdot \mathbf{B}_i = -\gamma\hbar\hat{\mathbf{I}} \cdot \mathbf{A}_i \cdot \hat{\mathbf{J}} \tag{1.26}$$

where $\mathbf{A}_i$ is a second rank tensor which describes the interaction, and $\hat{\mathbf{J}}$ represents the ultimate source of the internal magnetic or electric field, $\hat{B}_i$. Moreover, $\mathcal{H}_i$ can be written as the sum of two terms:

$$\hat{\mathcal{H}}_i = \hat{\mathcal{H}}_{iso} + \hat{\mathcal{H}}_{aniso} \tag{1.27}$$

where $\hat{\mathcal{H}}_{iso}$ is an isotropic term, which does not depend on the orientation with respect to $\mathbf{B}_0$, and $\hat{\mathcal{H}}_{aniso}$ is an anisotropic term, which does depend on the orientation. For each interaction, the isotropic term is proportional to the trace of the tensor $\mathbf{A}_i$ being:

$$A_{iso} = \frac{1}{3}Tr\{\mathbf{A}\} = \frac{1}{3}\{A_{11} + A_{22} + A_{33}\} \tag{1.28}$$

In the NMR spectra, $\hat{\mathcal{H}}_{iso}$ gives rise to a narrow signal, at a frequency which is independent of the orientation with respect to the external magnetic field. On the other hand, the anisotropic term makes the energy of the Zeeman states depend on the molecular orientation; as a consequence, when a powder sample is considered, the NMR signal of a single site, called the *powder pattern*, is very broad, and its shape and linewidth depend on the properties of the interaction, reflecting the isotropic distribution of molecular orientations in the powder. This kind of linebroadening, which is due to the superposition of the signals arising from different molecular orientations, is classified as *inhomogeneous*.

In the following paragraphs the Hamiltonians of the main internal interactions will be described, with a particular focus on the interactions important for the nuclei investigated in this thesis. Perturbation theory was used, so that each internal Hamiltonian was treated as a perturbation of the main Zeeman term $\hat{\mathcal{H}}_0$. For most of the internal interactions, it can be demonstrated that the sole contribution to the perturbative Hamiltonian significantly affecting the energy of the spin system comes from terms commuting

with $\hat{\mathcal{H}}_0$. This contribution is called *secular* Hamiltonian, and it will be indicated in the following as $\hat{\mathcal{H}}^{sec}$. $\hat{\mathcal{H}}^{sec}$ perturbs the energies and the eigenfunctions of the spin system with first and zeroth order corrections, respectively. This means that the eigenfunctions are the same as $\hat{\mathcal{H}}_0$, but characterized by different energy values.

1.5.1 The principal axis frame

The interaction tensor $\mathbf{A}_i$ in equation 1.26 is defined in the laboratory frame. However, it is convenient to express the interaction tensor in a frame internal to the spin system, so that it can be exclusively related to the properties of the spin system itself. The most convenient frame is the *Principal Axis Frame* (PAF): it is a frame internal to the spin system, in which the interaction tensor has a simple, diagonal form. The diagonal elements of the interaction tensor expressed in the PAF are called principal components of the tensor. The tensors $\mathbf{A}_i$ in the laboratory ($\mathbf{A}_i^{lab}$) and in the PAF ($\mathbf{A}_i^{PAF}$) frames

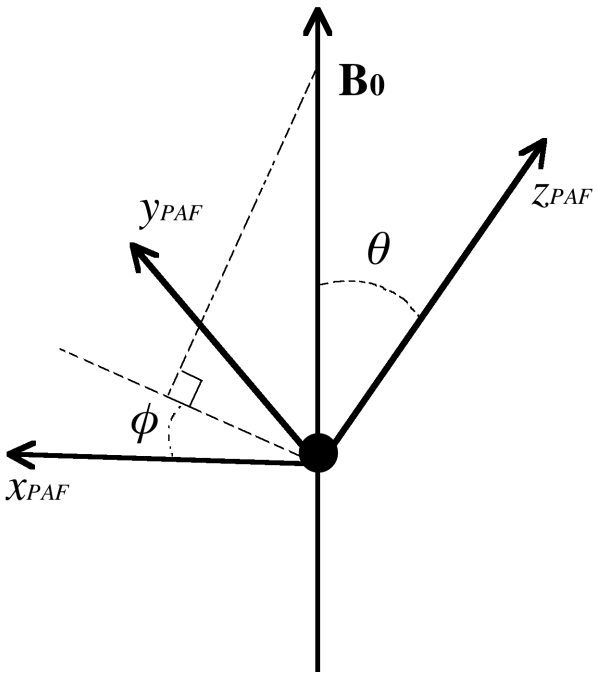

Figure 1.2: Euler angles, θ and ϕ, defining the orientation of the *Principal Axis Frame* (PAF), with respect to external magnetic field $\mathbf{B_0}$.

are related by the following equation:

$$\mathbf{A}^{PAF} = \mathbf{b_0^{PAF}} \cdot \mathbf{A}_i^{lab} \cdot \mathbf{b_0^{PAF}} \tag{1.29}$$

where

$$\mathbf{b_0^{PAF}} = \begin{pmatrix} \sin\theta\cos\phi \\ \sin\theta\sin\phi \\ \cos\theta \end{pmatrix} \tag{1.30}$$

The angles θ and ϕ in 1.30 are the Euler angles that define the orientation of the PAF with respect to the external magnetic field $\hat{B}_0$, as shown in Figure 1.2.

1.5.2 The chemical shielding interaction

The chemical shielding interaction occurs between the nuclear spin and the magnetic fields generated by the surrounding electrons, and it can be described by the orientational dependent Hamiltonian:

$$\hat{\mathcal{H}}_{cs} = \hbar\gamma\hat{\mathbf{I}} \cdot \boldsymbol{\sigma} \cdot \mathbf{B_0} \tag{1.31}$$

where $\boldsymbol{\sigma}$ is the chemical shielding tensor in the laboratory frame. Passing to the PAF, and applying the secular approximation, the following expression can be obtained:

$$\begin{aligned} \hat{\mathcal{H}}_{cs}^{sec} = {} & \hbar\omega_0\sigma_{iso}\hat{I}_z + \\ & \frac{1}{2}\omega_0(\sigma_{zz}^{PAF} - \sigma_{iso}) \left[3\cos^2\theta - 1 + \frac{\sigma_{xx}^{PAF} - \sigma_{yy}^{PAF}}{\sigma_{yy}^{PAF} - \sigma_{iso}} \sin^2\theta\cos 2\phi\right] \hat{I}_z \end{aligned} \tag{1.32}$$

where σ_{xx}^{PAF}, σ_{yy}^{PAF}, and σ_{zz}^{PAF} are the principal components of the chemical shielding tensor, and $\sigma_{iso} = \frac{1}{3}(\sigma_{xx}^{PAF} + \sigma_{yy}^{PAF} + \sigma_{zz}^{PAF})$. Two features in 1.32 need to be noticed. First, $\hat{\mathcal{H}}_{cs}^{sec}$ contains both an isotropic and an anisotropic contribution, the first and the second terms in 1.32, respectively, the latter depending on the Euler angles θ and ϕ described in section 1.5.1. Second, both the terms in $\hat{\mathcal{H}}_{cs}^{sec}$ contain only the $\hat{I}_z$ operator, meaning that, in the sole presence of a chemical shielding interaction, z is still the quantization axis of the spin system. In other words, $\hat{\mathcal{H}}_{cs}^{sec}$ alters the energy of the Zeeman states, which remain the eigenstates of the perturbed Hamiltonian. Due to the anisotropic term

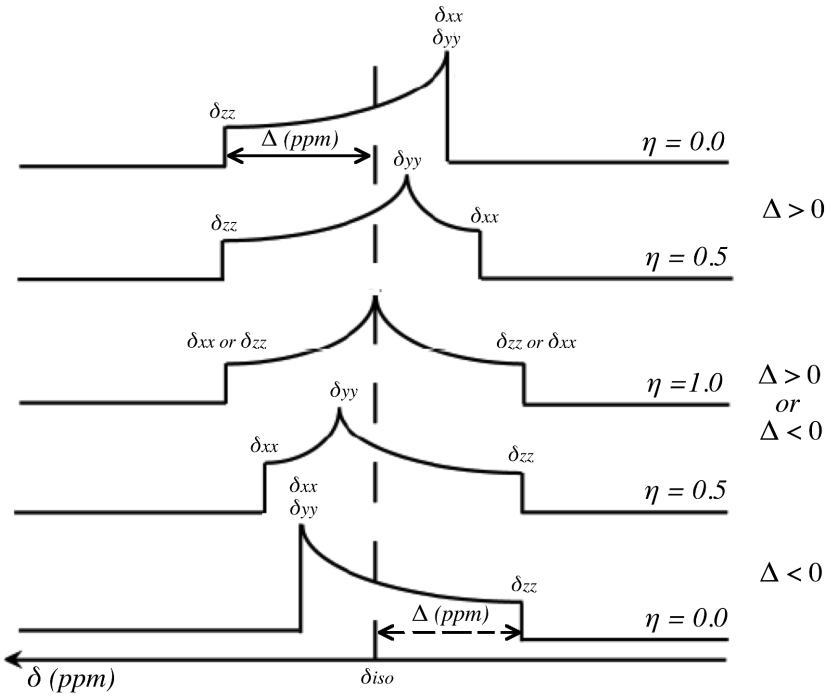

Figure 1.3: Powder patterns determined by the chemical shielding interaction for different values of the asymmetry parameter (η), for negative and positive values of the anisotropy parameter (Δ). The correspondence between the discontinuities in the powder patterns and the principal components of the chemical shielding tensor expressed in *chemical shift* is reported.

in 1.32, known as *chemical shift anisotropy* (CSA), the spectrum of a powder sample in static conditions is given by the superimposition of the signals deriving from all the possible orientations with respect to $\mathbf{B_0}$. The results are *powder patterns* similar to those reported in Figure 1.3. It is interesting to notice that from a suitable analysis of the shape of the powder patterns it is possible to extract information on the *chemical shielding* interaction. For example, as shown in Figure 1.3, each powder pattern is characterized by the presence of discontinuities at frequency values that correspond to the principal components of $\boldsymbol{\sigma}$. In order to extract the information on the chemical shielding interaction from NMR spectra, it is convenient to express the interaction tensor in the PAF in the scale of chemical shift,[1] and to introduce the parameters of *isotropic chemical shift* (δ_{iso}), *chemical shift anisotropy* (Δ(ppm)), and *asymmetry* (η), conventionally

[1]The scale of *chemical shift* (δ) is defined as:

$$\delta = \frac{\omega - \omega_{ref}}{\omega_0} * 10^6 (ppm) \tag{1.33}$$

defined as [2]:

$$\delta_{iso} = \frac{1}{3}\left(\delta_{xx} + \delta_{yy} + \delta_{zz}\right) \tag{1.34}$$

$$\Delta = \delta_{zz} - \delta_{iso} \tag{1.35}$$

$$\eta = \frac{\delta_{yy} - \delta_{xx}}{\Delta} \tag{1.36}$$

where the principal components δ_{xx}, δ_{yy}, and δ_{zz} are ordered according to $\mid \delta_{zz} - \delta_{iso} \mid \geq \mid \delta_{xx} - \delta_{iso} \mid \geq \mid \delta_{yy} - \delta_{iso} \mid$, and $\mid \delta_{zz} - \delta_{yy} \mid \geq \mid \delta_{xx} - \delta_{yy} \mid$. According to this definition Δ can have both positive and negative values, while η can assume only positive values between 0 and 1.

As shown in Figure 1.3, δ_{iso} corresponds to the *chemical shift* of the isotropic signal, which does not depend on the orientation, Δ is related to the width of the powder pattern, while the parameter η determines its shape. Physically, Δ is a measure of the strength of the CSA interaction, which determines the width of the distribution of frequencies due to the presence of an isotropic distribution of molecular orientations, while η depends on the symmetry of the electrons distribution around the nucleus. For example, $\eta = 0$ corresponds to a cylindrical symmetry of the chemical shift tensor ($\delta_{xx} = \delta_{yy}$), that is determined by an axial distribution of the electrons around the nucleus.

1.5.3 The Dipolar Interaction

The dipolar interaction is the through-space or direct interaction between the magnetic moments of two nuclear spins, here indicated as I and S. The Hamiltonian for the dipolar interaction is:

$$\hat{\mathcal{H}}_D = -2\hbar\hat{\mathbf{I}} \cdot \mathbf{D} \cdot \hat{\mathbf{S}} \tag{1.37}$$

where $\mathbf{D}$ is the dipolar coupling tensor, with principal components equal to $-d/2$, -$d/2$, d, where d is the dipolar coupling constant:

$$d = \hbar(\frac{\mu_0}{4\pi})\frac{\gamma_I\gamma_S}{r^3} \tag{1.38}$$

where ω and ω_{ref} are the NMR frequencies of the nucleus in the substance under investigation and in a reference substance, respectively. According to this definition, δ is in ppm units, and is independent of the value of the external magnetic field B_0.

The constant d is a measure of the strength of the dipolar coupling, which, as shown by Eq. 1.38, rapidly decreases with the internuclear distance, r, between the interacting spins. As we can deduce from its principal components, $\mathbf{D}$ is traceless, meaning that there are not isotropic contributions to $\hat{\mathcal{H}}_D$. Transforming to spherical, polar coordinates, the dipolar Hamiltonian becomes:

$$\hat{\mathcal{H}}_D = -d[A + B + C + D + E + F] \tag{1.39}$$

where:

$$\begin{aligned} A &= \hat{I}_z\hat{S}_z(3\cos^2\theta - 1) \\ B &= -\tfrac{1}{4}[\hat{I}_+\hat{S}_- + \hat{I}_-\hat{S}_+](3\cos^2\theta - 1) \\ C &= -\tfrac{3}{2}[\hat{I}_z\hat{S}_+ + \hat{I}_+\hat{S}_z]\sin\theta\cos\theta e^{-i\phi} \\ D &= -\tfrac{3}{2}[\hat{I}_z\hat{S}_- + \hat{I}_-\hat{S}_z]\sin\theta\cos\theta e^{+i\phi} \\ E &= -\tfrac{3}{4}[\hat{I}_+\hat{S}_+]\sin^2\theta e^{-2i\phi} \\ F &= -\tfrac{3}{4}[\hat{I}_-\hat{S}_-]\sin^2\theta e^{+2i\phi} \end{aligned} \tag{1.40}$$

For the dipolar coupling, the secular approximation can be usually applied, so that only the terms A and B in 1.40, which commute with $\hat{\mathcal{H}}_0$, significantly contribute to the perturbed Hamiltonian. However, different results are obtained depending on wether the interacting nuclei are of the same, *homonuclear dipolar coupling*, or of different, *heteronuclear dipolar coupling*, species.

Homonuclear dipolar coupling

In the case of the *homonuclear dipolar coupling*, both the terms A and B in 1.40 significantly contribute to the secular Hamiltonian, that is:

$$\hat{\mathcal{H}}_D^{sec} = -d(A + B) \tag{1.41}$$

Analogous to the case for the chemical shielding interaction, the term A contains only the operators $\hat{I}_z$ and $\hat{S}_z$, so that it maintains the quantization axis along $\mathbf{B_0}$, affecting only the energies of the Zeeman states. In contrast, the term B contains the ladder operators $\hat{I}_+$ and $\hat{I}_-$, which mix the Zeeman states. In other words, the term B corre-

sponds to a transverse magnetic field oscillating at the Larmor frequency of the observed nucleus, which causes a continuous exchange of energy between the interacting spins. This mechanism, also known as $flip - flop$, is responsible for a continuous change of the states of the spins, which occurs locally with conservation of the total energy of the spin system. When more than two interacting spins are present, the effect on the NMR spectra is a dramatic broadening of the signal arising from each molecular orientation. This kind of broadening, classified as *homogeneous broadening*, is the most important factor affecting the proton NMR spectra of solids, where the signals are usually very broad, with typical widths of tens of kHz.

Heteronuclear dipolar coupling

When I and S are different species, the term B in 1.40 is negligible. In this case, the secular Hamiltonian is:

$$\hat{\mathcal{H}}_D^{sec} = -dA = -d\hat{I}_z\hat{S}_z(3\cos^2\theta - 1) \tag{1.42}$$

Containing only the term A in 1.40, $\hat{\mathcal{H}}_D^{sec}$ of the heteronuclear dipolar coupling affects

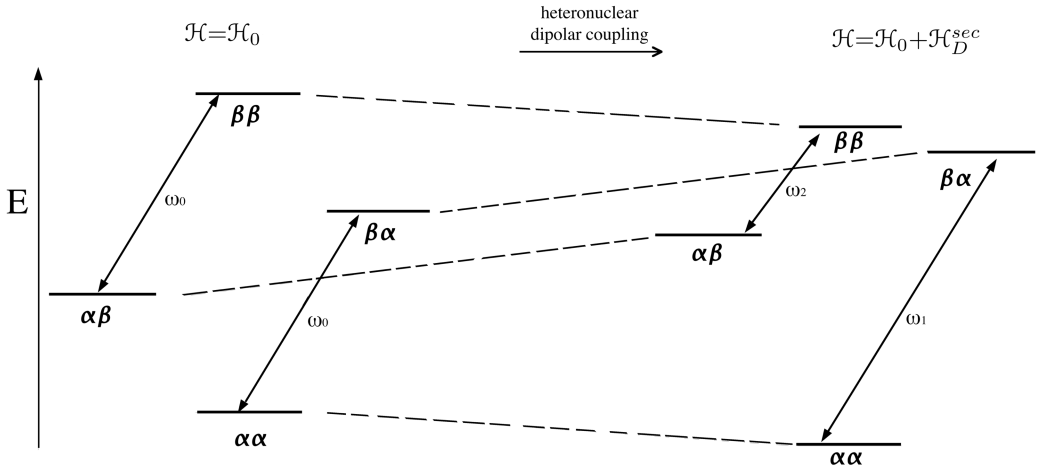

Figure 1.4: Energy levels of a pair of spins I and S of different species in the presence only of the Zeeman interaction ($\hat{\mathcal{H}}_0$) (left), and in the presence of both the Zeeman and the heteronuclear dipolar interactions ($\hat{\mathcal{H}}_0 + \hat{\mathcal{H}}_D$) (right) for a given molecular orientation.

only the energy of the Zeeman states, as in the case of the chemical shielding interaction. Considering the case of spins with I and $S = \frac{1}{2}$, at a defined orientation with respect to $\mathbf{B_0}$, the effect of the heteronuclear dipolar Hamiltonian on the energy levels is that described in Figure 1.4. The two transitions $|\alpha\alpha\rangle \longrightarrow |\beta\alpha\rangle$ and $|\alpha\beta\rangle \longrightarrow |\beta\beta\rangle$, both occurring at the Larmor frequency ω_0 of the spin in the presence of the sole Zeeman interaction, under the effect of the dipolar coupling are characterized by two different frequencies, ω_1 and ω_2, which depend on the angle formed by the internuclear vector with $\mathbf{B_0}$. The spectrum of a powder sample in the presence of a single pair of coupled nuclei is shown in Figure 1.5; the lineshape is obtained by the superimposition of the two signals arising from the transitions in Figure 1.5, for an isotropic distribution of molecular orientations with respect to $\mathbf{B_0}$. Also in this case, from the *powder pattern* it is possible to extract information on the dipolar coupling interaction, and consequently on the internuclear distance between the interacting nuclei. In particular, when a single pair of spins is considered, the dipolar coupling constant corresponds to the distance between the two maxima of the powder pattern (Figure 1.5).

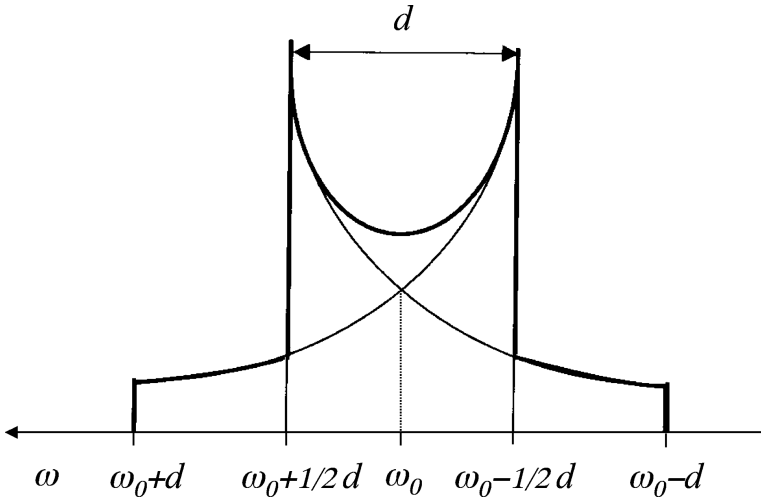

Figure 1.5: Powder pattern determined by the heteronuclear dipolar interaction between a single pair of spins.

1.5.4 The J-coupling interaction

The J-coupling interaction, or scalar interaction, is the coupling between the magnetic moments of two nuclear spins occurring under the influence of the bonding electrons, which modify the magnetic fields felt by two nuclei. So, this interaction occurs through the chemical bonds between the two nuclei, and, for this reason, is defined as an indirect coupling. The form of the J-coupling Hamiltonian is similar to that of the dipolar coupling one:

$$\hat{\mathcal{H}}_J = -\hbar\gamma\hat{\mathbf{I}} \cdot \mathbf{J} \cdot \hat{\mathbf{S}} \tag{1.43}$$

However, in this case, the tensor $\mathbf{J}$ has a non-zero trace, so that both the isotropic and anisotropic terms are present.

1.5.5 The Quadrupolar interaction

In contrast to the interactions described in the previous paragraphs, having a magnetic nature, the quadrupolar coupling is an electric interaction that occurs between the electric quadrupole generated by the charge distribution at the nucleus and the gradient of the electric field generated by the surrounding electrons. The corresponding Hamiltonian is:

$$\hat{\mathcal{H}}_Q = \frac{eQ}{6I(2I-1)\hbar}\hat{\mathbf{I}} \cdot \mathbf{V} \cdot \hat{\mathbf{I}} \tag{1.44}$$

where eQ is the electric quadrupole moment (e denotes the proton electric charge) of the nucleus, and $\mathbf{V}$ is a tensor describing the electric field gradient at the nucleus. As in the case of the dipolar interaction, $\mathbf{V}$ is traceless, so that no isotropic terms are present. It is worth noticing that the quadrupolar interaction exists only for nuclei with $I > \frac{1}{2}$; this condition corresponds to a non-spherical charge distribution in the nucleus, so that the corresponding electric quadrupole moment is non-zero.

1.6 The NMR of solids and liquids

As discussed in the previous sections, the different spin interactions of chemical shielding, J-coupling, dipolar and quadrupolar couplings are described by different internal Hamiltonians, each containing parameters characteristic of the considered interaction. A common feature of all the internal Hamiltonians is the presence of an anisotropic term, depending on the molecular orientation with respect to the external magnetic field $\hat{B}_0$, which is responsible, in powder samples, for a broadening of the NMR signal, according to the isotropic distribution of molecular orientations.

The anisotropic Hamiltonians, and, as a consequence, their contributions to the NMR spectra, are modulated by the molecular motions in a way that depends on the physical state the samples. Here, the two extreme situations of the liquid and solid states are considered. In liquids, the very fast isotropic Brownian motions of the molecules have the effect to average out the anisotropies of the internal interactions, so that only the isotropic terms contribute to the NMR spectra. This is the reason why in solution NMR the spectra are characterized by highly-resolved sharp lines determined by the chemical shielding and the J-coupling interactions, which are the only interactions characterized by non-zero isotropic terms. However, the other internal interactions, that is the dipolar and quadrupolar couplings, although not affecting the NMR spectra, still influence the relaxation processes. Conversely, in solids the molecular motions are usually very slow and anisotropic, so that they might be able to modulate to some extent, but not to completely average out the anisotropic Hamiltonians. The result is that solid-state NMR spectra are affected by the anisotropic terms of the internal interactions, which for powder samples lead to powder patterns similar to those described in the previous sections. This is not necessarily a disadvantage, considering that from the powder pattern we can extract useful information on the internal interactions, possibly related to the structural and/or dynamic properties of the system. However, most commonly, the presence of more that one internal interaction, as well as the superposition of signals arising from different sites can complicate the SSNMR spectra to such extent that any information they might contain is obscured.

1.7 Solid State NMR: high resolution techniques

In order to improve the resolution of SSNMR spectra, high-resolution techniques have been developed. In the following sections, the most important high resolution techniques, routinely used in SSNMR, will be described. These are Magic Angle Spinning (MAS) and High Power Decoupling.

1.7.1 Magic Angle Spinning

Magic Angle Spinning (MAS) consists of the mechanical rotation of the sample around an axis that forms a "magic" angle, θ_R, of 54.74° with the axis of $\mathbf{B_0}$, as shown in Figure 1.6. The sample is placed in a cylindric rotor, usually made of zirconia, able to rotate at very high frequencies, of the order of tens of kHz. The idea behind this technique is that a fast MAS rotation would be able to partially reproduce the effect of the brownian motions present in the liquid state, and to average out the anisotropic components of the interactions. Indeed, the MAS rotation induces the angles θ and ϕ in the internal

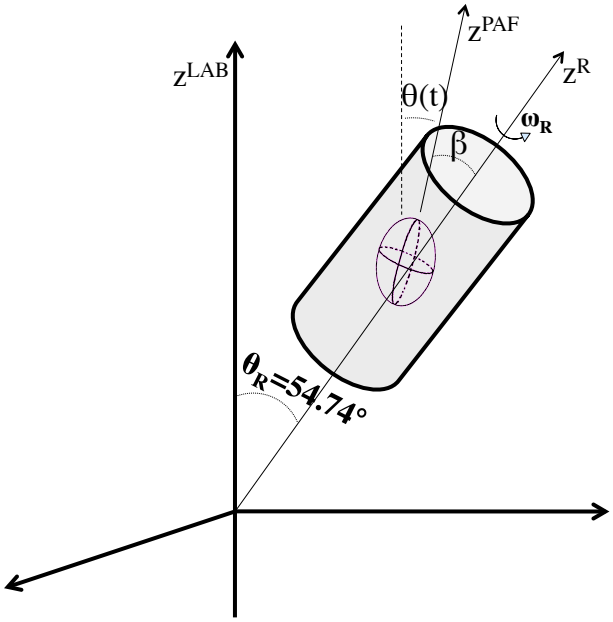

Figure 1.6: Magic angle spinning (MAS).

Hamiltonians to be time dependent. The choice of the magic angle is due to the fact that when $\theta_R = 54.74°$ the average over time of the term $(3cos^2\theta - 1)$, present in the anisotropic Hamiltonians of the internal interactions:

$$\left\langle 3cos^2\theta - 1 \right\rangle = \left(3cos^2\theta_R - 1\right) \cdot \left(3cos^2\beta - 1\right) \tag{1.45}$$

is equal to zero, as it is in the liquid state, being zero the factor $(3cos^2\theta_R - 1) = 0$. The angles θ_R, θ, and β are defined in Figure 1.6. In particular, it can be demonstrated that MAS is able to completely average out the anisotropic component of an internal interaction, when the frequency of rotation, ω_R, is at least 3 or 4 times greater than the anisotropy of the interaction, that is the width of the static signal. When the latter condition is verified for all the interactions, liquid-like spectra are obtained, where only the isotropic signals are present. At the time of writing, cutting edge systems able to achieve MAS frequencies of about 100 kHz have been developed; however, the routine MAS frequencies achievable with an ordinary instrumentation are of the order of 15-30

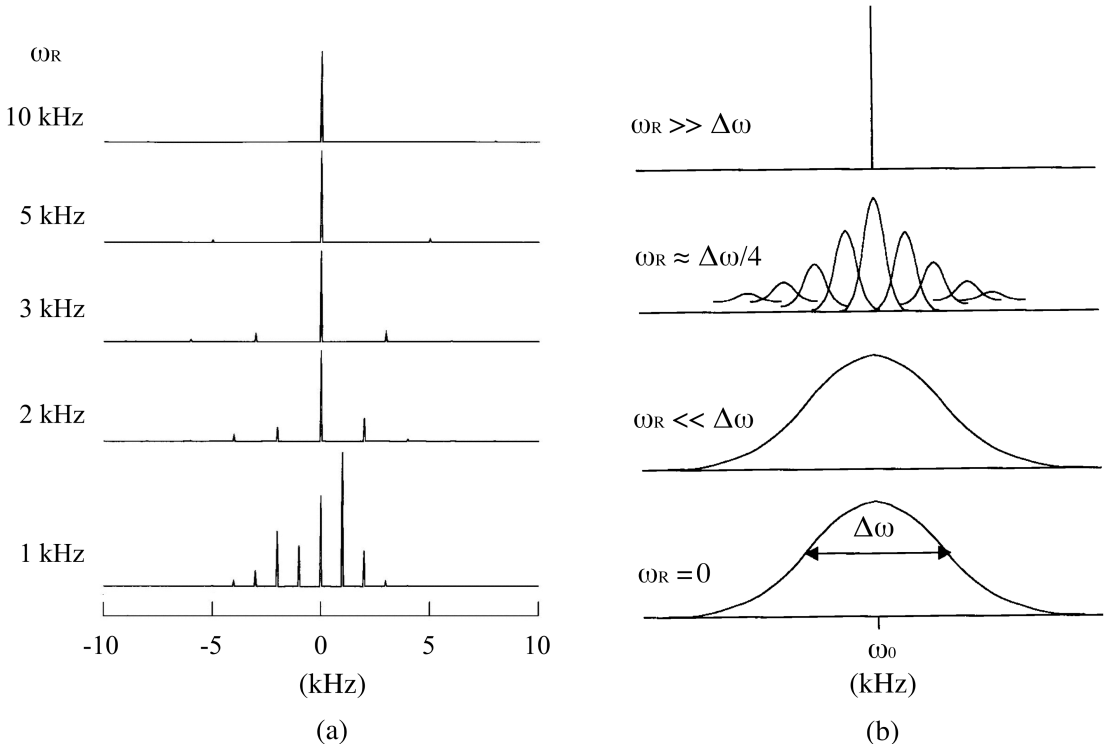

Figure 1.7: Effect of the frequency of the MAS rotation (ω_R) on the solid state NMR signal in the presence of *heterogeneous* (a) and *homogeneous* (b) line broadening.

kHz, which are often smaller than the anisotropies of the most common interactions. If this is the case, MAS produces in the spectrum a set of sharp lines, called *spinning sidebands*, in addition to the isotropic signal, as shown in Figure 1.7a. The spinning sidebands have the peculiarity to be set at multiples of ω_R apart from the isotropic signal, and the profile of their intensities contains information on the anisotropic interactions affecting the nuclear site under investigation. The origin of the spinning sidebands is related to the fact that in the presence of MAS the spin Hamiltonians are time dependent, containing, beside the isotropic term, trigonometric functions which are modulated by the frequencies ω_R and $2\omega_R$ [2].

It is worth to notice that the behaviour described above is strictly true only in the presence of *heterogeneous* linebroadening. The effect of MAS is different when the NMR spectra are affected by *homogeneous* line broadening, which is much harder to remove. As shown in Figure 1.7b, in the case of *homogeneous* linebroadening MAS does not significantly affect the NMR signal when ω_R is lower than the linewidth ($\Delta\omega$) of the static signal; single narrow peaks at the isotropic frequencies are obtained only when $\omega_R >> \Delta\omega$.

1.7.2 High-power decoupling

The high-power decoupling aims at removing the effect of the homonuclear or heteronuclear dipolar interactions from the SSNMR spectra, by physically decoupling the interacting spins. The most common case is that of a dilute spin, such as ^{13}C (natural abundance of 1.1%), observed in the presence of a network of ^{1}H or other abundant nuclei. When a powder sample is considered, the ^{13}C-^{1}H dipolar interaction causes the broadening of the ^{13}C signals in the NMR spectrum, as described in section 1.5.3. The effect of the dipolar interaction can be removed by continuously applying a high power pulse (*Continuous Wave*, CW) on the ^{1}H channel during the acquisition of the ^{13}C signal, which results in decoupling the two nuclei. The CW is the simplest decoupling sequence available, but its efficiency is often limited. More efficient and complicated decoupling sequences have been developed, which consist of trains of multiple pulses with a particular phase modulation; examples are the TPPM, and the SPINAL-64 sequences [5, 6].

A similar approach can be used to remove the broadening due to the homonuclear dipolar coupling from the spectra of abundant nuclei as ^{1}H. Phase-modulated multiple pulse sequences, such as WAHUHA, MREV-8, CRAMPS, and DUMBO [2, 7, 8] have been developed, so that at certain windows within the sequence the homonuclear dipolar interaction is zero; by properly sampling the acquisition of the signal throughout the sequence, it is possible to remove the effects of this interaction from the spectrum.

1.8 Relaxation processes

A system away from equilibrium, left unperturbed for a sufficiently long time, tends to evolve until the thermal equilibrium is regained. The mechanisms through which systems go back towards their equilibrium conditions are called relaxation processes. In NMR it is possible to distinguish two relaxation mechanisms, that are the *spin-lattice* and the *spin-spin* relaxations. As the definition suggests, the *spin-lattice* mechanism implies transfers of Zeeman-like energy, due to the presence of a quantization axis for the spin polarization, from the spin system to the surrounding lattice. This kind of mechanism governs, for example, the recovery of the magnetization along the z axis after the application of a rf field, that is called *longitudinal* relaxation; the evolution of the longitudinal magnetization during relaxation is usually described by an exponential function with a characteriztic time constant commonly denoted as T_1. On the other hand, the *spin-spin* relaxation mechanism occurs through a continuous exchange of energy within the spin system, with conservation of the longitudinal magnetization, and, as a consequence, of the Zeeman-like energy; this process governs the decay of the transverse magnetization formed after the application of the rf field, which is called transverse relaxation; the function which describes the transverse relaxation, not necessarily exponential, is characterized by a characteristic time constant, commonly denoted as T_2. In general the longitudinal and the transverse realxation processes can be treated as independent, since they occur with very different time scales; indeed, in solid sample, the T_1 and T_2 time constants are of the order of seconds and microseconds, respectively.

Finally, a third relaxation process needs to be mentioned, that is the *spin-lattice*

relaxation in the *rotating frame*; this relaxation, characterized by the time constant $T_{1\rho}$, concerns the decay of the transverse magnetization in the presence of an oscillating rf field perpendicular to $\hat{B}_0$ (*spin lock* field). In the solid-state $T_{1\rho}$ is usually of the order of milliseconds.

1.8.1 Relaxation and dynamics

In order for a relaxation process to occur, some incoherent forces must be present that induce the system to evolve. In NMR the relaxation of the spin system is induced by the fluctuations of the local magnetic fields, arising from the internal interactions, under the effect of the molecular motions. The homonuclear and heteronuclear dipolar couplings are often the main interactions contributing to the relaxation processes for systems of abundant and dilute spins, respectively. Nonetheless, especially in the solid state, also the other interactions can give non-negligible contributions.

The relaxation mechanism in NMR is usually described through a statistical approach, by first introducing the correlation function $G(\tau)$, following the equation:

$$G(\tau) = \langle \mathbf{b}(t) \cdot \mathbf{b}(t+\tau) \rangle \tag{1.46}$$

where the brackets indicate an average over the ensemble at the equilibrium. $G(\tau)$ correlates the values of the fluctuating local field $\mathbf{b}$ at the time t ($\mathbf{b}(t)$) and $t+\tau$ ($\mathbf{b}(t+\tau)$), and decays with τ, the more rapidly the higher the frequency of the fluctuation is. The spectrum of frequencies of the fluctuating field is obtained through the Fourier transform of $G(\tau)$, according to the equation:

$$J(\omega) = \int_{-\infty}^{\infty} G(\tau) e^{-i\omega\tau} d\tau \tag{1.47}$$

where $J(\omega)$ is called spectral density function, and is related to the power available for relaxation at the fluctuation frequency ω. Different models have been developed on the basis of which $G(\tau)$ and, as a consequence, $J(\omega)$ assume different expressions. The

simplest one is based on the theory of Bloembergen-Purcell-Pound (BPP) [9], according to which $G(\tau)$ and $J(\omega)$ follow the expressions:

$$G(\tau) = \left\langle b^2(t) \right\rangle e^{\frac{-\tau}{\tau_c}} \tag{1.48}$$

and

$$J(\omega) = \frac{2\tau_c}{1+\omega^2\tau_c^2} \left\langle b^2(t) \right\rangle \tag{1.49}$$

where τ_c is the correlation time of the motion, related to the inverse of its frequency. The constant τ_c represents the characteristic time at which the correlation function $G(\tau)$ decays: rapid fluctuations of $\mathbf{b}(t)$ are characterized by small values of τ_c, and slow fluctuations by larger values.

In order to understand the relationship between relaxation processes and dynamics, it is useful to introduce the relaxation rate function R_k, that is the inverse of the relaxation time constant T_k. Indeed, R_k can be expressed as a combination of spectral density functions, according to the general equation:

$$R_k = \sum_{i=0}^{n} a_i J(\omega_i) \tag{1.50}$$

When the homonuclear dipolar coupling is the only interaction significantly contributing to relaxation, as in the case of abundant nuclei, and when a single motional process is present, the expression of the R_k functions relative to the *longitudinal*, *transverse*, and *spin lattice in the rotating frame* relaxation processes are:

$$R_1 = \frac{3}{2} K_I \left[J_1(\omega_0) + J_2(2\omega_0) \right] \tag{1.51}$$

$$R_2 = \frac{3}{2} K_I \left[\frac{1}{4} J_0(0) + \frac{5}{2} J_1(\omega_0) + \frac{1}{4} J_2(2\omega_0) \right] \tag{1.52}$$

$$R_{1\rho} = \frac{3}{2} K_I \left[\frac{1}{4} J_0(2\omega_1) + \frac{5}{2} J_1(\omega_0) + \frac{1}{4} J_2(2\omega_0) \right] \tag{1.53}$$

where ω_0 is the Larmor frequency, and ω_1 is the frequency of the *spin lock* field ($\mathbf{B}_1$), defined as $\omega_1 = \gamma_I B_1$; the constant K_I is characteristic of the observed nucleus, and has the expression:

$$K_I = \left(\frac{\mu_0}{4\pi}\right)^2 \gamma_I^4 \hbar^2 I(I+1) \tag{1.54}$$

It is worth noticing that the expression in Eq. 1.54 only holds for a couple of dipolar coupled spins. When an ensemble of dipolar coupled spins is considered, the multiplicative constant in Eqs. 1.51-1.53 is related to the fraction of the second moment that corresponds to the dipolar interactions averaged by the motional process under consideration, and its value must be experimentally determined. Many texts make use of normalized $J(\omega)$ expressions, in which the term $\langle b^2(t)\rangle$ in 1.49 is not present; the latter is then included in the multiplicative factor in R_k. By using normalized spectral density functions obtained with the BBP model, and calculating $\langle b^2(t)\rangle$ for an isolated pair of spins with internuclear vector r, constant in modulus and subjected to isotropic rotational diffusion, Eqs. 1.52-1.54 becomes:

$$R_1 = \frac{2}{5r^6} K_I \left[\frac{\tau_c}{1+\omega_0^2\tau_c^2} + \frac{4\tau_c}{1+4\omega_0^2\tau_c^2}\right] \tag{1.55}$$

$$R_2 = \frac{3}{5r^6} K_I \left[\tau_c + \frac{5}{3}\left(\frac{\tau_c}{1+\omega_0^2\tau_c^2}\right) + \frac{2}{3}\left(\frac{\tau_c}{1+4\omega_0^2\tau_c^2}\right)\right] \tag{1.56}$$

$$R_{1\rho} = \frac{2}{5r^6} K_I \left[\frac{3}{2}\left(\frac{\tau_c}{1+4\omega_1^2\tau_c^2}\right) + \frac{5}{3}\left(\frac{\tau_c}{1+\omega_0^2\tau_c^2}\right) + \frac{\tau_c}{1+4\omega_0^2\tau_c^2}\right] \tag{1.57}$$

By using eqs. 1.55-1.56, it is possible to show that each relaxation process is particularly sensitive to dynamics processes with a characteristic frequency close to the value $\omega_i = \gamma_I B_i$. This is evident from Figure 1.8, where the curves of T_1, T_2, and $T_{1\rho}$ as functions of the correlation time τ_c are reported. The longitudinal relaxation has a strong sensitivity towards molecular motions occurring at a frequency of the order of the Larmor frequency ω_0, that is usually in the range of tens-hundreds of MHz, as shown by the minimum in the curve of T_1 around the corresponding value of τ_c (Figure 1.8). In particular, note the shift of the minimum of the T_1 curve towards higher motional frequencies, i.e. smaller τ_c values, when the Larmor frequency is increased, in the case shown in Figure 1.8, from

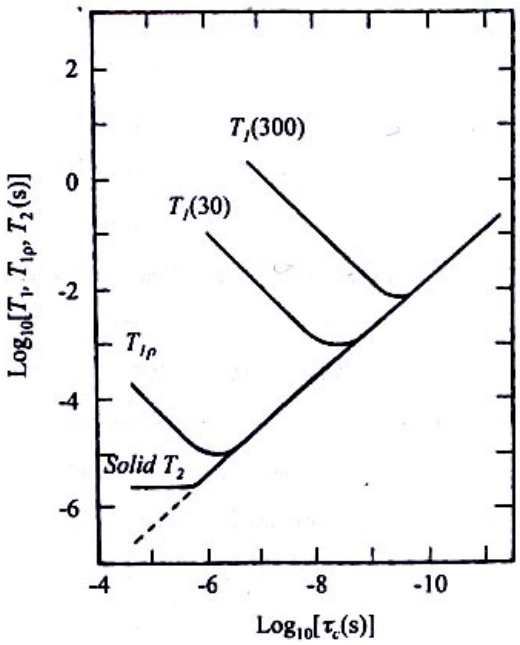

Figure 1.8: Curves of the relaxation times T_1, $T_{1\rho}$ and T_2 as a function of the correlation time of the motion τ_c. The curves are obtained for a pair of protons at an internuclear distance of 1 Å, under conditions of validity of the BPP theory. For T_2, at the higher values of τ_c, the dashed line represents the trend estimated on the basis of the Redfield theory [1], while the solid one that obtained by using the Bloembergen model for solids in *rigid lattice* conditions ($\tau_c > T_2$) [10].

30 to 300 MHz. A similar trend is observable for $T_{1\rho}$, but the minimum is at values of τ_c corresponding to motional frequencies of the order of the *spin lock* frequency ω_1, usually in the range of tens-hundreds of kHz. A different behaviour is shown by the *spin-spin transverse* relaxation, and its characteriztic relaxation time T_2. On the basis of the equation 1.56, T_2 should monotonically increase over all the frequency range. However, we have to consider that the analytical treatment here used is strictly valid only within the limits of the Redfield theory, that is for $\tau_c < T_2$ [1]. This condition is called *motional narrowing regime*, while the opposite situation, for which $\tau_c > T_2$, is defined *rigid lattice regime*. In the *rigid lattice regime* other models need to be used to describe the *transverse* relaxation. One of them is that proposed by Bloembergen to

treat the relaxation processes in solids when $\tau_c > T_2$ [10]. As it is shown in Figure 1.8, T_2 is not sensitive to molecular motions until τ_c does approach values of the same order of magnitude of T_2.

1.9 Spin Diffusion

Spin Diffusion consists in the spatial diffusion of longitudinal magnetization, which tends to average out its gradients present throughout the sample along the axis of the external magnetic field $\mathbf{B_0}$. This phenomenon, peculiar to solids, is mostly effective in systems of abundant nuclei, such as protons, being based on the mutual exchange of energy between nuclear spins coupled through the homonuclear dipolar interaction. As discussed in section 1.5.3, the B term of $\mathcal{H}_D$, containing the $I^+S^- + I^-S^+$ operator, induces continuous transfers of energy from a spin to a near, coupled spin, through the mutual *flip-flop* mechanism, which conserves the net longitudinal magnetization, but determines local variations of the spin states. However, the *flip-flop* mechanism by itself cannot explain

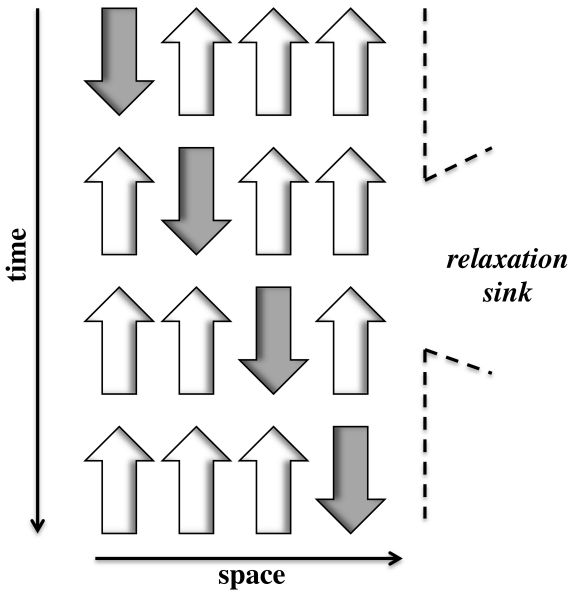

Figure 1.9: Representation of the diffusion of the longitudinal magnetization towards the *relaxation sink* of the system, through a series of *flip-flop* transitions. The arrows indicate the Zeeman states of each nuclear spins, and each line represents the same portion of the spins system at different times.

the phenomenon of *spin diffusion*. Indeed, in order for a diffusion of magnetization throughout the sample to occur, the presence of a gradient of longitudinal magnetization is necessary, able to drive the flux of magnetization toward a region of the sample commonly defined as a *relaxation sink*. The gradient of longitudinal magnetization could be experimentally created by selectively exciting a specific region of the sample, or, in heterogeneous materials, it could be generated by differences in the intrinsic *spin lattice* relaxation rates R_1 or $R_{1\rho}$ of different domains. The diffusion mechanism is schematically illustrated in Figure 1.9, and can be described by the diffusion law [11]:

$$\frac{\partial \mathbf{M}(\mathbf{r},t)}{\partial t} = D(r)\frac{\partial^2 \mathbf{M}(\mathbf{r},t)}{\partial^2 t} \tag{1.58}$$

where $\mathbf{M}$ and D are the magnetization and the diffusion coefficient at the position defined by the vector $\mathbf{r}$ in the sample. By solving Eq. 1.58, it is possible to obtain an expression for the average diffusion path $\langle r \rangle$, in the hypothesis of a non-spatial dependence of the diffusion coefficient, that is:

$$\left\langle r^2 \right\rangle = nD\tau \tag{1.59}$$

where n can assume values from 1 to 6 depending on the geometrical model used to describe the diffusion process, and τ is the time for which *spin diffusion* is allowed to proceed.

Thanks to the equation 1.58, the study of the *spin diffusion* process allows information on the domain sizes in heterogeneous systems to be obtained, in a spatial range approximately between 0.5 and 200 nm. For example, in this thesis, the influence of *spin diffusion* on the ^1H longitudinal relaxation time T_1 have been exploited to determine the degree of homogeneity of polymeric multicomponent materials. Indeed, in heterogeneous samples, in which domains characterized by different intrinsic ^{1}H T_1 and $T_{1\rho}$ relaxation times are present, leading to the formation of gradients of longitudinal magnetization, *spin diffusion* tends to equalize the relaxation rates over the whole sample, so that average ^{1}H T_1 and $T_{1\rho}$ values are usually measured. In particular it can be demonstrated that the average of ^{1}H T_1 and $T_{1\rho}$ is complete, so that the same experimental values are measured for all the nuclei in the sample, when the dimension of the smallest domains

are smaller than 100-200 Å and 10-20 Å, respectively, according to the typical values assumed by D and to the time scales of the corresponding relaxation processes.

Chapter 2

Nanomorphology and dynamics in advanced functional materials: the role of solid-state NMR

2.1 Advanced functional materials: the importance of morphology control

In the last decades the interest in materials able to execute specific functions useful for the development of new technologies and applications in many different fields, such as biotechnology, computer technology, clean energy production, food packaging etc., has grown continuously. The definition of functional materials, today used by important scientific journals [12], refers to the characteristic of materials to possess particular native properties and functions of their own [13]. These can include, for example, ferroelectricity, piezoelectricity, magnetism, energy storage, ion or electron conductivity functions etc. Functional materials include materials with various chemical natures, which can be organic, inorganic (ceramics, metals, polymers), or hybrid organic-inorganic. Examples of functional materials are liquid crystals, semiconductors, superconductors, sensors, porous materials, light emitting materials, biological materials, energy materials, or magnetic materials etc..

For all these different classes of materials, the functional behaviour is strongly related to their structural and dynamic properties on a nanometric and sub-nanometric scale. For this reason, the investigation of these properties is very important to understand the origin of the functional macroscopic behaviour, smoothing the way to the development of better performing materials.

In this thesis the structural, dynamic, and morphological properties of materials belonging to three classes of functional materials, i.e. smart materials, polymeric ion exchange membranes, and polymeric photoactive materials, were investigated. In the following paragraphs the functional properties typical of these classes of functional materials will be discussed, along with the state of the art on the knowledge of the correlations between their functional and nanometric and sub-nanometric structural and dynamic properties.

2.1.1 Stimuli-responsive polymeric materials for smart applications

Nowadays polymeric materials have a great importance in our lives, being used as components in most of the objects of common use, from food packages to electronic and computer devices. The wide diffusion of polymeric materials is mainly due to their advantageous properties: good mechanical, chemical and thermal properties are often accompanied by low costs, high flexibility and easy processability. In addition, the availability of an almost unlimited range of possible polymers and polymers combinations allows a wide range of materials with different and easy tuneable properties to be realized. Today fast technological progresses in many fields such as medicine, biotechnology, electronics, informatics, and food packaging have raised the interest in developing polymeric materials that combine the already known chemical, thermal and mechanical properties with an additional "smart" behaviour. A material is classified as "smart" when it shows a responsive behaviour, that could be chemical, mechanical, electrical or chromogenic, to a specific external stimulus of a different nature, thermal, mechanical, electric, radiative etc. [12,14–16]. Depending on the kind of response, various classes of smart materials can

be distinguished. For example, chromogenic polymeric materials undergo colour changes under the effect of specific mechanical, thermal, electrical or radiative stimuli [17, 18]. So-called actively moving polymers (AMP) are able to change their shape under the effect of an external stress, such as, for example, a thermal stimulus [19]; electromechanical active polymers (EAP) are systems able of transducing electric into mechanic energy and vice versa [20–23]; polymeric photoactive materials can also be classified as smart, giving an electrical response to the absorption of the solar light. The latter class of materials will be the subject of one of the following paragraphs inherent to polymeric materials for solar cells devices. The ability of a material to translate environmental changes into modifications of its structural, mechanical, and physical properties, as in the case of chromogenic polymers and AMP, can be very useful especially in the fields of sensoristic and food packaging. For example, in the field of food packaging, the use of smart coatings for both flexible and rigid packages could be very useful for the traceability of the products, as well as for monitoring the correct mantainance of the conservation requirements, in terms, for example, of conservation temperature, exposure to solar light or applications of mechanical stresses. On the other hand, polymeric materials able to execute an active job, mechanical or electrical, under the effect of an external solicitation, as EAP do, have recently found interesting applications in many fields, such as robotics, biotechnology, optics, computer technology etc.. Some examples are implantable actuators as components of artificial organs, such as stimulators of cardiac tissue, tuneable lenses for adaptive optics for cameras and phones, tactile displays etc. [20–23].

A common feature of this wide class of materials is the origin of their smart properties, lying in their structural and dynamics properties on a molecular and supramolecular scale. The relationship between "microscopic" and macroscopic properties can be very complex, depending on the interplay between many factors and on the kind of material and smart functionality. A complete review of the literature concerning the structural and dynamic properties at the molecular and supramolecular levels and their correlations with the responsive function for all the classes of smart materials is not possible within this thesis, and it is not the purpose of this paragraph. However, in order to give the idea of the importance of understanding and controlling the "microscopic" properties

mainly related with the smart behaviour, some examples will be described concerning two classes of smart materials, which are AMP and chromogenic polymeric materials.

Two classes of AMP can be distinguished, shape memory (SMP) [19, 24–28] and shape changing (SCP) polymers [29, 30]. SMP are able to pass from a temporary shape, obtained through a deformation process, to their permanent original shape under the effect of an external, usually thermal, stimulus [27, 28]. In contrast, SCP change their shape during the application of an external stimulus, and recover the original shape when the solicitation is removed. In both cases, the origin of the responsive behaviour lies in the structure and interaction properties of the polymeric material, which is usually made of an elastic polymer network containing switches and netpoints. The switches are responsible for the material deformation, while the netpoints determine the permanent shape of the polymer network. The former are usually represented by the polymeric amorphous and crystalline domains, which can easily undergo phase transitions or structural rearrangements, while the latter correspond to the interconnection points (cross-linking) between the different polymeric domains through physical and/or covalent interactions [31–33]. For example, in thermal responsive AMP the switches are polymeric crystalline and/or amorphous domains with low melting or glass transition temperatures, respectively [34–39]. In recent works, Messori et al. studied SMP constituted by semi-crystalline poly(ϵ-caprolactone) (PLC), in which the net points were covalent cross-links between methacrylate or triethoxysilane terminated PLC chains. In these materials the transition temperature from the temporary to the permanent shape was the melting temperature of crystalline PLC [27]. The responsive behaviour of AMP can be easily tailored by opportunely tuning properties such as the density of cross-links, the polymer structure (linear or branched), the mobility of the amorphous phase. In thermal responsive SMP, by varying these parameters it is possible to tune the transition temperature, the broadness of the transition temperature interval, or the number of possible transitions. The possibility of achieving more than one transition temperature is the basis of so-called two-ways SMP, in which the transition from the temporary to the permanent shape is reversible [28].

One of the studies that I carried out within my PhD work concerned the characteri-

zation of the phase properties of luminescent polymeric indicators with a threshold temperature, constituted by a PLA-based polymeric matrix containing a styrene-derivative as a dye. Different classes of chromogenic polymeric materials can be identified on the basis of the kind of external solicitation determining the chromogenic response [17, 18]. Moreover, as recently reported by A. Pucci et al. [17], two kinds of strategies are possible to confer optical properties to a thermoplastic polymeric material: the first is to disperse organic dyes within the polymeric matrix (dye-polymer blends), while the second is to insert chromophoric units into the thermoplastic polymer backbone through the formation of covalent bonds. The first approach, being the more versatile in terms of possible combinations of thermoplastic polymer and chromophore, is the most commonly used, and it was used also for the materials studied within this thesis. The chemico-physical mechanism at the basis of the smart properties of the dye-polymer blends is the change of the absorption or emission properties of the dye in passing form the isolated monomer to their aggregates. Indeed, in the aggregates, interactions between the commonly present aromatic rings, such as π-stacking interactions, can determine a significant lowering of the energy gaps between the HOMO and LUMO electronic levels of the dye, with a red shift of its absorption and emission spectra. The application of an appropriate external stimulus to the polymer-dye system, by inducing transformations in the morphological properties of the polymeric matrix triggers, the transition of the dye from the monomeric to the aggregate forms or vice versa, determining a consequent change of the absorption/emission properties. For example, for thermochromic polymeric materials, whose optical properties are responsive to thermal stimuli, the phase transitions occurring within the polymeric matrix under heating, such as cold crystallization processes, might determine the aggregation of the dye, initially present in the monomeric form, within the polymeric amorphous domains. On the other hand, in mechanochromic polymeric materials, which respond to mechanical solicitations, a mechanical stress, such as the elongation of the polymeric film, usually determines a rearrangement of the polymer network, which favours the dispersion of the dyes, initially present as aggregates. Concluding, in dye-polymer blends the chromogenic properties are determined by the structural properties of the dye before and after the external stimulus. In turn, the

form, monomers or aggregates, in which the dyes are present within the polymeric matrix, is strongly dependent on the phase and morphological properties of the polymer network; for this reason, the detailed investigation of these properties and of their transformations under external stimuli is also of fundamental importance to understand the optical properties of the materials, and/or to tailor the devising to obtain the desired performances.

2.1.2 Polymeric ion exchange membranes for fuel and electrolytic cells

Polymeric electrolyte exchange membranes for the ion transport in electrochemical devices have become very popular in the field of fuel and water electrolysis cells [40–44]. The main advantages of using polymeric materials are their easy processability and high flexibility, allowing, for example, the realization of miniaturized devices, which could find application in the field of portable electronics. Among the noteworthy features there are also low operating temperatures and high power densities. However, several drawbacks prevent the diffusion of the so-called polymer electrolyte fuel or water electrolysis cells on a large scale. The main issues are the low durability of the polymeric membrane, which undergoes relatively fast degradation processes during long-terms operations, and the costs due to the need of using expensive materials and catalysts.

Two possible kinds of polymer electrolyte exchange membranes can be distinguished: the proton exchange membrane (PEM), and the anion exchange membrane (AEM). As the definitions suggest, PEM and AEM differ for the kind of ions which are transported through the membrane, which are protons in the case of PEM, and anions, usually hydroxyl (OH^-) anions, in the case of AEM. In general, a polymer electrolyte membrane is constituted by hydrophobic domains, which mainly determine the mechanical properties of the membrane, and hydrophilic domains, which are directly involved in the ionic transport mechanisms. PEM are usually realized with fluorinated polymers, the most common of which is NAFION, containing acidic groups, usually sulphonic acid groups, responsible for the ion-conductive properties. On the other hand, AEM are commonly

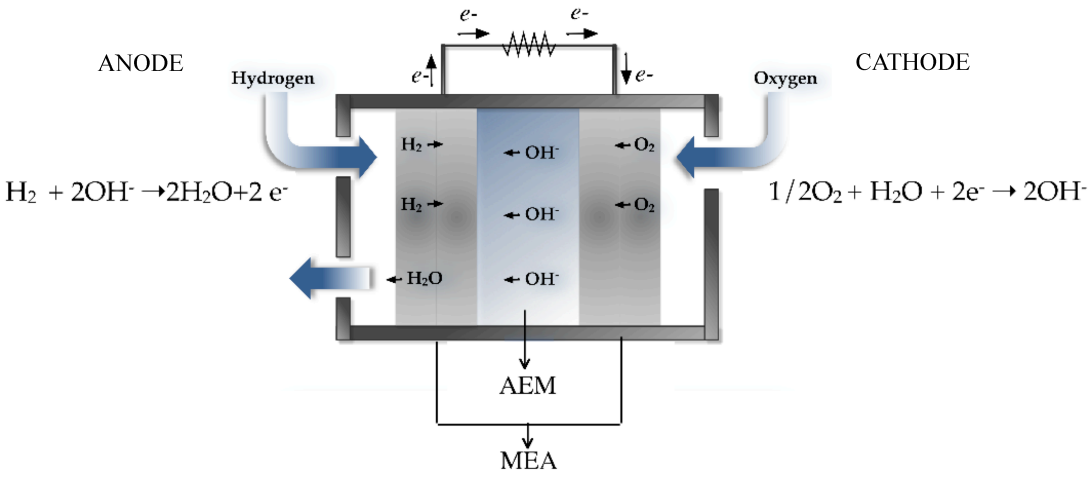

Figure 2.1: Scheme of a hydrogen fuel cell with a polymeric anion exchange membrane (AEM).

realized with fluorinated or hydrogenated polymers containing cationic groups, usually ammonium salt groups, which provide sites for the anion exchange. In Figure 2.1, the scheme of an AEM-based hydrogen fuel cell, classified as solid alkaline fuel cell (SAFC), is shown. This device exploits the redox reaction between hydrogen and oxygen to produce clean electrical energy, water being the only sub-product of the reaction. The heart of a SAFC, as well as, in general of a polymer electrolyte fuel cell, is the so-called membrane-electrodes assembly (MEA), which is constituted by the anion exchange membrane, the two electrodes (the anode and the cathode), and the catalysts, usually supported on the electrodes. At the cathode and at the anode the oxygen reduction and the hydrogen oxidation occur, respectively, according to the electrochemical half-reactions:

$$\frac{1}{2}O_2 + H_2O + 2e^- \longrightarrow 2OH^- \tag{2.1}$$

$$H_2 + 2OH^- \longrightarrow 2H_2O + 2e^- \tag{2.2}$$

In order for the overall reaction to occur with the production of electrical energy, it is necessary to establish an electrical contact between the electrodes, for the transport of the OH^- anions from the cathode to the anode; as shown in Figure 2.1, this function is performed by the AEM. Commonly, the ion transport in polymeric ion-exchange membranes is facilitated by the presence of a protic liquid, such as water, which is adsorbed

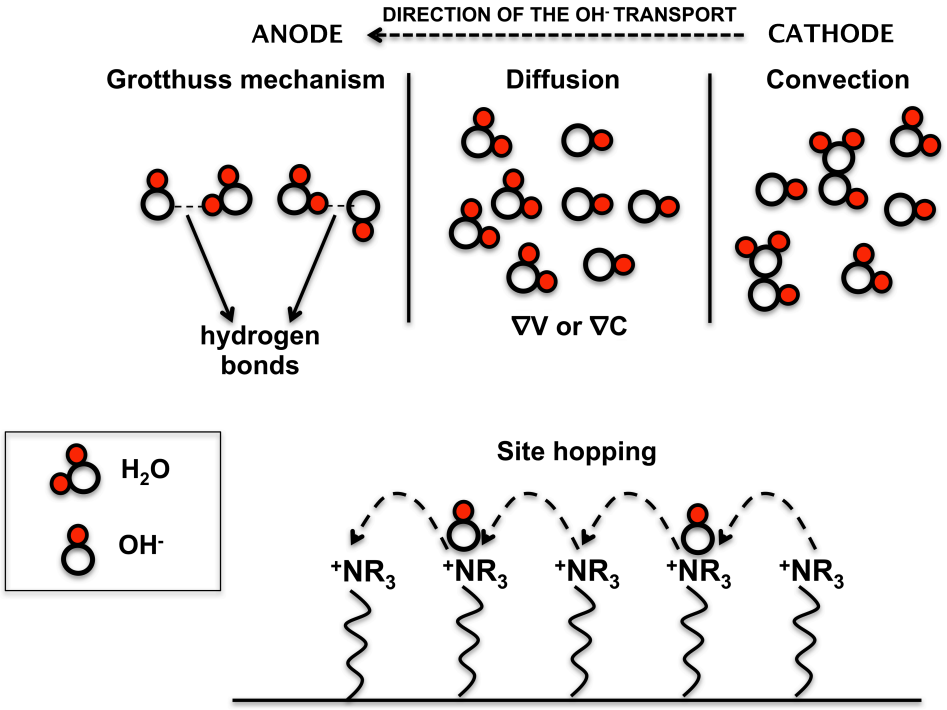

Figure 2.2: Representation of the possible OH^- transport mechanisms, Grotthuss, convection, diffusion and site-hopping, in a polymeric anion exchange membrane (AEM). ∇V and ∇C denote the electric potential and OH^- concentration gradients, respectively.

within the membrane thanks to the presence of hydrophilic groups. Due to the limitations in the operating temperature determined by the problems of water evaporation, water-free systems have also been developed, which, however, are characterized by lower ion conductivity. Several efforts have been addressed to the understanding of the ions transport mechanism through polymer electrolyte membranes in fuel cells. In the case of hydrated PEM and AEM, four main mechanisms were identified, which are represented in Figure 2.2 [44]:

- the Grotthuss mechanism, according to which OH^- (or H^+) diffuse through the hydrogen bonded network of water molecules, by the formation/cleavage of hydrogen-bonds;

- the diffusion mechanism, according to which OH^- (or H^+) diffuse through the water domains under the effect of electrical potential (V) and/or concentration (C) gradients;

- the convective mechanism, according to which the moving OH^- (or H^+) anions drag the water molecules with them, thus creating a convective flow of water molecules across the membrane;

- the hopping mechanism, that is the hopping of OH^- (or H^+) anions on the ammonium sites present in the membrane.

The first three mechanisms are also known as vehicular mechanisms, while the fourth one is defined as structural. On the basis of the functions and mechanisms described above, it is possible to predict the properties that a polymeric electrolyte exchange membrane should have in order to realize a well-performing electrochemical device. The main requirements are high proton or anion conductivity, low permeability to reactants (oxygen, hydrogen, or other possible fuels such as methanol), related to the problem of fuel *cross-over* in operating conditions, chemical and thermal stability, and, finally, durability. In the past years, a significant portion of the scientific research in the field was dedicated to the optimization of these properties. In particular, while PEM have been object of much attention in the past, recently the research interests have been mainly focused on AEM. One of the main advantages of AEM with respect to PEM concerns the cost of the catalysts, necessary for the final fuel or electrolysis cell to work: indeed, while with PEM, due to the acidic conditions, expensive, noble metals-based (usually Pt-based) catalysts are required, with AEM lower-cost catalysts, based on less precious metals such as cobalt, silver, or nickel, can be used. Moreover, also the problem of fuel *cross-over* results to be strongly reduced. The main drawback is that AEM are characterized by quite low ion-diffusion coefficients, which strongly limit their conductive properties in fuel cells compared to PEM. So, in the past decade, large efforts have been addressed to the development of AEM systems combining improved ion-conductive properties with chemical and thermal stability, and long-terms durability.

The macroscopic properties of a polymer electrolyte exchange membrane have their origin in the structural, dynamic and morphological properties of the membrane itself, and the investigation of these properties and of their correlations with the macroscopic ones could be very important to develop materials with improved performances [45–47].

Even if several studies concerned the structural characterization of proton and anion exchange membranes, a full comprehension of how and which microscopic features can influence the macroscopic behaviour of the membrane has not been achieved so far. In general, the structural and dynamic properties of the hydrophobic polymeric domains, such as phase properties, porosity, and degree of mobility, seem to be related to the mechanical properties of the membrane, such as mechanical flexibility and resistance, which, in turn, determine the durability of the membrane under operating conditions. However, an influence of the phase properties, and in particular of the segmental motions of the polymeric domains on the ion-conduction properties of the membrane, is very likely. On the other hand, the hydrophilic groups, represented by the acidic and the cationic groups in PEM and AEM, respectively, are mainly responsible for the ion-transport properties, and, in hydrated systems, they are in contact with the water domains. For example, both the ion conductivity and the water uptake are demonstrated to increase with the ion exchange capacity (IEC), that is related to the concentration of acidic or cationic groups in the polymeric membrane. Moreover, several studies demonstrated that the phase separation between the hydrophobic and the hydrophilic domains plays a fundamental role in determining the ion-conduction properties of the membrane. Indeed a good separation favours the formation of water domains large enough to allow the presence of loosely bound and free water, leading to an increased ion conductivity. On the other hand, too large water domains might increase the permeability to the fuel molecules, causing problems in terms of fuel *cross-over*, and it might also compromise the mechanical stability and durability of the MEA. Finally, the motional processes involving the hydrophilic groups can be strongly related to the mechanism of ion exchange, determining the efficiency of the structural ion mechanism transport.

2.1.3 Polymeric photoactive materials for solar cells

Exploiting solar energy is one of the most promising way to face today's increasing energy demand, and large efforts have been addressed to the development of photovoltaic (PV) devices combining improved conversion efficiencies with more competitive costs of materials and manufacturing. Indeed, today's PV technology is based on expensive in-

organic semiconductors, which require high fabrication costs, preventing this alternative source of energy from being extensively used [48–51]. The most promising alternatives to the inorganic PV technology are the so-called organic photovoltaic devices (OPV), which are based on organic semiconductors containing alternating C-C and C=C bonds; the electron delocalization due to the presence of conjugated structures determines the semiconducting properties of these materials. OPV devices are divided in two main categories according to their constituent molecules, which can be small organic molecules or polymers, requiring different synthesis, purification and device fabrication procedures. Solar cells based on polymeric materials, the so-called *Polymeric Solar Cells* (PSC), are particularly appealing, since they have important advantages, such as the large availability of low-cost polymeric materials, the easy and inexpensive fabrication and processing procedures, and the high-flexibility which enlarges the panorama of possible applications also to the portable electronic market. Indeed, many film-forming techniques, for both the small laboratory (spin coating, doctor blading, and casting from solvent) and the large industrial (roll-to-roll coating) scales of production, followed by different post-treatment procedures, such as, for example, thermal or solvent annealing, can be used, leading to films with different thickness, mechanical and photoactive properties [52]. However, the breakthrough of the PSC technology to the industrial production is limited by several unsolved issues, such as the scarce thermal stability and durability of the polymeric materials, which can easily undergo degradation processes under use, and, most of all, the non-competitive values of power conversion efficiency achieved so far. Indeed, the highest values of *power conversion efficiency*, obtained for polymer-fullerene systems, do not overcome 7-8 % for the single cell [49].

In Figure 2.3 the scheme of a generic PSC is illustrated. As already mentioned above, the main difference between polymeric and inorganic solar cells concerns the photoactive layer, which is constituted either by inorganic or polymeric semiconductors, respectively. The photoactive layer is the component of the solar cell device which is responsible for the harvesting of the solar light, and its conversion into electric energy. In PSC it is constituted by two components, playing the roles of electron *donor* and *acceptor*, which can be inserted in the same organic macromolecule, as block copolymers, or, more commonly,

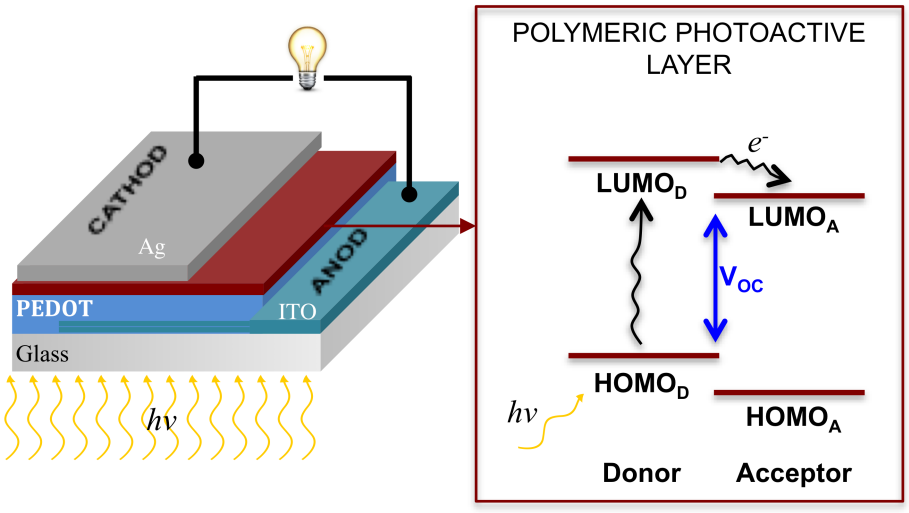

Figure 2.3: On the left, scheme of a polymeric solar cell (PSC), with Ag- and ITO- based electrodes as cathode and anode, respectively. On the right, HOMO and LUMO electrons level distribution of the donor and the acceptor.

which are present as different components placed in contact to each other. While in the inorganic semiconductors the absorption of the solar light leads directly to the formation of two separate charges, in polymeric photoactive materials, due to the larger energy gaps between the electronic levels, the solar light is absorbed by the donor, promoting an electronic transition from the Highest Occupied (HOMO) to the Lowest Unoccupied (LUMO) molecular orbital, with the formation of an exciton. In order for two separate charges to be formed, the exciton must reach the *donor-acceptor* interface, where the energy offset between the HOMO-LUMO energy levels of the donor and the acceptor provides the driving force for the dissociation of the exciton, as shown in Figure 2.3. In this process, an electron is transferred from the LUMO of the donor to the LUMO of the acceptor, leading to the formation of separate positive (holes) and negative (electrons) charges, which are collected at the corresponding electrodes throughout the donor and acceptor domains, respectively. The operating mechanism described above suggests that many factors may interplay to influence the efficiency (η) of the final PSC, usually expressed as the product of three parameters, according to the equation [49, 51]:

$$\eta = J_{SC} \cdot V_{OC} \cdot FF \tag{2.3}$$

where J_{SC} is the short circuit current, V_{OC} the open circuit voltage, and FF the fill factor. The factors that mainly affect η can be resumed in the following aspects:

- the efficiency of the absorption of the solar light, related to the overlap between the solar spectrum and the absorption spectra of the donor and acceptor;
- the efficiency of exciton dissociation, mainly related to the energy offset between the electronic levels of the donor and the acceptor;
- the efficiency of the diffusion of the exciton toward the *donor-acceptor* interface, which needs to be fast enough to limit the occurrence of the exciton recombination phenomenon;
- the efficiency of charge transport towards the electrodes, which is related to the semiconducting properties of the polymeric materials.

Numerous studies demonstrated that J_{SC} and V_{OC} are strongly dependent on the electronic properties of the donor and the acceptor, and can be increased by finely tuning the structural properties of the corresponding polymers. In particular J_{SC} results to be mainly influenced by the absorption properties of the donor towards the solar light, and it can be increased by decreasing the energy gap between the corresponding HOMO and LUMO energy levels, to extend the absorption spectrum to the longer wavelengths. On the other hand, the open circuit voltage V_{OC} is proportional to the energy difference between the LUMO of the acceptor and the HOMO of the donor, as shown in Figure 2.3, and it determines the efficiency of the exciton dissociation at the *donor-acceptor* interface. Different combinations of *donor* and *acceptor* have been explored in the attempt to optimise both J_{SC} and V_{OC}, and the best results were obtained for polymer-fullerene photoactive materials, where conjugated polymers, such as, for example, poly(thiophene) (as P3HT) and poly(phenylene vinylidene) (as MDMO-PPV) derivatives, work as electron *donors*, and fullerene derivatives (as PCBM) work as electron *acceptors* [48–50].

Finally, the filling factor FF was demonstrated to be strongly dependent on the efficiencies of the exciton diffusion to reach the *donor-acceptor* interface, and on the charge carriers transport toward the electrodes [48–50]. Both these aspects are strongly related

to the morphological properties of the polymeric material, which are known to play a critical role in determining the performances of the final PSC [51, 53–56] . Different

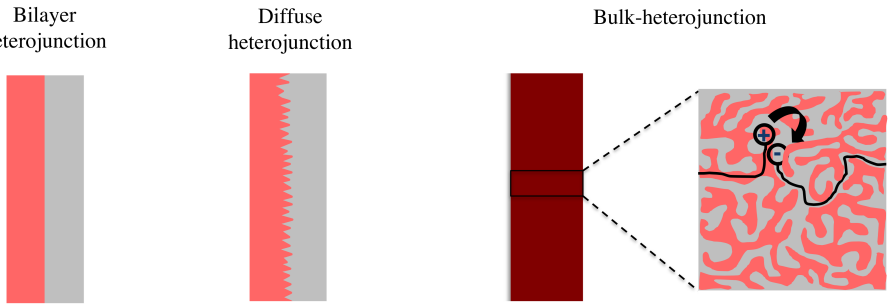

Figure 2.4: Bilayer, diffuse and bulk-heterojunction morphologies of polymeric photoactive layers for solar cell devices. The different colours indicate the donor and acceptor domains.

ways of assembling of the donor and acceptor domains have been developed, the most representative of which are illustrated in Figure 2.4 [51]. The most promising results were obtained with the so-called *Bulk-HeteroJunction* (BHJ) photoactive layer, in which the *donor* and *acceptor* are intimately mixed on a nanometric scale. The main advantage of BHJ is the extended interfacial area between donor and acceptor domains, which strongly increases the probability of the exciton dissociation over the recombination phenomenon. The morphological features that seem to mostly affect, in a very complicated and not completely understood way, the *power conversion* efficiency of BHJ PSC are the phase properties of the *donor* and *acceptor* domains, and, on a larger scale, the degree of mixing between donor and acceptor. A high structural order in the *donor* and *acceptor* domains, due, for example, to a high content of crystalline phase, might facilitate both the exciton diffusion and the transport of the charge carriers. Moreover, an intimate mixing between *donor* and *acceptor* domains, decreasing the length of the path of the exciton towards the *donor-acceptor* interface, favours the exciton dissociation process. On the other hand, the phase separation, to a certain extent, of donor and acceptor domains, probably increasing the linearity of the paths of the charge carriers towards the electrodes, and so limiting the occurrence of decaying phenomena, could contribute to the increase of η. Tuning the morphological properties of BHJ photoactive materials is considered of fundamental importance in the field of PSC, and different methods of synthesis, assembling and film-forming, as well as different post-treatment procedures, have

been explored in order to achieve optimal morphologies. In particular, the morphology of BHJ polymer blends results to be very sensitive to preparation and processing parameters, such as the kind of solvent, the concentrations the different components in the initial solution, the presence of additives, conditions of solvent or thermal annealing. For example it is known that in polymer-fullerene photoactive blends, a high concentration of the fullerene derivative, overcoming its solubility limits in the casting solvent, leads to the formation of acceptor domains of overly large dimensions, so that the efficiency of the PSC results is dramatically reduced. Also the heating of the pre-formed photoactive film, the so-called thermal annealing, was found to significantly affect the performances of the final devices, due to induced morphological changes. For example, it was demonstrated that the thermal annealing of P3HT/PCBM photoactive blends, at a temperature of about 150 °C, results in an increase of the power conversion efficiency [49, 51]; this seems ascribable to the occurrence of a phase separation at the interface between the *donor* and *acceptor*, which probably facilitates the charge transfer to the corresponding electrodes, without compromising the efficiency of the exciton dissociation process. Conversely the annealing of MDMO-PPV/PCBM photoactive blends was found to cause a decrease of η; indeed, in this case, the extent of the phase separation between MDMO-PPV and PCBM is too large, with the formation of large PCBM crystals, strongly reducing the contact area between donor and acceptor [49].

2.2 The role of solid-state NMR: some applications to the study of advanced functional materials

Solid state NMR is known to be one of the most powerful spectroscopies for the investigation of the structural, phase and dynamic properties of solid materials; indeed, it allows both crystalline and amorphous materials made of organic and/or inorganic components to be studied, being able to give information on wide spatial (1 Å-1000 Å) and motional frequency ranges (Hz-GHz) [2, 3, 57]. This is allowed by the possibility of observing different nuclei (^{1}H, ^{19}F, ^{13}C, ^{29}S, ^{21}P etc.), and the availability of a wide

variety of high- and low-resolution techniques for the determination of different nuclear properties.

As far as the structural properties are concerned, the isotropic chemical shift, determined through the analysis of MAS spectra, can contain detailed information on structural and/or conformational properties at the molecular level. For example, it is known that polyethylene (PE) chains in *all-trans* and *trans-gauche* conformations are responsible for ^{13}C signals resonating at different isotropic chemical shift of about 33 and 31 ppm, respectively [58]. Since the *all-trans* and the *trans-gauche* conformations are typical of PE crystalline and amorphous phases, ^{13}C MAS spectra of a PE containing sample allow the presence of crystalline and amorphous domains to be identified, and also quantified [59, 60]. Further information on the molecular structure and geometry can be obtained by determining the tensors of anisotropic interactions, such as CSA and quadrupolar interactions, through low-resolution or recoupling experiments. Within this thesis, the so called R recoupling sequences were used to recouple ^{19}F and ^{1}H CSA in crystalline zirconium phosphonates, with the aim to find correlations between the CSA parameters and the structural and geometrical features of the different crystalline sites [61]. Furthermore, the determination of the homonuclear and heteronuclear dipolar couplings, whose strength is proportional to the inverse of the cube of the inter-nuclear distance, through correlations (such as HETCOR and DQMAS) or recoupling (such as REDOR and DRAMA) experiments can be very useful to characterize the interactions, such as hydrogen or covalent bonds, present at the interface between different components and/or domains [2]. The morphological properties of the samples on a spatial range between 10 and 1000 Å can also be investigated by exploiting the spin diffusion process described in section 1.9. As already mentioned in section 1.9, the measurement of ^{1}H T_1 and $T_{1\rho}$, which tend to be averaged to one single value by spin diffusion, allows information on the degree of homogeneity of a multiphasic system, on the spatial ranges of 100 Å-200 Å and 10 Å-20 Å, respectively, to be obtained. Moreover, through more complex Goldman-Shen experiments it is possible to determine domains dimensions up to about 1000 Å, by measuring and analysing the evolution of the proton longitudinal magnetization after the creation of a magnetization gradient in the sample.

Dynamic properties on different motional regimes can also be investigated, thanks to the large availability of SSNMR techniques for studying the effect of molecular motions on different nuclear properties. In particular, it is worth to notice that SSNMR spectroscopy is sensitive only to reorientational motions which are able to change the orientation of the interaction tensors with respect to the external magnetic field. Three motional regimes can be investigated through SSNMR: slow, intermediate, and fast, corresponding to reorientational motions with characteristic frequencies in the ranges of 1-1000 Hz, 1-1000 kHz, and 1-1000 MHz, respectively. Motional processes in the slow regimes, such as interconformational or exchange processes, can be investigated through 1D or 2D exchange experiments. Furthermore, various SSNMR nuclear features, such as the static lineshape, T_2 and $T_{1\rho}$ relaxation times, are sensitive to motions in the intermediate regime. The static lineshape and T_2 relaxation times are both affected by motional processes with characteristic frequencies of the same order of the width of the static signal, which can span from a few Hz to tens and hundreds of kHz in the presence of the most common interactions. On the other hand $T_{1\rho}$ relaxation process is particularly efficient when motions with frequency of the order of kHz are present (section 1.8). Finally, motional processes occurring in the fast motional regime are usually investigated through the determination of T_1 relaxation times, which, as already mentioned in section 1.8, are sensitive to reorientational motions with characteristic frequencies of the order of the Larmor frequency of the observed nucleus. In the previous section it

was shown the importance of the control of the structural and dynamic properties on a molecular and supramolecular scale in the development of functional materials with the required macroscopic behaviour. Even if the combination of microscopy (SEM, TEM, AFM), X-ray and calorimetric techniques (DSC) is at present the most popular and widely used approach to investigate these properties, the role of SSNMR is becoming more and more important, as demonstrated by the increasing number of applications in the literature [62–97]. Since the researched information depends on the kind of functional material, in terms of both "microscopic" properties and final functional behaviour, different SSNMR approaches are required to investigate the structural and/or dynamic

properties of interest. In the following some examples of applications of SSNMR to the study of different classes of advanced functional materials will be reported.

Stimuli-responsive polymeric materials for smart applications

To the best of my knowledge, the number of applications of SSNMR to the study of smart materials is still limited compared to the extent of the scientific literature in this field [62–68]. Only few examples can be found in which SSNMR was applied to the study of chromogenic materials, which, nevertheless, demonstrate the potential of this spectroscopy for investigating the chemical, structural and phase transformations responsible for the colour change of these material under an external stimulus [63, 64]. For example, Shirley et al used ^{13}C MAS experiments to study the structural and chemical changes occurring in 10,12-pentacosadiynoic acid (PCDA) after the addition of different aromatic compounds [64]. In particular they demonstrated that the increase of the temperature of the PCDA transition from blue to red after the addition of cyclopentadiene is due to the occurrence of a Diels-Alders reaction between cyclopentadiene and the PCDA triple bond. Indeed, the chemical addition of cyclopentadiene sterically hinders the conformational rotation around the C-C bonds adjacent to the triple bond, responsible for the colour change. The occurrence of the Diels-Alder addition was detected by observing differences in ^{13}C MAS spectra, acquired before and after UV irradiation, due to the formations of new bonds and chemical environments. The utility of SSNMR was also shown for the study of shape memory polymers [65–68]. M. Bertmer et al. found ^{13}C CP/MAS experiments a very useful and simple tool to investigate the covalent cross-link density in polymer networks made from oligo[(L-lactide-*ran*-glycolide)]dimethacrylates as a function of several parameters, such as average molecular weight and UV irradiation times [66]. These materials showed a shape memory behaviour, recovering the permanent shape after heating above the polymer T_g. In particular, they found that the quaternary carbon signal of methacrylate at about 44 ppm allowed the direct determination of the cross-link density, which was found to linearly decrease with the polymer molecular weight, and to rapidly increase with the UV irradiation time. Moreover, by means of double quantum ^{1}H build-up curves for the measurement of the strength of the homonu-

clear dipolar interactions, they observed a increase of the dipolar coupling strength in passing from the permanent to the temporary shape. The fact that the build-up curve of the original polymer network, before undergoing shape programming, was found to almost exactly coincide with that of the polymer network after recovering the permanent shape nicely demonstrated the complete reversibility of this process.

Polymeric ion exchange membranes for fuel and electrolytic cells

The utility of SSNMR in the field of ion exchange polymer electrolytes has been largely demonstrated, as also reviewed in recent works [79,80]. In particular, there are many examples in which SSNMR was applied for the investigation of different structural and/or dynamic aspects of proton exchange membrane. Some of the most interesting information achievable through SSNMR concern hydrogen-bonds network, mobility, proton-exchange and diffusion mechanism within water domains [73, 75, 80, 82]; structural and dynamic properties of the acidic or cationic groups responsible for the ion transport [72, 80, 81]; changes in the structural properties of the polymer backbone and sidechains under use, which could be useful to understand the main sources of membrane degradation [76–78]. The properties of the water domains in hydrated PEM or AEM play a fundamental role in determining the efficiency of the ion transport, and there are many SSNMR studies in which ^{1}H MAS, ^{1}H DQMAS, ^{2}H NMR, and pulse field gradient (PFG) techniques were successfully used for determining the hydrogen-bonding, dynamic, and diffusivity properties of water within the polymer network [80]. Dan E. Demco et al. investigated the anisotropy of the water-diffusion exchange mechanism in perfluorinated sulphonic acid (PFSA) ionomer membrane containing silica nanoparticles as inorganic fillers, by using PFG NMR [75]. In order to get information on the anisotropy of the water diffusion channels, two experiments were carried out with the magnetic field gradient parallel and perpendicular to the membrane plane. By analysing the experimental data through a suitable model, the authors found a correlation between both the water diffusion and exchange between free and bound water and the content of silica nanofiller. In particular, they found that the anisotropy of the diffusion process, given by the relative difference between the water diffusivity parallel and perpendicular to the membrane plane, de-

creases by increasing the silica content. Interesting results on the water penetration in Nafion-based membrane under fast MAS were obtained by S. Ding et al. by means of a multinuclear solid-state NMR approach, mainly based on the observation of water ^{1}H and ^{17}O nuclei [82]. By acquiring ^{1}H and ^{17}O spectra at different orientations of the membrane with respect to $\mathbf{B_0}$ they observed a significant variation of the chemical shift with orientation, indicating a slight anisotropy of susceptibility of the membrane. Moreover, they observed an increase of both chemical shift and linewidth of the proton signal by increasing the MAS frequency. A similar trend was also observed from "time resolved" ^{1}H MAS spectra, acquired at increasing times of MAS rotation at 12 kHz. From these results they concluded that the MAS rotation forced the water molecules to penetrate into regions inaccessible to static samples, possibly forming strong hydrogen bonds with the Nafion sulfonic acid groups. This could lead to an increase of structural heterogeneity and/or to a decrease of molecular mobility, which could both explain the increase of linewidth in the MAS spectra. The characterization of the hydrogen bond interactions, and the investigation of the dynamic processes involving the cationic and/or the anionic groups present in the polymeric exchange membrane is also very important to understand the molecular origin of the ion transport efficiency of a polymeric membrane. This is particularly crucial for membranes where the site-hopping mechanism prevails over the vehicular mechanism through water or other protic liquid electrolyte domains (paragraph 2.1.2). G. R. Goward et al. investigated the hydrogen bonding network and dynamic properties of benzimidazole-alkyl phosphonates systems, which could be inserted as ion carriers groups in polymeric exchange membranes, by means of ^{1}H DQMAS, variable temperature ^{1}H MAS, and ^{31}P CODEX experiments [81]. By combining ^{1}H MAS and DQMAS experiments, the hydrogen bonding network was characterized. Furthermore, variable temperature ^{1}H MAS and ^{31}P CODEX experiments revealed the occurrence of a 3-fold reorientational motions of the phosphonate groups, which leads to the interchange between the protons involved in N$\cdots$H$\cdots$O and O$\cdots$H$\cdots$O hydrogen bonds, between the same phosphonate groups and the N-H and O-H groups belonging to the adjacent benzimidazole and phosphonate groups, respectively. This proton interchange is considered to be of crucial importance in favouring the site-hopping mechanism for the ion

transport through the membrane. Finally, in several works SSNMR was used to study the degradation processes in polymeric exchange membrane. K. Muller et al. investigated the degradation of Nafion membranes with variable thickness by means of ^{19}F and ^{13}C MAS experiments [76]. From the analysis of the spectra of the membranes before and after in situ tests they found that degradation processes mainly involve the polymer side chains, and that they were more pronounced by decreasing the membrane thickness, suggesting the presence of a degradation mechanism proceeding from the membrane surface.

Polymeric photoactive materials for solar cells

Another class of materials for which SSNMR revealed to be very useful is that of polymeric photoactive materials for solar cells. In this field SSNMR was used to study the phase and, less commonly, the dynamic properties of donor and acceptor both as neat compounds and in the final photoactive materials, as well as to investigate the morphological properties of the photoactive blends in terms of mixing degree and phase separation at the interface between donor and acceptor domains [83–97]. To these aims the SSNMR techniques of main utility are ^{13}C and ^{1}H MAS experiments, for the study of the phase properties of the different organic domains, variable temperature T_1 and $T_{1\rho}$ measurements, for the study of the dynamic processes, and techniques investigating the spin diffusion process, such as Goldmann Shen experiments, and the measurements of ^{1}H T_1 and $T_{1\rho}$, for the study of the degree of homogeneity of the photoactive material. Poly(3-alkylthiophenes) are one of the most promising classes of conductive polymers for photovoltaic applications, commonly used as donor in polymeric BHJ photoactive materials. Several studied were carried out in which their structural, phase and dynamic properties, such as π-stacking interaction, phase transitions between different crystalline forms, degree of mobility of both main and side chains, were investigated by means of SSNMR techniques [83–88]. K. Saalwachter et al exploited the sensitivity of ^{13}C chemical shift and ^{13}C -^{1}H dipolar interaction to conformational properties and degree of mobility of polymeric materials, respectively, to investigate the thermal phase transitions and the dynamic properties of poly(3-hexylthiophenes) with different molecular

weights, by means of ^{13}C MAS and DIPSHIFT experiments [86]. Thanks to the difference between the ^{13}C chemical shift of methyl groups in side chains with all-trans (about 15 ppm) and disordered conformations (about 14 ppm), variable temperature ^{13}C MAS experiments allowed the observation, around 60 °C, of the transition between two different P3HT crystalline phases characterized by higher and lower all-trans conformational order of the hexylic side-chains. On the other hand, through variable temperature DIPSHIFT experiments, the dynamic behaviour of the polymer main and side chains over the temperature range around the phase transition (20-70 °C) was investigated. Indeed the DIPSHIFT experiments allow the strength of the ^{1}H-^{13}C dipolar coupling, which is known to decrease by increasing the degree of mobility, to be measured. While the polymer main chain resulted to be almost unaffected by the phase transition, remaining quite rigid, the mobility of the hexylic sidechains was found to significantly increase above 60 °C. A similar study was carried out by K. Yazawa et al. on higher molecular weight P3HT, undergoing a transition from rigid to plastic crystalline phase, the latter being characterized by a higher mobility of P3HT main chain [87]. In their work the dynamic properties were investigated through the analysis of variable temperature ^{13}C T_1 data. SSNMR spectroscopy was proved to be a powerful technique also to measure the nanoscale structure of *donor-acceptor* photoactive blends, as demonstrated by numerous studies reported in the literature [90–97]. A. J. Heeger et al. investigated the structural properties at the interface between the donor and acceptor domains in P3HT/PCBM BHJ blends before and after thermal annealing at 150 °C, by means of ^{1}H MAS and ^{1}H-^{13}C HETCOR experiments [96]. By the observation of the correlation between the ^{13}C and ^{1}H signals of PCBM C_{60} carbons and P3HT aliphatic protons, which was found to be strong and weak in the HETCOR spectra of the blends before and after annealing, respectively, they concluded that a molecular separation between P3HT and PCBM at the interface occurs following the annealing. There are also several examples in which the morphological properties and the degree of mixing between donor and acceptor on a larger scale were investigated exploiting the process of proton spin diffusion. D. L. VanderHart et al. used Goldman Shen experiments to study the degree of homogeneity in P3HT/PCBM BHJ photoactive blends subjected to different thermal treatments [97].

Through the Goldman Shen experiment, a magnetization gradient for the ^{1}H nuclei was created by modulating the signal on the basis of the isotropic chemical shift; then the evolution of the longitudinal magnetization was recorded and analysed. By comparing the experimental data with the curves simulated for increasing values of the domain dimensions, the authors concluded that PCBM domains with different dimensions, from few nanometers to tens of nanometers, were dispersed in a P3HT matrix. Moreover, they found that PCBM domains became on average larger after annealing at 150 °C, that is the material became morphologically more heterogeneous. It is worth to notice that both the separation of P3HT and PCBM at the interface, and the increase of phase separation between the two components, being possibly associated with the formation of more linear "channels" for the charges transport, could contribute to determine the increase of efficiency of the final solar cell after thermal annealing. Finally, Adriaensen et al. exploited the sensitivity of ^{1}H T_1 to the phase and morphological properties of PCBM (longer T_1 should correspond to larger and well-formed crystalline PCBM domains), for studying how these properties depend on the preparation and post-treatment procedures of the PCBM film [89]. Moreover, in several works they demonstrated the utility of ^{1}H T_1 and $T_{1\rho}$ data to investigate the morphological properties and the degree of homogeneity of different PCBM-donor BHJ blends [90, 92–94].

Chapter 3

Study of the structural, phase and dynamic properties of a new LDPE-based anion exchange membrane for water electrolysis

3.1 Introduction

Polymeric anion exchange membranes have become very popular in the field of fuel cell technology, providing several advantages with respect to the proton exchange ones, such as the use of more economic catalysts, faster kinetics at the electrodes, and decrease of fuel cross-over. These properties along with the advantages deriving form the use of low-cost, easy processable, and highly flexible polymeric materials could also be appealing for water electrolysis devices, which produce hydrogen from water decomposition, even if, interestingly, AEM have not been widely used for this kind of application [98, 99]. The main drawback of AEM concerns the values of OH^- conductivity, which are low compared to the proton conductivities in PEM.

In paragraph 2.1.2, it was shown how the performances of a polymeric exchange membrane, such as ion exchange capacity, water-uptake, ion conductivity, hydrogen per-

meability, stability and durability, are determined by the structural, phase, and dynamic properties of both the hydrophilic and hydrophobic components on a molecular and supramolecular scale. The investigation of these properties and the understanding of their correlations with the macroscopic behaviour is very important to optimize AEM performances. To this aim SSNMR can give and has already given an important contribution, as shown in section 2.2. Indeed, the possibility to determine various nuclear properties through different SSNMR techniques can be exploited to obtain important information on the structural and dynamic properties of different AEM components, such as the hydrophobic components, the hydrophilic functional groups, and the water domains.

In this chapter a SSNMR study of a novel AEM for water electrolysis is presented [100].

3.2 Materials and aims

The SSNMR study presented in this chapter arises from a collaboration with Dr. Andrea Pucci and coworkers, Dipartimento di Chimica e Chimica Industriale, Università di Pisa, and ACTA S.p.A., who developed and tested a novel polymeric anion exchange membrane, to be applied in water electrolysis devices. The membrane object of this study is constituted by 1,4-diazabicyclo(2.2.2)octane (Dabco) ammonium salts, grafted to a low-density poly(ethylene)(LDPE) film through 4-Vinylbenzyl chloride (VBC) moieties (Figure 3.1). VBC-Dabco ammonium salt groups are the hydrophilic groups directly involved in the ion transport, while LDPE constitutes the hydrophobic domains, and determines the structural, mechanical, and stability properties of the membrane, as well as properties such as water-uptake and ion-conductivity. In particular, LDPE was selected because, beside being a low-cost commodity, it shows an interesting combinations of properties such as stability in severe electrochemical environments, hydrophobicity, negligible swelling, good mechanical properties under demanding environments; moreover LDPE films can be easily functionalized through radical grafting processes, as that used in this work [101].

The structural, dynamic and morphological properties of the LDPE-g-VBC-Dabco membrane on a nanometric and sub-nanometric scale were completely unknown, and the investigation of these properties, beside being interesting by itself, was considered very important to understand the final performances of the membrane. For example, the structure, and the degree of mobility of the VBC-Dabco functional groups, as well as their distribution throughout the membrane, could influence the efficiency of the ion transport. The latter, along with the water-uptake, could also be related to the phase and dynamic properties of the LDPE domains. An other important aspect to be investigated was the degree of cross-linking of the Dabco salt, that is the formation of Dabco bridges (cross-links) between two different VBC moieties, which could affect the mechanical stability of the membrane [102]: high degrees of cross-linking usually lead to worse mechanical properties and stability.

The aim of the SSNMR study was to investigate these properties by combining suitable SSNMR techniques. ^{13}C MAS spectra are known to be very useful to study the structural properties of organic domains; in this thesis they were used to obtain information on the conformational properties of the VBC-Dabco groups, the degree of cross-linking of Dabco moieties, as well as to investigate the phase properties of LDPE. ^{13}C domain-selective CP/MAS experiments, through which it is possible to distinguish different ^{13}C nuclei on the basis of the degree of mobility of the corresponding domains, were used to obtain information on the average dynamic behaviour of both the VBC-Dabco moieties and the LDPE domains. The degree of averaging of the ^{1}H T_1 and $T_{1\rho}$ under the effect of the spin diffusion process gives information on the degree of homogeneity of the system on the 10-20 Å and 100-200 Å spatial scales. Here, measurements of ^{1}H T_1 and $T_{1\rho}$ were found useful to investigate the morphological properties of the LDPE matrix, as well as the distribution of the VBC-Dabco groups among the crystalline and amorphous domains of LDPE.

Before going through the SSNMR results, some details concerning the preparation of the LDPE-g-VBC-Dabco anion exchange membrane, as well as the main results from a preliminary IR, DSC and SEM structural characterization, and from electrochemical and in cell electrolysis tests, will be reported. Both the preparation and the structural

and electrochemical characterization were carried out by Andrea Pucci and coworkers in collaboration with ACTA S.p.A.

3.2.1 Preparation and IR, DSC, EDS characterization

The LDPE-g-VBC-DABCO anion exchange membrane was prepared through a two-steps preparation process illustrated in Figure 3.1 [100]. The first step consisted in the grafting of the VBC functionalizing monomer to LDPE by means of a radical reaction: the LDPE film was soaked in a solution of VBC containing 0.07 % of the benzophenone photointiator, and then it was irradiated with UV radiation at 70 °C for 30 min. In the following, the VBC functionalized LDPE film will be indicated as LDPE-g-VBC. In the second step the chlorine atoms of the VBC -CH_2Cl groups were replaced with Dabco moieties through a nucleophilic substitution reaction. This step, which is called ammination or quaternization reaction, was carried out by keeping the film in a methanol solution containing a large excess of Dabco with respect to -CH_2Cl groups (amine/-CH_2Cl molar ratio of about 100) at 60 °C for 72 h. The LDPE, LDPE-g-VBC, and LDPE-g-VBC-Dabco films were characterized by means of IR, DSC, and EDS (Energy-dispersive X-ray spectroscopy) [100].The observation of the IR bands relative to the C=C aromatic double bonds at 1610 and 1510 cm^{-1}, the bending of the -CH_2Cl at 1265 cm^{-1}, the bending of the C=C-H units at 840 cm^{-1}, and the stretching C-Cl at 675 cm^{-1} in the IR spectrum of LDPE-g-VBC confirmed the functionalization of LDPE with VBC units. Similarly, the disappearance of the band of the -CH_2Cl bending in the IR spectrum of LDPE-g-VBC-Dabco proved the occurrence of the substitution of the chlorine atoms in

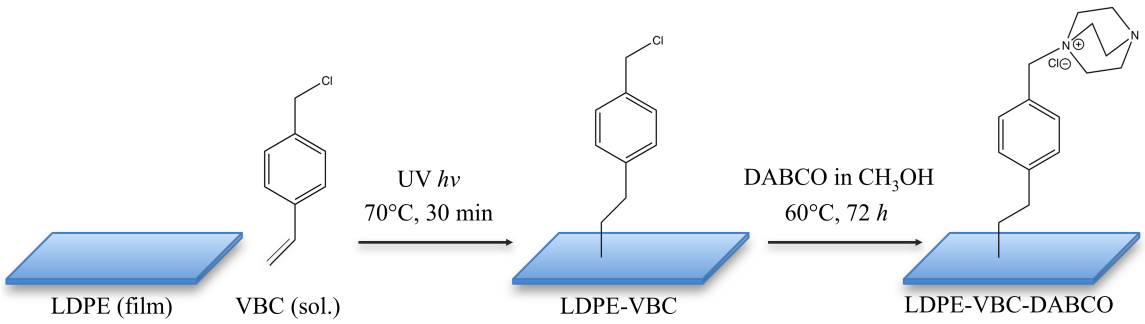

Figure 3.1: Preparation of the LDPE-g-VBC-Dabco anion exchange membrane.

-CH_2Cl with Dabco. EDS analysis on LDPE-g-VBC allowed to determine the degree of functionalization in terms of chlorine atoms content, which was found to be about 16 % and 6.5 % in the film surface and bulk, respectively.

Finally the phase properties of LDPE in the neat and LDPE-g-VBC films were preliminarily investigated by means of DSC. In both cases the thermograms showed the presence of an endotherm peak at about 110 °C, ascribable to the melting of crystalline LDPE; however the lower melting endotherm calculated for the functionalized film (ΔH = 104.2 J/g for LDPE and 87.1 J/g for LDPE-g-VBC) suggested that polymer crystallinity could be partially affected by the functionalization process.

3.2.2 Electrochemical characterization and electrolysis tests

The electrochemical properties of ion-exchange capacity (IEC), water-uptake (WU), hydrogen permeability, through-plane and in-plane conductivities of the final LDPE-g-VBC-Dabco membrane were determined, as well as its in cell performances, in terms of current density vs applied voltage, hydrogen production, and degradation [100]. These measurements and tests were performed on the LDPE-g-VBC-Dabco membrane converted to the carbonate (ion conductivity and WU measurements) or oxidrylic (IEC measurements and in cell tests) forms, where the chloride counteranions were substituted with CO_3^{2-} and OH^- anions, respectively. The results were then compared with the properties of a benchmark alkaline membrane, used as a reference. In Table 3.1 the results obtained for the electrochemical properties at different temperatures are reported. IEC is determined by the amount of functional hydrophilic groups present in the membrane, and, as mentioned in paragraph 2.1.2, it seems to be strongly related to the ion conductivity of the membrane, higher IEC usually corresponding to higher conductivities. In this work IEC was determined by titrating the excess of HCl in a water solution after the reaction with the OH^- groups present in the LDPE-g-VBC-Dabco membrane. The water-uptake is a measure of the capacity of the membrane to absorb water, and it seems to determine both the ion conductivity and the mechanical stability of the membrane. On the one hand, high water contents should favour the ion transport through the membrane, i.e. higher conductivity values. However, this leads to stronger

Table 3.1: Comparison between the electrochemical characterization of a LDPE-g-VBC-Dabco membrane and a benchmark membrane as a function of temperature.

	T (°C)	LDPE-g-VBC-Dabco	Benchmark
IEC (meq/g)	30	1.5	1.8
WU (wt%)	30	81	61
	45	91	70
	60	94	75
σ_{IP} (mS/cm) HCO_3^-/CO_3^{--} form	30	14	15
	45	19	19
	60	25	25
σ_{TP} (mS/cm) HCO_3^-/CO_3^{--} form	30	10	6
	45	14	11
	60	17	19
Hydrogen Permeability ($mol \cdot cm \cdot cm^{-2} \cdot sec^{-1} \cdot kPa^{-1}$) HCO_3^-/CO_3^{--} form	30	3.4×10^{-13}	2.1×10^{-13}
	45	5.8×10^{-13}	2.7×10^{-13}
	60	7.5×10^{-13}	3.3×10^{-13}

mechanical stresses, compromising the mechanical resistance of the membrane. In this work the water-uptake (WU) was calculated as:

$$WU = \frac{WU_{wet} - WU_{dry}}{WU_{dry}} \tag{3.1}$$

As we can see from Table 3.1, the results obtained for the electrochemical properties were very promising, being very similar to those found for the benchmark membrane. The larger differences concerned the WU and the hydrogen permeability properties, whose values are both significantly higher for LDPE-g-VBC-Dabco than for the benchmark membrane. The high values of WU are still within a range in which the mechanical stability is not compromised. Normally an acceptable value of WU is assumed to be lower than 100% at temperatures below 50 °C. On the other hand, the high hydrogen permeability could lead to problems of fuel cross-over under operating conditions. The electrochemical properties of LDPE-g-VBC-Dabco allowed electrolysis tests to be performed. These showed that the in-cell performance of LDPE-g-VBC-Dabco was slightly worse, but still comparable to those of the benchmark membrane. In particular, lower current density and hydrogen production, as well as faster degradation under operating conditions were found for the LDPE-g-VBC-Dabco membrane. The lower levels of hy-

drogen production could be related to the problem of fuel cross-over, enhanced in LDPE-g-VBC-Dabco due to the higher values of hydrogen permeability; furthermore, the fact that LDPE-g-VBC-Dabco underwent faster degradation processes could be explained by the higher electrical resistance of this membrane with respect to the benchmark one, as also shown by the lower values of conductivity.

3.3 SSNMR techniques

Different ^{13}C and ^{1}H high resolution techniques were combined to study the LDPE-g-VBC-Dabco membrane. The following paragraphs contain a description of the principal SSNMR techniques employed in this work.

3.3.1 ^{13}C CP/MAS domain-selective experiments

^{13}C CP/MAS domain-selective experiments have been widely used within the SSNMR group in Pisa for studying the phase properties of polymeric systems; indeed, useful information can be obtained from the selective observation of polymeric domains with different degree of mobility [59, 60]. These experiments are the ^{13}C CP/MAS, ^{13}C CP/-MAS with short *contact time*, and the ^{13}C Delayed-CP/MAS experiments: the first allows ^{13}C isotropic signals arising from both rigid and mobile to be observed, while ^{13}C CP/MAS with short *contact time*, and the ^{13}C Delayed-CP/MAS experiments are able to select signals from more rigid and more mobile polymeric domains, respectively.
Cross polarisation (CP) is a technique commonly used in SSNMR to enhance the signals arising from dilute spins in NMR spectra. In the following, we will assume ^{1}H and ^{13}C to be the abundant and the dilute spins, respectively, being also the case of this study. CP is based on the transfer of transverse magnetization (in the rotating frame) from the abundant ^{1}H to the dilute ^{13}C spin system, during the simultaneous application of transverse rf fields to the ^{1}H and ^{13}C channels. The magnetization transfer can occur only if the Hartmann-Hann condition is satisfied [2]:

$$\gamma_H B_H = \gamma_C B_C \tag{3.2}$$

where γ_H and γ_C denote the proton and carbon gyromagnetic ratios, while B_H and B_C indicate the strengths of the rf magnetic fields applied on the proton and carbon channels, respectively. The angular frequency $\gamma_H B_H$ ($\gamma_C B_C$) assumes values corresponding to frequencies in Hz ($\frac{\gamma_H B_H}{2\pi}$) of the order of tens of kHz. The scheme of a generic ^{1}H-^{13}C CP experiment, with ^{1}H decoupling applied during the signal acquisition, is shown in Figure 3.2. The intensity of ^{13}C transverse magnetization created through CP depends on the duration of the CP pulses, which is called the contact time (ct). Considering a pair of dipolar coupled ^{1}H and ^{13}C nuclei, for which the conditions $T_{1\rho}(H) >> T_{CH}$ and $T_{1\rho}(C) >> T_{CH}$ are satisfied, the evolution of the ^{13}C magnetization (M) follows the equation [103]:

$$M(ct) = M_{eq}(e^{-\frac{ct}{T_{1\rho}(H)}} - e^{-\frac{ct}{T_{CH}}}) \tag{3.3}$$

where $T_{1\rho}(H)$ is the spin lattice relaxation time of the nucleus ^{1}H in the rotating frame, and T_{CH} is a time costant called the *cross-polarisation* time. T_{CH} depends on the dipolar interaction between the coupled ^{1}H and ^{13}C nuclei, becoming shorter when the strength of the ^{1}H-^{13}C dipolar interaction increases. In Figure 3.3 the M vs ct curves are reported for two different T_{CH} values of 5 ms and 10 ms. In both cases, the ^{13}C magnetization exponentially increases in the first part of the curve, when $ct << T_{1\rho}(H)$, according to the approximate equation $M_{eq}(1 - e^{-\frac{ct}{T_{CH}}})$; for longer ct values, also the

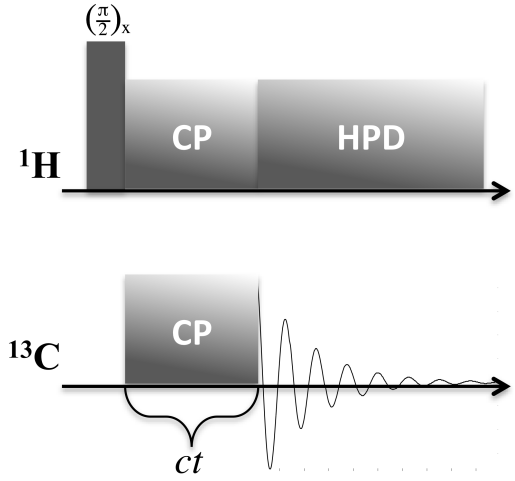

Figure 3.2: ^{13}C-^{1}H cross polarisation (CP) experiment, typically carried out under MAS conditions (^{13}C CP/MAS). ^{1}H high power decoupling (HPD) is performed during the acquisition of the ^{13}C signal.

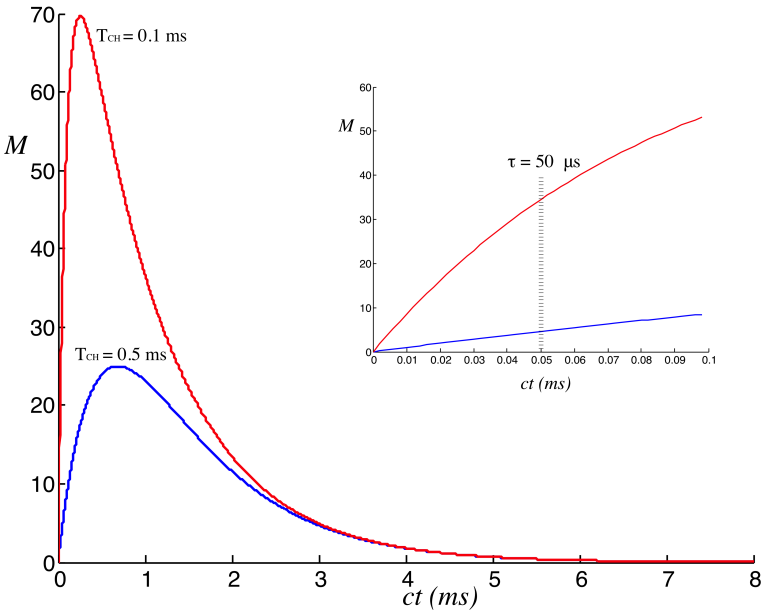

Figure 3.3: Evolution of the ^{13}C transverse magnetization (M) during the CP pulses in function of the contact time (ct). The curves are calculated for $T_{1\rho}$ = 1 ms, and T_{CH} = 0.5 (blue) and 0.1 ms (red).

term $e^{-\frac{ct}{T_{1\rho}(H)}}$ give a significant contribution to Eq. 3.3, leading to a progressive decrease of $M(ct)$. It is interesting to notice that the build up of M for short ct depends on the T_{CH} time constant, being faster for shorter T_{CH} (Figure 3.3). This behaviour suggests a way to select the magnetization of domains characterized by strong ^{1}H-^{13}C dipolar

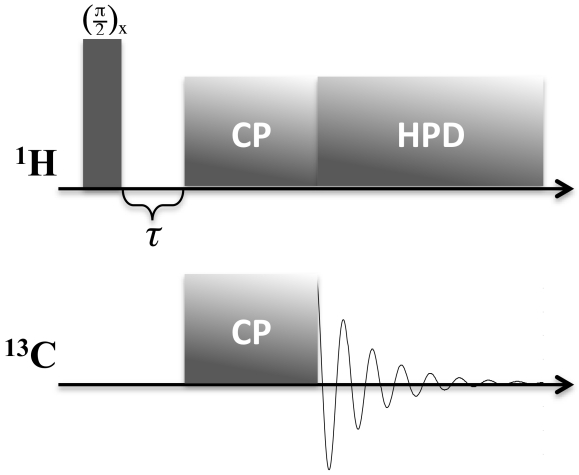

Figure 3.4: ^{13}C-^{1}H delayed cross polarisation experiment, typically carried out under MAS conditions (^{13}C Delayed-CP/MAS). A delay τ is present between the excitation $\frac{\pi}{2}$ pulse on the ^{1}H channel and the CP pulses. ^{1}H high power decoupling (HPD) is performed during the acquisition of the ^{13}C signal.

coupling interaction, i.e. shorter T_{CH}, by performing CP experiments with short values of *ct* (detail in Figure 3.3). Since the dipolar coupling interaction tends to be averaged in the presence of fast reorientational motions, leading to longer T_{CH}, the use of short *ct* allows the selective observation of the signals arising from the most rigid domains of the sample.

In the ^{13}C Delayed-CP/MAS experiment a delay (τ) is inserted respect to CP between the $\frac{\pi}{2}$ excitation pulse on the ^{1}H channel and the CP pulses, as shown in Figure 3.4 [104]. During τ the ^{1}H transverse magnetization decays according to the $spin-spin$ relaxation mechanism, regulated by the time constant T_2: a shorter T_2 corresponds to a faster decay and vice versa. Since ^{1}H T_2, being mainly determined by the strength of the ^{1}H-^{1}H homonuclear dipolar couplings, monotonically increases with the molecular mobility, by setting a suitably long τ delay in the ^{13}C Delayed-CP/MAS sequence, it is possible to isolate the ^{13}C signals arising from regions of the sample with a higher degree of mobility.

3.3.2 Measurement of ^{1}H T_1 and $T_{1\rho}$

^{1}H T_1 and $T_{1\rho}$ relaxation processes can be measured by using different techniques, which can be based on direct or indirect measurements. In the first case, the decay of ^{1}H magnetization is directly observed, while in the second case the proton relaxation parameters are determined by observing the decay of ^{13}C magnetization (or other dilute spin) created by CP. The second strategy is that used within this work, and allows to highlight differences in the T_1 and $T_{1\rho}$ of protons belonging to different components or regions of the samples, exploiting the high resolution of ^{13}C spectra.

Inversion recovery-^{13}C CP/MAS experiments

^{1}H T_1 was measured using the inversion recovery-^{13}C CP/MAS sequence, which is represented in Figure 3.5 [58]. A π pulse is applied on the proton channel to achieve the inversion of the ^{1}H signal. Then, the ^{1}H spin system is allowed to relax according to the longitudinal *spin-lattice* relaxation mechanism during a variable delay τ, which is progressively increased during the measurement. After the relaxation delay τ, a $\frac{\pi}{2}$ pulse

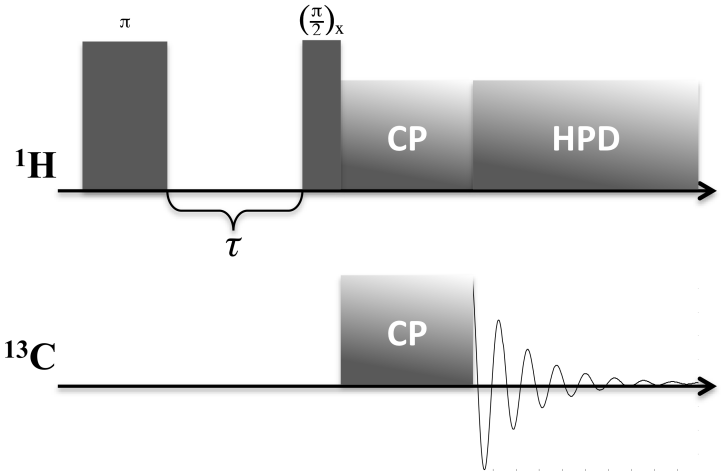

Figure 3.5: Inversion recovery coupled with ^{1}H-^{13}C CP/MAS experiment for the measurement of ^{1}H T_1.

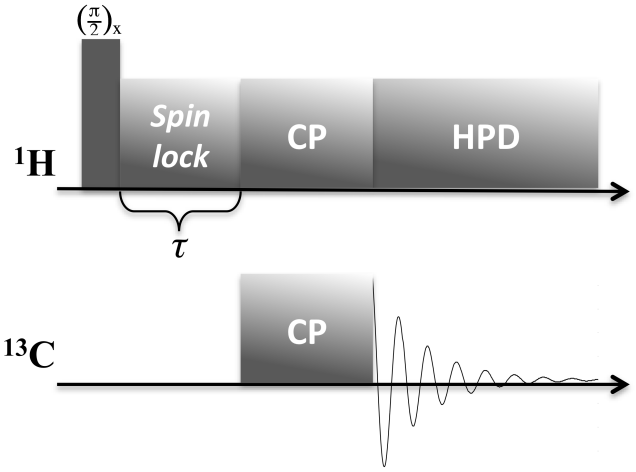

Figure 3.6: Variable spin-lock coupled with ^{1}H-^{13}C CP/MAS experiment for the measurement of ^{1}H $T_{1\rho}$.

is applied on the proton channel, followed by CP pulses, and the acquisition of the ^{13}C signal.

^{1}H T_1 is determined by fitting the experimental build-up curve of the ^{13}C signal intensity with the equation:

$$M(t) = M_{eq}(1 - Ae^{-\frac{t}{T_1}}) \tag{3.4}$$

where $M(t)$ is the magnetization at time t, and A is a parameter which takes into account

possible pulses imperfections. In ideal conditions, A assumes the value of 2.

Variable spin-lock-^{13}C CP/MAS experiments

In order to measure ^{1}H $T_{1\rho}$ a spin-lock pulse of variable duration (τ) is inserted between a $\frac{\pi}{2}$ pulse on the proton channel and the CP pulses, as shown in Figure 3.6 [105]. During the application of the spin-lock field with a rf amplitude of the order of kHz, the ^{1}H magnetization decays under the effect of the spin-lattice relaxation mechanism in the rotating frame, regulated by the time constant $T_{1\rho}$. In the presence of a single component ^{1}H $T_{1\rho}$ is measured by fitting the experimental decay curve with a monoexponential decay function.

3.4 Results and discussion

In order to get information on how the different steps of the preparation process affect the structural, phase and dynamic properties of the LDPE matrix and VBC groups, the SSNMR study was carried out on the LDPE-g-VBC-Dabco system as well as on the LDPE-g-VBC intermediate and the pristine LDPE film. As far as the final LDPE-g-VBC-Dabco membrane is concerned, the chlorinated membrane was studied before undergoing hydration and/or exchange processes.

3.4.1 ^{13}C domain-selective CP/MAS experiments

In Figure 3.7 the ^{13}C CP/MAS spectra of LDPE, LDPE-g-VBC and LDPE-g-VBC-Dabco recorded with ct = 1 ms are reported. All the spectra show an intense signal at about 31-33 ppm ascribable to PE carbons. Furthermore, in the spectrum of LDPE-g-VBC a signal at about 46 ppm and a group of signals at about 120-150 ppm, ascribable to VBC CH_2Cl and aromatic carbons, respectively, can be observed [106]. The latter signals are also present in the spectrum of LDPE-g-VBC-Dabco together with two signals at 45.8 and 52.9 ppm ascribable to Dabco carbons, one and two bonds far from the ammonium moiety, respectively [107]. The disappearance of the -CH_2Cl carbon signal in passing from the spectrum of LDPE-g-VBC to that of LDPE-g-VBC-Dabco, and the corresponding

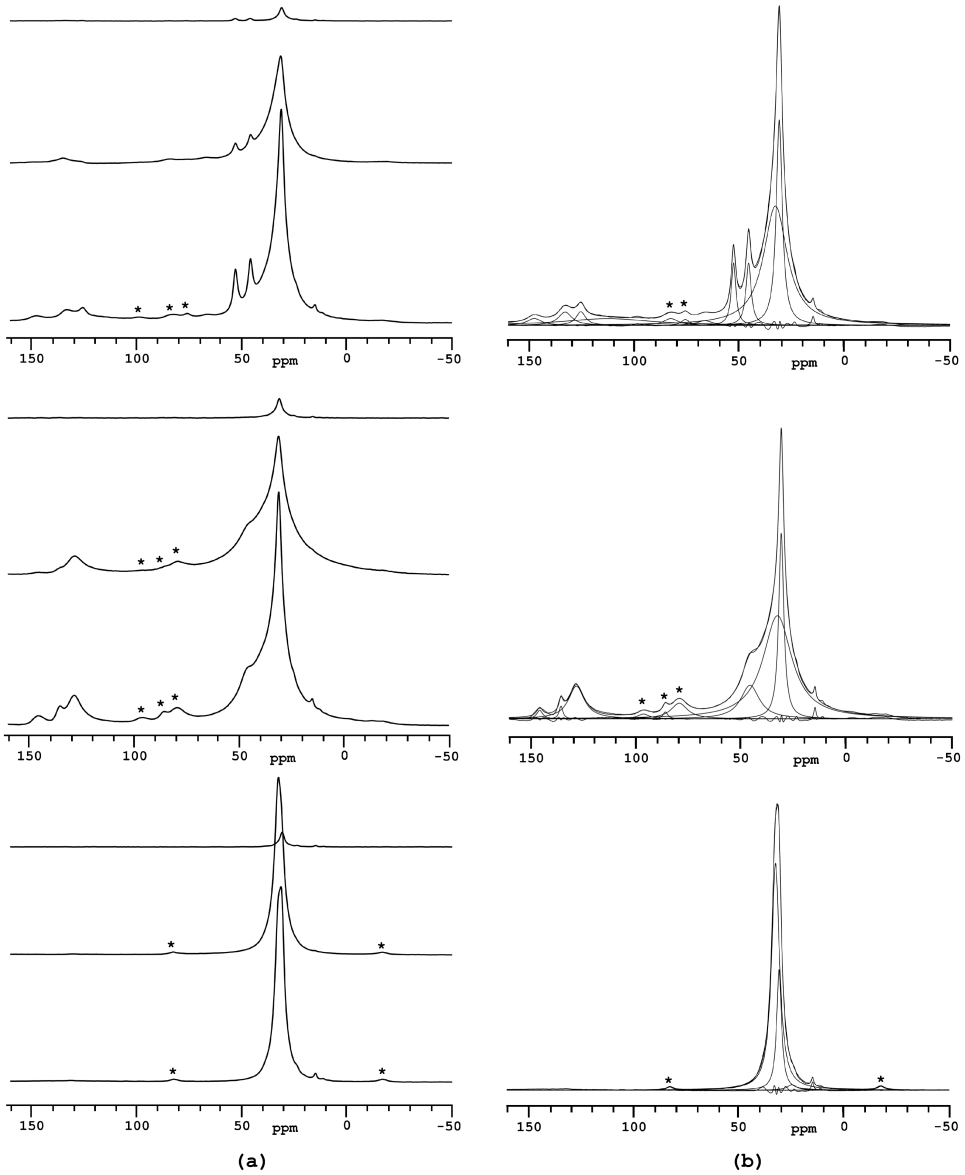

Figure 3.7: (a) From bottom to top: ^{13}C domain-selective spectra of pristine LDPE, LDPE-g-VBC, and LDPE-g-VBC-Dabco films. For each sample, from bottom to top, the ^{13}C CP/MAS spectra recorded with ct = 1 ms and 50 μs, and the ^{13}C-Delayed CP/MAS spectrum are reported. (b) From bottom to top: spectral deconvolutions of the ^{13}C CP/MAS spectra recorded with ct = 1 ms relative to LDPE, LDPE-g-VBC, and LDPE-g-VBC-Dabco.

appearance of those arising from Dabco carbons, indicate that the ammination reaction was complete, in agreement with FT-IR results. On the other hand, the similar intensity shown by the two Dabco signals at 45.8 and 52.9 ppm suggests that most of Dabco does not cross-link, likely due to the relevant molar excess of amino groups with respect to the grafted chlorobenzylic moieties (that is, amine/-CH_2Cl mol. ratio $\sim$ 100) used during the ammination process.

In order to obtain information on the phase and dynamic behaviour of the different sample components, ^{13}C domain-selective experiments were performed. In particular, ^{13}C CP/MAS spectra with ct = 1 ms and 50 μs and ^{13}C Delayed-CP/MAS spectra with τ = 100 μs were acquired. While in the ^{13}C CP/MAS spectrum with ct = 1 ms signals arising from both rigid and mobile domains should be present, in the ^{13}C CP/MAS with ct = 50 μs and in the ^{13}C Delayed-CP/MAS spectra signals arising from rigid (characterized by short T_{CH}) and mobile domains (characterized by long proton T_2) can be selectively observed, respectively. The ^{13}C domain-selective spectra of all the samples are reported in Figure 3.7a. As far as LDPE-g-VBC-Dabco is concerned, the quite high intensity of all the signals in the ^{13}C CP/MAS spectrum recorded with ct = 50 μs and their substantial suppression in the ^{13}C Delayed-CP/MAS one indicate that PE, VBC and Dabco are all quite rigid. This is also confirmed by the ^{1}H MAS spectra (Figure A.1), where the signals belonging to LDPE, VBC and Dabco start to be partially resolved only at a MAS frequency of 20 kHz. Almost the same behaviour can be observed for LDPE and VBC signals in the ^{13}C domain-selective spectra of LDPE and LDPE-g-VBC, suggesting that the average mobility of these components does not change significantly during the preparation process.

Information on the phase properties of the LDPE matrix was also obtained. PE is a semicrystalline polymer above the glass transition temperature (T_g $\sim$ -120 °C for LDPE [108]). It is known that in ^{13}C high resolution SSNMR spectra PE amorphous and crystalline fractions, characterized by PE chains experiencing fast trans-gauche interconformational jumps and in all-trans conformation, respectively, give rise to two easily distinguishable signals: the former at about 31 and the latter at about 33 ppm. As it can be observed in Figure 3.7, two signals ascribable to amorphous and crystalline

Table 3.2: Chemical shift (δ), linewidth (Δ), and integral (**I**) determined for the signals of crystalline (**c**) and amorphous (**a**) LDPE through deconvolution of the ^{13}C CP/MAS spectra recorded with ct = 1 ms. **I** is calculated as the percentage of the integral relative to **a** (**c**) with respect to the sum of the integrals of **a** and **c**.

	a			**c**		
	δ (ppm)	**Δ (Hz)**	**I (%)**	**δ (ppm)**	**Δ (Hz)**	**I (%)**
LDPE	30.8 ± 0.1	280 ± 30	26 ± 4	32.6 ± 0.1	440 ± 10	74 ± 4
LDPE-g-VBC	31.0 ± 0.1	340 ± 10	26 ± 1	32.8 ± 0.1	1600 ± 100	74 ± 1
LDPE-g-VBC-Dabco	31.1 ± 0.1	380 ± 30	36 ± 4	32.8 ± 0.1	1600 ± 100	64 ± 4

LDPE fractions are resolved in the ^{13}C CP/MAS spectrum of LDPE recorded with ct = 1 ms, but they are no longer distinguishable in those of LDPE-g-VBC and LDPE-g-VBC-Dabco. In order to get a better understanding of the phase behaviour of LDPE, a spectral decovolution of the ^{13}C CP/MAS spectra recorded with ct = 1 ms was performed, and the results are reported in Figure 3.7b and Table 3.2. In particular, even though the ^{13}C CP/MAS spectra are not quantitative, we found, in agreement with the DCS results, that both crystalline and amorphous PE fractions are present not only in LDPE, but also in LDPE-g-VBC and LDPE-g-VBC-Dabco, and that the crystalline fraction slightly decreases in passing from LDPE and LDPE-g-VBC to LDPE-g-VBC-Dabco. On the other hand, we observed a 3-4 fold increase of the linewidth of crystalline PE signal in passing from LDPE to LDPE-g-VBC and LDPE-g-VBC-Dabco. This suggests that, similar to the case previously reported by other authors for neat LDPE at temperature higher than 25 °C [109], in the functionalized systems LDPE chains in the crystalline phase experience a motion with a characteristic frequency in the range of kHz, which interferes with the proton decoupling field. This hypothesis is further supported by ^{13}C spectra acquired at increasing temperature (from 25 °C to 70 °C, not reported here), which show that the linewidth of the crystalline PE signal is strongly dependent on temperature, i.e. on the frequency of the motion (Figure 3.8).

The behaviour of VBC aromatic carbon signals in the spectra of LDPE-g-VBC and LDPE-g-VBC-Dabco (Figure 3.9) is also worthy to be discussed. An evident change in the distribution of these signals in passing from LDPE-g-VBC to LDPE-g-VBC-Dabco

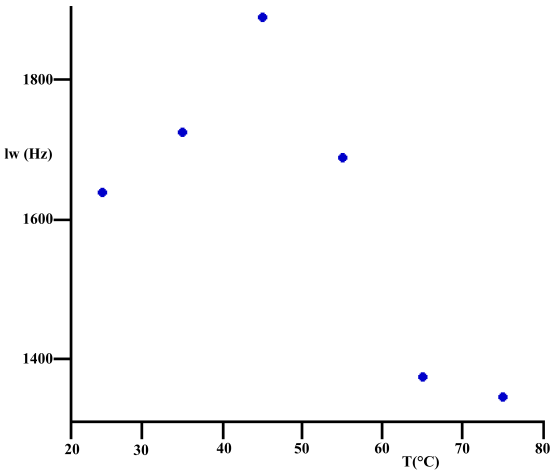

Figure 3.8: Dependence of the linewidth of the crystalline PE carbon signal on temperature, reported for LDPE-g-VBC. The values of linewidths were obtained by deconvolution of ^{13}C CP/MAS spectra recorded at different temperatures in the range between 25 and 75°C. The observed trend (increasing up to a temperature of about 45 °C and then decreasing) is in agreement with the presence of a motion in the range of kHz which interferes with the frequency of the decoupling field.

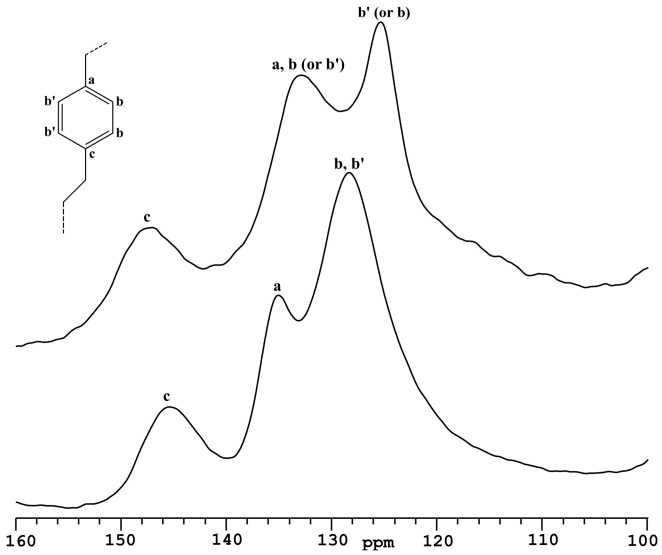

Figure 3.9: Assignment of the VBC aromatic carbon signals in the ^{13}C CP/MAS at *ct* of 1 ms spectra of LDPE-g-VBC (bottom) and LDPE-g-VBC-Dabco (top).

can be observed. In particular, beside the expected shifts of a and c carbons to lower (from 135.1 ppm to 132.9 ppm) and higher (from 145.4 ppm to 147.5 ppm) chemical shifts, respectively, we have to hypothesize a splitting of the signal arising from b and b' carbons (from one signals at about 128.4 ppm to two signals at about 125.4 and 132.9 ppm). This assignment was performed on the basis of the relative areas of the signals and of the ^{1}H-^{13}C HETCOR spectrum recorded for LDPE-g-VBC-Dabco (Figure A.2). In the latter, for instance, a strong correlation peak between the ^{13}C peak at 125.4 ppm and the ^{1}H peak at about 6.8 ppm is present, suggesting that the ^{13}C peak at 125.4 ppm arises from tertiary aromatic carbons. The presence of two very distinct signals for b, b' carbons in LDPE-g-VBC-Dabco seems to be ascribable to conformational rather than chemical effects. Indeed, it seems more likely to be due to the freezing of the inter-conformational motions of the VBC aromatic moiety following the functionalization with Dabco. Under this hypothesis, the two peaks at 125.4 and 132.9 ppm would be therefore ascribable to b and b' carbons on the two sides of the aromatic ring, experiencing quite different chemical environments due to the frozen conformation of the ring itself.

3.4.2 ^{1}H T_1 and $T_{1\rho}$ relaxation times

In order to obtain information on the degree of homogeneity of the LDPE-g-VBC-Dabco membrane, proton T_1 and $T_{1\rho}$ relaxation times have been measured by means of high resolution CP/MAS experiments. Indeed in a composite system spin diffusion tends to average proton T_1 and $T_{1\rho}$ of the various components to a different extent, depending on the dimensions of the corresponding domains. In particular, single T_1 and $T_{1\rho}$ values are observed when the system is homogeneous on 100-200 Å and 10-20 Å spatial ranges, respectively. The results obtained for the LDPE-g-VBC-Dabco system are summarized in Table 3.3. Two significantly different $T_{1\rho}$ values have been determined for PE and Dabco protons, as expected, since the distance in the molecular structure between these components is of the order of 10 Å. On the contrary very similar T_1 values were measured for all protons in the sample, indicating a substantial homogeneity of the whole system on a 200 Å spatial scale. By looking more closely at the data, however, it is possible to see that Dabco and amorphous LDPE protons have the same T_1 value within the

Table 3.3: Proton T_1 and $T_{1\rho}$ relaxation times measured from ^{13}C CP/MAS spectra for the LDPE-g-VBC-Dabco sample. The values obtained for the carbon signals arising from crystalline (**c**) and amorphous (**a**) LDPE and from Dabco (peaks at 45.8 and 52.9 ppm) are reported.

T_1 (s)				$T_{1\rho}$ (ms)			
LDPE		Dabco		LDPE		Dabco	
a	c	45.8 ppm	52.9 ppm	a	c	45.8 ppm	52.9 ppm
0.87 ± 0.03	0.99 ± 0.04	0.81 ± 0.04	0.82 ± 0.05	1.54 ± 0.03	1.97 ± 0.05	3.25 ± 0.08	3.08 ± 0.06

experimental error, while the value for crystalline LDPE is slightly higher. This suggests that the VBC-Dabco grafting preferentially occurred on the amorphous LDPE regions, rather than in the crystalline ones.

3.5 Experimental details

SSNMR experiments were carried out on a dual-channel Varian InfinityPlus 400 spectrometer, equipped with a 7.5 mm Cross Polarization/Magic Angle Spinning (CP/MAS) probehead, working at 400.03 MHz for proton, at 79.47 MHz for silicon-29 and at 100.61 MHz for carbon-13. All the experiments were performed under MAS and high-power decoupling conditions, with a MAS frequency of 5 kHz, a decoupling field of about 30 kHz and a ^1H 90° pulse duration of 5.1 μs. The ^{13}C CP/MAS spectra were obtained acquiring 20000 transients with a recycle delay of 5 s, using contact times (*ct*) of 1 ms or 50 μs. The ^{13}C-Delayed CP/MAS spectra were recorded inserting a 100 μs delay between the ^1H 90 pulse and the contact time, thus allowing the magnetization of proton nuclei having very short spin-spin relaxation times to completely dephase [104]. Proton spin-lattice relaxation times in the laboratory (T_1) and in the rotating ($T_{1\rho}$) frames were measured using the inversion recovery-CP/MAS [58] and the variable spin-lock time-CP/MAS [105] sequences, respectively. For these measurements each spectrum was recorded using a *ct* of 1 ms, and acquiring 100 and 400 transients for the inversion

recovery-CP/MAS and the variable spin-lock time-CP/MAS experiments, respectively. The 2D ^{13}C-^{1}H-^{13}C FSLG-HETCOR [110] spectrum was recorded acquiring 80 rows and 400 transients. Where not specified, the experiments were performed at room temperature and using air as spinning gas. TMS was used as a primary chemical shift reference for all nuclei, while hexamethylbenzene and adamantane as secondary references for ^{13}C, and ^{1}H, respectively.

3.6 Conclusions

This work showed how the combination of different high-resolution SSNMR experiments was useful to characterize in details the structural, phase, and morphological properties of the novel LDPE-g-VBC-Dabco anion exchange membrane.

Useful informations on the structure of the VBC-Dabco unit, as well as on the phase properties of LDPE were obtained from the analysis of ^{13}C CP/MAS spectra. The fraction of Dabco experiencing the cross-linking processes was found to be negligible, probably due to the large excess of Dabco with respect to -CH_2Cl groups used in the ammination reaction. Both crystalline and amorphous LDPE domains are present, with a crystalline content which decreases in passing from LDPE-g-VBC to LDPE-g-VBC-Dabco, in agreement with the DSC results.

^{13}C CP/MAS domain-selective spectra allowed information on the dynamic behaviour of the system to be obtained. At 25 °C both the crystalline and amorphous LDPE domains, as well as the VBC-Dabco groups, are found to be quite rigid. In particular, VBC moieties seem to be frozen in different conformations in passing from LDPE-g-VBC to LDPE-g-VBC-Dabco. In both LDPE-g-VBC and LDPE-g-VBC-Dabco, LDPE chains in crystalline domains are found to experience a motion in the range of kHz, whose frequency significantly increases by increasing temperature from 25 to 70 °C. A contribution of this motion to the observed increase of ion conductivity with temperature (Table 3.1) cannot be ruled out.

Finally, from the measurements of ^{1}H T_1, the LDPE crystalline and amorphous domains were found to be homogeneously distributed on a 200 Å spatial range, with the

VBC-Dabco groups which seems to be preferentially grafted to the amorphous ones. It is possible that the ammination process induces the passage of LDPE crystalline to amorphous domains, which is also in agreement with the observed decrease of LDPE crystallinity.

Chapter 4

Study of phase transitions in PLA/PBS-based luminescent indicators with a threshold temperature by means of variable temperature SSNMR experiments

4.1 Introduction

Smart materials able to produce specific responses to a multitude of external stimuli, such as chemical, mechanical and thermal solicitations, arise a great interest thanks to their utility in many different demanding applications (paragraph 2.1.1). Food packaging is one of the fields that could mostly benefit from the use of innovative intelligent plastic devices, able to keep memory of the "history" of the packaged materials during transport and storage [111–116].

In this framework chromogenic polymeric materials able to give optical responses to mechanical, thermal or chemical solicitations can play an important role, and large efforts have been addressed to the development of systems with tailored and optimised

performances [17, 18]. One of the most common and flexible approaches is to disperse organic dyes in thermoplastic polymeric matrices, which confer the desired mechanical properties to the material; the optical response is often based on the aggregachromic behaviour of the dye, which is the change of its optical properties in passing from the state of isolated monomer to that of aggregate.

The aggregation or disaggregation of the dye in polymeric matrices is determined by transformations of the structural and/or phase and/or dynamic properties of the polymeric domains induced by the external stimulus. The comprehension of these processes is of fundamental importance in order to realize systems with the desired smart behaviour. To this aim SSNMR can give an important contribution, thanks to the possibility of studying many different nuclear properties sensitive to different structural and dynamic properties of polymeric domains, in wide spatial and motional ranges (section 2.2).

This work is an example of SSNMR application aimed at understanding the processes lying behind the thermochromic behaviour of novel smart luminescent indicators.

4.2 Materials and aims

The SSNMR study described in this chapter was carried out within the POLOPTEL project (funded by Cassa di Risparmio di Pisa), in collaboration with Prof. Giacomo Ruggeri, Dr. Andrea Pucci and coworkers (Dipartimento di Chimica e Chimica Industriale, Universit di Pisa), who devised and realized novel thermal responsive chromogenic materials based on biodegradable polymers for rigid packaging applications.

The materials studied here are sketched in Figure 4.1: they are films constituted by a polymeric blend of poly(lactic acid) (PLA) and poly(1,4-butylene succinate) (PBS), with weight ratio 85/15, containing a small amount (0.07 %) of the dye 4,4-bis(2-benzoxazolyl)stilbene (BBS) [117]. In the following they will be indicated as PLA85PBS15. The use of PLA-based materials responds to the increasing demand for biodegradable plastics and biobased polymer products from annually renewable agricultural resources, such as corn or sugarcane [118–120]. In particular, PLA combines the advantage of being available from renewable resources with thermomechanical properties easily tuneable by

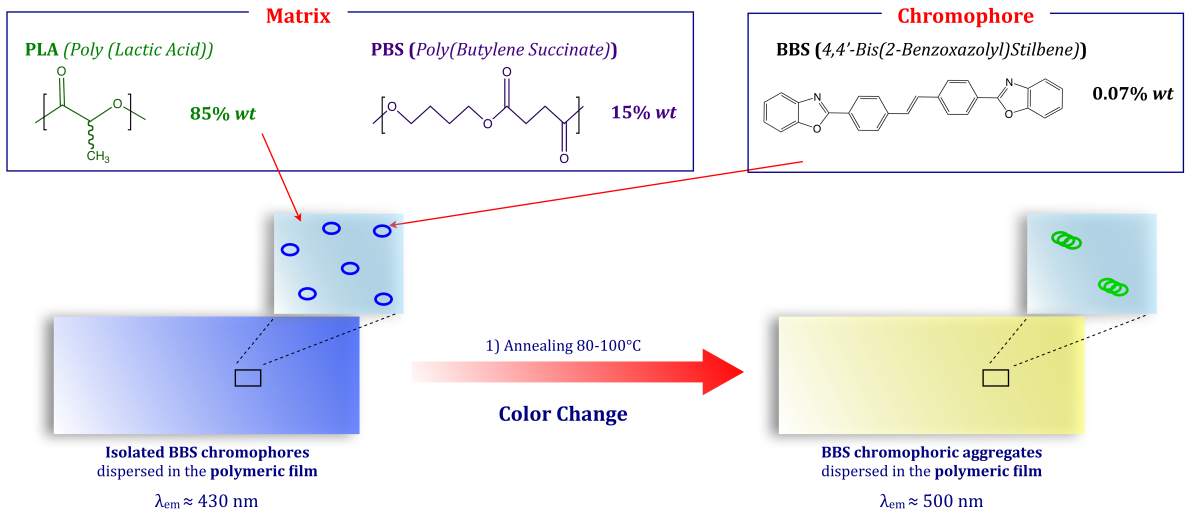

Figure 4.1: PLA85PBS15 thermochromic indicators.

means of different approaches, such as, for example, the blending with elastomeric polymers, which act as softening agents [121–127]. In PLA85PBS15 films PBS has the role of improving the thermo-mechanical behaviour of PLA, while maintaining the biodegradability of the material. Previous DSC and SEM results showed that PLA and PBS are characterized by a high compatibility in blends, without giving rise to completely miscible amorphous phases [117]; indeed two glass transition temperatures at about -30 ° and 60 °C were observed for PBS and PLA in PLA85PBS15, similar to those of the amorphous phases of the corresponding neat polymers, while a single T_g around 50 °C was expected on the basis of the Fox equation in the case of complete miscibility [117]. As far as BBS is concerned, it belongs to a well-known class of stilbene derivatives generally employed as optical brighteners in many polymer articles and textiles. BBS was found to be a very satisfactory additive for food packaging from thermoplastic materials, owing to the excellent dispersibility in polymeric matrices [117]. Moreover, its properties comply with the US Food and Drug Administration (FDA) regulations [128]. BBS shows remarkable aggregation-dependent opto-electronic properties: a red shift of the emission band attributable to a $\pi \longrightarrow \pi^*$ transition, from about 430-450 (blue) to 500 nm (green), was observed in passing from the monomer to the aggregate, due to the formation of $\pi - \pi$ stacking interactions between the planar chromophore moieties in the aggregates [129, 130]. From a previous screening, BBS was found to be highly

soluble in PLA amorphous domains even at temperatures above PLA glass transition: indeed, emission spectra at room temperature of BBS containing PLA films indicated that BBS was mainly present in the monomeric form up to concentrations of about 0.15-0.2 wt% [117]. On the other hand, BBS was found to be less soluble in PBS amorphous phases, where, at room temperature, it forms aggregates starting from low concentrations of about 0.05 wt % [117].

In a recent work it was demonstrated that PLA85PBS15 shows a thermal responsive luminescent behaviour, changing colour, from blue to green, when heated in the temperature range 70 °C -100 °C (annealing) [117]. Emission spectra confirmed that the change of colour was due to the aggregation of BBS (emission band around 500 nm), which was present in the monomeric form in the pristine PLA85PBS15 film (emission band around 430-450 nm) (Figure 4.1). It is worth noticing that BBS aggregation on heating only occured to a very small extent in PLA film, due to the already mentioned high solubility of BBS in PLA amorphous domains; conversely, due to low solubility, below 50-60 °C BBS tends to progressively aggregate in PBS amorphous domains, leading to a scarce optical stability of PBS/BBS blends. These findings prevented the use of either PLA or PBS films containing BBS as thermal responsive optical indicators. The novel smart behaviour of PLA85PBS15 film probably originates from the unique combination of the structural, dynamic and phase properties of PLA and PBS; particularly, 15 wt% was found to be the ideal amount of PBS to confer the desired properties to the film, lower and higher contents leading to a worse thermal responsiveness and a lower optical stability at room temperature, respectively [117].

Numerous structural and dynamic processes involving the polymeric matrix could interplay to drive the thermal-induced BBS aggregation in PLA85PBS15 films, and the understanding of these phenomena, beside its intrinsic interest, appears very important to devise and develop systems with similar or even improved properties. The SSNMR study presented in this chapter aimed at investigating the phase transitions occurring in PLA and PBS domains under heating, by combining high-resolution ^{13}C CP/MAS experiments and variable temperature ^{1}H FID analysis. Indeed, as it will be shown

later, ^{1}H FID analysis is very useful to study the phase properties of polymeric domains, allowing both structural and dynamic information to be obtained. In addition to the PLA85PBS15 luminescent indicator, PLA pellets and PLA film containing the 0.07 % of BBS, in the following simply referred to as PLA, were also studied for comparison.

4.3 DSC and fluorescence results

In order to get a detailed comprehension of the phase and dynamic processes occurring in the PLA85PBS15 polymeric matrix under heating, and of their contribution to induce BBS aggregation, it was of fundamental importance to compare and combine SSNMR results with DSC and fluorescence spectroscopy data. In this section the main results obtained from the spctrofluorimetric and DSC study will be reported. All the DSC and spectrofluorimetric measurements were carried out by Prof. Giacomo Ruggeri, Dr. Andrea Pucci and coworkers.

In Figure 4.2a the fluorescence emission spectra ($\lambda_{exc.}$ = 277 nm) obtained for the PLA85PBS15 film, pristine and subjected to annealing at different temperatures, from 65 to 95 °C, are reported. As we can see, the spectral features interestingly depend on the annealing temperature. In particular, it can be noticed a progressive development of the BBS aggregate band at about 480-500 nm, whose intensity overwhelms the emission contribution of the isolated BBS chromophores (400-450 nm). An overall red-shift of the emission spectrum by increasing temperature can also be observed, which is ascribable to autoabsorption phenomena. In Figure 4.3, the emission intensity variation at 490 nm as a function of temperature is reported. The figure highlights the existence of a threshold temperature at about 85 °C after which the band at 490 nm starts to steeply increase, corresponding to a rapid formation of BBS aggregates. These results were compared with those obtained for PLA film. The emission profile of PLA film appeared much less reshaped than that of PLA85PBS15 films, even after thermal annealing at 100 °C for 50 min (Figure 4.2b). In particular, the emission intensity variation at 490 nm did not exceed the value of 1.5 (Figure 4.2b), while it reaches the value of 10 in PLA85PBS15

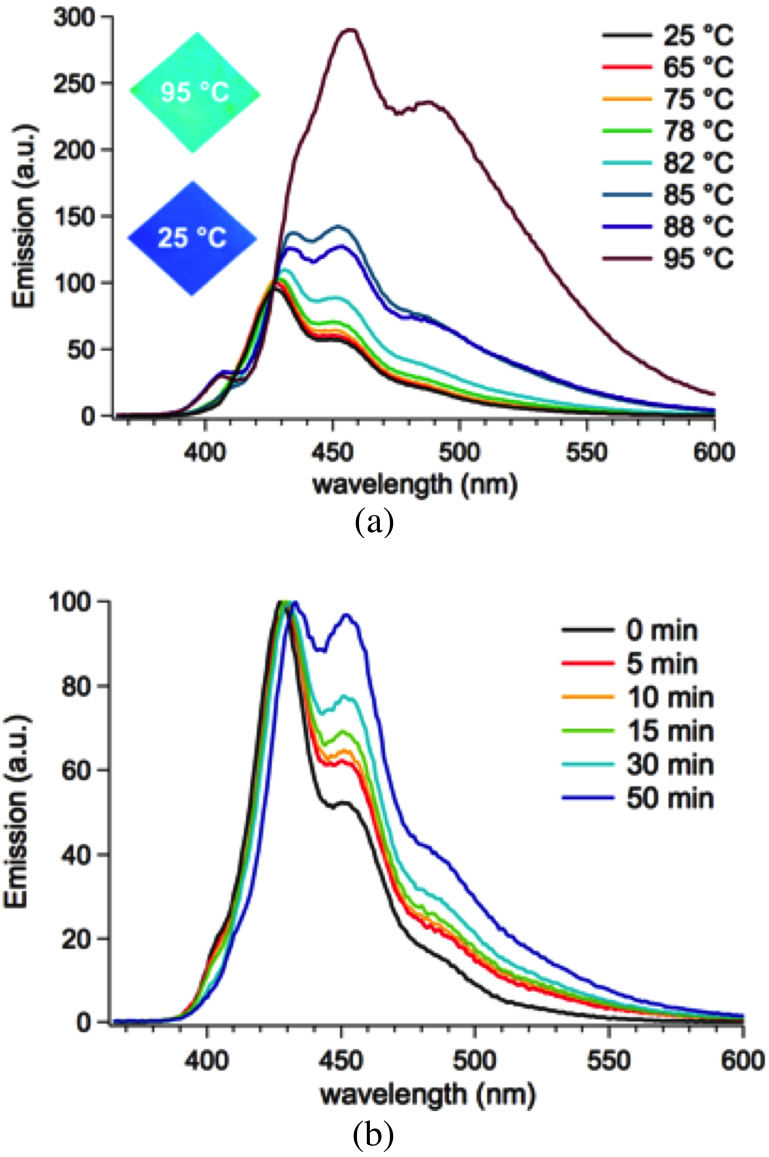

Figure 4.2: (a) Fluorescence emission spectra ($\lambda_{exc.}$ = 277 nm) of PLA85PBS15 films containing the 0.07 wt% of BBS as a function of the annealing temperature and (inset) pictures of the films at 25 °C (blue emission) and after annealing at 95 °C (green emission) taken under irradiation at 366 nm. For all cases the annealing time was 10 min. (b) Fluorescence emission spectra ($\lambda_{exc.}$ = 277 nm) of PLA films containing the 0.07 wt% of BBS as a function of the annealing time at 100 °C. The spectra are normalized to the intensity of the isolated BBS molecular peak (about 430 nm).

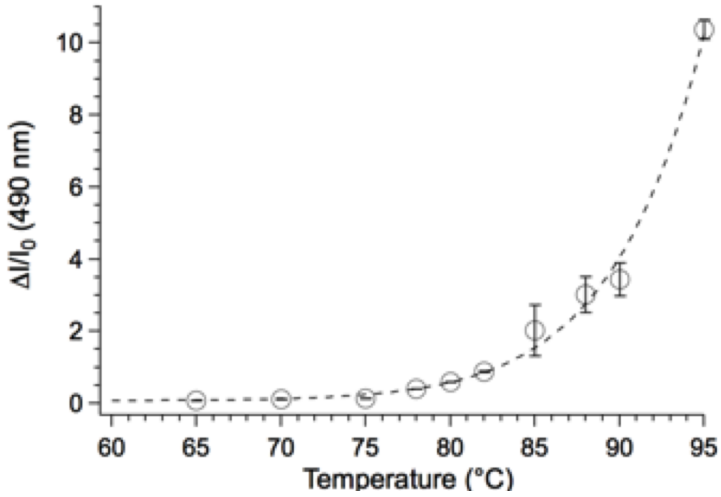

Figure 4.3: Plot of the emission intensity variation at 490 nm as calculated from PLA85PBS15 spectra as a function of the annealing temperature. The ratio values are an average of three measurements performed on different portions of the same film.

(Figure 4.3).

In order to obtain information on the phase transitions occurring in PLA and PBS domains, possibly correlated with the aggregation behaviour of BBS, DSC measurements were performed for both PLA and PLA85PBS15 films. In Figure 4.4, the first heating DSC scans are shown. The DSC thermogram of pristine PLA85PBS15 in the 40 - 180°C temperature range shows the occurrence of at least four thermal transitions at about 60, 107, 114 and 140-150 °C. The peak at about 60 °C corresponds to the glass transition of amorphous PLA, while the endothermic peaks at about 114 °C and 140-150 °C are ascribable to the melting of crystalline PBS and PLA, respectively. An exothermic transition around 114 °C can also be observed, arising from the cold crystallization of both PLA and PBS domains. It is worth noticing that the melting endotherms derive from the PBS and PLA crystalline fractions originally present in the sample, as well as from those formed for cold crystallization during the DSC scans. The DSC thermograms of PLA85PBS15 films subjected to 10 min of thermal annealing at various temperatures, going from 75 to 100 °C, were also acquired (Figure 4.4). A progressive decrease of the intensity of the cold crystallization peak with increasing temperature, accompanied by an increase of the magnitudes of PBS and PLA melting peaks, can be observed; this is

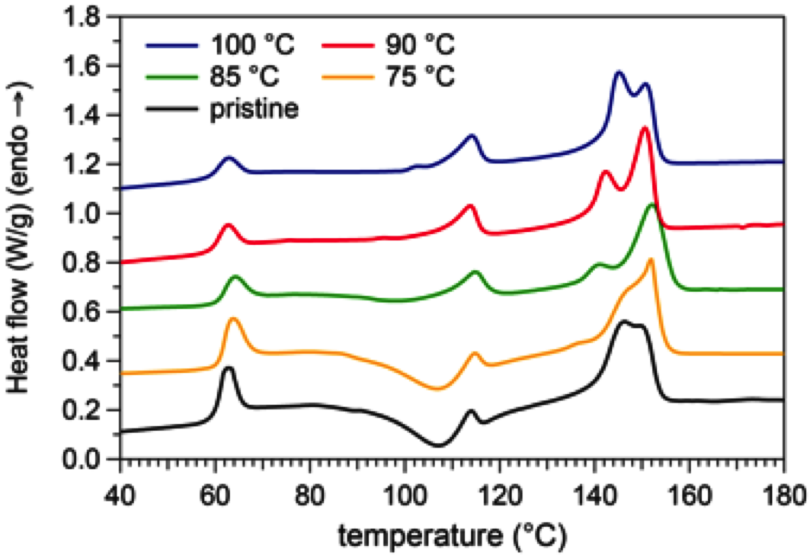

(b)

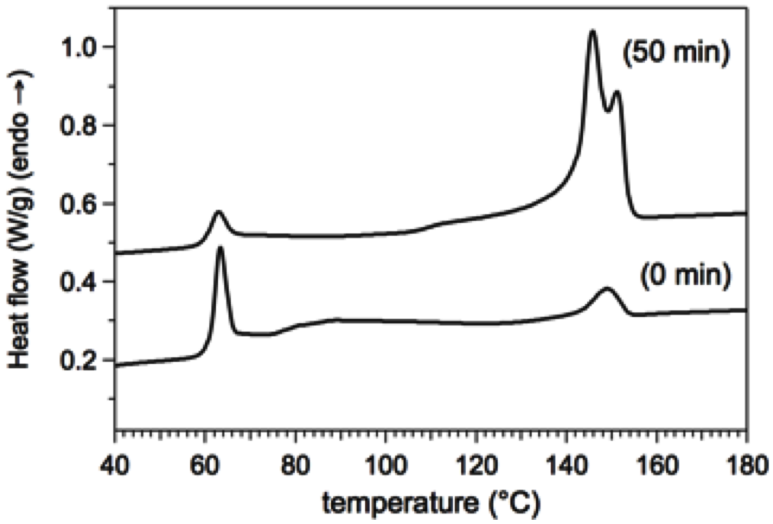

(a)

Figure 4.4: First heating DSC scans of (a) PLA films before and after annealing at 100 °C for 50 min and (b) PLA85PBS15 films before and after thermal annealing at different temperatures. All samples contain the 0.07 wt% of BBS.

due to the fact that the thermal annealing above 70-75 °C induces the cold crystalization of both PBS and PLA, with an effectiveness that increases by increasing the annealing temperature. A different behaviour was observed for the PLA film. The first heating DSC scan obtained for the pristine PLA film does not show the occurrence of cold crystallization. Indeed it is known that, in the neat polymer, PLA cold crystallization is unfavoured from a kinetic point of view. The fact that it is detectable in the DSC thermogram of PLA85PBS15 film is mainly due to the presence of PBS, which crystallizes at around 100 °C, and acts as crystallization nucleus for PLA. It is worth to notice that in passing from pristine PLA film to PLA film subjected to annealing at 100 °C for 50 min, the magnitude of PLA melting peak significantly increases, meaning that the thermal annealing can promote PLA cold crystallization even in absence of PBS.

In Table 4.1 the degrees of crystallinity calculated for PBS and PLA fractions from the corresponding melting peaks are reported. In PLA85PBS15 films, PLA and PBS crystallinity increases with annealing temperature, from 28% to 50% and from 2 % to 12 %, respectively. As already mentioned, this is due to the cold crystallization occurring with the thermal annealing, which increases with increasing temperature. In particular, PBS crystallinity significantly increases, from 3 to 9 % in passing from 80 to 85 °C, which interestingly corresponds to the threshold temperature for BBS aggregation (Figure 4.3). It is worth to notice that for PLA films a crystalline content of about 50 % is reached only after 50 min of thermal annealing at 100 °C (Table 4.1).

Comparing DSC and fluorescence data, there are evident similarities between the behaviour of the emission of BBS aggregates and the crystallization degrees of PBS and PLA domains, both increasing with the annealing temperature (Figure 4.2 and Table 4.1). These results suggest a correlation between the cold crystallization of PBS and PLA and the formation of BBS aggregates. In particular, the crystallization of the polymeric domains could be one of the driving forces for BBS aggregation in the remaining amorphous domains. This interpretation is further supported by the fact that in PLA films, where cold crystallization occurs to a much lower extent with respect to the PLA85PBS15 film, also BBS aggregation under heating is much less pronounced.

Table 4.1: Thermal behaviour of PLA and PLA85PBS15 films (first heating scan) containing the 0.07 wt% of BBS. The thermal properties were evaluated on films previously prepared at 200 C for 4 min, Pmax = 5 atm, then heated from 30 C to 200 C at 10 C/min. Polymer crystallinity χ (%) was calculated according to equation:

$$\chi = \frac{\Delta H_m}{\Delta H_m^\circ} \frac{100}{f}$$

where ΔH_m and ΔH_m° are the experimental melting enthalpy and that of the perfect PLA (ΔH_m°, 93.1 J/g) [131] or PBS crystal (ΔH_m°, 220.0 J/g) [132], and f is the polymer (PLA or PBS) fraction in the blend.

Sample	T annealing (°C)	t annealing (min)	PLA χ (%)	PBS χ (%)
PLA	-	-	4	-
PLA	100	15	30	-
PLA	100	25	43	-
PLA	100	50	52	-
PLA85PBS15	-	-	28	2
PLA85PBS15	75	10	32	2
PLA85PBS15	80	10	33	3
PLA85PBS15	85	10	34	9
PLA85PBS15	90	10	42	13
PLA85PBS15	100	10	50	12

4.4 SSNMR

This section contains brief descriptions of the techniques and methods used in this work, as well as a report of the results from the SSNMR study. In the first two paragraphs the solid echo pulse sequence, which was used in this thesis to acquire on resonance FIDs, and the method of FID analysis are described. In the last paragraph the SSNMR results obtained for PLA pellets, as well as on PLA and PLA85PBS15 films are reported.

4.4.1 Solid Echo

In the direct excitation experiment, an experimental delay of the order of some μs, usually called dead time (t_R), is inserted between the excitation $\frac{\pi}{2}$ pulse and the signal acquisition, during which the exciting radiofrequency is let to completely decay. However, it can be demonstrated that t_R values comparable to the effective T_2, as it is the case in rigid solids, cause significant distortions of the NMR spectra, as described in ref. [103]. In order to overcome this problem echo experiments, such as spin echo and solid echo, aimed at refocusing the NMR signal, can be used.

The spin echo pulse sequence, that is $(\frac{\pi}{2})_x - \tau_1 - (\pi)_y - \tau_2 - acq$, can be used for liquids, and for solids when only first rank interactions, such as the chemical shielding interaction, are present. τ_1 and τ_2 are time delays, such that τ_1 $(\tau_2) < T_2$ [103]. Let's consider the case in which only the chemical shielding interaction is present. During τ_1 the different components of the transversal magnetization evolve under the effect of the

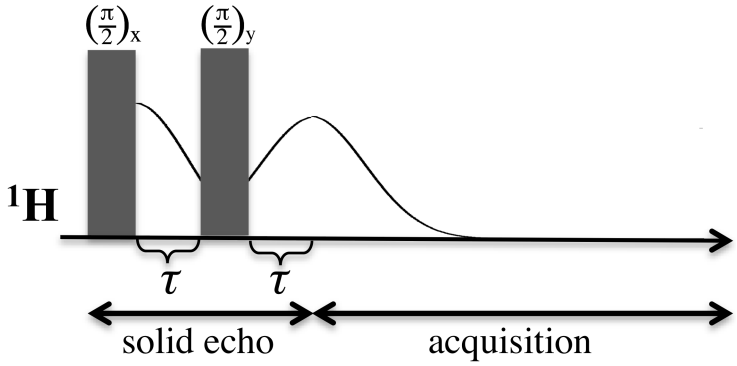

Figure 4.5: Solid echo pulse sequence. The evolution of the on resonance ^{1}H signal during the sequence and the acquisition is also shown.

chemical shielding interaction, and simultaneously dephase according to the corresponding T_2; the final block of the sequence, that is $(\pi)_y - \tau_2$, has the effect of refocusing the different components of the NMR signal, preceding around $\mathbf{B}_0$ at different frequencies, i.e. different chemical shifts, on the y axis. The maximum NMR signal is theoretically observed when $\tau_1 = \tau_2$.

When second-rank tensor interactions, such as the quadrupolar and the homonuclear dipolar couplings, are present, a similar effect is obtained by using the solid or quadrupolar echo pulse sequence, which is represented in Figure 4.5 [103]. Note that the refocusing $(\pi)_y$ pulse of the spin echo sequence is replaced by a $(\frac{\pi}{2})_y$ pulse. In this case the refocusing of NMR signal cannot be explained by using the vectorial model, but the use of the density matrix (section 1.3) is necessary.

In this work we used the solid echo pulse sequence to acquire ^{1}H FIDs, in which the ^{1}H-^{1}H dipolar coupling was the dominant interaction, under on resonance and static (no MAS) conditions.

4.4.2 ^{1}H FID analysis

The ^{1}H FID analysis consists in the fitting of the ^{1}H FID, acquired under on resonance and static conditions, with a linear combination of functions, chosen among exponential, Gaussian, Weibullian, Pake and Abragamian functions, each characterized by a different ^{1}H T_2 relaxation time [133]. In the solid state, the on resonance conditions for protons, that is when no differences in ^{1}H chemical shifts are detectable, are usually obtained by working at low magnetic field. In this work a magnetic field corresponding to a ^{1}H Larmor frequency of 24 MHz was used.

In Figure 4.6 an example of ^{1}H FID analysis is reported, in which the experimental ^{1}H FID is fitted with a linear combination of a Gaussian function with a short T_2 value (T_{2A}), and two exponential functions characterized by ^{1}H T_2, T_{2B} and T_{2C}, longer than T_{2A}, with $T_{2C} \gg T_{2B}$. This analysis is very useful for investigating the phase and morphological properties of polymeric materials, allowing domains with different degree of mobility, such as, for example, crystalline and amorphous domains above T_g, to be identified and quantified. Indeed, ^{1}H T_2 in solids is generally determined by ^{1}H-^{1}H dipolar

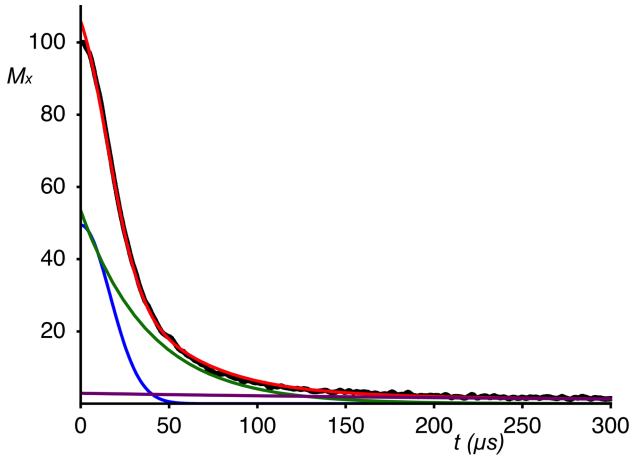

Figure 4.6: Fitting of the ^{1}H FID of PLA85PBS15 acquired under on resonance conditions at 70 °C. The figure reports the experimental FID (⋯), the fitting function:

$$Fit\_Func = C_A A + C_B B + C_C C = C_A e^{-(\frac{t}{T_{2A}})^2} + C_A e^{-\frac{t}{T_{2B}}} + C_C e^{-\frac{t}{T_{2C}}}$$

(−), and the single components: a Gaussian function with a short T_2 of 20 μs (A) (−), an exponential function (B) with an intermediate T_2 of 40 μs (B) (−), and an exponential function with a very long T_2 of about 300 μs (C) (−).

couplings: longer T_2s correspond to proton domains with a higher mobility. Moreover, the coefficients of each function in the linear combination represent the fractional population of protons characterized by the corresponding T_2.

4.4.3 Results

^{13}C CP/MAS experiments

In Figure 4.7 the ^{13}C CPMAS spectra of the PLA85PBS15 films subjected or not to annealing at 80-90 °C, acquired at 20 and 75 °C, are shown. The main signals at about 16, 70, and 170 ppm are ascribable to PLA CH_3, CH and CO carbons, respectively, while the small ones at about 27, 66, and 174 ppm to PBS CH_3, CH_2, and CO carbons, respectively.

At 20 °C in the unannealed film all the PLA carbons give rise to broad signals ascribable to amorphous PLA. In the film subjected to annealing a splitting of all the PLA carbon signals is observed, which indicates the presence of a PLA crystalline fraction [134–137], possibly formed by PLA cold crystallization. In particular, the features of

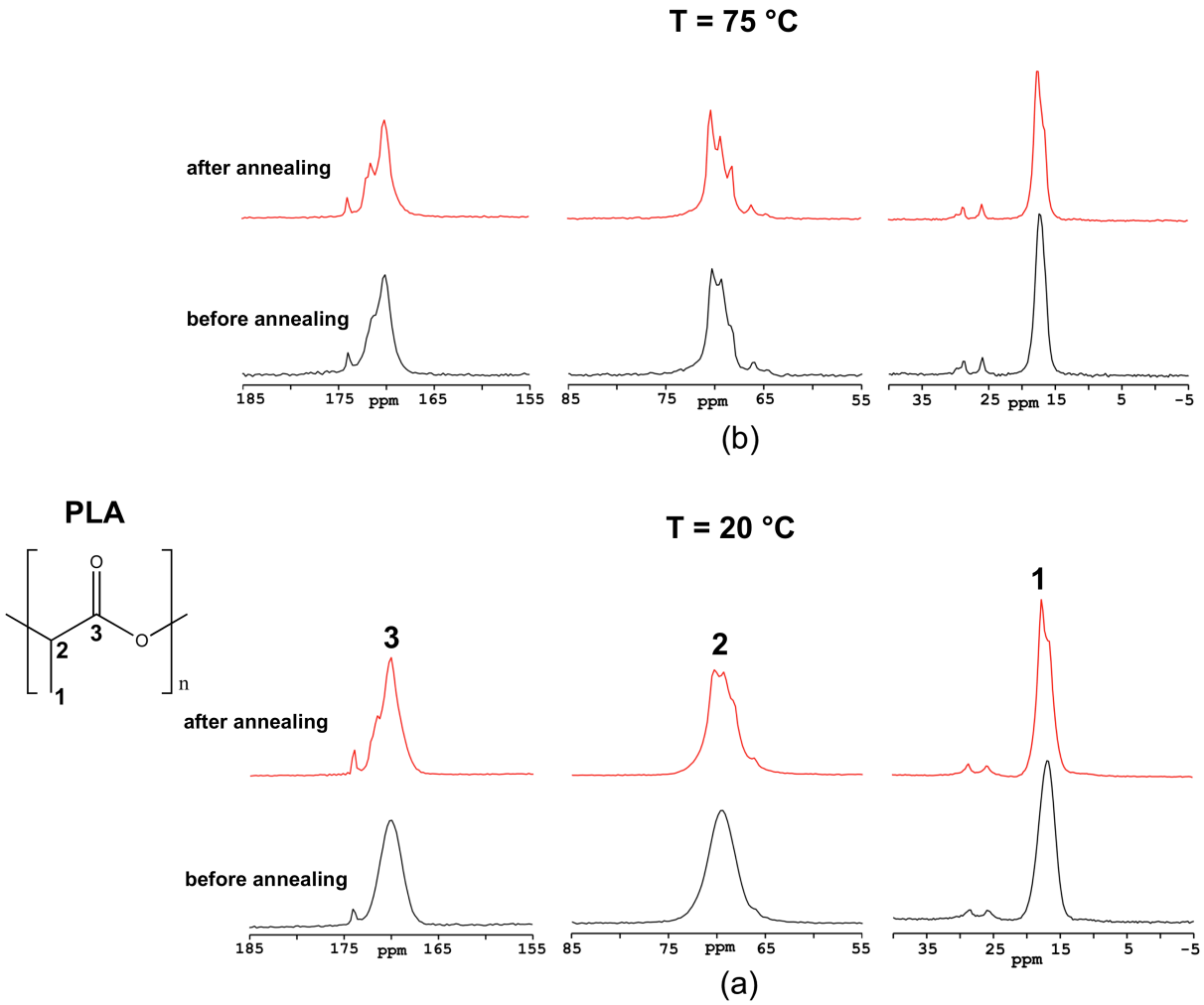

Figure 4.7: Expansions from the ^{13}C CP/MAS spectra of PLA85PBS15 before (bottom) and after (top) annealing, acquired at 20 °C (a) and 75 °C (b).

the ^{13}C spectrum are typical of PLA chains in a helical 10_3 conformation, which is characteristic of the α crystalline form of poly(L-lactic acid); the multiple resonance lines in the ^{13}C spectrum are believed to reflect the different conformations and packings of CH_3, CH, and CO carbons along the chain [137].

In the spectra acquired at 75 °C the splitting of the PLA carbon signals is observable for both the films subjected or not to annealing, indicating that at 75°C the cold crystallization process has already started.

Variable temperature ^{1}H FID analysis

In order to further investigate the phase transformations occurring in the polymeric matrix of PLA85PBS15 under heating, we acquired and analysed the on resonance ^{1}H FID at increasing temperature, in the temperature range 40-100 °C. At each temperature the experimental FID was fitted through the linear combination of functions (Figure 4.6):

$$Fit\_Func = C_A A + C_B B + C_C C = C_A e^{-(\frac{t}{T_{2A}})^2} + C_A e^{-\frac{t}{T_{2B}}} + C_C e^{-\frac{t}{T_{2C}}} \quad (4.1)$$

A is a Gaussian function with a short ^{1}H T_2 of about 20 μs; B is an exponential function with a ^{1}H T_2 which increases from 30 to about 200 μs with increasing temperature; C is an exponential function with a very long ^{1}H T_2 of about 300 μs.

As far as PLA pellets and film are concerned, considering that PLA is a semi-crystalline polymer with a T_g of about 60 °C [117], A was ascribed to rigid crystalline and glassy PLA domains, B to highly viscous amorphous PLA, whose mobility is expected to increase with temperature, and C to polymeric end chains, and, for the high temperature FIDs (85-100 °C), to very mobile amorphous PLA. According to this interpretation, the coefficient C_A can be related to the percentage of crystalline and glassy PLA. In Figure 4.8 the trends of C_A with temperature found for the PLA pellets and

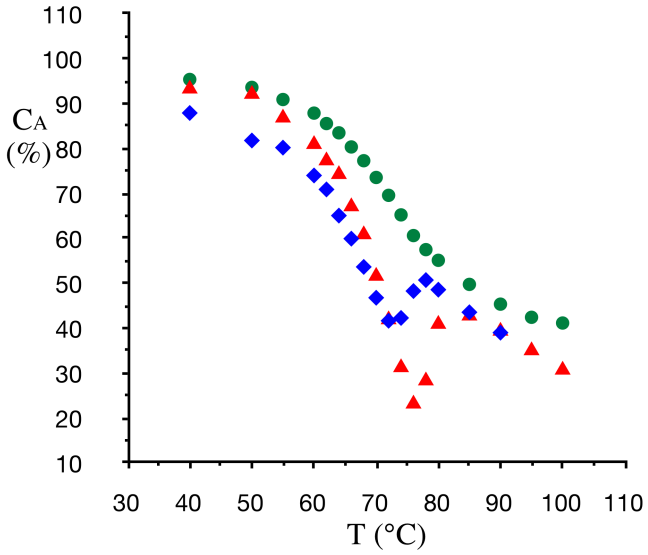

Figure 4.8: (a) C_A vs temperature curves obtained for neat PLA pellets (●), PLA film (▲), and PLA85PBS15 (♦).

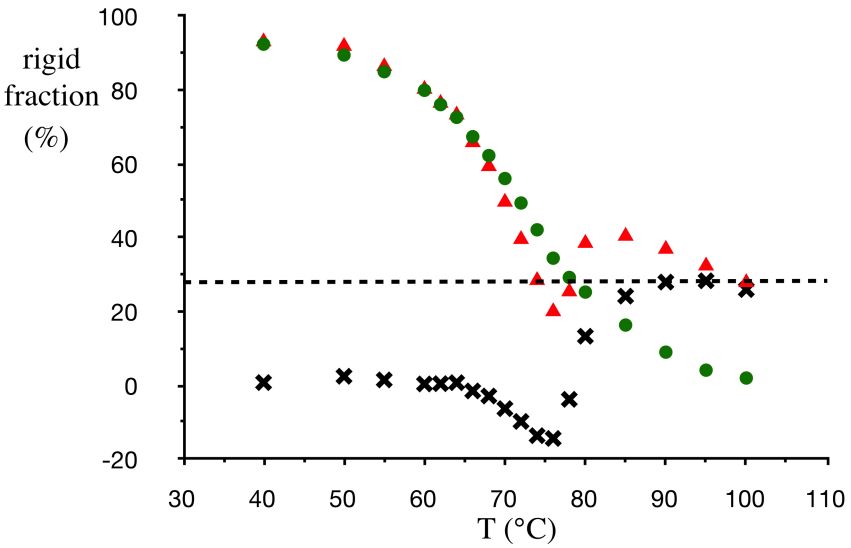

Figure 4.9: Determination of the final crystalline fraction of PLA in the PLA film. The percentages of the glassy amorphous PLA in the PLA pellets (●) and PLA film (▲), determined as described in the text, are shown. The difference between ▲and ● (**X**) is also reported.

film are reported. In neat PLA pellets C_A is almost constant up to about 50 °C, and then it regularly decreases tending to a plateau for high temperature values. This trend nicely represents the glass transition of PLA amorphous domains, which gradually pass from a rigid glassy state to a more mobile viscous one, and shows how this process is extended over a wide temperature range (50-100 °C). The residual rigid fraction of about 40 % present at high temperatures can be ascribed to crystalline PLA, which does not undergo phase transitions in this temperature range. Different results were obtained for the PLA film, for which a discontinuity in the decrease of C_A can be observed at about 75-80 °C: C_A decreases up to about 75 °C, increases from 75 to 80 °C, and then starts to decrease again but with a lower slope. This behaviour can be explained with the superimposition of the glass transition process with the cold crystallization of PLA. In particular, the latter would be responsible for the increase of C_A at about 75-80 °C, due to the increase of the PLA crystalline fraction. In order to separate the two contributions, we used the C_A curve of the neat PLA pellets as a reference for the glass transition process. More specifically, we subtracted the crystalline fraction estimated from Figure 4.8 (40 %), which should remain constant under heating, from the experimental C_A, and we rescaled the result by 100/60, thus obtaining the trend of the amorphous fraction.

This is reported in Figure 4.9, along with that obtained in a similar way for the PLA film, obtained by subtracting a crystalline fraction of 4 %, estimated on the basis of DSC result, and properly rescaled. The difference between the two rescaled curves was also calculated and it is reported in Figure 4.9. The difference is almost zero up to about 65 °C, it decreases, assuming negative values, between 65 and 75 °C, and finally it increases approaching an asymptote for high temperatures. This indicates that the rate of the glass transition process is almost the same in the PLA pellets and film for temperatures below 70 °C, and it becomes faster in the film when the temperature of PLA cold crystallization is approached. The increase of the curve above 75 °C is representative of the increase of the crystalline fraction due to PLA cold crystallization occurring in the film, and the value of the asymptote at high temperatures corresponds to the final crystalline fraction of PLA. This is found to be about 30 %, in agreement with the DSC results for the sample annealed at 100 °C for 15 min (Table 4.1).

As far as the PLA85PBS15 film is concerned, the experimental C_A, reported in Figure 4.8, shows a discontinuity at about 70 °C, similar to that found for the PLA film, which can be mainly attributed to the occurrence of PLA cold crystallization. It is worth to notice that in PLA85PBS15 the cold crystallization of PLA seems to take place at lower temperatures than in the PLA film, suggesting that PBS favours the kinetics of the process, possibly acting as nucleation agent. Moreover, in PLA85PBS15 the contribution of PBS to the ^{1}H FID cannot be completely neglected, being its fractional population of protons about 20 %. From DSC, it is known that at room temperature, in a film not subjected to annealing, PBS domains are almost completely amorphous, and well above the glass transition temperature ($T_g \sim$ -30 °C) [117]. Therefore it would be reasonable to expect that PBS mostly contributes to the B and C components. Nevertheless, in PLA85PBS15 the high initial value measured for C_A, significantly greater than the expected value of 80 %, indicates that at 40 °C a significant fraction (about 50 %) of PBS is quite rigid. This might be due to an interaction between PLA and PBS domains, which could determine a stiffening of PBS domains at the interface.

Information on the mobility of the viscous PLA domains can also be obtained from the ^{1}H T_2 of the component B (T_{2B}). In Figure 4.10 the trend of T_{2B} with temperature

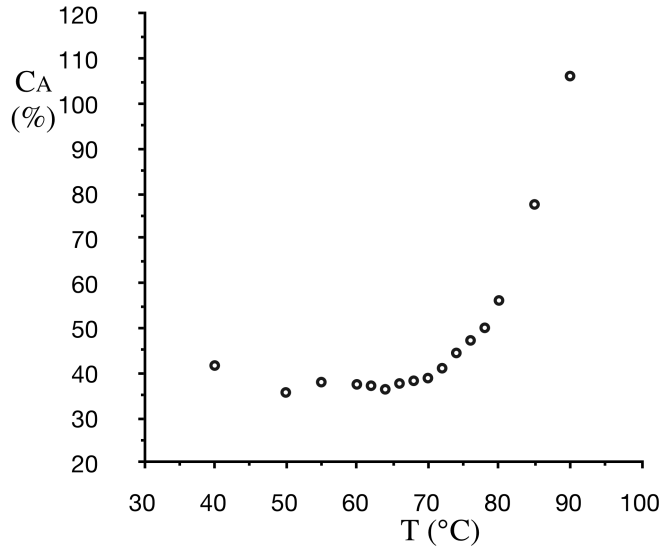

Figure 4.10: T_{2B} vs temperature curve obtained for PLA85PBS15.

obtained for PLA85PBS15 is reported. Similar results were found for the PLA pellets and PLA film (here not shown). T_{2B} is almost constant at the value of 40 μs up to about 70 °C, and then it steeply increases indicating a corresponding increase of the mobility of the amorphous PLA domains. This clearly shows that up to 70 °C the heat supplied to the PLA85PBS15 film is used almost completely to convert the glassy PLA domains into viscous, and only above 70 °C, when a significant fraction (almost 50 %) of glassy PLA has undergone glass transition (see Figure 4.8), it can be available to increase the mobility of the viscous phase.

4.5 Discussion

The combination of SSNMR, DSC and spectrofluorimetric experiments allowed us to get insights into the morphological and phase behaviour of the polymeric matrix in PLA85PBS15 threshold temperature luminescent indicators.

The measurement and analysis of ^{1}H FID at variable temperatures has clearly appeared as a very powerful approach to investigate the morphological and phase behaviour of polymeric systems, alternative or complementary to DSC. Indeed, with respect to

DSC, ^{1}H FID analysis allows both quantitative structural and dynamic information to be obtained.

A good agreement was found between DSC and SSNMR concerning the phase transitions occurring in PLA and PBS domains under heating. The variation of the weights of the different components in Eqn. 4.1 with temperature and the comparison among different samples allowed us to separate the contributions arising from PLA glass transition and cold crystallization (Figures 4.8 and4.9). Cold crystallization was found to occur in both PLA and PLA85PBS15 films, but not in PLA pellets (Figure 4.8). The latter was used as a reference for the glass transition process, which was found to be a quite slow process, extending over a wide temperature range, from 40 to 100 °C. In agreement with DSC results, PLA cold crystallization in PLA85PBS15 film was found to occur at lower temperatures than in PLA film, confirming that PBS may act as a nucleation agent, inducing PLA to crystallize (Figure 4.8). The influence of PBS on the kinetics of PLA crystallization suggests an effective interaction between the two polymers (thermodynamically immiscible but highly compatible) [117], which are possibly intimately mixed at the interface within the film, as also indicated by the stiffening of PBS domains with respect to the neat polymer, as observed by ^{1}H FID analysis.

Finally, the measurement of ^{1}H T_2 allowed the variation of the mobility of viscous PLA with temperature to be investigated, information which is not achievable by DSC (Figure 4.10).

Aiming at the rationalization of the observed luminescence phenomena, spectrofluorimetric and calorimetric investigations confirmed that the peculiar behaviour of the PLA/PBS blend in terms of aggregation/disaggregation of BBS with varying temperature is related to the effects provided by the temperature on both polymer phase behaviour and mobility of polymeric chains. In particular, the presence of 15 wt% of PBS in the blend, in which the dye appeared less soluble than in PLA [117], was found to be the key factor to promote BBS aggregation (Figure 4.2). Accordingly, BBS aggregation in PLA film appeared less favoured upon thermal stress even at a temperature higher than PLA T_g (Figure 4.2a). An important role seems to be also played by PLA and PBS

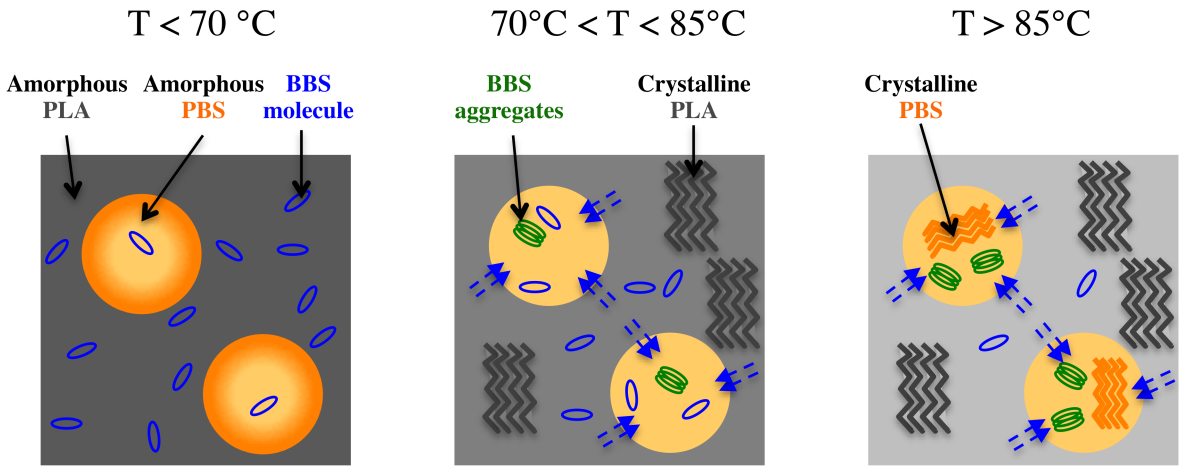

Figure 4.11: Representation of the mechanism of BBS aggregation in PLA85PBS15 under heating, as hypothesized on the basis of spectrofluorimetric, DSC and SSNMR results. The shade of colours, from the deeper to the lighter, represents the change of mobility of the polymers, from more rigid to more mobile fractions.

cold crystallization under heating. Inspection of the first heating scan of pure PLA film (Figure 4.4 and Table 4.1) showed that the annealing at 100 °C increases PLA crystalline content from 4 % to 30-50 %, depending on the annealing time. This behaviour well agrees with SSNMR ^{1}H FID analysis, from which a PLA crystalline content of about 30 % could be estimated (Figure 4.9), even though the thermal treatments experienced by PLA during DSC and SSNMR experiments cannot be straightforwardly compared. Nevertheless, the remarkable reduction of PLA amorphous phase attained during the thermal treatment is not able alone to promote effective BBS aggregation (Figure 4.2a), for which the presence of 15 wt% of PBS is needed. In keeping with that reported by Yokohara et al. [124] we observed that PLA crystalline content (determined by DSC) increased from 4 to 28 % in PLA85PBS15 blend with respect to pure PLA film (Table 4.1) [117]. Once thermal annealing was applied to PLA85PBS15 films from 75 °C to 100 °C, PLA crystallinity increased from 28 % to 50 % (the same value reached for PLA alone), while that of PBS from 2 % to about 12 % (Table 4.1). In particular, ^{13}C CPMAS NMR spectra confirmed that PLA crystallization takes place even when the sample is heated at 75 °C, and it is further promoted by annealing at 100 °C (Figure 4.7).

A steep increase of the mobility of the viscous PLA phase at temperatures higher than 70-75 °C (Figure 4.8) was also observed. It is worth to notice that this increase appears

very similar to that reported in Figure 4.3 and is related to the extent of aggregation of BBS chromophores evaluated by spectrofluorimetry.

These results suggest that during the thermal annealing of PLA85PBS15 films containing the 0.07 wt% of BBS the following steps towards BBS aggregation may occur:

- when relevant amounts of PLA amorphous phase give rise to cold crystallization, BBS isolated chromophores, originally dispersed in the PLA amorphous matrix, may come more in contact with the PBS amorphous domains, which are intimately connected with those of PLA: within PBS amorphous phase BBS molecules could tend to aggregate more easily than in PLA, given their worse solubility in the former;

- the heat supplied during annealing above 70 °C, when a significant fraction (almost 50 %) of glassy PLA has undergone glass transition (Figure 4.8), is available to increase the mobility of the viscous phase: such mobility could further favour the aggregation of BBS molecules;

- above 85 °C the increase of PBS crystallinity due to its cold crystallization seems to further promote the aggregation of BBS molecules.

Figure 4.11 shows a pictorial representation of the above described phenomena, occurring in PLA85PBS15 with increasing temperature.

4.6 Experimental

The ^{13}C CP/MAS experiments were carried out on a dual-channel Varian InfinityPlus 400 spectrometer, equipped with a 3.2 mm Cross Polarization/Magic Angle Spinning (CP/MAS) probehead, working at 400.03 MHz for proton and at 100.61 MHz for carbon-13, with ^{1}H and ^{13}C pulse durations of about 3 μs. All the spectra were acquired using a recycle delay of 5 s, a contact time of 5 ms, and a MAS frequency of 8 kHz. TMS was used as a primary chemical shift reference for all nuclei, while hexamethylbenzene was the secondary reference for ^{13}C. On-resonance ^{1}H free induction decays (FIDs) were recorded

on a Varian XL-100 spectrometer coupled with Stelar lock and PC-NMR acquisition systems, at a Larmor frequency of 24 MHz, using a ^{1}H pulse duration of 4 μs. A solid echo pulse sequence was used, accumulating 200 transients with a recycle delay of 3 s and an echo delay of 12 μs. ^{1}H FIDs were recorded by progressively increasing the temperature from 40 to 100 °C. For each experiment the temperature was left to equilibrate for 10 minutes before the acquisition. Considering that the experimental time was about 10 minutes, the sample was kept at each selected temperature for about 20 minutes. All the variable temperature measurements were carried out using air as heating gas.

4.7 Conclusions

The combined application of SSNMR, DSC, and spectrofluorimetry revealed effective in sheding light on the phenomenon of BBS aggregation in PLA and PLA/PBS blends, which is relevant for their application as intelligent films for packaging.

From a methodological standpoint, variable temperature ^{1}H FID analysis was demonstrated to be a very useful approach to investigate the phase behaviour of PLA and PLA/PBS blends, providing broth structural and dynamic information.

As far as materials are concerned, an explanation of BBS aggregation phenomenon as a function of temperature was attempted, in terms of both PLA/PBS phase behaviour and mobility of their amorphous phases. In the case of PLA we were able, by ^{1}H FID analysis, to disentangle glass transition and cold crystallization, occurring in very similar temperature ranges. Although in both PLA and PLA/PBS blend films similar amounts of crystalline PLA are formed through cold crystallization, which was previously hypothesized to play a fundamental role in BBS aggregation, this study allowed us to clarify that a key role is actually played by the presence of PBS. This role is probably not limited to the stimulation of PLA cold crystallization, found to occur at lower temperatures with respect to pure PLA, but also in "subtracting" BBS molecules to the PLA amorphous phase during cold crystallization, favouring their aggregation within PBS amorphous domains.

Chapter 5

Study of the morphology and dynamics of P3HT/PCBM photoactive blends

5.1 Introduction

In the last two decades, much effort has been devoted to the development of polymeric solar cells (PSC) that, respect to the traditional silicon solar cells, should lead to lower production costs and higher mechanical flexibility [51,55]. In PSC the photoactive layer, which is responsible for the harvesting of the solar light and its conversion into electric energy, is usually constituted by two organic components, called the donor, usually a conjugated polymer, and the acceptor, usually a fullerene derivative (paragraph 2.1.3). The donor absorbs the solar light, determining the excitation of its most external electron; the latter is then transferred to the acceptor at the donor-acceptor interface, leading to the formation of two separated charge carriers, the holes (positive charges) and the electrons (negative charges), which are transported towards the corresponding electrodes.

Despite the encouraging progresses made in the field, the power conversion efficiencies (PCE) achieved so far for PSC do not allow their commercial breakthrough. Nonetheless, it has been well understood that an improvement of the performance of these devices can

be obtained with an accurate control of their morphology (paragraph 2.1.3 [138,139]. In particular, it has been demonstrated that the bulk-heterojunction (BHJ) morphology, in which donor and acceptor are intimately mixed on a nanometer scale, leads to the best in cell performances. Further improvements could be achieved by fine tuning, adopting different preparation and/or post-treatment procedures, the phase, morphological, and dynamic properties of these materials, such as, for example, the degree of crystallinity of donor and acceptor domains, the phase separation and the interaction at the interface between the two components (section 2.1.3) [54]. The study of the dynamic properties, on a molecular and supra-molecular scale, of the photoactive materials represents a new approach that can be very important to better understand the molecular origin of the performances of the final device in terms of efficiency. Moreover, changes in the dynamic properties as a consequence of the blending or of the post-treatment processes might reflect changes in the morphology, which, as already said, play a crucial role in determining the efficiency of the final device.

Solid-State NMR spectroscopy (SSNMR) offers several tools for investigating the morphological, structural, and dynamic properties of BHJ photoactive materials, as demonstrated by the increasing number of works exploiting this technique (section 2.2) [90–97]. In particular, a detailed characterization of the molecular dynamic properties of BHJ components can be obtained from the SSNMR measurement and suitable analysis of a large set of nuclear relaxation times [140–143].

In this chapter a detailed SSNMR study of the phase, morphological and dynamic properties, in the kHz and MHz regimes, of BHJ poly(3-hexylthiophene)/[6,6]-phenyl-C61 butyric acid methyl ester (P3HT/PCBM) photoactive materials is presented.

5.2 Materials and aims

This work arises from a collaboration with ENI S.p.A, aimed at investigating, by means of SSNMR, the morphological and dynamic properties of different polymeric photoactive blends for solar cells prepared by ENI. For these materials, ENI carried out also the characterization of the electronic properties and the in cell tests. The final aim was

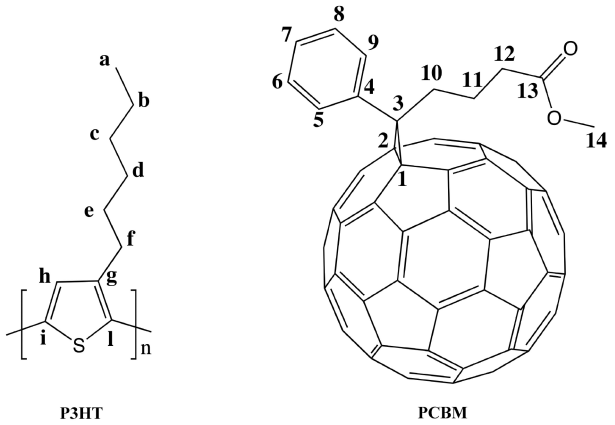

Figure 5.1: Structures of poly(3-hexylthiophene) (P3HT) and [6,6]-phenyl-C61 butyric acid methyl ester (PCBM).

to better understand the origin on a molecular and supramolecular scale of the in cell performances of these materials.

The materials object of this study are BHJ photoactive blends of P3HT, the donor, and PCBM, the acceptor. The structures of P3HT and PCBM are shown in Figure 5.1. This is one of the most popular combinations of donor and acceptor, mainly due to favourable electronic properties of the systems, in terms of both absorption of the solar light and electron transfer from P3HT to PCBM, as well as to easily tuneable morphological features. In particular, it has been largely demonstrated that thermal annealing at about 100-150 °C of the P3HT/PCBM blend determines an increase of the PCE of the final PSC [138], and much effort has been made to understand what really happens in the film during the annealing process [51, 96, 97]. Several studies, many of which using SSNMR, showed that thermal annealing induces a phase separation between P3HT and PCBM domains, which could explain the improvement of PCE. Indeed, the formation of more segregated P3HT and PCBM domains could lead, to a certain extent, to better percolated carrier pathways, favouring charge transport towards the electrodes. Nevertheless, in this regard, several aspects still need to be clarified.

In this work, SSNMR was used to investigate the morphological and dynamic properties of P3HT/PCBM blends in the ratio 1/0.8, pristine and subjected to thermal annealing for 30' at 150 °C [144]. ^{13}C CP MAS and ^{1}H FID analysis were used to investigate the phase properties of P3HT and PCBM domains. ^{1}H FID analysis, thanks to the

measurement of ^{1}H T_2, gave also information on the degree of mobility of the systems in the kHz regime. Measurements of ^{1}H T_1 under high resolution condition (indirect method) were used to investigate the degree of homogeneity of the P3HT/PCBM blend on the 100-200 Å scale. Since very little is known about the dynamic properties of these systems and their dependence on thermal annealing, the largest part of the study was dedicated to investigate the dynamic properties of P3HT in the MHz regime, by exploiting the measurement and analysis, through a simultaneous fitting to suitable theoretical models of ^{1}H and ^{13}C T_1 vs temperature curves, also recorded at different Larmor frequencies [140–143]. In order to observe the effect of both blending with PCBM and thermal annealing, the study was carried out on both neat P3HT and the P3HT/PCBM blends pristine and subjected to thermal annealing.

5.3 SSNMR techniques

5.3.1 Measurement of ^{1}H T_1: saturation recovery experiment

In this work ^{1}H T_1s were measured by using both direct, for the evaluation of the spin diffusion process, and indirect, for the variable temperature measurements, methods, using the saturation recovery pulse sequence. The sequences here used are represented in Figure 5.2. The initial train of $\frac{\pi}{2}$ pulses, separated by short delays τ_1 such that $\tau_1 << T_1$, saturates the ^{1}H longitudinal magnetization, so that, at the end of the train $M_z = 0$. During the following delay τ_2, M_z is allowed to recover according to the longitudinal spin-lattice relaxation, and the ^{1}H (Figure 5.2, top) or the ^{13}C signals, obtained by ^{1}H-^{13}C cross polarization (Figure 5.2, bottom), are then measured for different values of τ_2, in the case of the direct and indirect methods, respectively. ^{1}H T_1 is determined by fitting the experimental ^{1}H or ^{13}C signal build-up curves by means of mono- or multi-exponential functions. The main advantage of the saturation recovery approach with respect to the inversion recovery sequence described in paragraph 3.3.2 is the possibility to use very short recycle delays between two following scans. This is very useful to save experimental time, when a large number of transients need to be used, as in the case of

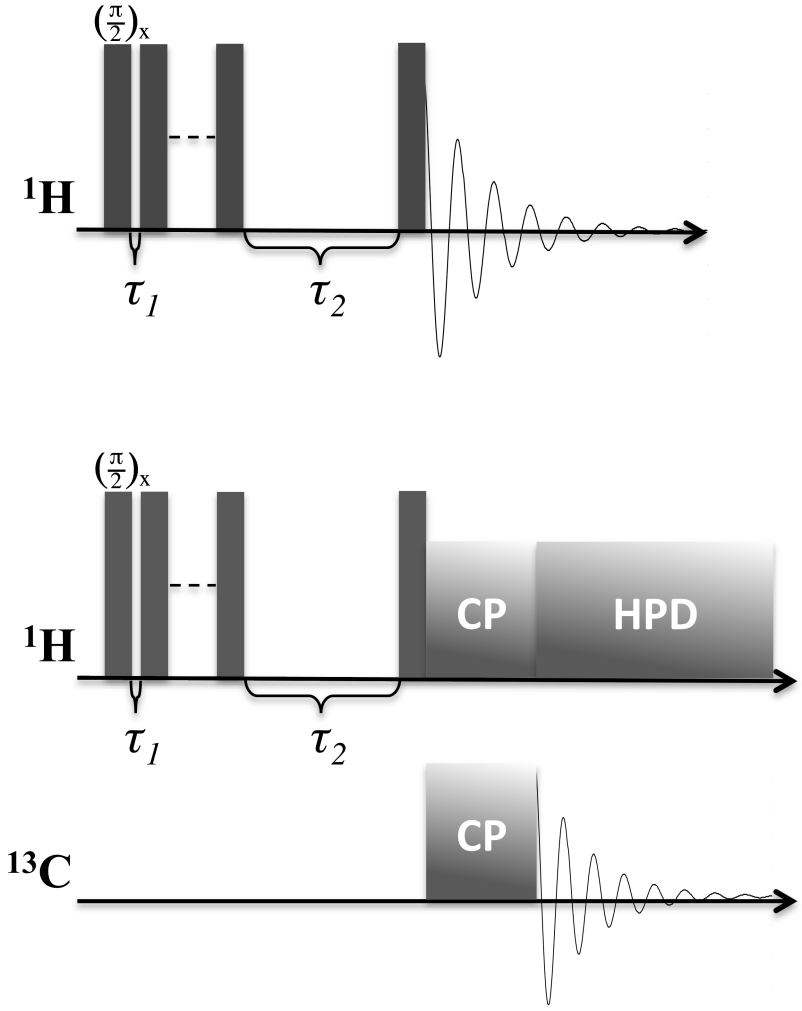

Figure 5.2: Saturation recovery pulse sequence for the direct (top) and indirect (bottom) measurement of ^{1} H T_1. For the indirect measurement, ^{1}H magnetization is transferred to ^{13}C through cross polarisation (CP), and high power decoupling (HPD) from ^{1}H is applied during the acquisition of ^{13}C signal.

the indirect measurements in which ^{13}C is observed, or numerous experiments need to be run, as in the case of the variable temperature measurements.

5.3.2 Measurement of ^{13}C T_1: Torchia experiment

In Figure 5.3, the Torchia pulse sequence for the measurement of ^{13}C T_1 is shown [145]. ^{13}C transverse magnetization is created by means of ^{1}H-^{13}C cross-polarisation, and then it is transferred to the z axis by means of a $\frac{\pi}{2}$ pulse. The ^{13}C spin system is then allowed to relax under the effect of the longitudinal spin-lattice relaxation mechanism during the delay τ, which is varied during the experiment. This is followed by a second $\frac{\pi}{2}$ pulse and the acquisition of the ^{13}C signal. Since the magnetization created by CP is larger in magnitude than the "Boltzmann" magnetization at the equilibrium, M_z progressively decreases with τ. ^{1}H T_1 is measured by fitting the experimental decay curve of the ^{13}C signal by means of an exponential function. It is worth to notice that the two-steps phase cycle of the sequence subtracts out the effect of the direct ^{13}C Boltzmann magnetization, so that the ^{13}C signal decays to zero for long τ. This sequence provides a double advantage in terms of sensitivity and experimental time. First, there is the

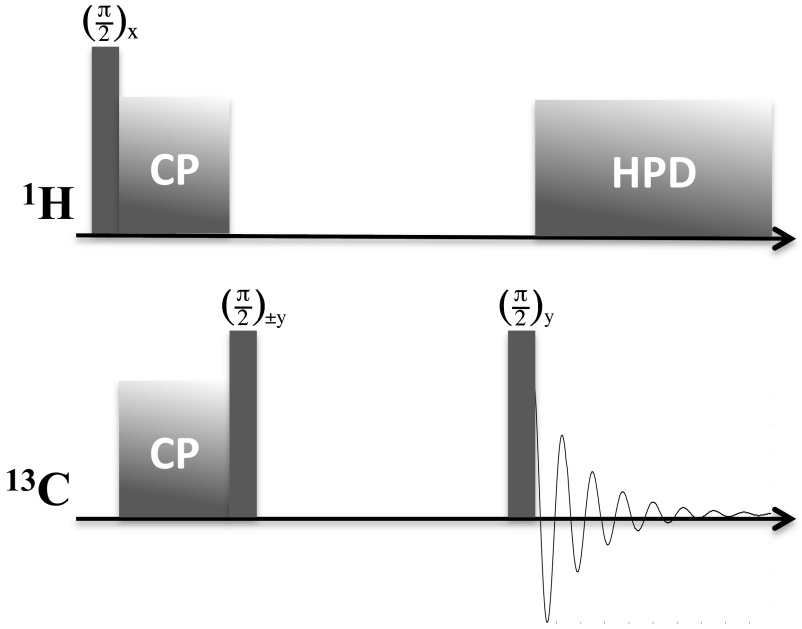

Figure 5.3: Torchia pulse sequence for the measurement of ^{13}C T_1. ^{1}H high power decoupling (HPD) is applied during the acquisition of ^{13}C signal.

enhancement of the ^{13}C signal provided by the use of ^{1}H-^{13}C cross polarization. Second, the recycle delay between two consecutive transients is determined by ^{1}H T_1, which is usually much shorter than ^{13}C T_1.

5.4 Theoretical basis

5.4.1 Longitudinal spin-lattice relaxation times

In NMR the longitudinal spin-lattice relaxation is mainly determined by the local fluctuations of inter-nuclear dipolar interactions under the effect of fast reorientational motions in the MHz frequency range (section 1.8). In particular, the efficiency of relaxation is maximum when the frequency of the motion is near to the Larmor frequency of the observed nucleus, which corresponds to a minimum in the longitudinal spin-lattice relaxation time (T_1) vs temperature curve.

5.4.2 ^{1}H relaxation

For protons the main sources of spin lattice relaxation are the fluctuations of the homonuclear dipolar couplings. For protons characterized by the same intrinsic relaxation time ($T_1(H)$), to which a single reorientational motion contributes, the spin-lattice relaxation rates ($R_1(H)$) can be written as [103]:

$$R_1(H) = \frac{1}{T_1(H)} = C\left[J(\omega_0) + 4J(2\omega_0)\right] \tag{5.1}$$

where ω_0 is the ^{1}H Larmor frequency, C is a constant related to the fraction of second moment corresponding to the dipolar interactions available for the relaxation process, and J(ω) is the spectral density function, containing the correlation time (τ) of the motion. In solid samples different motions can be effective for relaxation, so that protons experiencing different local motional situations would be characterized by different intrinsic $T_1(H)$ values. However, the measurement of intrinsic $T_1(H)$'s is prevented by spin diffusion which tends to average them to one single value, the completion of the averaging depending on the degree of homogeneity of the system. In particular, a single

T_1 value is measured when the system is homogeneous on a 100-200 Å scale [103]. In this case, the measured $T_1(H)$ value can be related to the population weighted rate average (PWRA) of the intrinsic $T_1(H)^i$ components following the equation:

$$\frac{1}{T_1(H)} = PWRA = \sum_{i=1}^{n} \frac{f_i}{T_1(H)^i} \tag{5.2}$$

f_i being the fractional population of protons with the intrinsic relaxation time $T_1(H)^i$. The same expression is valid when different $T_1(H)$ values are measured. In this case the experimental PWRA can be calculated as the weighted average of the measured $1/T_1(H)$'s. When each $T_1(H)^i$ is affected by one single motional process the following PWRA expression can be written [146, 147]:

$$PWRA = \frac{1}{T_1(H)} = \sum_{i=1}^{n} f_i C_i \left[J_i(\omega_0) + 4J_i(2\omega_0) \right] \tag{5.3}$$

where n is the number of independent motional processes. If different motions affect the single intrinsic $T_1(H)^i$, the equation will become much more complex. A case of particular interest for this study was that of two independent motions, I and II, with very high and very low frequency, respectively. In this case each $T_1(H)^i$ term in equation 5.2 follows the expression:

$$\frac{1}{T_1(H)^i} = C_i \left(\left[J_i^I(\omega_0) + 4J_i^I(2\omega_0) \right] + C_i^{II} \left[J_i^{II}(\omega_0) + 4J_i^{II}(2\omega_0) \right] \right) \tag{5.4}$$

where J_i^I and J_i^{II} are the spectral densities relative to the motional processes I and II, respectively, and C_i^{II} is a dimensionless parameter that can assume only values in the range 0-1, due to the fact that the slower motional process acts on a residual dipolar interaction that has been partially averaged by the faster motion.

5.4.3 ^{13}C relaxation

For non-quaternary carbon nuclei the longitudinal spin-lattice relaxation is mainly determined by the fluctuations of the heteronuclear dipolar interactions with directly bonded protons. If a single motional process affects the T_1 relaxation of a given carbon, the

corresponding relaxation rate $R_1(C)$ will follow the expression [103]:

$$R_1(C) = \frac{1}{T_1(C)} = \frac{N}{15r_{CH}^6} C_C \left[J(\omega_H - \omega_C) + 3J(\omega_C) + 6J(\omega_H + \omega_C) \right] \tag{5.5}$$

where N is the number of protons directly bonded to the observed carbon, r_{CH} is the ^{1}H-^{13}C inter-nuclear distance, ω_H and ω_C are the Larmor frequencies of ^{1}H and ^{13}C, respectively, and C_C is a constant related to the residual heteronuclear dipolar interactions available for relaxation. Neglecting the effects of vibrational motions, C_C can be calculated as:

$$C_C = \frac{3}{4} \left(\frac{\mu_0}{4\pi} \right)^2 \gamma_H^2 \gamma_C^2 \hbar^2 \tag{5.6}$$

It is worth noticing that for carbons the spin lattice relaxation is not affected by spin diffusion, and intrinsic $T_1(C)$'s, containing site-specific information on the local motional situation of the observed carbon, can be measured. Similarly to the case of protons, when two independent motions (I and II) characterized by very different frequencies affect the same relaxation process, the corresponding $R_1(C)$ can be written as:

$$\begin{aligned} R_1(C) = \frac{1}{T_1(C)} = \frac{N}{15r_{CH}^6} C_C \Big(& \left[J^I(\omega_H - \omega_C) + 3J^I(\omega_C) + 6J^I(\omega_H + \omega_C) \right] \\ & + C_C^{II} \left[J^{II}(\omega_H - \omega_C) + 3J^{II}(\omega_C) + 6J^{II}(\omega_H + \omega_C) \right] \Big) \end{aligned} \tag{5.7}$$

where C_C^{II} is a dimensionless parameter assuming values in the range 0-1, because the slower motion (II) acts on heteronuclear dipolar interactions already partially averaged by the faster one (I).

5.4.4 Models

As far as the spectral density function is concerned, in this work the simplest Bloembergen, Purcell and Pound (BPP) model was used, according to which the following normalized expression holds true (section 1.8) [9]:

$$J(\omega) = \frac{2\tau_c}{1 + \omega^2 \tau_c^2} \tag{5.8}$$

where τ_c is the correlation time of the motion, that is the inverse of its frequency. In order to fit the experimental trends of T_1 with temperature it is necessary to know the expression of τ_c as a function of temperature (T). In this work we used the Arrhenius expression:

$$\tau_c = \tau_\infty e^{\frac{U}{kT}} \tag{5.9}$$

where U is the activation energy of the motion and τ_∞ is the value of correlation time extrapolated to infinite temperature.

5.5 Results and discussion

5.5.1 Phase properties: ^{13}C CP/MAS spectra and ^{1}H FID analysis

In Figure 5.4 the ^{13}C CP/MAS spectra of neat components P3HT and PCBM, and of Blend A (blend before annealing) and Blend B (blend after annealing at 150 °C for 30', see experimental part) are reported. As far as PCBM is concerned, the signal of C_{60} carbons at about 140 ppm can be clearly observed in the spectra of neat PCBM, blend A and B. On the other hand, the side chain aromatic and aliphatic carbon signals, well visible in the spectrum of neat PCBM, are hardly distinguishable in those of the blends due to their intrinsic low intensity and their partial superposition with the more intense P3HT carbon signals. The detailed assignment of PCBM carbon signals is reported in Figure 5.4 [92, 96]. In the spectrum of neat P3HT the signals of a, b, internal $d - f$, and c carbons resonate at 14.7, 23.4, 30.6 e 32.6 ppm, respectively, and the aromatic carbon signals in the region 120-140 ppm. As recently reported in the literature [86], the chemical shifts and the lineshapes of P3HT carbon signals are sensitive to its phase and conformational properties. Crystalline and amorphous phases give rise to quite narrow

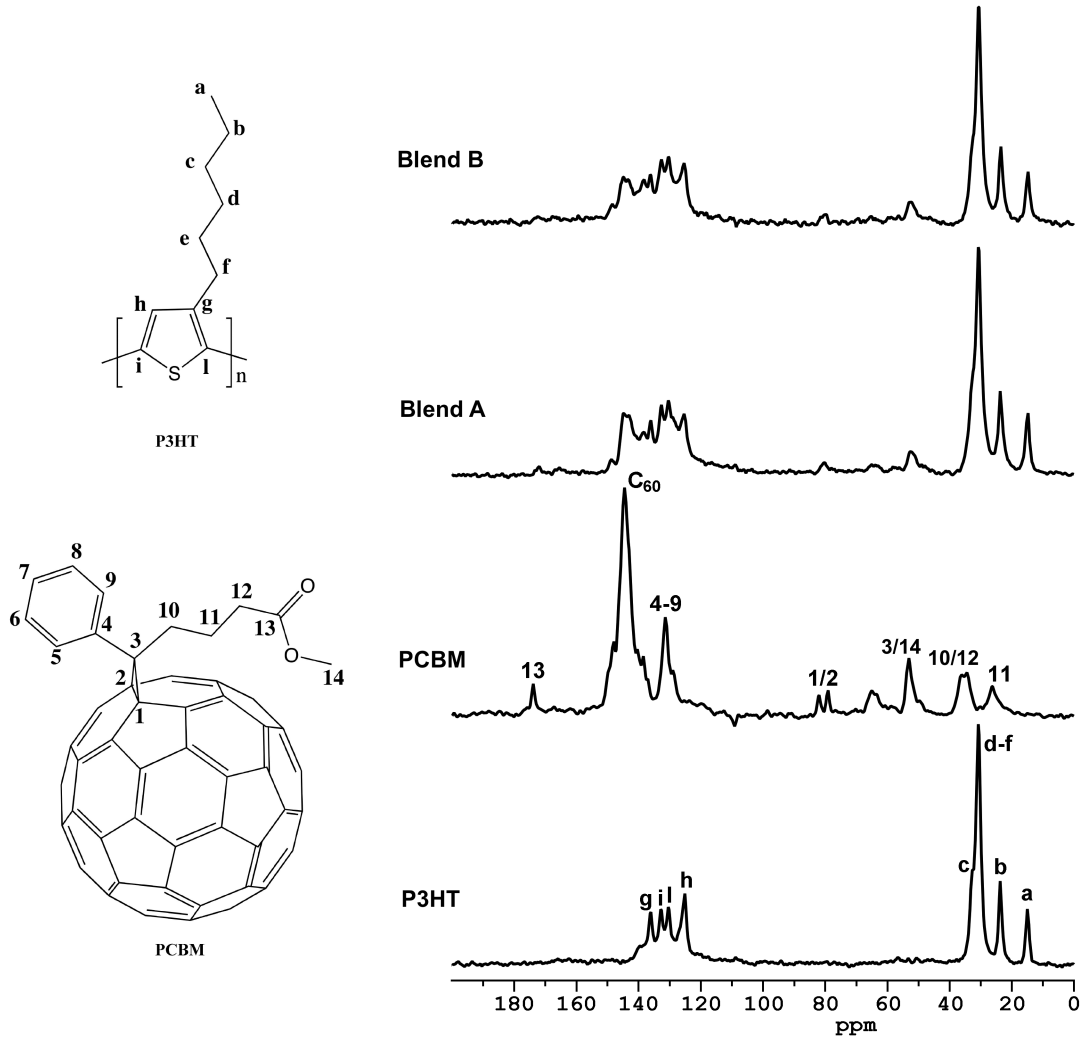

Figure 5.4: ^{13}C CP/MAS spectra recorded at a spinning frequency of 8 kHz, on, from bottom to top, neat P3HT, neat PCBM, Blend A and Blend B.

and very large aromatic carbons signals, corresponding to high and low structural order of the polymer backbones, respectively. Moreover, by means of SSNMR ^{13}C MAS spectra K. Saalwachter et al. observed the existence of two kinds of P3HT crystalline phases, I and II, characterized by side chains with low and high content of gauche conformations, respectively, the phase I being favored in low-molecular weight P3HT [86]. Indeed, the chemical shifts of a and $d-f$ carbon signals depend on the conformational properties of P3HT side-chains: a and $d-f$ should give rise to signals at about 15.5 and 33.6 ppm, respectively, when the side-chains are characterized by all-trans conformations, and at about 14.5 and 30.2, respectively, when a high content of gauche conformation is present. The spectrum of neat P3HT shown in Figure 5.4 suggests the presence of both crystalline and amorphous domains and that the crystalline ones are characterized by side chains with high content of gauche conformations. The features of P3HT carbon signals do not change significantly in the spectra of the blends with respect to neat P3HT.

In Figure 5.5 the experimental ^1H FID recorded for Blend A is reported as an example along with the corresponding fitting function, and the single components of the linear combination (two Gaussian and one exponential functions). In Table 5.1 the results of the FID analysis obtained for each sample are reported, together with the details of the fitting procedures. The principles and the methods at the basis of the ^1H FID analysis are described in section 4.4.2. In order to simplify the discussion, it is useful to identify four functions characterized by increasing T_2 values, corresponding to increasing degree of mobility: A) $T_2 \sim$ 20-30 μs, B) $T_2 \sim$ 50-60 μs; C) $T_2 \sim$ 100-150 μs; D) $T_2 \sim$ 500 μs. For neat P3HT and PCBM, the experimental FID resulted to be well reproduced by the combination of a main component of kind A, ascribable to protons in very rigid domains, and of a minor component of kind B for P3HT and C for PCBM, ascribable to protons in more mobile domains. These results clearly suggest a substantial rigidity in the frequency range of Hz-kHz for both P3HT and PCBM at room temperature. Moreover, even if a direct correspondence between the functions A and B (C) with crystalline and amorphous phases cannot be established, this analysis provided a clear indication of the presence of domains with different phase behavior in both P3HT and PCBM. In particular, it is likely that the shorter-T_2 component (A) mainly arises from

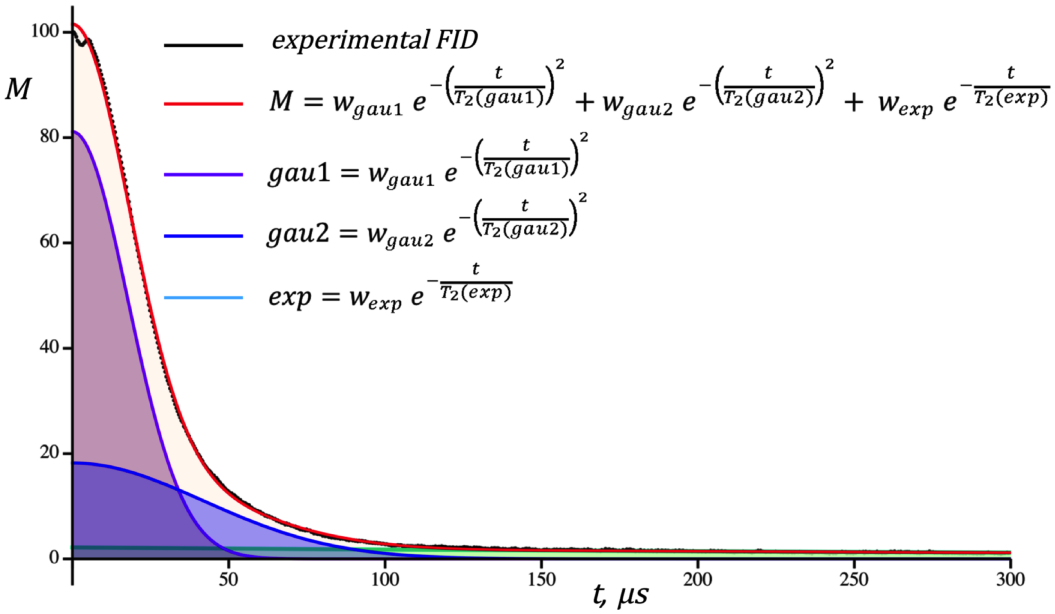

Figure 5.5: FID analysis relative to Blend A: experimental FID (black points), fitting function (red line), and single components of the linear combination, two Gaussian (gau1 and gau2) and one exponential function (exp) (purple, blue and light blue lines, respectively).

protons located in crystalline and/or glassy amorphous domains, while the longer-T_2 components (B and C) from protons in viscous amorphous domains. Passing to Blend A and B, the results of the fitting of the experimental FIDs are not significantly different from those that can be calculated on the basis of the blends' compositions, assuming that the behavior of the neat components does not change with blending. The only exception is the presence of a small fraction of a very mobile component (D), not observed for neat P3HT and PCBM, which can be ascribed to residual traces of solvent. The ^{1}H FID analysis and the ^{13}C spectral behaviour indicate that the mobility in the frequency range of Hz-KHz and the phase behavior of both P3HT and PCBM in the blends remain almost the same as in neat components and are not significantly affected by the annealing procedure. Different results have been obtained by other authors [54, 92, 97]: this could be explained with differences in the properties of the P3HT used (regioregularity and/or molecular weights) and/or in the blend preparation, that are known to significantly influence the phase behavior of both P3HT and PCBM.

Table 5.1: Results of the fitting of proton FID of neat P3HT and PCBM and their blends A and B.

	Function A		Function B		Function C		Function D	
	T_2 (µs)	wt %	T_2 (µs)	wt %	T_2 (µs)	wt %	T_2 (µs)	wt %
P3HT	27 $(g)^1$	75.6	56 $(g)^1$	24.4	-	-	-	-
PCBM	26 $(a)^1$	92.2	-	-	101 $(e)^1$	7.8	-	-
Blend Calc.[2]	26-27	79	56	19.5	100	1.5	-	-
Blend A	25 $(g)^1$	79.9	59 $(g)^1$	17.9	-	-	497 $(e)^1$	2.2
Blend B	26 $(g)^1$	79.6	59 $(g)^1$	19.2	-	-	497 $(e)^1$	1.2

[1]The letters g, a, and e indicate Gaussian, Abragamian and exponential functions, respectively. [2]The row "blend calc." contains the expected T_2 and wt% values under the hypothesis that the dynamic properties in the Hz-kHz regime of P3HT and PCBM do not change in passing from the neat components to the blends.

5.5.2 Phase separation: room-temperature $T_1(H)$ by ^{13}C detection

Useful information on the degree of mixing between P3HT and PCBM could be obtained from the measurement of proton T_1's at room temperature. Indeed, as already mentioned in section 5.4, in a heterophasic system a single $T_1(H)$ is measured for all the protons when the dimensions of the smallest domains are smaller than 100-200 Å. In order to selectively measure the T_1 of protons located in PCBM and P3HT domains in the blends, high-resolution saturation recovery-^{13}C CP/MAS experiments have been performed, allowing the measurement of these relaxation times through ^{13}C detection, i.e. exploiting carbon high-resolution spectra. In particular, while for neat components the ^{13}C full-spectrum integrals were measured, for the blends we performed deconvolutions of the ^{13}C spectra at different evolution times and we used the areas of the well-resolved signals of d and C_{60} carbons to determine individual relaxation times for P3HT and PCBM, respectively. All the different experimental relaxation curves were found to be well reproduced by mono-exponential functions. The values of $T_1(H)$ measured for the

Table 5.2: Proton spin-lattice relaxation times ($T_1(H)$) measured at room temperature at a Larmor frequency of 400 MHz for P3HT and PCBM in the neat samples and in Blend A and B.

	T_1(H) (s), T = 25 °C	
	P3HT	**PCBM**
P3HT	0.86	-
PCBM	-	12.0
Blend A	0.65	0.85
Blend B	0.78	1.31

different samples and components are reported in Table 5.2.

For neat P3HT and PCBM, the presence of a single $T_1(H)$ suggests that the crystalline and amorphous domains possibly present are intimately mixed on a spatial scale of 100-200 Å. On the other hand, for both Blend A and Blend B we measured two slightly but significantly different $T_1(H)$ values for P3HT and PCBM protons, both lower than those of the corresponding neat components, indicating an intimate but not completely homogenous mixing between P3HT and PCBM domains on a 100-200 Å spatial scale. For P3HT the decrease of $T_1(H)$ with respect to the neat polymer seems to suggest a change in P3HT dynamic behavior in the MHz frequency range. This aspect will be investigated in detail in the following section. On the contrary, the much lower $T_1(H)$ measured for PCBM protons in the blends with respect to neat PCBM should be mainly ascribed to the proximity of P3HT protons which, through spin diffusion, act as relaxation sink. However, also a change in PCBM MHz dynamics after blending with P3HT cannot be ruled out [89]. Finally, it can be observed that the difference between the $T_1(H)$ values of P3HT and PCBM increases in passing from Blend A to Blend B. A similar result was recently obtained also by other authors [91], and suggests an increased phase separation between P3HT and PCBM domains following annealing, correlated to an increased structural order that could favor the formation of efficient percolation pathways

for the charges transport toward the electrodes, thus enhancing the performance of the P3HT/PCBM solar cell, as already hypothesized in the literature [54, 96, 97].

5.5.3 Dynamics: Variable temperature $T_1(H)$ and $T_1(C)$

The MHz dynamics of P3HT in the systems under study was investigated by variable temperature measurements of both $T_1(H)$, at the two Larmor frequencies of 24 and 400 MHz, and $T_1(C)$ at the Larmor frequency of 100.6 MHz for temperatures between 20 and 80 °C. The measurement of $T_1(C)$ under high-resolution conditions allowed us to selectively determine this relaxation time for P3HT aliphatic carbons a, b, c, and $d-f$, and for the protonated aromatic carbon h (Figure 5.4), using suitable spectral deconvolution methods [148]. On the other hand, since the presence of spin-diffusion prevented $T_1(H)$ from giving site-specific information, this was measured by direct proton detection under low-resolution conditions. At each temperature all the experimental ^{1}H and ^{13}C relaxation curves were well reproduced by monoexponential functions. It is worth noticing that a single $T_1(C)$ could be measured for P3HT aliphatic carbons $d-f$, whose signals are heavily superimposed and could not be resolved. For this reason these carbons will be treated together in the following and globally indicated as carbons d. In order to obtain reliable and quantitative information on the reorientational motions of P3HT in the MHz frequency range, for each sample we performed a simultaneous fitting of all the experimental $T_1(H)$ and $T_1(C)$ vs temperature curves by using the models previously described, and taking into account all the motional processes that could contribute to T_1 relaxation. The fitting allowed the correlation time function (τ_c) of each motional process to be determined: in particular, for each motion the parameters of the fitting were the activation energy, U, the parameter τ_∞, and the constants C_H and C_C (section 5.4).

Neat P3HT

As far as neat P3HT is concerned, it is possible to identify at least seven independent motional processes that could contribute to T_1 relaxation: the inter-conformational motions of the methyl and of each methylene group of the hexyl side chain, and the twisting motion of the poly(thiophene) main chain. However, due to the high complexity of the system, it was necessary to introduce some approximations. In a first attempt, considering that the twisting motion of the main chain should be quite slow with respect to the very fast interconformational motions of the hexyl side group [87, 149], we hypothesized that its contribution to T_1 relaxation was negligible. Under this hypothesis the T_1 vs temperature curves of each alkylic carbon should be reproduced by a fitting function of the kind reported in equation 5.5, where the only source of relaxation is the interconformational motion of the corresponding methylene or methyl group. On the other hand, the $T_1(H)$ curves at the two Larmor frequencies should be fitted by a function of the kind reported in equation 5.3, where the terms of the linear combination correspond to the six interconformational motions of the hexyl side group. In order to further simplify the model and to reduce the possibility of correlations between different parameters, we introduced other two main approximations. As first we considered that the values of C_H and C_C were the same for all the alkylic methylene and methyl groups. Moreover, we assumed that the reorientational motions of all the methylene side groups were characterized by the same correlation time, while the methyl motion was treated independently. However, using this simplified model the fitting of the experimental T_1 vs temperature curves (here not reported) did not give satisfactory results.

In order to verify if this could be due to the neglect of the poly(thiophenic) main chain twisting motion, we included it in the model. The alkylic side chain groups are then supposed to experience a quite complex motion which can be described as the combination of two independent processes: the faster interconformational motion of each group and the slower tumbling of the entire side chain due to the twisting motion of the thiophenic main chain. In the following we will refer to these two contributions as interconformational and tumbling motions, respectively. On this basis the $T_1(C)$ of the

side chain carbons obeys the following equation:

$$R_1(C)^i = \frac{1}{T_1(C)^i} \tag{5.10}$$

$$= \frac{N_i}{15r_{CH}^6} C_C \left(\left[\frac{2\tau_i}{1+(\omega_H-\omega_C)^2\tau_i^2} + 3\frac{2\tau_i}{1+\omega_C^2\tau_i^2} + 6\frac{2\tau_i}{1+(\omega_H+\omega_C)^2\tau_i^2} \right] \right.$$

$$\left. + C_{Ci}^{thio} \left[\frac{2\tau_{thio}}{1+(\omega_H-\omega_C)^2\tau_{thio}^2} + 3\frac{2\tau_{thio}}{1+\omega_C^2\tau_{thio}^2} + 6\frac{2\tau_{thio}}{1+(\omega_H+\omega_C)^2\tau_{thio}^2} \right] \right)$$

where $\tau_i = \tau_{\infty i} e^{\frac{U_i}{kT}}$ are the correlation times relative to the interconformational motions of the methylic (τ_a) or methylene (τ_{int}) groups, while $\tau_{thio} = \tau_{\infty thio} e^{\frac{U_{thio}}{kT}}$ is the correlation time of the tumbling motion. The parameter C_{Ci}^{thio} should assume values between 0 and 1, and could be different for carbons a, b, c and d due to the different motional amplitude of their interconformational motions, which increases along the chain from d to a, causing in principle a more efficient averaging of the dipolar couplings. In order to reliably determine the parameters relative to the main chain twisting motion, and so the correlation time function τ_{thio}, we introduced in the fitting also the experimental T_1 vs temperature curve relative to the protonated thiophene carbon h. It is worth to notice that in the model here used we completely neglected the contribution of chemical shift anisotropy to the T_1 relaxation of the thiophenic carbon h, contrary to the hypothesis in [87]. Indeed in our case $T_1(C)$ of carbon h was significantly lower than those of the quaternary thiophenic carbons, thus justifying to neglect CSA contribution. As far as $T_1(H)$ curves are concerned, we used the following fitting function:

$$R_1(H) = \frac{1}{T_1(H)} = C_H \left(f_a \left[\frac{2\tau_a}{1+\omega_H^2\tau_a^2} + 4\frac{2\tau_a}{1+4\omega_H^2\tau_a^2} \right] \right. \tag{5.11}$$

$$\left. + f_{int} \left[\frac{2\tau_{int}}{1+\omega_H^2\tau_{int}^2} + 4\frac{2\tau_{int}}{1+4\omega_H^2\tau_{int}^2} \right] + C_H^{thio} \left[\frac{2\tau_{thio}}{1+\omega_H^2\tau_{thio}^2} + 4\frac{2\tau_{thio}}{1+4\omega_H^2\tau_{thio}^2} \right] \right)$$

The first two terms in the square brackets refer to the contributions of the interconformational motions of the methylic (a) and methylenic ($b-d$) groups, f_a and f_{int} being the fractional populations of the corresponding protons. The third term takes into account the contributions of the main chain twisting motion to the relaxation of proton h and $a-d$ and C_H^{thio} is:

$$C_H^{thio} = f_a C_{Ha}^{thio} + f_{int} C_{Hint}^{thio} + f_h K \tag{5.12}$$

where C_{Ha}^{thio} and C_{Hint}^{thio} are defined similarly to C_i^{II} in equation 5.4. f_h represents the fractional population of the proton h, and K responds to the equation $C_{Hh} = KC_H$. Since proton h is expected to experience a weaker homonuclear dipolar coupling than $a-d$ protons, K should assume values between 0 and 1. All this considered, the constant C_H^{thio} is expected to assume a positive value less than 1.

All the $T_1(H)$ and $T_1(C)$ data were simultaneously fitted to the above described equations by optimizing the parameters reported in Table 5.3. In Figure 5.6 all the experimental T_1 vs temperature curves and the corresponding fitting functions are shown, while in Table 5.3 the values of the optimized parameters relative to the different motional processes are reported. From Figure 5.6 it can be clearly observed that the fitting model here used allowed all the experimental $T_1(H)$ and $T_1(C)$ data to be well reproduced. The results of the fitting indicate that, as expected, the alkylic side chain is much more mobile than the main chain. This can be clearly observed from the minima of the $T_1(C)$ curves that occur at increasing temperatures in passing from carbons a to $b-d$ to h, also indicating that within the alkylic side chain the methyl group is, as expected, the most mobile. To this respect it is useful to report the calculated values of correlation times at room temperature, that are about 80 ps and 300 ps for the interconformational motions of methyl and methylene groups, respectively, and 2570 ps for the twisting motion of the main chain. Looking at the calculated $T_1(C)$ vs temperature curves relative to carbons $b-d$, it is evident the presence of one narrower and one broader minimum at about -25 and +30 °C, respectively, which derive from the contributions of the interconformational and tumbling motions, respectively. In particular, since we assumed that τ_{int} was the same

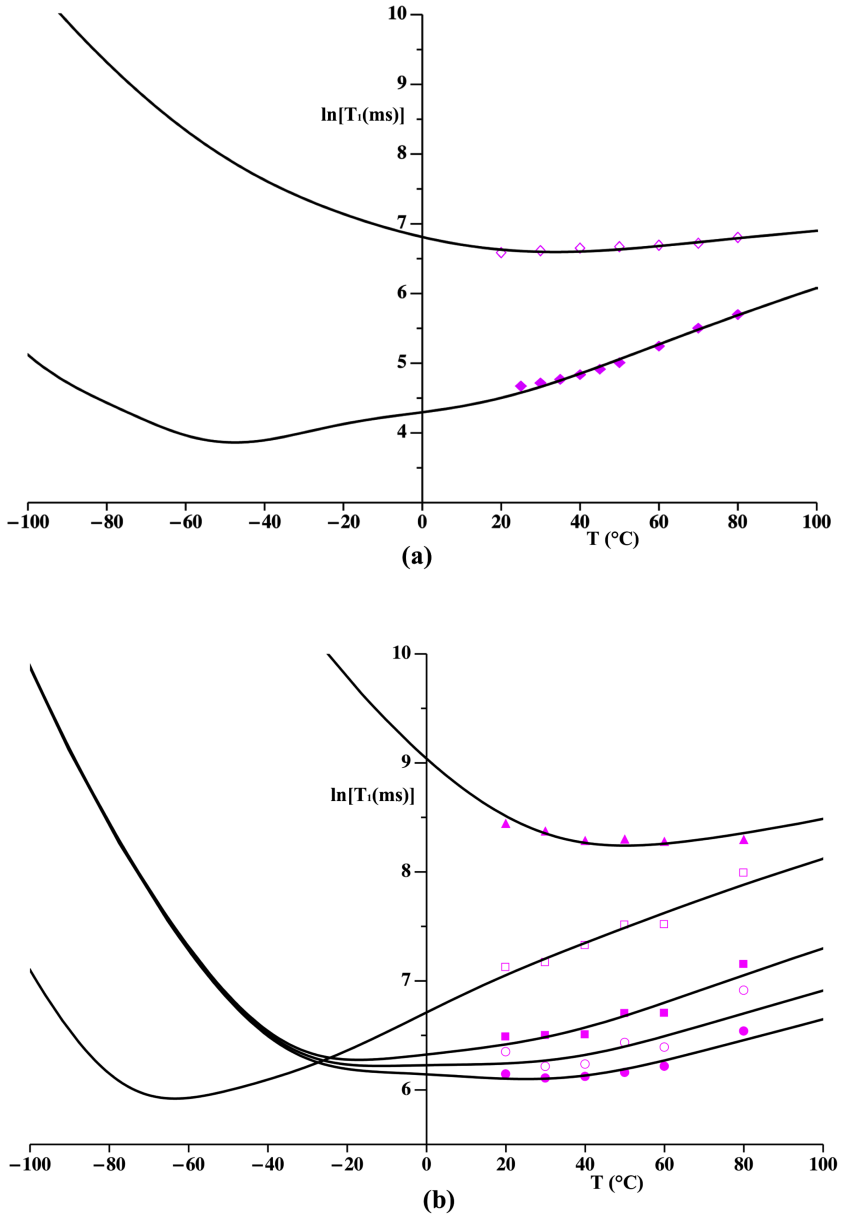

Figure 5.6: (a) Experimental $T_1(H)$ vs temperature curves obtained for neat P3HT at the two Larmor frequency of 24 (◊) and 400 MHz (⧫), with the corresponding fitting functions (lines). (b) Experimental $T_1(C)$ vs temperature curves obtained for carbons a (□), b (■), c (○), d (●), and h (▲) in neat P3HT, with the corresponding fitting functions.

Table 5.3: Results of the simultaneous fitting of all the $T_1(C)$ and $T_1(H)$ vs temperature curves obtained for neat P3HT, Blends A, and B. Activation energies, U, are in kJ/mol, constants C_H are in s^{-2}, while C_C and C_{Ch} are in $s^{-2}nm^6$. The number of digits reported for each parameter reflects the estimated error. It must be noticed that the errors on the individual parameters, such as r and U, are quite large due to their strong correlation, but their combined physically relevant parameter τ_c is affected by a much minor error, as reported in the text.

	U_a [1]	U_{int} [2]	U_{thio}	r_a [3]	r_{int} [2,3]	r_{thio} [3]	C_H	C_H^{thio}	C_C	C_{Ca}^{thio} [1]	C_{Cb}^{thio} [1]	C_{Cc}^{thio} [1]	C_{Cd}^{thio} [1]	C_{Ch}
P3HT	16	20	23	-13	-13	-12.5	0.9	0.3	2 x 10^9	0.1	0.2	0.5	0.7	3 x 10^8
Blend A	24	27	(f)[4]	-14	-14	(f)[4]	1.5	0.2	(f)[4]	0.1	0.3	0.4	0.8	(f)[4]
Blend B	16	17	(f)[4]	-13	-13	(f)[4]	1.7	0.2	(f)[4]	0.1	0.3	0.2	0.7	(f)[4]

[1]The subscripts a, b, c, and d refer to the motional processes of the P3HT alkylic side chain groups a, b, c, and d, respectively, that should be characterized by different values of C_{Ci}^{thio}. [2]The subscript int refers to the interconformational motions of the P3HT internal alkylic side-chain groups $b-d$, which we hypothesized to occur at the same correlation time τ_{int}. [3]r_i is a parameter related to the correlation time extrapolated at infinite temperature, $\tau_{\infty i}$, by the equation: $\tau_{\infty i} = 10^{r_i}$. [4] In the rows relative to Blends A and B, (f) indicates that a parameter was not optimized during the fitting, but was fixed at the value obtained for neat P3HT.

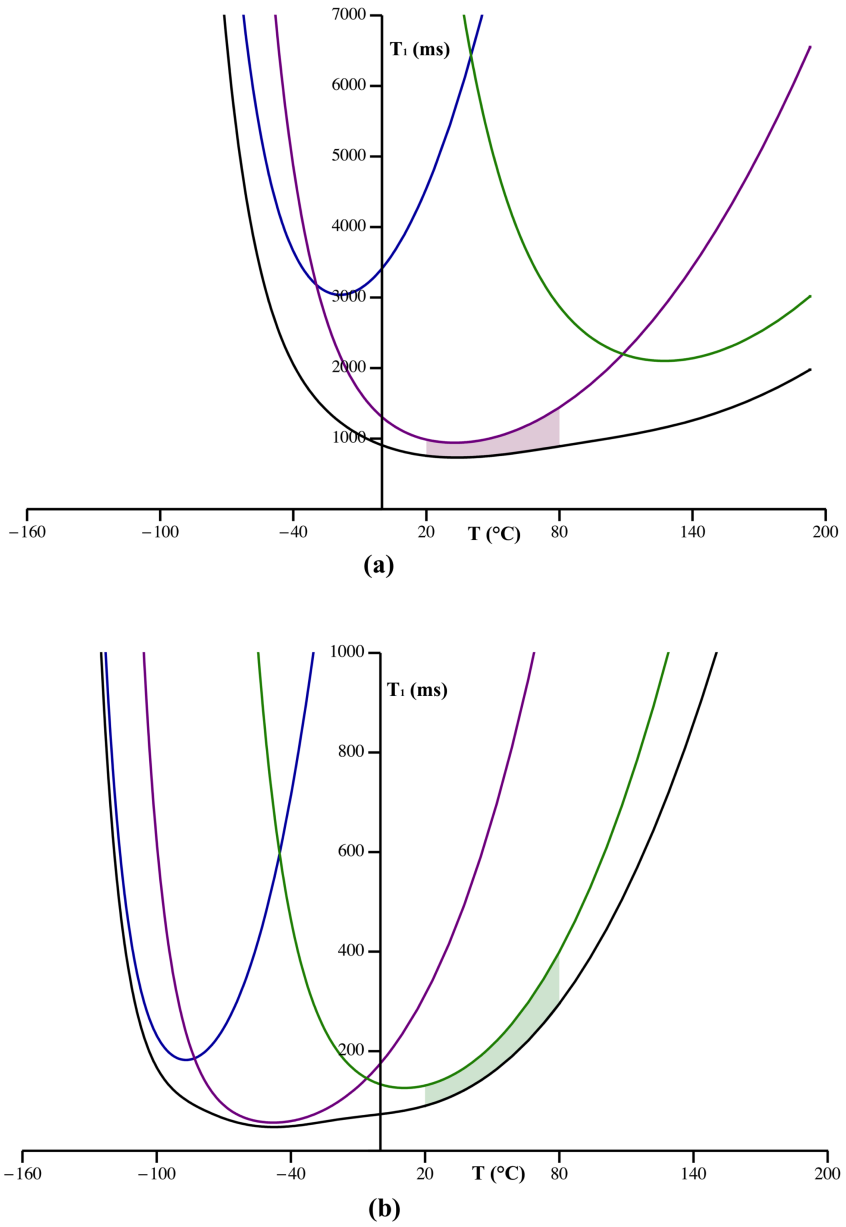

Figure 5.7: Optimized fitting functions (in black) for the $T_1(H)$ vs temperature curves of neat P3HT at the Larmor frequency of 400 (a) and 24 (b) MHz, together with the single contributions of the interconformational motions of the methyl and methylene groups (in blue and purple, respectively), and of the thiophenic twisting motion (in green). In both (a) and (b) the main contribution to $T_1(H)$ in the temperature range 20-80 °C is highlighted.

for all methylene groups, the differences among their calculated ^{13}C T_1 vs temperature curves can derive only from different C_{Ci}^{thio} values. In particular, C_{Ci}^{thio} best-fitting values were found to decrease in passing from d to c to b to a, indicating a corresponding decrease of the contribution of the tumbling motion. This is in agreement with the expected corresponding increase of the amplitude of the interconformational motions. The physical consistency of the fitting results supports the validity of the approximated model used, and confirms that the contribution of the thiophenic twisting motion to both $T_1(H)$ and $T_1(C)$ relaxation processes could not be neglected. The importance of this contribution becomes clearer if we look at the optimized $T_1(H)$ vs temperature curves, reported in Figures 4a and b along with the single contributions defined in Equation 5.11. At 400 MHz (Figure 5.7a), as expected on the basis of the ^{13}C T_1 vs temperature curves, the main contribution to the $T_1(H)$ relaxation in the investigated temperature range (20 − 80 °C) seems to derive from the interconformational motions of the methylene groups, whose $T_1(H)$ curve is characterized by a minimum within this temperature range. The contributions of the methyl and main chain motions are clearly less important, being in the very fast and slow motional regimes, respectively. However, passing from 400 to 24 MHz (Figure 5.7b) the weights of the different contributions significantly change. Indeed, as expected, at 24 MHz the minima of all the $T_1(H)$ curves are shifted to lower temperatures. As a consequence, the curve relative to the main chain twisting motion results to have a minimum at around 10 °C, and, as it is evident from Figure 5.7b, this becomes the main contribution to $T_1(H)$ in the temperature range 20-80 °C. On the other hand, the interconformational motions of methyl and methylene groups are in the fast motional regime, and their contribution to $T_1(H)$ decreases.

Blends P3HT/PCBM

In order to obtain information on the dynamic behavior of P3HT in the photoactive blends with PCBM before and after annealing (Blend A and B), we applied an experimental and methodological approach similar to that employed for the study of neat P3HT. In the case of P3HT/PCBM blends, PCBM motional processes, and in particular the reorientational motions of its aliphatic and aromatic groups, could in principle

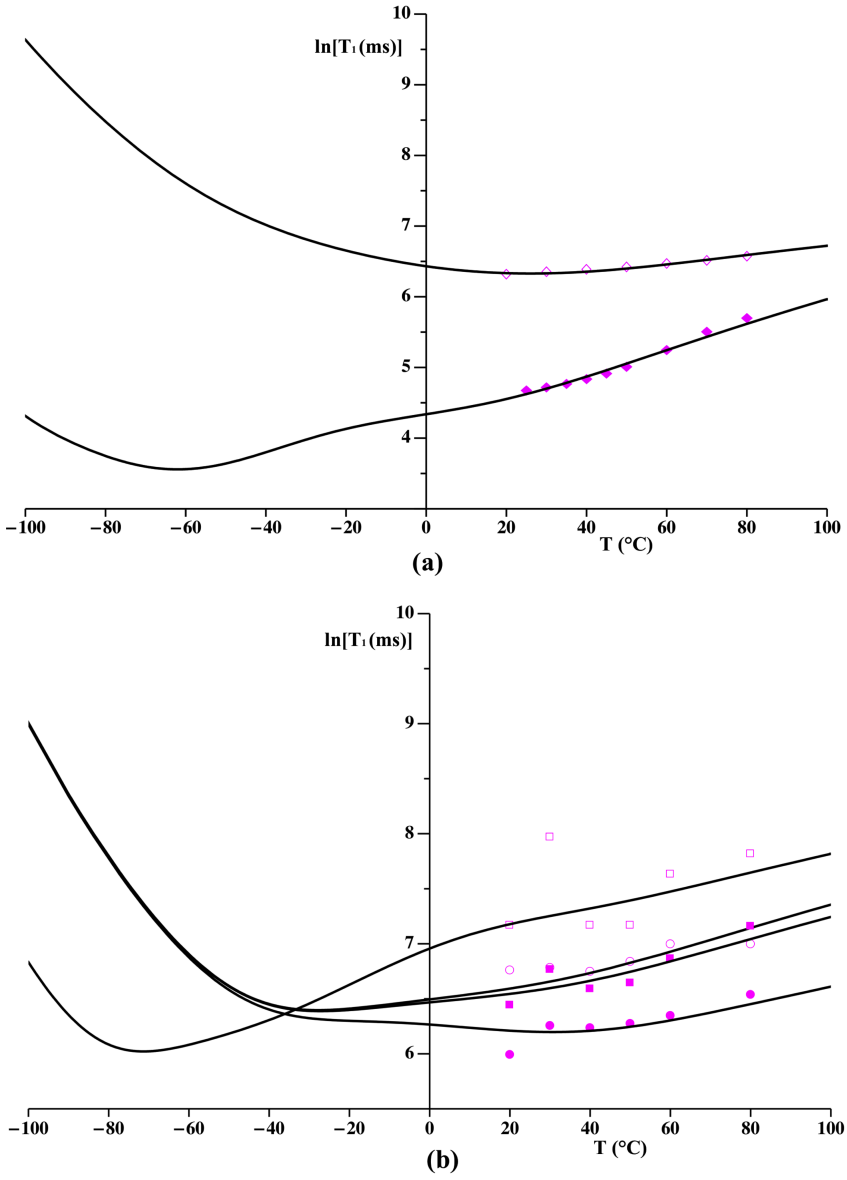

Figure 5.8: (a) Experimental $T_1(H)$ vs temperature curves obtained for Blend B at the Larmor frequencies of 24 (⧫) and 400 MHz (◊) with the corresponding fitting functions (lines). (b) Experimental $T_1(C)$ vs temperature curves obtained for carbons a (□), b (■), c (○), and d (●) in Blend B, with the corresponding fitting functions.

contribute to $T_1(H)$ together with those of P3HT. However, taking into account the contributions of PCBM motions in the global fitting of ^{1}H and ^{13}C T_1 vs T curves was not a straightforward task due to both the high complexity of the resulting fitting model, and to the scarce intensity of PCBM aliphatic carbon signals, which hindered a reliable determination of the corresponding $T_1(C)$. On the other hand, we could safely neglect the PCBM motions in the analysis on the basis of room-temperature $T_1(H)$ values. Indeed, $T_1(H)$ measured for neat PCBM was found to be much higher (12 s) than that measured for neat P3HT (0.7 s), and in the blends, in spite of spin diffusion, the T_1 value measured for PCBM protons was still higher than that measured for P3HT ones (Table 5.2). As far as P3HT is concerned, the same motional processes described for the neat polymer were considered, and the parameters of the motions were determined by fitting the experimental $T_1(H)$ and $T_1(C)$ vs temperature curves using the same fitting model applied in the case of neat P3HT. However in the case of the blends, a reliable determination of the $T_1(C)$ vs temperature curve relative to the P3HT carbon h was not possible due to the strong superimposition of its signal with those of PCBM aromatic carbons in the ^{13}C MAS spectra (Figure 5.4). For this reason the parameters of the thiophenic twisting motion in the blends could not be optimized in the fitting procedure, and they were fixed to the values obtained for neat P3HT.

In Figure 5.8 the fitting of the $T_1(H)$ and $T_1(C)$ vs temperature curves relative to blend B is shown, and in Table 5.3 the best-fitting parameter values are reported. For both blends A and B the fitting model allowed all the experimental T_1's to be well reproduced. In both the blends the interconformational motions of the side chain resulted to be faster than that of the thiophenic main chain, and the contribution of the tumbling motion to the ^{13}C T_1 of methyl and methylene was found to decrease in passing from d to a (see C_{Ci}^{thio} values in Table 5.3). Comparing the results obtained for the blends and for neat P3HT it is evident that the optimized parameters relative to the interconformational motions of P3HT significantly change in passing from neat polymer to Blend A as well as from Blend A to Blend B. This suggests that both the blending with PCBM and the annealing treatment affect the dynamic properties of P3HT in the MHz frequency range. In particular, comparing the different correlation time functions in the temperature range

20-50 °C, the mobility of the side chains seem to decrease in passing from neat P3HT to Blend A, and to increase in passing from both P3HT and Blend A to Blend B. The correlation time values calculated at 25 °C for the interconformational motions were found to be about 80, 100, 60 ps (methyl group) and 300, 355, 270 ps (methylene groups) for P3HT, Blend A, and Blend B, respectively. The errors on these correlation times were estimated to be about 10-15 %. These differences can be tentatively correlated with changes in the morphological properties. In particular the decrease of mobility of the side chains in passing from P3HT to Blend A could be associated with the intimate mixing with PCBM which is typical of the bulk-heterojunction morphology. On the other hand an increase of phase separation between P3HT and PCBM after annealing, already hypothesized on the basis of the high-resolution $T_1(H)$ measurements, could be associated with an increase of free volume and hence to an increase of mobility of the alkylic side-chains.

5.6 Experimental

The high resolution ^{13}C experiments and the measurements of proton T_1 relaxation times at the ^{1}H and ^{13}C Larmor frequencies of 400.3 and 100.62 MHz, respectively, were carried out on a dual-channel Varian InfinityPlus 400 spectrometer, equipped with a 3.2 mm Cross Polarization/Magic Angle Spinning (CP/MAS) probehead, with typical ^{1}H and ^{13}C $\frac{\pi}{2}$ pulse durations of about 3 μs. All the ^{13}C MAS spectra were recorded using a spinning frequency of 8 kHz and under high-power decoupling from protons. The measurements of proton T_1 under high-resolution conditions were performed by means of a saturation recovery-^{13}C CP/MAS pulse sequence, using a contact time of 8 ms, and accumulating about 600 transients. The variable temperature measurement of proton T_1's were performed by direct proton observation under static conditions using the saturation recovery pulse sequence, accumulating 16 transients. Carbon T_1 relaxation times were measured using the Torchia pulse sequence, with a recycle delay of 3.5 s, a contact time of 1 ms, and accumulating about 200-300 transients. The MAS experiments were carried out using air as spinning gas. TMS was used as a primary chemical shift

reference for all nuclei, while hexamethylbenzene was the secondary reference for ^{13}C.

The measurements of proton free induction decays (FIDs) and T_1 at the ^1H Larmor frequency of 24 MHz were carried out on a Varian XL-100 spectrometer coupled with a Stelar PC-NMR acquisition system, using ^1H pulse duration of about 4 μs. Proton FIDs were acquired under on resonance conditions through a solid echo pulse sequence, using a recycle delay of 1 s for neat P3HT and P3HT/PCBM blends, and of 10 s for neat PCBM, and accumulating 3600 transients for neat P3HT and about 14000 transients for neat PCBM and the blends. Proton T_1 relaxation times were measured by means of an inversion recovery-solid echo pulse sequence, using the same recycle delays than for recording FIDs, accumulating 4000-12000 transients. Variable temperature measurements were carried out using air as heating gas. When not specified measurements were performed at room temperature.

5.7 Conclusion

The multinuclear, multitechnique solid-state NMR approach here applied was effective in giving detailed phase, morphological and dynamic information on P3HT/PCBM blends. Phase properties were mainly investigated by ^{13}C CP/MAS spectra and ^1H FID analysis, while information on phase separation was obtained by looking at the effects of proton spin diffusion on proton spin-lattice relaxation times. However, the obtainment of detailed dynamic information required the measurement of variable-temperature $T_1(H)$ at two different Larmor frequencies, as well as site-specific carbon spin-lattice relaxation times.

The analysis of relaxation data, to which most of this work is devoted, was carried out by means of a sophisticated model taking into account the motions of all the methyl and methylene groups of P3HT hexyl side chain, as well as the twisting of P3HT main chain. To the best of our knowledge, this is the first time that a detailed dynamic investigation was carried out on these materials and, more in general, on a polymeric blend.

It is here suggested that in the non annealed P3HT/PCBM blend the two components are quite intimately mixed, and that the dynamics of P3HT side chains is more hindered

than in neat P3HT. In contrast, after annealing at 150 °C, the blend exhibits a larger degree of P3HT/PCBM phase separation, with a consequent increase in the mobility of P3HT side chains, arising from the availability of a larger free volume. The observed slight increase in the phase separation and in the mobility of P3HT side chains should lead to the formation of nanoscale aggregates, constituting better percolated carrier pathways able to accelerate the charge transport in BHJ solar cells, as already hypothesized [55, 96, 97].

Chapter 6

An approach for the measurement of ^{19}F CSA in polymeric materials under magic angle spinning

6.1 Introduction

As described in section 1.5, NMR spectra of solid samples are affected by the anisotropic contributions of the internal interactions, causing inhomogeneous or homogeneous broadening of the signals of powder samples. In the case of inhomogeneous broadening, the lineshape of the NMR signal reflects the isotropic distribution of molecular orientations in the powder. Differently, the homogeneous broadening, which arises from the homonuclear dipolar interaction, is due to the continuous exchange of Zeeman energy between dipolarly coupled nuclear spins of the same species, and equally affects signals of spins in different molecular orientations.

The anisotropic terms of the internal Hamiltonians contain useful information on the structural and dynamic properties of the samples, which can be extracted by the experimental determination of the characteristic interaction parameters, i.e, anisotropy (Δ) and asymmetry (η) in the case of the chemical shift anisotropy, dipolar coupling constant in the case of the heteronuclear and homonuclear dipolar couplings etc..

In SSNMR, there are various possible approaches to the measurement of the interaction parameters. The simplest one consists in the analysis of the static lineshapes of the NMR signal from 1D spectra. This is feasible only for very simple samples, containing few non-equivalent spins. Another possible approach is the analysis of the spinning sideband profiles, acquired under MAS (section 1.7.1). Indeed, it was demonstrated that the information about the principal components of the interaction tensors is encoded in the sideband patterns of NMR spectra of powder samples [150, 151] . In the case of very congested SSNMR spectra, where the superimposition of signals arising from multiple non-equivalent spins, each affected by various anisotropic interactions, obscures any useful information, the reliable determination of the interaction parameters is possible only with more complex 2D recoupling experiments. These techniques combine MAS rotation with rotor synchronized pulse sequences able to recouple the interaction of interest. The result is a 2D spectrum that correlates the isotropic chemical shift (direct dimension) with the anisotropic part of the interaction of interest (indirect dimension). It is worth noticing that this approach maintains the advantages of the high resolution techniques, allowing to separate the anisotropic contributions arising from different sites in the sample. Different recoupling techniques have been developed, able to selectively recouple different anisotropic interactions, such as the chemical shift anisotropy [152, 153], the homonuclear and heteronuclear dipolar coupling [154, 155], and the quadrupolar coupling [156].

In this thesis RN_n^ν symmetry-based recoupling sequences were used to recouple ^{19}F and ^{1}H CSA in different samples. These are among the most flexible recoupling sequences, since the opportune combination of the symmetry numbers N, n and ν allows to selectively reintroduce specific nuclear spin interactions under different experimental conditions, for example MAS frequency and rf amplitude [61, 157–159].

6.2 Materials and aims

This work was carried out during a six-months period that I spent in the SSNMR laboratory of Prof. Jeremy Titman, at the School of chemistry of the University of Nottingham. This collaboration arose from the interest of the SSNMR group in Pisa in measuring the CSA of ^{19}F nuclei present in zirconium phosphonates, in order to find some correlations between the ^{19}F CSA parameters and the crystalline structures of these materials. To this aim, in the group of Prof. J. Titman I could avail of advanced SSNMR instrumentation, such as a high field magnet (^{1}H Larmor frequencies of 600 MHz) and a *ultrafast* MAS 1.3 mm probe, allowing sophisticated high-resolution SSNMR experiments for the measurement of ^{19}F CSA to be carried out. Especially, I could take advantage of the experience of J. Titman and coworkers in the use of symmetry-based RN_n^ν recoupling sequences for the measurement of CSA of abundant nuclei. In particular, in a recent work they successfully developed a novel experiment based on RN_n^ν sequences for the recoupling of ^{1}H CSA under *ultrafast* MAS conditions (MAS frequencies exceeding 50 kHz) [160]. The determination of CSA anisotropies for systems of abundant nuclei can be difficult due to the presence of strong homonuclear dipolar interactions, which broaden the signals and reduce the spectral resolution. In the case of ^{1}H nuclei this is particularly challenging also because the chemical shift interaction is relatively small. Nevertheless, several recoupling experiments have been recently developed, which can be employed for recoupling ^{1}H CSA also in relatively complex powder samples [159, 161, 162]. The application of similar experiments to the nucleus ^{19}F (natural abundance 100%) was interesting, since, to the best of our knowledge, RN_n^ν sequences were never applied to the determination of ^{19}F CSA. Even if the spectral resolution for ^{19}F is not as critical as for ^{1}H (^{19}F is an abundant nucleus, but fluorine atoms are often not abundant in a sample), and the larger values of ^{19}F CSA often allow its determination from the analysis of 1D powder pattern or spinning sideband profiles, the use of high resolution recoupling techniques could be useful in the case of particularly congested ^{19}F spectra.

In the zirconium phosphonates of interest the measurement of ^{19}F CSA was complicated by the heteronuclear dipolar coupling between ^{19}F and the ^{1}H nuclei, present

in the samples, as well as by the very large values of ^{19}F CSA, with Δ of the order of 200 ppm. On the one hand, the ^{19}F-^{1}H heteronuclear dipolar coupling could affect both the spinning-sideband profiles in ^{19}F MAS spectra and, as it is explained in the following section, the recoupled patterns obtained from 2D RN_n^ν experiments, making difficult the reliable determination of the CSA parameters. On the other hand, it was challenging to find a R sequence able to recouple such large values of CSA, under experimental conditions, in terms of MAS rates and rf amplitudes, accessible with the available instrumentation.

For these reasons, a large part of the period that I spent in Nottingham was dedicated to set up an experimental approach for the reliable determination of large ^{19}F CSA in the presence of ^{1}H-^{19}F dipolar coupling. The method was first tested on simpler "reference" samples, and then applied to the more complex zirconium phosphonates. In the present chapter, the method used for the measurement of ^{19}F CSA is described, and the results obtained on the two reference samples, polytetrafluoroethylene (PTFE) and polyvinylidene fluoride (PVDF), are reported. The application of this method to the study of the more complex zirconium phosphonates will be described in the following chapter.

As far as the methodological approach is concerned, two different methods for the measurement of ^{19}F CSA were used and compared on both PTFE an PVDF: the analysis of the spinning sideband profiles obtained at different MAS frequencies, and the use of suitable RN_n^ν recoupling sequences. SIMPSON simulations allowed to identify RN_n^ν sequences able to successfully recouple ^{19}F CSA with anisotropy values of the order of 200 ppm, as well as to evaluate the effect of the ^{1}H-^{19}F dipolar interaction on the recoupled patterns. The comparison of ^{19}F CSA parameters determined by the more conventional method of the spinning sideband analysis and by the use of RN_n^ν recoupling sequences was useful to test the effectiveness and reliability of the selected RN_n^ν sequences in reintroducing ^{19}F CSA, as well as to evaluate the limits of the two methods in terms of errors on the determined CSA parameters.

6.3 R symmetry-based recoupling sequences

This section contains a brief description of the principles at the basis of the recoupling of nuclear spin interactions by means of RN_n^ν, with specific reference to the sequences employed in this thesis.

The ability of a recoupling sequence to reintroduce a specific nuclear spin interaction can be explained in terms of symmetry principles, related to the rotational properties of the nuclear interaction Hamiltonians [61]. The Hamiltonian of each nuclear spin interaction can be expressed as a product of three terms, expressing its transformation properties under the effect of rotations of the molecular framework (*space* part), of the nuclear spin polarization (*spin* part), and of the external magnetic field (*field* part) [61]. Each term is related to an irreducible spherical tensor characterized by a rank, called *rotational rank*, which depends on the nuclear spin interaction. The *rotational ranks* of the *space* (l), *spin* (λ), and *field* parts relative to the most common homonuclear spin interactions are summarized in Table 6.1. Space and spin tensors with ranks l and λ

Table 6.1: Rotational ranks of the most common homonuclear interactions.

Interaction	Space rank (l)	Spin rank (λ)	Field rank
Isotropic chemical shift	0	1	1
Chemical shift anisotropy	2	1	1
J-coupling	0	0	0
Homonuclear dipolar coupling	2	2	0

have $2l+1$ and $2\lambda+1$ space and spin components, identified by the quantum numbers $m = -l, -l+1 \cdots, +l$ and $\mu = -\lambda, -\lambda+1, \cdots, +\lambda$, respectively. Under MAS and on resonance conditions, the hamiltonian of the interaction Λ can be expressed as a superimposition of $((2l+1)\times(2\lambda+1))$ components:

$$\hat{\mathcal{H}}^{\Lambda} = \sum_{m=-l}^{+l} \sum_{mu=-\lambda}^{+\lambda} \hat{\mathcal{H}}^{\Lambda}_{lm\lambda\mu} \tag{6.1}$$

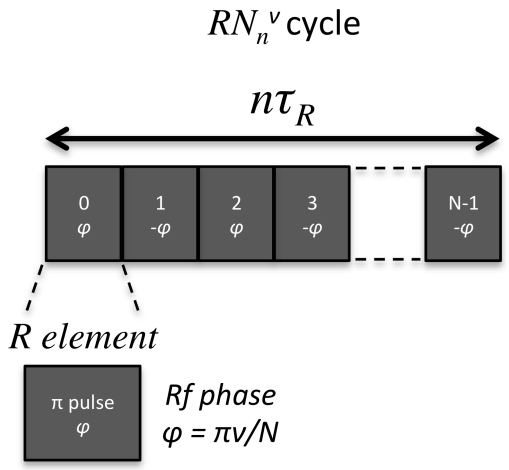

Figure 6.1: Scheme of a generic RN_n^ν recoupling cycle.

Rotations of the molecular frame, induced by the MAS, and of the nuclear spin polarization, induced by the pulse sequence, have the effect to interconvert the $2l+1$ space and $2\lambda+1$ spin components, respectively, according to the transformation equation reported in ref. [61]. The symmetry properties of a recoupling sequence determine characteristic selection rules, such that only specific space and spin components can be recoupled by the sequence. Interestingly, it is usually possible to find symmetries able to selectively recouple only interactions characterized by a specific combination of the ranks l and λ.

In this thesis, recoupling sequences belonging to the RN_n^ν symmetry class were used, where N, n, and ν are integers. In Figure 6.1 the scheme of a generic RN_n^ν recoupling cycle is shown. This is formed by N inversion elements (R), repeating within n rotor periods (τ_R) of the MAS rotation. Each element has a duration of $\frac{n\tau_R}{N}$ and a phase of the rf field alternated between $-\phi$ and $+\phi$, where $\phi = 2\pi\nu/N$. Due to the phase alternation, N must be an even number, the block consisting of $\frac{N}{2}$ pairs of elements $R_\phi R_{-\phi}$. In this work, R elements are constituted by simple π pulses, but composite pulses providing an overall magnetization inversion can also be used. Using the Average Hamiltonian Theory and considering only the first-order correction, it can been shown that the selection rules for a generic RN_n^ν recoupling sequence are:

$$\hat{\overline{\mathcal{H}}}^{\Lambda(1)}_{lm\lambda\mu} = 0 \qquad if \quad mn - \mu\nu \neq \frac{N}{2} Z_\lambda \tag{6.2}$$

where $\overline{\hat{\mathcal{H}}}^{\Lambda(1)}_{lm\lambda\mu}$ is the average, i.e. averaged over a period $T = n\tau_R$ of the pulse sequence, interaction Hamiltonian, approximated to the first order [61]. Z_λ is an integer number, which assumes even values $Z_\lambda = 0, \pm2, \pm4, \pm6 \cdots$, if λ is even, and odd values $Z_\lambda = \pm1, \pm3, \pm5, \pm6, \pm7 \cdots$, if λ is odd.

In order to predict the nuclear spin interactions recoupled by a given RN^ν_n sequence, it useful to introduce the space spin selection diagrams, examples of which are reported in Figure 6.2. On the left of a space spin selection diagram, the different values of the first term, $mn - \mu\nu$, in Eq. 6.2, split up in a *space* part, mn, and a *spin* part, $\mu\nu$, are reported. On the right, there is a barrier containing holes at the values $\frac{N}{2}Z_\lambda$. The pathways which pass through the holes represent the values of $mn - \mu\nu$ that do not satisfy Eq. 6.2, corresponding to the symmetry-allowed $\overline{\hat{\mathcal{H}}}^{\Lambda(1)}_{lm\lambda\mu}$ terms recoupled by the sequence.

In Figure 6.2 the space-spin selection diagrams relative to the sequences used in this thesis, that are $\mathrm{R12}^4_5$ and $\mathrm{R8}^2_1$, are reported. In the case of $\mathrm{R12}^4_5$, the combination of N, n and ν, set to 12, 5, and 4, respectively, allows the recoupling of the space-spin components $\{l, m, \lambda, \nu\}$ $\{2, 2, 1, 1\}$ and $\{2, -2, 1, -1\}$ of the CSA tensor, while no components of the homonuclear dipolar coupling are symmetry-allowed. In contrast, the $\mathrm{R8}^2_1$ recouples space-spin components of both the CSA ($\{2, 2, 1, -1\}$ and {2,-2,1,1}) and the homonuclear dipolar ($\{2, 2, 1, 1\}$ and {2,-2,1,-1}) interactions. It is worth noticing that under single channel RN^ν_n sequences, CSA and heteronuclear dipolar interactions are characterized by the same *space* and *spin rotational ranks*, and, as a consequence, are subjected by the same selection rules. In other words, a sequence able to reintroduce CSA interactions also reintroduces, if present, heteronuclear dipolar couplings involving the nucleus under observation. Differently, when the same RN^ν_n is applied at both the Larmor frequencies of the dipolarly coupled nuclear spins, the *spin* rank λ of the heteronuclear dipolar coupling changes, passing from 2 to 1, so that it can be separated from the CSA interaction.

As described in [61], RN^ν_n sequences have also the effect to multiply the symmetry-allowed terms by a complex number, $k_{lm\lambda\mu}$, called *scaling factor*, having magnitude less than one. The result is a reduction of the magnitude of the symmetry-allowed terms.

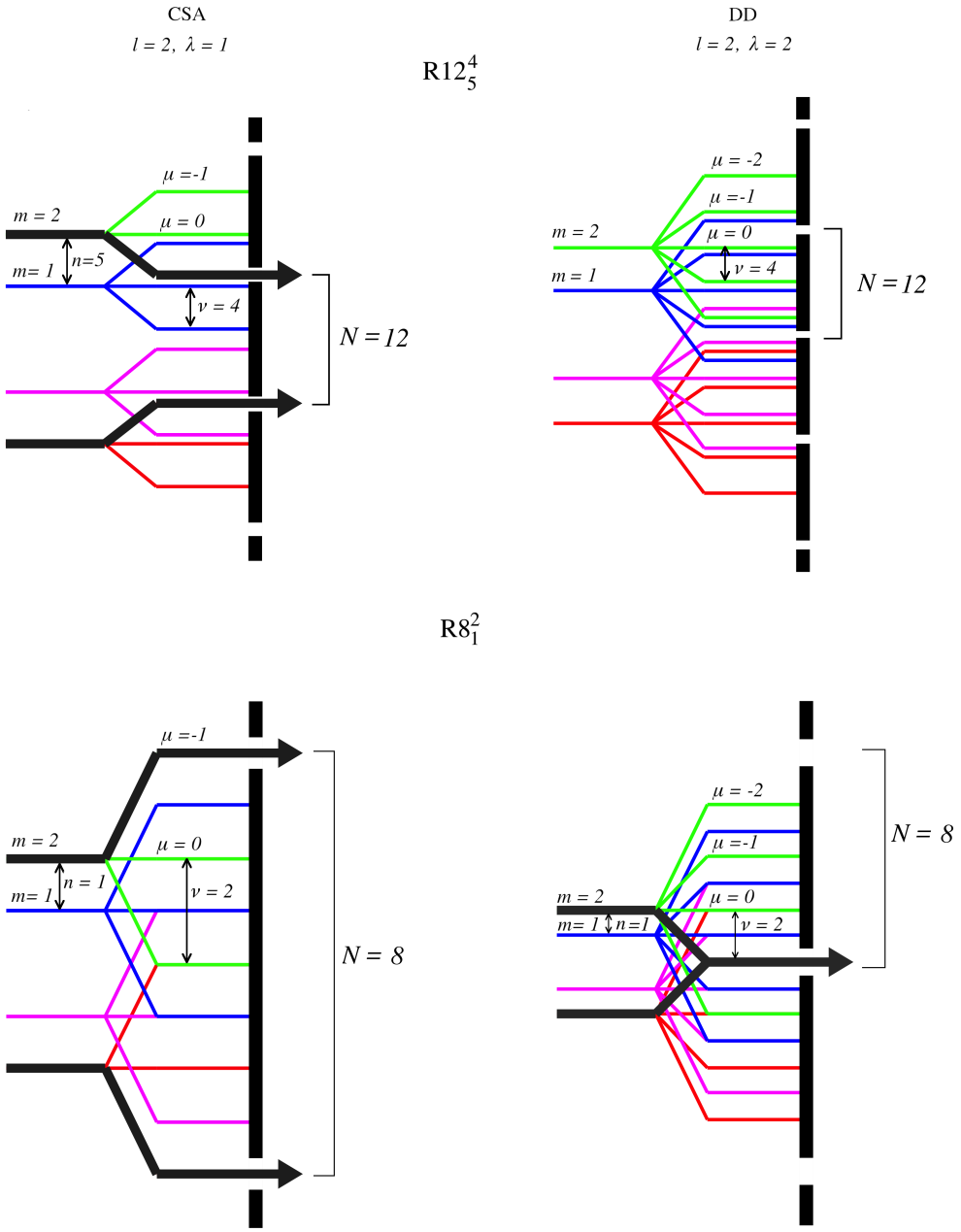

Figure 6.2: Space-spin selection diagrams of CSA (left) and homonuclear dipolar coupling (DD) (right) interactions relative to the recoupling sequences R12$^4_5$ (top) and R8$^2_1$ (bottom). A generic RN$^\nu_n$ sequence is able to reintroduce space-spin components of a nuclear spin interaction with *space* and *spin* ranks l and λ, respectively, if the selection rule $mn - \mu\nu = \frac{N}{2}Z_\lambda$, with $m = -l, -l+1, , +l$ and $\mu = -\lambda, -\lambda+1, , +\lambda$, is satisfied. Z_λ is an integer which assumes even or odd values according to the parity of λ. Each diagram shows on the left all the possible components of the interaction tensor, split up in *space* (mn) and *spin* ($\mu\nu$) parts, and on the right a barrier containing holes at $\frac{N}{2}Z_\lambda$. The space-spin components with $l = 2$ and $m = 0$ are omitted, because they are always zero under MAS conditions [61].

The expression of $k_{lm\lambda\mu}$, whose value depends on the recoupling sequence, is very complicated, and is reported in [61].

In Figure 6.3, the pulse sequence of a generic 2D RN_n^ν recoupling experiment is shown. This experiment produces a 2D spectrum, correlating the isotropic chemical shift (first dimension) to the chemical shift anisotropy (second dimension), rescaled by a factor which depends on the pulse sequence. Since the samples under investigation were characterized by long ^{19}F T_1, the $\frac{\pi}{2}$ excitation pulse is preceded by a saturation recovery sequence. The signal is acquired after an integer number, M, of RN_n^ν recoupling cycles, as those reported in Figure 6.1. M is incremented during the sequence, and determines the second dimension of the resulting 2D FID (time t_1 in Figure 6.3). In order to obtain 2D recoupling spectra, the 2D FID are Fourier transformed with respect to both t_2, related to the direct dimension as shown in Figure 6.3, and t_1. In particular, since during t_1 the evolution of longitudinal magnetization is observed, quadrature detection is not appropriate, and a real Fourier transform is applied with respect to t_1. This leads to recoupled patterns symmetrical about the origin, which, in the case of CSA interaction, do not allow positive and negative Δ to be distinguished. It is worth noticing that in the sequence reported in Figure 6.3 the signal is sampled at intervals $n\tau_r$, i. e. the duration of a complete RN_n^ν cycle. Consequently the spectral width (sw) in the second dimension can be calculated as $sw = \frac{1}{n\tau_R}$.

Even if the Average Hamiltonian Theory is strictly valid only for integer multiples of complete RN_n^ν cycle, the theory seems to work also for incomplete cycles. The acquisition of the signal after an incomplete cycle, i.e. after a number of R elements less than N, is here called oversampling, and it is convenient, for example, when an increase of sw in the second dimension is necessary. In the case of oversampling, the sw in the second dimension can be calculated as $sw = \frac{N}{OS}\frac{1}{n\tau_R}$, where OS is the number of R elements after which the signal is acquired, with $OS < N$. However, there is a complication arising from the use of incomplete cycles, related to the fact that the rf propagator multiplying the average internal Hamiltonian in the pulse sequence propagator could be not proportional to the unity operator, as conversely it is in the case of complete cycles.

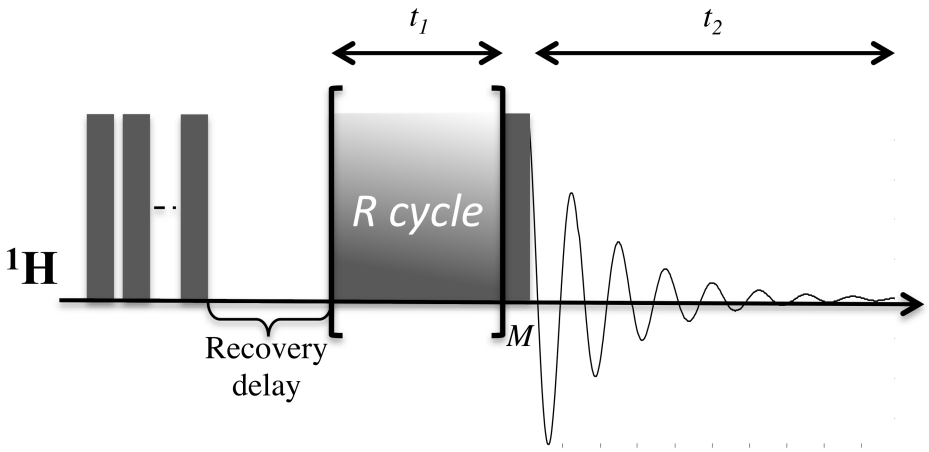

Figure 6.3: Scheme of the pulse sequence of a 2D recoupling experiment based on a generic RN_n^ν pulse sequence.

Experimentally, this could lead to sidebands, which could overlay with the recoupled patterns in the second dimension.

6.4 Results

In this section, the main results obtained from a preliminary study, based on SIMPSON simulations, for the research of suitable RN_n^ν sequences for CSA recoupling is presented, along with the results of experimental measurements of ^{19}F CSA parameters for PTFE and PVDF.

6.4.1 SIMPSON simulations

A significant part of the research activity was addressed to search for RN_n^ν sequences able to recouple ^{19}F CSA characterized by large anisotropy values of the order of 200 ppm, as those of the fluorine atoms in the zirconium phosphonates studied here. This was done by performing simulations of the recoupled patterns using the SIMPSON package [163], at the ^{1}H Larmor frequency of 600 MHz, corresponding to the magnetic field at which the experiments were preformed. The main difficulty was to combine large spectral widths and/or low scaling factors in the second dimension, necessary to recouple the whole CSA pattern, with experimental conditions, in terms of MAS frequency and rf amplitudes,

which could be supported by the instrumentation available. From SIMPSON simulations two sequences were identified, the $R8_1^2$ and the $R12_5^4$, which, in particular experimental conditions, are able to recouple such large CSA. For $R12_5^4$ a very low scaling factor of 0.155 was calculated by Hou et al. [157], while for $R8_1^3$ an empirical scaling factor with respect to the real magnitude of Δ can be estimated about 0.3-0.4. The latter was calculated by dividing the half-widths of the simulated recoupled patterns at Δ = 100 and 200 ppm by the real values of Δ, 100 or 200 ppm. The MAS frequencies at which these sequences give the best results are 39 and 65 kHz for the $R8_1^2$ and the $R12_5^4$, respectively. Moreover, in order to have sufficiently wide spectral widths, oversampling was necessary, and in both cases we acquired a point after four pulses of the RN_n^ν cycle. In these conditions, $\frac{\pi}{2}$ pulse durations and spectral widths in the second dimension were 3.2 μs and 39 kHz for $R12_5^4$, and 1.6 μs and 78 kHz for $R8_1^2$, being 1.5 μs the lower limit of $\frac{\pi}{2}$ pulse duration for the 1.3 mm probe used. In Figure 6.2 the space-spin selection diagrams of $R8_1^2$ and the $R12_5^4$ are shown. While $R12_5^4$ reintroduces only the CSA and the heteronuclear dipolar interactions, $R8_1^2$ also reintroduces the homonuclear dipolar coupling.

In order to explore the sensitivity of $R12_5^4$ and $R8_1^2$ towards the different interactions, we performed SIMPSON simulations, whose results are shown in Figures 6.4, 6.5, 6.6 and 6.7. It is worth noticing that the outer sidebands visible in the simulated patterns are due to the use of incomplete cycles. The performance of the sequences was investigated for ranges of Δ of 100-200 ppm, which are typical of the samples object of this study (PTFE, PVDF, and zirconium phosphonates, respectively), as estimated by the width of the corresponding sidebands patterns. It is worth noticing that for such large values of Δ the patterns recouped by $R12_5^4$ and $R8_1^2$ are not very sensitive to rf inhomogeneities, which were not taken into account in the simulations.

In Figure 6.4 and 6.5 the effects of the CSA parameters Δ and η on the recoupled patterns are shown, respectively. The dependence on Δ was investigated for $\eta = 0$, while that on η for the two Δ values of 100 and 200 ppm. As far as Δ is concerned, the width of the recoupled pattern is expected to increase by increasing Δ. This effect is more

evident on the patterns recoupled by both $R12_5^4$ and $R8_1^2$ when Δ is of the order of 100 ppm. When Δ is of the order of 200 ppm, the width of the pattern slightly increases with Δ under $R8_1^2$; under $R12_5^4$ the increase of the width of the recoupled pattern is observable only up to $\Delta \sim 200$ ppm, while for higher values a further increase of Δ affects the shape of the pattern, which becomes progressively broader and irregular, rather than its width. As far as η is concerned, this parameter is supposed to mostly affect the shape of the recoupled pattern: this is evident under both $R8_1^2$ and $R12_5^4$, for both the ranges of Δ investigated. The dependence on the ^{19}F-^{1}H dipolar coupling in the presence of CSA was investigated for $\Delta = 100$ or 200 ppm and $\eta = 0$, and the results are shown in Figure 6.6. The study was carried out for values of the dipolar coupling constant between 0 and 14 kHz, which correspond to ^{19}F-^{1}H inter-atomic distances of ∞ (no dipolar coupling) and 2 Å, respectively. When the CSA is the main interaction in the spin system, a single dipolar coupling seems to determine a splitting of the pattern determined by the CSA, which increases with the strength of the dipolar interaction. In particular, when Δ is in the range of 100 ppm the splitting becomes evident for values of the dipolar coupling constant higher than 6 and 4 kHz with $R12_5^4$ and $R8_1^2$, corresponding to ^{19}F-^{1}H distances shorter than 2.7 and 3.0 Å, respectively. When the CSA is about 200 Å, under $R8_1^2$ the splitting starts to be evident above a dipolar coupling constant of 8 kHz (i.e. ^{19}F-^{1}H distances shorter than 2.4 Å), while, in the range of dipolar couplings investigated, only a broadening of the pattern, which becomes more evident when the dipolar coupling constant is higher than 8 kHz, is observable under $R12_5^4$.

In Figure 6.7 the variation of the pattern obtained under $R8_1^2$ with the ^{19}F-^{19}F dipolar interaction is shown for values of the dipolar coupling constant between 0 and 14 kHz. The simulations were carried out in the presence of the CSA interaction, with $\Delta = 100$ or 200 ppm and $\eta = 0$, and considering a single ^{19}F-^{19}F coupling.

As we can see, for the range of dipolar coupling constants here investigated, the recoupled pattern is not significantly affected by the homonuclear dipolar coupling interaction. Nevertheless it can be noticed that, differently from the heteronuclear dipolar interaction, the ^{19}F-^{19}F dipolar coupling determines a broadening of the recoupled pattern, which starts to be really relevant for values of the dipolar coupling constant above

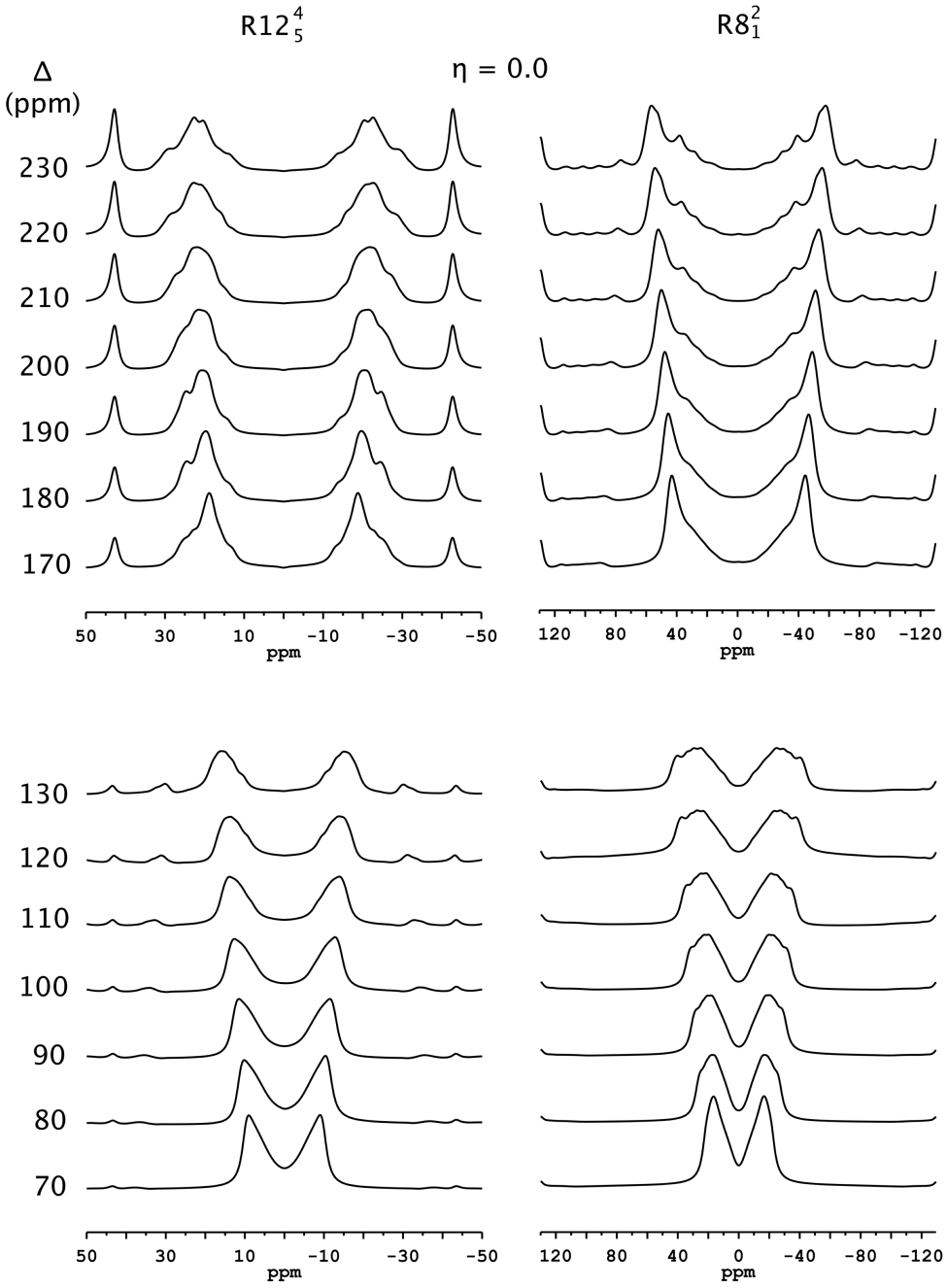

Figure 6.4: Dependence of the patterns recoupled by the $R12_5^4$ and $R8_1^2$ sequences on the chemical shift anisotropy (Δ). Two ranges of Δ were investigated, that are 70 -130 ppm and 170 - 230 ppm. All the simulations were performed with the asymmetry parameter η equal to 0, and using a Lorentzian line-broadening of 800 and 1200 Hz for the 70 -130 ppm and 170 - 230 ppm ranges of Δ, respectively. MAS frequencies of 65 and 39 kHz were used for $R12_5^4$ and $R8_1^2$, respectively.

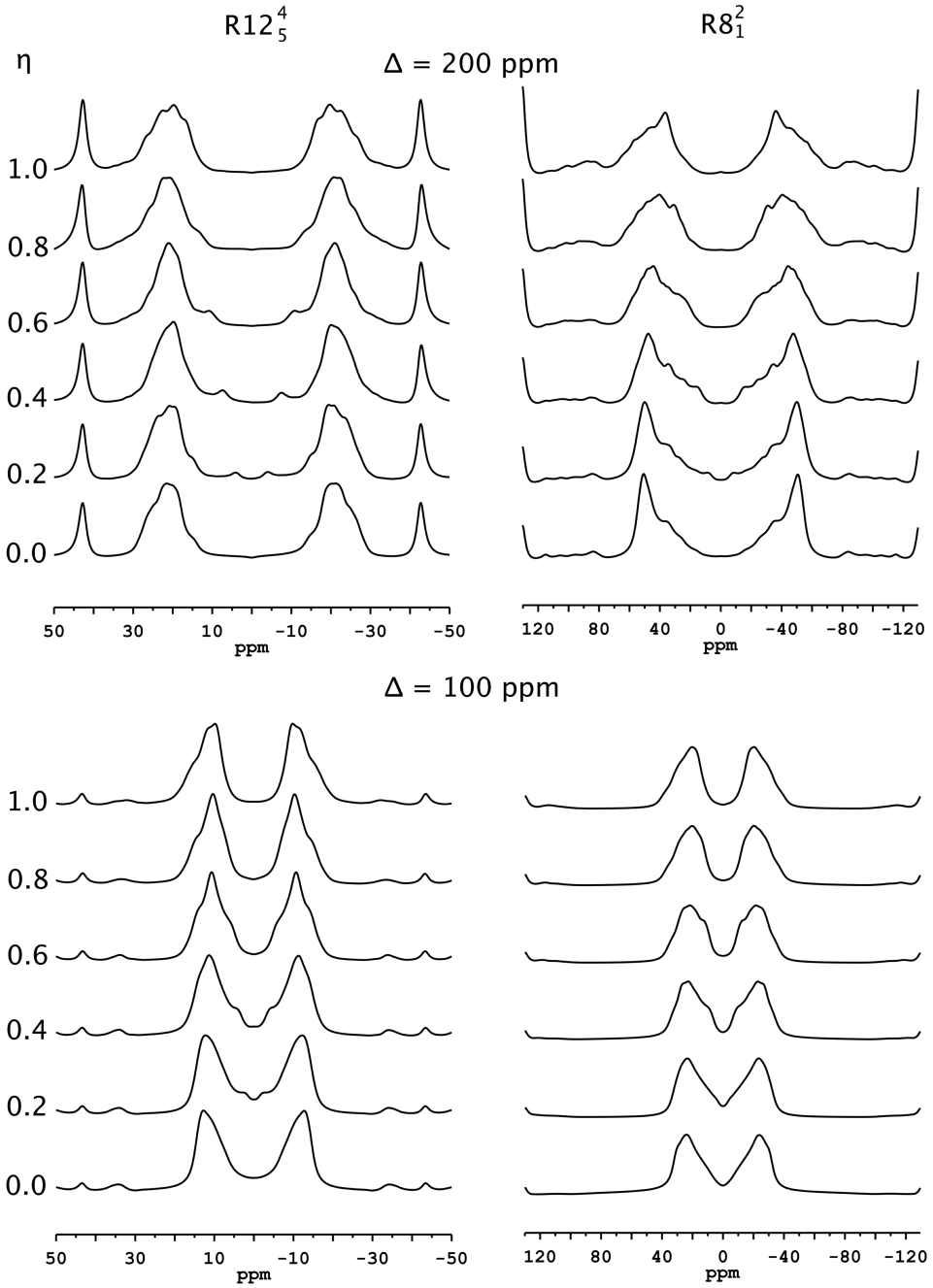

Figure 6.5: Dependence of the patterns recoupled by the R12$_5^4$ and R8$_1^2$ sequences on the chemical shift asymmetry parameter (η). Simulations were carried out by varying η from 0.0 to 1.0 at the two Δ values of 100 and 200 ppm. All the simulations were performed using a Lorentzian line-broadening of 800 and 1200 Hz for Δ = 100 and 200 ppm, respectively, and MAS frequencies of 65 and 39 kHz for R12$_5^4$ and R8$_1^2$, respectively.

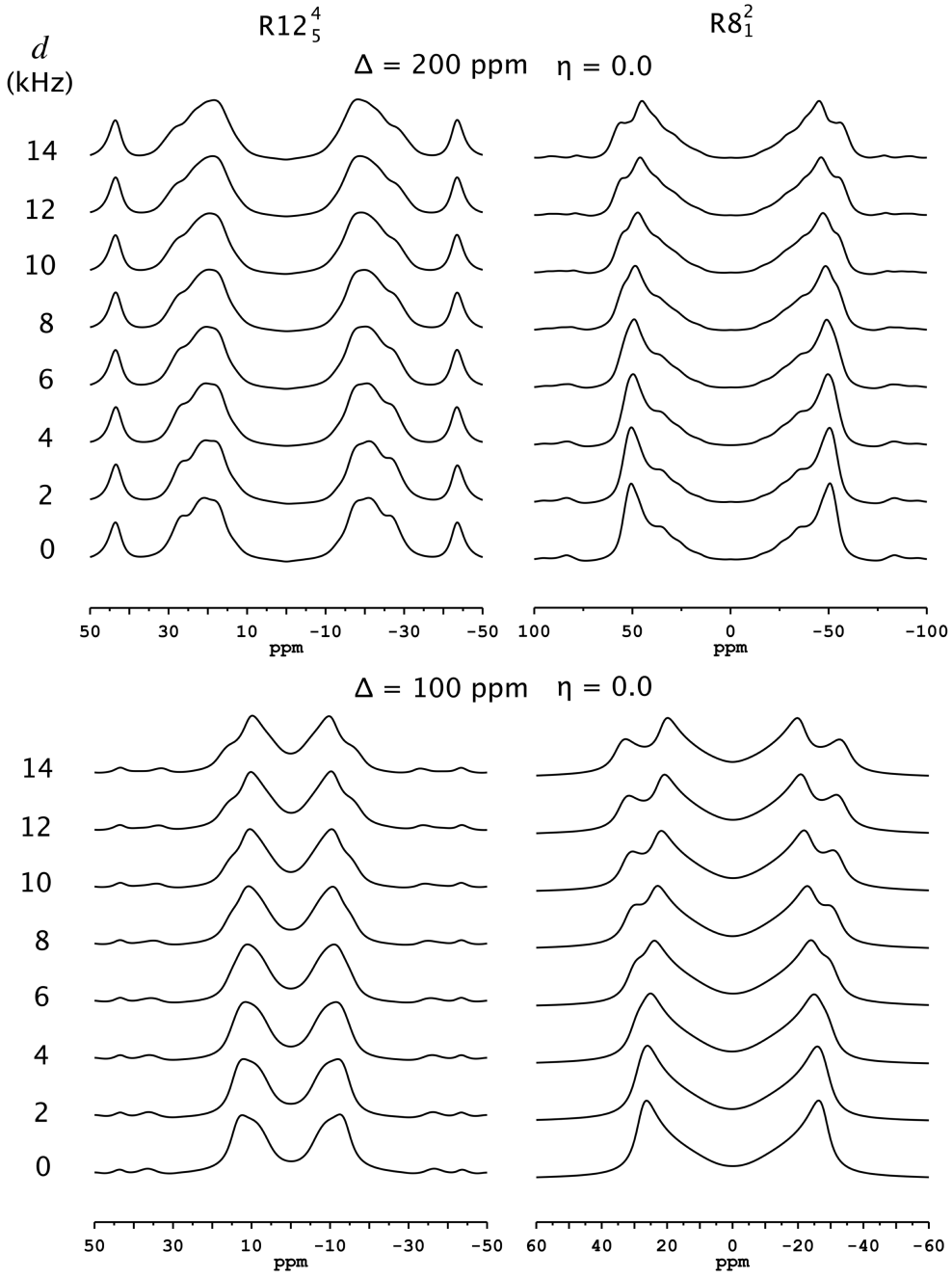

Figure 6.6: Dependence of the patterns recoupled for the nucleus ^{19}F by the R12$_5^4$ and R8$_1^2$ sequences on the ^{19}F-^{1}H dipolar coupling constant. The simulations were carried out considering a single ^{19}F-^{1}H dipolar coupling in presence of the ^{19}F CSA interaction. The dipolar coupling constant was varied from 0 to 14 kHz with the CSA parameters $\eta = 0$ and Δ = 100 (bottom) or 200 (top) ppm. All the simulations were performed using a Lorentzian line-broadening of 800 and 1200 Hz for Δ = 100 and 200 ppm, respectively, and MAS frequencies of 65 and 39 kHz for R12$_5^4$ and R8$_1^2$, respectively.

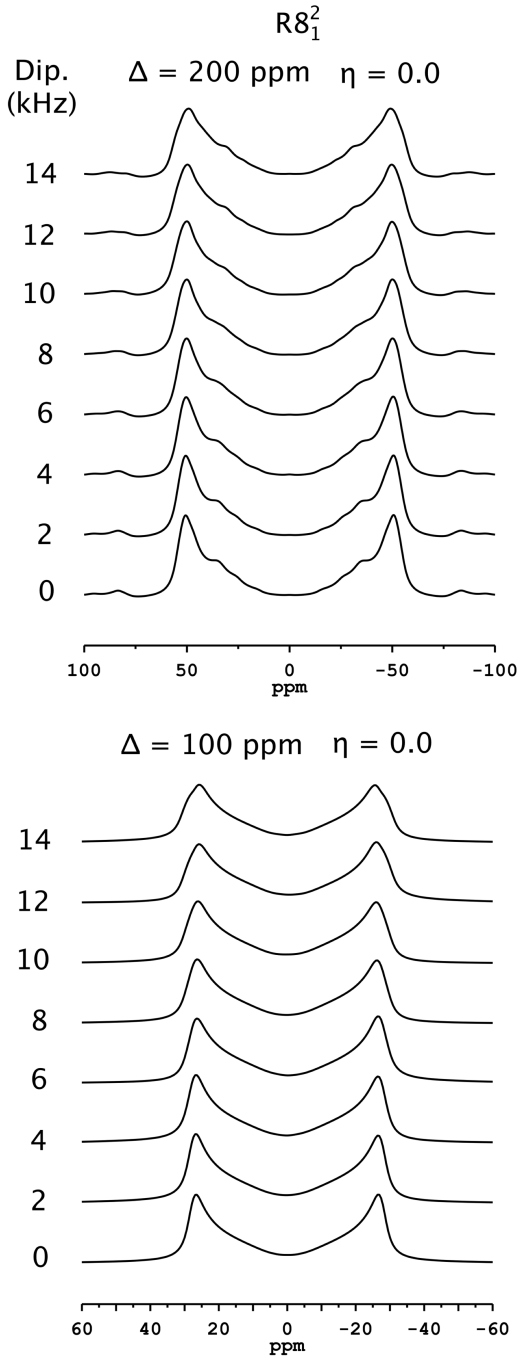

Figure 6.7: Dependence of the patterns recoupled for the nucleus ^{19}F by the R8$_1^2$ sequence on the ^{19}F-^{19}F dipolar coupling constant. The simulations were carried out considering a single ^{19}F-^{19}F dipolar coupling in presence of the ^{19}F CSA interaction. The dipolar coupling constant was varied from 0 to 14 kHz, with CSA parameters $\eta = 0$ and $\Delta = 100$ or 200 ppm. All the simulations were performed using a Lorentzian line-broadening of 800 and 1200 Hz for $\Delta =$ 100 and 200 ppm, respectively, and MAS frequencies of 65 and 39 kHz for R12$_5^4$ and R8$_1^2$, respectively.

10 kHz, i.e. ^{19}F-^{19}F inter-atomic distances below 2.2 Å.

In conclusion, two RN_n^ν recoupling sequences, $R12_5^4$ and $R8_1^2$, were identified as able to reintroduce large ^{19}F CSA interactions. Under both these sequences, the recoupled patterns are significantly sensitive to both Δ and η parameters. On the other hand, especially for values of Δ of the order 200 ppm, the recoupled patterns do not seem significanly affected by ^{19}F-^{1}H dipolar interaction, unless quite strong couplings (^{19}F-^{1}H internuclear distances $\leq$ 2.4 Å) are present. As far as $R8_1^2$ is concerned, ^{19}F-^{19}F homuclear dipolar coupling interaction determines a broadening of the recoupled pattern, which is evident only in strongly dipolar coupled systems. All this considered, since in the zirconium phosphonate under investigation ^{19}F nuclei are not subjected to very strong dipolar interactions (^{19}F-^{19}F and ^{19}F-^{1}H internuclear distances should be always $>$ 2.8 Å), $R12_5^4$ and $R8_1^2$ seemed to be promising sequences for the determination of ^{19}F CSA parameters in these samples. Their experimental behaviour was first tested on the simpler systems of PTFE and PVDF. In addition to the ^{19}F CSA interaction, in PTFE ^{19}F nuclei are affected only by the homonuclear dipolar interaction, while in PVDF ^{19}F-^{1}H dipolar coupling is also present. The main advantage of PTFE and PVDF compared to the zirconium phosphonates are the lower values of ^{19}F CSA, which should make experimentally easier the recoupling of this interaction. The results obtained for PTFE and PVDF are reported in the following paragraphs.

6.4.2 Experimental results

^{19}F MAS spectra

In Figure 6.8 the ^{19}F MAS spectra of PTFE and PVDF acquired at the ^{19}F Larmor frequency of 564 MHz and a MAS frequency of 65 kHz are reported.

In the spectrum of PTFE a single isotropic signal at about -123 ppm arising from the CF_2 groups is observable. The presence of both PTFE crystalline and amorphous domains cannot be ruled out, but their signals are not resolved in the spectrum.

In the spectrum of PVDF, there are three main signals at about -82, -97, and -91

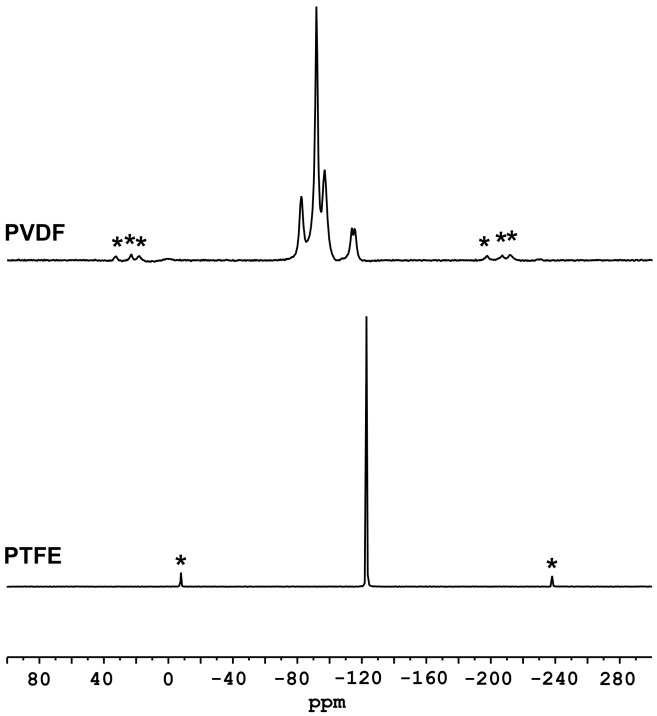

Figure 6.8: ^{19}F MAS spectra acquired at the MAS frequency of 65 kHz of PTFE (bottom) and PVDF (top). Spinning sidebands are marked with the symbol $*$.

ppm: the first two can be ascribed to crystalline PVDF in the α form, and the other to amorphous PVDF. The α crystalline form of PVDF, which can be easly obtained through crystallization from the melt at any temperature, is constituted by two antiparallel chains with a tg+ tg- conformation [164, 165]. The two signals at -82 and -97 ppm observable in the ^{19}F MAS spectra arise from two inequivalent fluorine atoms present in the unit cell. Moreover, two less intense signals are observable at about -110 ppm, ascribable to head-to-head and tails-to-tails imperfections, mostly present in the amorphous domains.

Measurement of ^{19}F chemical shift anisotropy (CSA)

Analysis of the spinning sidebands profile: method of rotational echoes.

The profile of spinning sidebands was measured from the 1D ^{19}F MAS spectra acquired at MAS frequencies going from 5 to 65 kHz. The use of different MAS frequencies aimed at separating the contributions of the different anisotropic interactions (chemical shift anisotropy, homonuclear and heteronuclear dipolar couplings), which are modulated

Table 6.2: Chemical shift anisotropy (Δ) and asymmetry (η) parameters calculated for PTFE and PVDF by averaging those obtained by the analysis of the profile of spinning sidebands at different MAS frequencies (5, 15, 25, 35 kHz for PTFE, and 15, 25, 35 kHz for PVDF). For PVDF only the results obtained for the signals (at -97 and -82 ppm) arising from the crystalline fraction are reported.

	Samples		
Average CSA parameters	**PTFE**	**PVDF**	
	-123 ppm	**-97 ppm**	**-82 ppm**
Δ (ppm)	72 ± 2	101 ± 2	101 ± 2
η	0.5 ± 0.2	0.5 ± 0.1	0.5 ± 0.1

differently by the MAS rotation. Each spectrum was analysed by means of a deconvolution procedure that gave the intensities profile of the spinning sidebands. In order to get information on the CSA parameters, the experimental profiles were fitted using the SIMPSON Opt package [166], with a model based on the shape of the MAS rotational echoes [2, 150]. Indeed, it is demonstrated that each rotational echo of the FID contains all the information to describe the MAS spectrum, and its Fourier transform yields the array of the spinning sidebands intensities [150]. In this work the spectra calculated from the simulated first rotational echoes of the FID were fitted to the experimental profiles. In the simulation a number of points between 16 and 32 were used, depending on the number of spinning sidebands in the experimental spectra. All the simulations were carried out considering that only the CSA interaction was present.

The results of the fitting obtained at each MAS frequency for the PTFE and PVDF samples are reported in Table B.1 . Apart from the results obtained at the highest MAS frequencies (45 kHz, 55 kHz, and 65 kHz), for which the spinning sidebands are probably not intense enough to reliably determine the CSA parameters, the values of the chemical shift anisotropy and asymmetry parameters obtained at the different MAS frequencies are quite similar and consistent among each other for both PTFE and PVDF. In Table 6.2 the chemical shift anisotropy and asymmetry parameters calculated by averaging those obtained at the lowest MAS frequencies (5, 15, 25, 35 kHz for PTFE, and 15, 25,

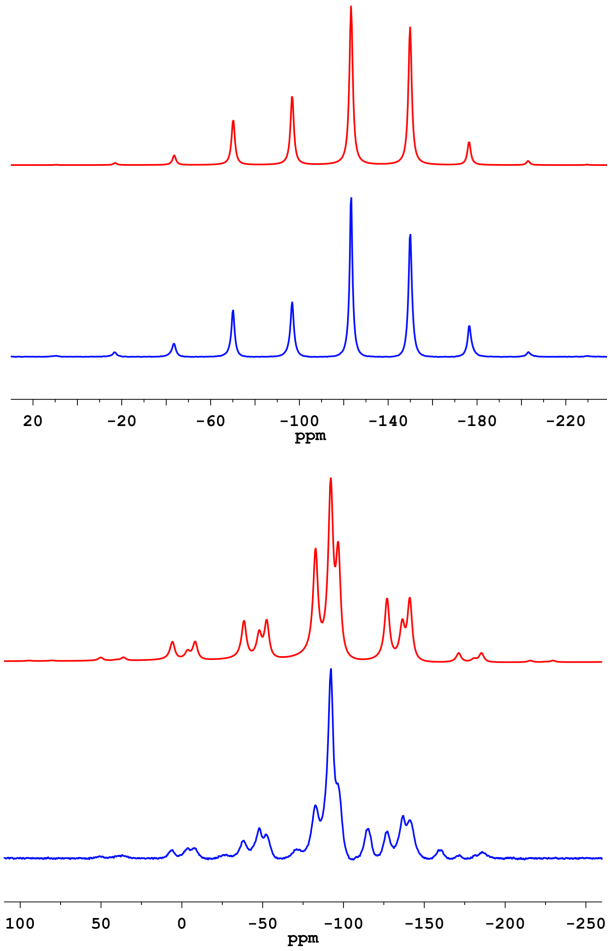

Figure 6.9: Comparison between the experimental (blue) and simulated (red) spectra of, from top to bottom, PTFE and PVDF. MAS frequencies of 15 and 25 kHz were used, for PTFE and PVDF, respectively. The simulations were performed using the CSA parameters reported in Table 1, using a Lorentzian line-broadening of 1000 and 2000 for PTFE and PVDF, respectively.

35 for PVDF) are reported. In Figure 6.9, the experimental spectra at a MAS frequency of 15 kHz and those simulated using the CSA parameters in Table 6.2 are compared. As we can see, the method here used to determine the ^{19}F CSA allowed the experimental data to be very well reproduced. In the case of PVDF this also means that at the MAS frequencies here used the ^{19}F-^{1}H heteronuclear dipolar coupling interaction is averaged out by the MAS rotation.

$R12^4_5$ and $R8^2_1$ sequences

$R12^4_5$ and $R8^2_1$ experiments were carried out on both PTFE and PVDF. The resulting two-dimensional maps, showing in the first dimension the ^{19}F MAS spectrum and in the second one the recoupled patterns for each isotropic peak, are reported in Figures 6.10 and 6.11. In order to determine the ^{19}F CSA parameters, we performed SIMPSON simulations of the recoupled patterns for values of Δ and η going from 30 to 90 ppm and 0 to 1, respectively, in the case of PTFE, and from 70 to 130 and 0 to 1, respectively, in the case of PVDF. All the simulations were carried out considering that only the CSA interaction was present. The results of the simulations were compared with the experimental patterns of the different isotropic peaks in the second dimension, and the contour plots of the root mean squares (rms) as a function of Δ and η were determined (Figures 6.12 and 6.13). The minimum of rms corresponds to the values of Δ and η, for which there is the best match between the simulated and the experimental patterns. These values are reported in Table 6.3, while in Figure 6.10 and 6.11 the comparison between the corresponding simulated and experimental patterns is shown for PTFE and PVDF, respectively.

As far as PTFE is concerned, a good match between simulated and experimental patterns was obtained for both $R12^4_5$ (Figure 6.10 (a)) and $R8^2_1$ (Figure 6.10 (b)). However, for $R8^2_1$ the experimental pattern is significantly broader than the simulated one, possibly due to the network of ^{19}F-^{19}F dipolar couplings present in PTFE, not considered in the simulations. Moreover, the values Δ and η obtained by using these two sequences are quite different: under $R8^2_1$ the best-fitting parameters Δ and η (70 ppm and 0.2) are about 20 and 60 % smaller, respectively, than those obtained using $R12^4_5$ (85 ppm and

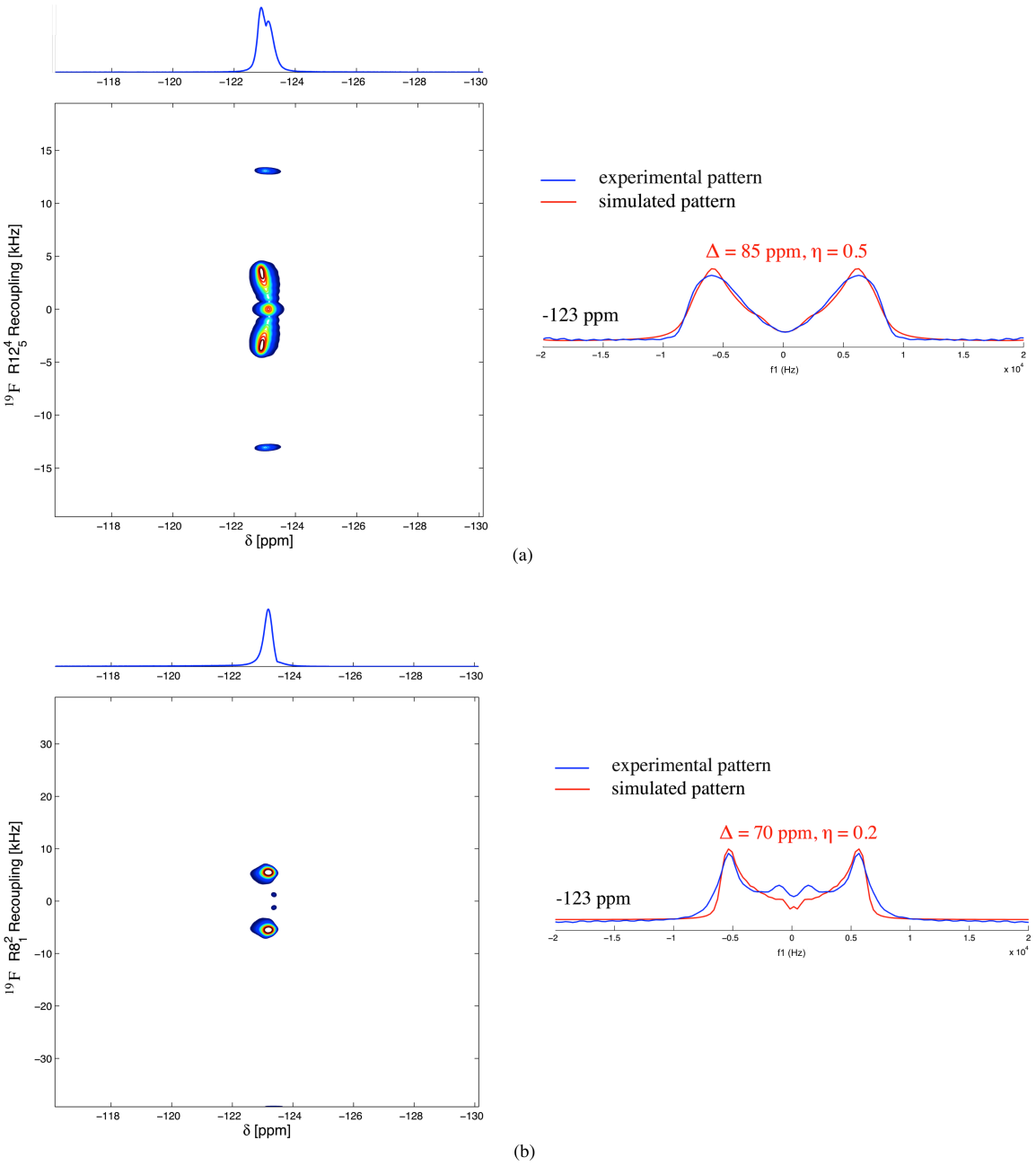

Figure 6.10: Left: experimental ^{19}F 2D recoupling spectra obtained for PTFE using the R12$^4_5$ (a) and R8$^2_1$ (b) sequences. The 2D spectra correlate the ^{19}F isotropic chemical shifts (first dimension) with the corresponding recoupled patterns (second dimension). Right: comparison between the experimental recoupled patterns obtained for the PTFE isotropic peak at -123 ppm under R12$^4_5$ (a) and R8$^2_1$ (b) and the patterns simulated by using the best-fitting CSA parameters determined as described in the text. The simulations were performed by using a Lorentzian line-broadening of 800 Hz.

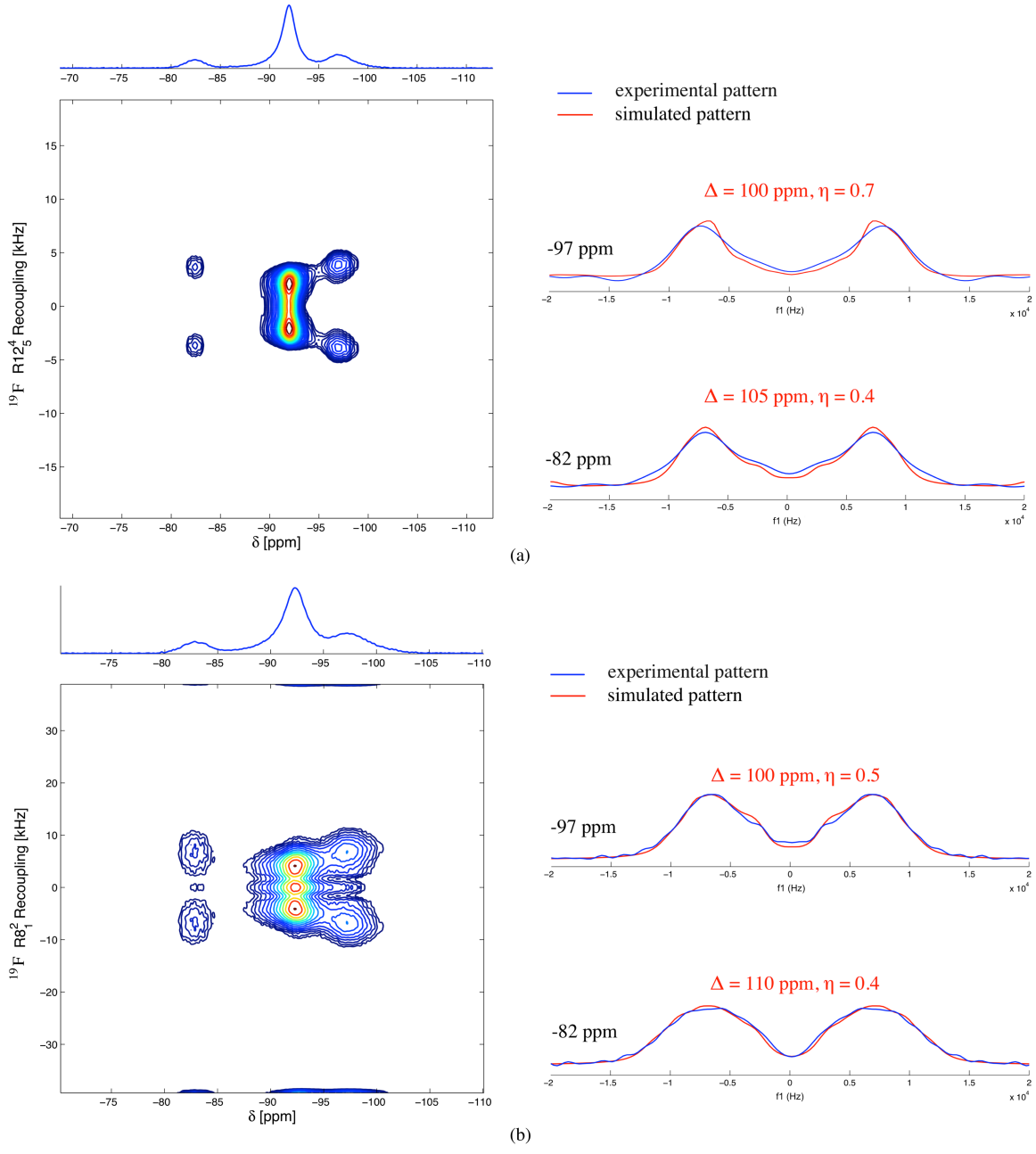

Figure 6.11: Left: experimental ^{19}F 2D recoupling spectra obtained for PVDF using the $R12_5^4$ (a) and $R8_1^2$ (b) sequences. The 2D spectra correlate the ^{19}F isotropic chemical shifts (first dimension) with the corresponding recoupled patterns (second dimension). Right: comparison between the experimental patterns recoupled under $R12_5^4$ (a) and $R8_1^2$ (b) for the ^{19}F isotropic peaks at -97 and -82 ppm of PVDF, with the patterns simulated by using the best-fitting CSA parameters determined as described in the text. The simulations were performed with a Lorentzian line-broadening of 1000 Hz.

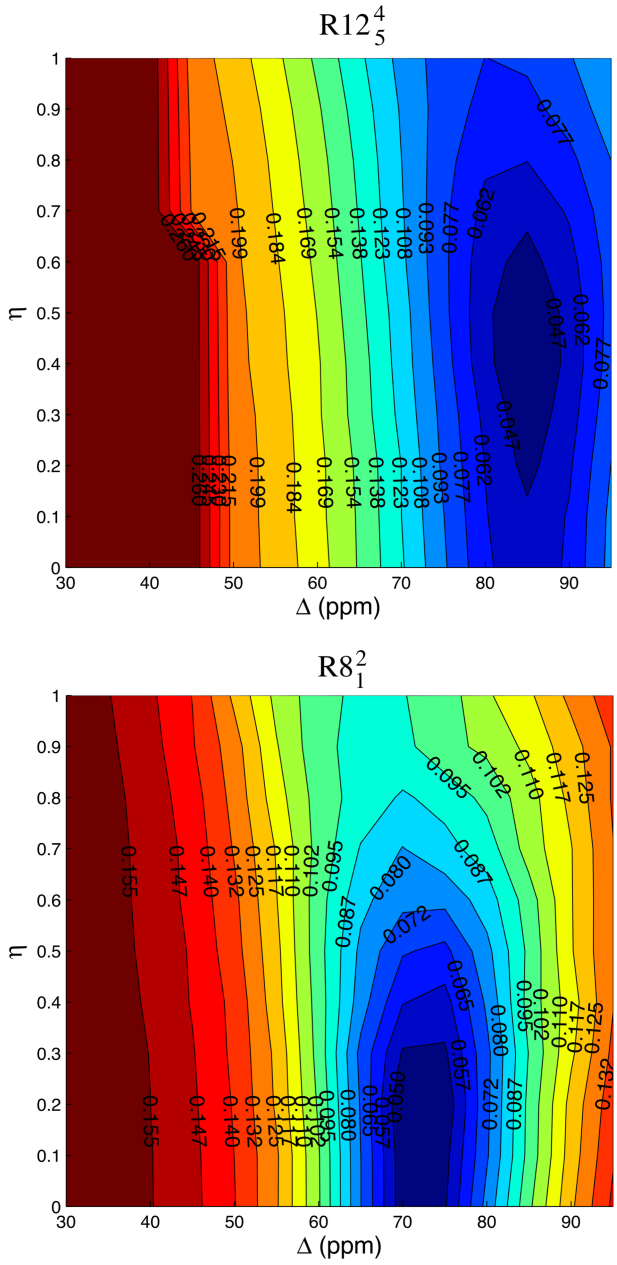

Figure 6.12: Contour plots of the normalized root mean squares of the differences between the experimental and simulated patterns recoupled by the R12$^4_5$ and R8$^2_1$ sequences, as a function of the CSA parameters Δ (ppm) and η, obtained for the ^{19}F isotropic signal at -123 ppm of PTFE.

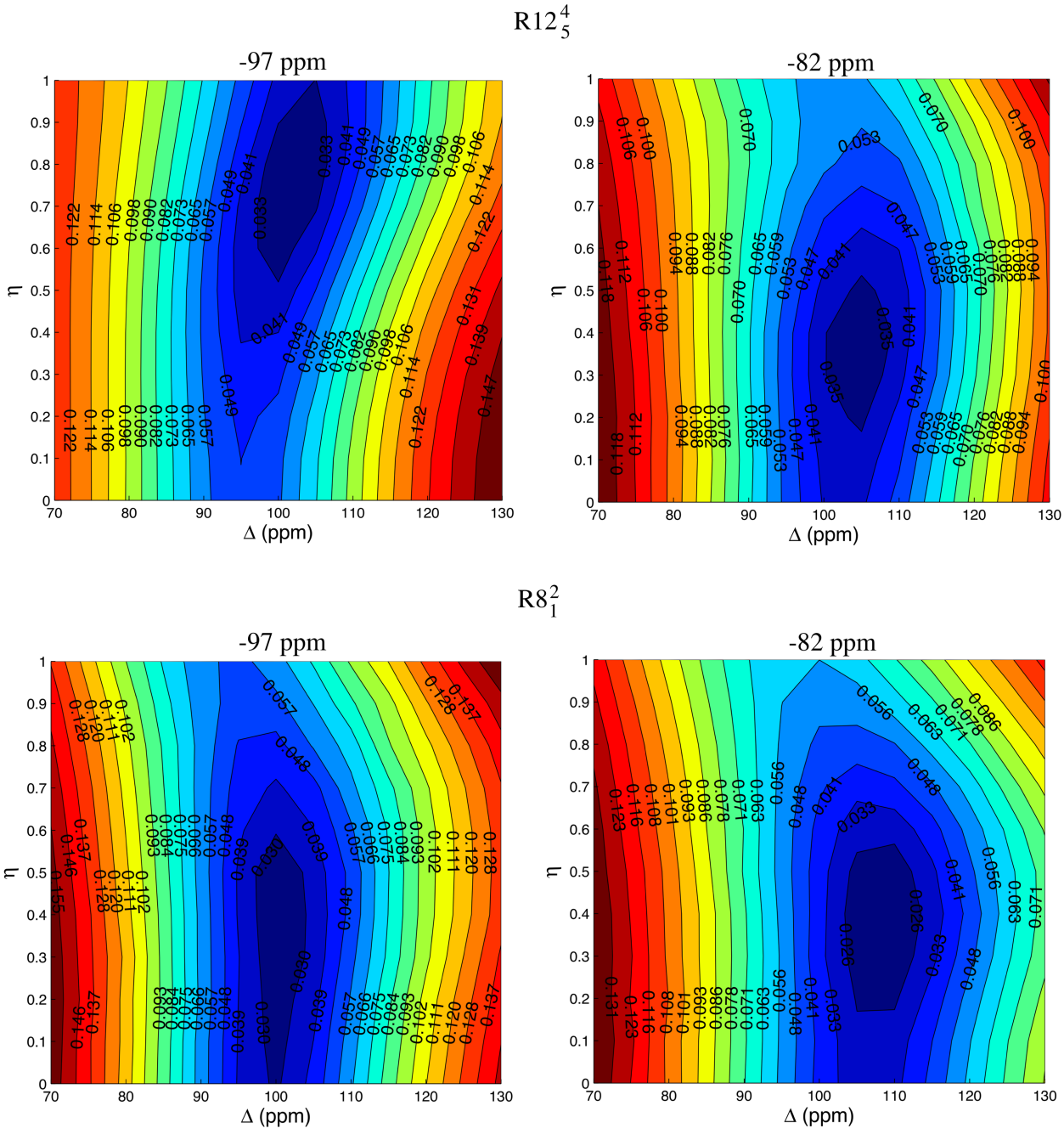

Figure 6.13: Contour plots of the normalized root mean square of the differences between the experimental and simulated patterns recoupled by the R12$^4_5$ and R8$^2_1$ sequences, as a function of the CSA parameters Δ (ppm) and η, obtained for the ^{19}F isotropic signals at -97 and -82 ppm of PVDF.

Table 6.3: ^{19}F best-fitting chemical shift anisotropy (Δ) and asymmetry (η) parameters determined for the different isotropic signals of PTFE and PVDF by means of the $R12_5^4$ and $R8_1^2$ recoupling sequences, following the procedure described in the text.

		Samples		
R sequence	**CSA parameters**	**PTFE**	**PVDF**	
		-123 ppm	**-97 ppm**	**-82 ppm**
$R12_5^4$	Δ (ppm)	85	100	105
	η	0.5	0.7	0.4
$R8_1^2$	Δ (ppm)	70	100	110
	η	0.2	0.5	0.4

0.5).

As far as PVDF is concerned, the results for both the peaks at -97 and -82 ppm, arising from the crystalline fraction of the polymer, are reported. A good match between simulated and experimental patterns was obtained with both $R12_5^4$ (Figure 6.11 (a)) and $R8_1^2$ (Figure 6.11 (b)). In this case, the ^{19}F-^{19}F homonuclear and ^{19}F-^{1}H heteronuclear dipolar couplings, even if present, do not seem to significantly affect the experimental patterns. Moreover there is a very good agreement between the values of Δ and η obtained through the two sequences (Table 6.3).

6.5 Discussion

The CSA parameters of ^{19}F nuclei in PTFE and PVDF were determined by two alternative approaches: the analysis of the spinning sideband patterns acquired under different MAS frequencies, and the use of the $R12_5^4$ and $R8_1^2$ recoupling sequences, selected on the basis of SIMPSON simulations. The experimental data were analysed through suitable fitting procedures, as described in section 6.4.2, for the determination of ^{19}F CSA parameters, under the hypothesis that only the CSA interaction was present. In both cases, a good reproduction of the experimental data was obtained, confirming that heteronuclear and homonuclear dipolar interactions do not significantly affect either the sidebands profiles or the recoupled patterns under $R12_5^4$ and $R8_1^2$ (Figures 6.9, 6.10, and

6.11).

However, aiming at evaluating the experimental efficiency of $R12_5^4$ and $R8_1^2$ in recoupling ^{19}F CSA, and at estimating the reliability of the determined CSA parameters, a comparison between the results obtained with the two methods could be very useful. From the analysis of the spinning sidebands profile, $\Delta = 72$ ppm and $\eta = 0.5$ were determined for PTFE, while $\Delta = 101$ ppm and $\eta = 0.5$ were found for both the fluorines of PVDF, resonating at -97 and -82 ppm (Table 6.2). From the variation of the values obtained under different MAS frequencies, the uncertainties on Δ and η were estimated of about 2 ppm and 0.2 for PTFE, and 2 ppm and 0.1 for PVDF. Similar values of Δ and η were obtained by the analysis of the patterns recoupled under $R12_5^4$ and $R8_1^2$ (Table 6.3). The largest difference is between the values of Δ determined for PTFE fluorines by the analysis of the spinning sideband profile (72 ppm) and by using $R12_5^4$ (85 ppm). To this regard, it is worth noticing that from the contour plots in Figures 6.12 and 6.13 the uncertainty on the values of Δ determined under both $R12_5^4$ and $R8_1^2$ can be estimated of about 5-10%, considering 0.05 as upper limit for rms. Largest uncertainties can be estimated for η. However, the interpretation of the rms contour plots in terms of errors on the determined CSA parameters is not straightforward, since rms values are also affected by differences in the baselines between the experimental and the simulated patterns. Even if the determination of the minimum of rms seems to be reliable to identify the best-fitting simulation, the uncertainties on the CSA parameters might be overestimated, also considering the consistency of the values of Δ and η at the minima with those determined through sideband patterns analyses.

All this considered, the good agreement between the results independently obtained by means of different experiments, carried out in completely different experimental conditions, is very encouraging. Indeed it supports a good accuracy of the CSA parameters determined through the two approaches. In particular, if the CSA parameters determined through the more conventional method of sidebands patterns analysis are taken as reference values, this demonstrates that, also experimentally, the patterns recoupled under $R12_5^4$ and $R8_1^2$ can be used for reliable measurements of ^{19}F CSA.

6.6 Experimental

All the experiments were performed on a Bruker Avance 600 MHz spectrometer, corresponding to ^{1}H and ^{19}F Larmor frequencies of 600 and 564 MHz, respectively, equipped with a 1.3 mm probe. The ^{19}F MAS spectra were acquired accumulating 8 scans, using a $\frac{\pi}{2}$ pulse duration of 1.5 μs and a recyle delay of 2 s. As far as the recoupling experiments are concerned, due to the long ^{19}F T_1 relaxation times in the zirconium phosphonates, the investigation of which was the motivation of this preliminary study, a train of saturation pulses followed by a recovery delay was introduced before the RN_n^ν sequence, that allowed a short recycle delay of 1 s to be used. Recovery delays of 60 s were used, accumulating 32 scans in the first dimension. The $R12_5^4$ and $R8_1^2$ experiments were performed at MAS frequencies of 65 and 39 kHz, respectively. The MAS frequency is related to the duration of each π degree pulse of the R sequence, which was 6.4 and 3.2 μs for the $R12_5^4$ and the $R8_1^2$, respectively. In order to have spectral widths in the second dimension sufficiently wide to include the whole ^{19}F recoupled pattern, we applied oversampling during the RN_n^ν sequence by acquiring a point every four R elements. The 2D spectra were obtained by Fourier transforming the 2D FID with respect to both the first and second dimensions. Complex and real Fourier transfoms were applied to the first and the second dimensions, respectively. The recoupled patterns were obtained by extracting the slices corresponding to each isotropic peak. The experimental patterns were affected by a spike at 0 ppm, probably arising from molecular orientations not fully recoupled by the sequence [160]. This was suppressed by subtracting an exponential decay from the decay of the signal in the second dimension, before performing the real Fourier transform. The exponential function was determined by the fitting of the last points of the experimental decay.

All the simulations and fittings were performed by using SIMPSON 3.1.0 [163]. In the simulations of the ^{19}F recoupled by the RN_n^ν sequences, a spike at 0 ppm was also present, and removed by applying a DC offset to the simulated FID. For the fittings of the ^{19}F MAS spectra the SIMPSON Opt package was used [166].

6.7 Conclusions

Two symmetry-based recoupling sequences, $R12_5^4$ and $R8_1^2$, able to reintroduce large CSA interaction (Δ of the order of 200 ppm) under high field and fast MAS conditions were identified. These sequences showed a scarce sensitivity toward heteronuclear and, in the case of $R8_1^2$, homonuclear dipolar couplings, and they could be potentially used for the determination of ^{19}F CSA parameters in complex systems affected by both these two interactions.

2D recoupling experiments based on $R12_5^4$ and $R8_1^2$ were developed and tested on two "reference" samples, PTFE and PVDF. The CSA parameters obtained through these sequences were found to be in good agreement with those determined by sideband patterns analyses. This suggests that both the methods allows to determine CSA parameters with good accuracy.

In particular, the analysis of sideband patterns acquired at different MAS frequencies seems to be a quite reliable method for determining ^{19}F CSA parameters, with uncertainties of about 2 ppm and 0.1-0.2 for Δ and η, respectivey. Larger uncertainties can be estimated for the CSA parameters, and especially for the asymmetry parameters η, determined by means of $R12_5^4$ and $R8_1^2$.

Concluding, when it is possible, the analysis of the spinning sideband profile for the measurement of ^{19}F is preferable to the use of recoupling experiments, being simpler and less time consuming, and producing lower uncertainties on the measured CSA parameters. Nevertheless recoupling experiments can be useful in the case of congested ^{19}F MAS spectra, with scarce resolution in isotropic chemical shifts. In this is the case, $R12_5^4$ and $R8_1^2$ are suitable sequences for the measurement of large ^{19}F CSA.

Chapter 7

^{19}F and ^{1}H chemical shift and dipolar coupling tensors in zirconium phosphonates

7.1 Introduction

Important information on structural and dynamic features of solid materials can be extracted from both isotropic and anisotropic components of internal spin interactions. The use of SSNMR data for extracting crystallographic information is well known under the name of "NMR Crystallography" [167–170]. Presently, much of the reported work concerns the use of SSNMR data to refine crystallographic information obtained by X-ray diffraction, but it was demonstrated that accurate structures can be determined also without diffraction data [171, 172].

In a recent work, J. K. Harper well illustrated possible uses of chemical shift tensors in the field of NMR Crystallography [170]. As explained in [170], chemical shift tensors mainly reflect structural properties over a short range of few angstroms, which are chemical, structural, and conformational properties at the nucleus under observation. However, information on the surrounding lattice can also be obtained. Indeed, strong electrostatic forces or hydrogen bonds can directly affect the various components

of chemical shift tensors [168]. Moreover, particular lattice features can influence the conformational properties around the observed nucleus, so indirectly affecting its chemical shift tensor. For example, in carbonyl groups, ^{13}C shift tensors, and especially δ_{22} components, of carbonyl carbons are extremely sensitive to the length of the hydrogen bond C=O$\cdots$H [173]. Moreover, both the isotropic and anisotropic components of the ^{1}H chemical shift tensors are found very sensitive to the presence of hydrogen bonds. In particular, both isotropic chemical shift and chemical shift anisotropy parameters usually increase by decreasing the hydrogen bond length, i.e. by increasing the strength of the interaction [174–176].

Apart form "NMR crystallography", other interesting applications are reported in the literature, in which the chemical shift interaction was used to obtain structural information on both crystalline and amorphous materials. An interesting application concerns the pharmaceutical field, where CSA tensors can be used to discriminate between different polymorphs of an API (Active Pharmaceutical Ingredient) [177]. Finally, a representative example concerning amorphous and disordered systems is the work recently [178] published by A. Rawal et al., where the authors exploited ^{29}Si CSA filtered experiments to distinguish among different molecular environments in cements [179].

7.2 Materials and aims

Zirconium phosphonates have been extensively studied because of their potential as functional materials. In addition to their chemical and thermal stability, one of the most advantageous properties of zirconium phosphonates is their structural variability, which is at the origin of their versatility toward lots of different applications. In general, zirconium phosphonates are formed by octaedra-tedrahedra combinations, where zirconium centres with octahedral symmetry are coordinated to a variable number of oxygens of surrounding phosphonic ligands [178, 180–184]. By using different reaction conditions and, in particular, different phosphonic ligands it is possible to obtain lots of different one-, two-, or three- dimensional structures, depending on the number of covalent and/or non-covalent bonds formed between the phosphonate groups and the

zirconium complexes [178]. Morevover, one or more of many different functional groups can be added, which can confer new and varied functional properties.

Depending on their structural properties and functionalities, zirconium phosphonates can be used for a wide variety of applications, such as proton exchange membrane [185–188], heterogeneous catalysts [189–192], fillers for polymeric materials [187,193,194], drug delivery systems [195], etc. Recently, Y. Tang and coworkers prepared novel mesoporous zirconium phosphonates for oral colon-targeted delivery of nucleic acids, where the functional groups in the phosphonic ligands endows the materials pH-controllable release function [195]. Changing application field, in a recent work M. Casciola et al. developed a novel and efficient synthetic approach for preparing nanosized zirconium alkylphosphonates to be used as nanofillers in polymeric materials [194]. Finally, there are many examples concerning the use of zirconium phosphonates for catalysis applications. One of these is the work of S. Calogero and coworkers, who recently sintetized several L-proline functionalized zirconium phosphonates, and tested their catalytic activity in the asymmetric aldol addition of p-nitrobenzaldehyde to cyclohexanone [190].

The investigation of the structure of zirconium phosphonates is very important to understand the origin of their functional properties, with the final aim of exploiting this knowledge to prepare systems with similar or improved performances. Since the great part of zirconium phosphonates are crystalline materials, usually obtained in the form of powders, one of the main techniques for the study of their structural properties is Powder X-Ray Diffraction (PXRD). However, SSNMR can also give an important contribution, complementary and/or alternative to PXRD, since a wide variety of nuclear properties can be measured, which are related to many different structural parameters. In particular, as mentioned in the introduction to this chapter, the utility of SSNMR in understanding the structure of crystalline materials is well known. Nevertheless, its applications to the study of zirconium phosphonates are very few, and mainly limited to the observation of the nucleus ^{31}P [187, 196–198].

The work presented in this chapter is the continuation of the study carried out in the lab of Prof. Jeremy Titman, University Nottingham, a preliminary part of which was described in chapter 6. Exploiting the techniques described in chapter 6 for the measure-

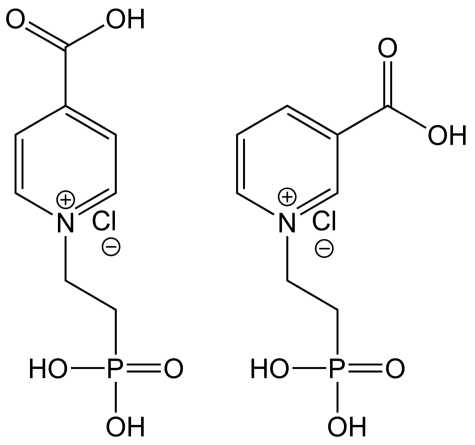

H_3L^1 H_3L^2

Figure 7.1: Structures of the phosphono-carboxylate ligands H3L1 and H3L2.

ment of large ^{19}F CSA interactions, we explored the sensitivity of ^{19}F CSA parameters to the structural properties of zirconium phosphonates, by studying compounds with different crystalline structures, already known from PXRD. The study was carried out on three different zirconium phosphonates prepared by the group of F. Costantino, Department of Chemistry, University of Perugia (Italy), who have a more than twenty-year experience in this field [180–183, 185–187, 190, 191, 194]. The samples were prepared according to the procedure described in [178], using the two novel phosphono-carboxylate ligands H_3L^1 and H_3L^2 shown in Figure 7.1. The labelling and formula of these samples are:

- sample **1**, prepared using the phosphorous ligand H_3L^1, with formula $ZrF_2(HF)(PO_3CH_2CH_2NC_5H_4CO_2)$
- sample **1a**, prepared by heating sample **1** at the temperature of 280 °C, with formula $ZrF_2(PO_3CH_2CH_2NC_5H_4CO_2)$
- sample **2**, prepared using the phosphorous ligand H_3L^1, with formula $ZrF_2(PO_3CH_2CH_2NC_5H_4CO_2)$

The crystalline structures of these compounds determined by PXRD were determined by F. Costantino and coworkers, and are described in [178]. Sample **1** is characterized

by a 1D chains structure constituted by ZrO_3F_3 octahedra and PO_3C tetrahedra. Different chains are connected through the isonicotinic group of the ligand H_3L^1, with the carboxylic group hydrogen-bonded to the equatorial ^{19}F of a ZrO_3F_3 group belonging to the adjacent chain. In sample **1a**, the H$\cdots$F hydrogen bond is substituted by a covalent bond between the carboxylic group and the zirconium atom, following heating of sample **1** with loss of a HF molecule. Both **1** and **1a** are characterized by the presence of a single Zr centre in the unit cell. Finally, sample **2** is characterized by 1D chains of ZrO_4F_2 octahedra and PO_3C tetrahedra organized in a layered structure. Similarly to sample **1a**, the carboxylic group of the ligand H_3L^2 is covalently bonded to the zirconium atom of the adjacent chain. However, differently form both **1** and **1a**, **2** possesses two different Zr centres in the unit cell.

The SSNMR study also aimed at clarifying some structural features of samples **1**, **1a**, and **2**, such as the H$\cdots$F hydrogen bond length in **1**, which were not completely understood on the basis of PXRD data. To this regard, the analysis of ^{1}H *ultrafast* MAS spectra, as well as the measurement of ^{1}H CSA and ^{19}F-^{1}H dipolar interactions gave important contributions.

7.3 Results

7.3.1 ^{19}F MAS spectra

In Figure 7.2a and b the ^{19}F MAS spectra of samples **1**, **1a**, and **2** acquired at the Larmor frequency of 564 MHz and at the MAS frequency of 65 kHz are reported. As we can see, the spectra of the three samples show significant differences, which are related to differences in the structural properties of the corresponding unit cells. In agreement with [178], the spectrum of **1** shows two main groups of signals at about 0 and 40 ppm, ascribable to the hydrogen-bonded equatorial and to the two axial fluorine atoms of ZrO_3F_3 octahedra, respectively. Differently from [178], the use of a higher field allowed us to observe that the signal at about 40 ppm is given by the superimposition of two peaks at the slightly different chemical shifts of 39 and 41 ppm. This result suggests a

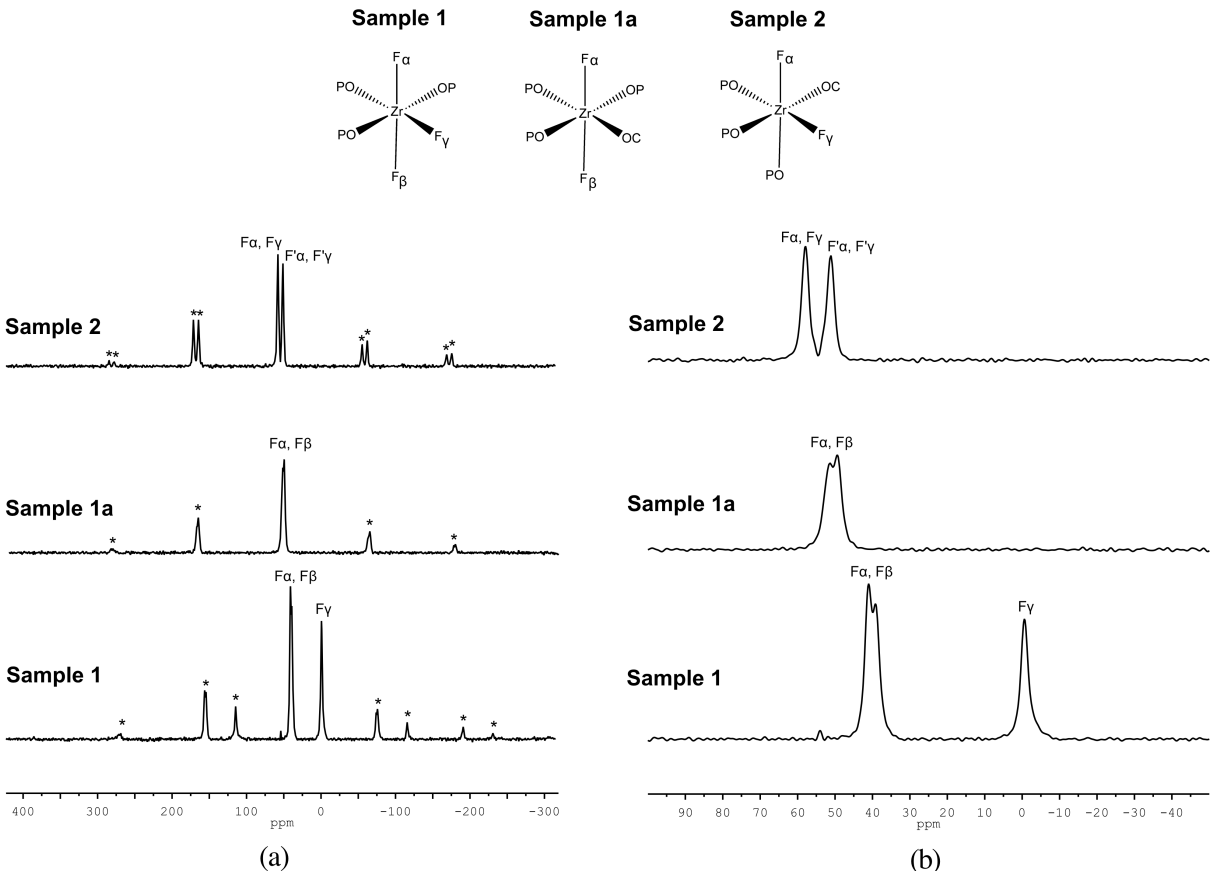

Figure 7.2: (a) ^{19}F MAS spectra acquired at the MAS frequency of 65 kHz of, from bottom to top, samples **1**, **1a**, and **2**. Spinning sidebands are marked with the symbol $*$. The spectrum of sample **2** was assigned under the hypothesis that the two different isotropic signals arise from two different sites in the unit cells. F and F' indicate fluorine atoms located in two different sites in the unit cell. (b) Corresponding expansions of the regions of the isotropic signals.

slight distortion from the octahedral geometry around the Zr centre, in agreement with PXRD data [178]. In the spectrum of **1a** only one group of signals at about 50 ppm can be observed, arising from the two axial fluorine atoms bonded to the Zr centre. Also in this case two partially superimposed peaks can be resolved at the chemical shifts of 49 and 52 ppm, indicating a slight distortion from the octahedral geometry, again in agreement with PXRD data. The absence of a peak at 0 ppm can be explained with the loss of the equatorial fluorine atom (as HF) following heating of **1**, and confirms the assignment of this peak to the hydrogen-bonded fluorine. Finally, in the spectrum of **2** two signals can be observed at 51 and 58 ppm, whose assignment is not clear on the basis of the sole chemical shift data. Indeed, they can be assigned either to two different fluorine atoms around the same Zr centre, chemically inequivalent because of geometrical distortions, or to fluorine atoms belonging to the two different sites in the unit cell.

7.3.2 Measurement of ^{19}F CSA

^{19}F CSA interactions in samples **1**, **1a**, and **2** were measured exploiting both methods of spinning sideband analysis and of use of suitable RN^{ν}_{n} recoupling sequences described in chapter 6. In the following the results obtained by the two approaches are reported.

Analysis of the spinning sidebands profile: method of rotational echoes.

^{19}F MAS spectra at different MAS frequencies, going from 15 to 65 kHz, were acquired for samples **1**, **1a**, and **2**. The resulting spinning sideband patterns were fitted by using the SIMPSON Opt package, as described in section 6.4.2. Since the zirconium phosphonates here studied contain both protons and fluorine atoms, ^{19}F-^{1}H dipolar interactions might contribute to the MAS spectra, preventing CSA parameters to be clearly determined. For this reason, ^{1}H-decoupled ^{19}F MAS spectra were acquired, together with non-decoupled ^{19}F MAS spectra at various MAS frequencies. The ^{1}H-decoupled spectra were recorded using a 2.5 mm HF probe available at the UK 850 MHz Solid-State NMR Facility, University of Warwick, of which I could temporary avail within the period in Jeremy Titman's group. In contrast, the non-decoupled ^{19}F MAS spectra were acquired

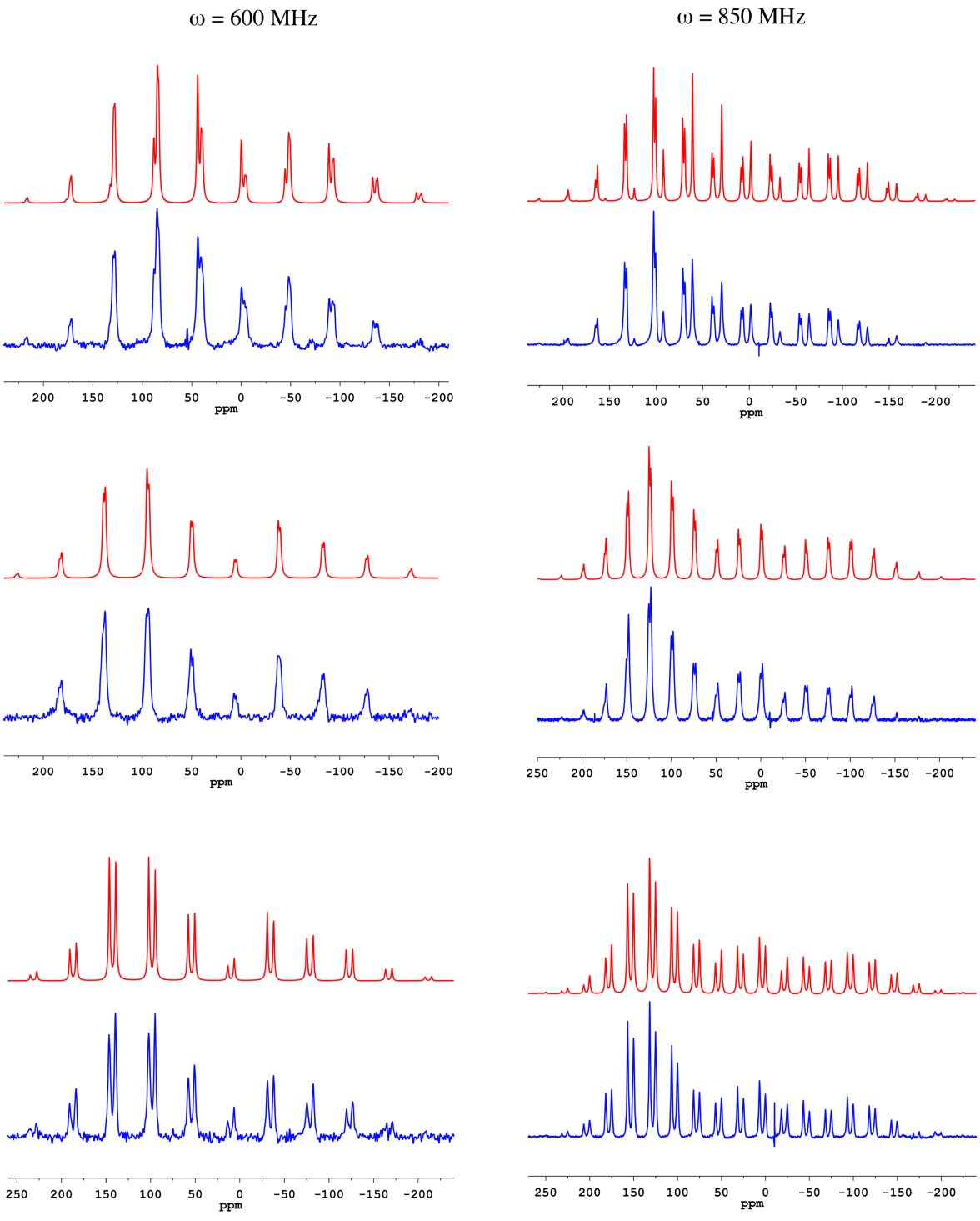

Figure 7.3: (a) Comparison between the simulated (red) and experimental (blue) ^{19}F MAS spectra recorded at the proton Larmor frequency of 600 MHz and at the MAS frequency of 25 kHz of, from top to bottom, samples **1**, **1a** and **2**. (b) Comparison between the simulated (red) and experimental (blue) ^{1}H-decoupled ^{19}F MAS spectra at the proton Larmor frequency of 850 MHz and at the MAS frequency of 20 kHz (25 kHz for sample **1**) of, from top to bottom, samples **1**, **1a** and **2**. All the simulations were perfomed considering only the CSA interaction and using Δ and η parameter values reported in Table 7.1.

Table 7.1: Chemical shift anisotropy (Δ) and asymmetry (η) parameters determined for samples **1**, **1a** and **2** by averaging the values obtained by the fitting of the spinning sideband profiles at different MAS frequencies and magnetic fields, under ^{1}H decoupling (Larmor frequency of about 800 MHz; MAS frequencies of 20 and 32 kHz for **1a** and **2**, and of 15 and 25 kHz for **1**) and not (Larmor frequency of about 564 MHz; MAS frequencies of 15, 25, 35, and 45 kHz).

	Samples						
Average CSA parameters	**1**			**1a**		**2**	
	0 ppm	**39 ppm**	**41 ppm**	**49 ppm**	**52 ppm**	**51 ppm**	**58 ppm**
Δ (ppm)	-175 ± 3	-217 ± 4	-196 ± 2	-225 ± 3	-201 ± 5	-230 ± 2	-224 ± 3
η	0.3 ± 0.1	0.3 ± 0.1	0.3 ± 0.1	0.3 ± 0.1	0.2 ± 0.1	0.3 ± 0.1	0.1 ± 0.1

at the proton Larmor frequency of 600 MHz, using the SSNMR facilities available at the University of Nottingham.

In Table C.1 in appendix C the CSA parameters obtained from the analyses of the spectra acquired at the different MAS frequencies, under ^{1}H decoupling and not, are reported. Similarly to what found for PTFE and PVDF (section 6.4.2), apart from the highest MAS frequencies, the variation among the CSA parameters obtained by this set of independent measurements is very small, suggesting that MAS rotation at frequencies above 15 kHz is enough to efficiently average out the ^{19}F-^{1}H dipolar couplings. This is true also for the signal at 0 ppm in the spectrum of sample **1**, arising from the hydrogen-bonded fluorine atom. In Table 7.1 the results obtained by averaging the CSA parameters determined from the spectra acquired at the slower MAS frequencies ($\leq$ 45 kHz), under ^{1}H-decoupling or not, are reported, and in Figure 7.3 the experimental and simulated spectra are compared. As we can see, the simulated spectra reproduce very well the experimental ones, both under ^{1}H decoupling and not. For all the samples negative Δ were measured, with large absolute values of the order of 200 ppm.

$R12_5^4$ and $R8_1^2$ sequences

^{19}F CSA parameters for samples **1**, **1a**, and **2** were also determined by using the $R12_5^4$ and $R8_1^2$- based recoupling experiments developed and tested as described in chapter 6. The

Table 7.2: ^{19}F best-fitting chemical shift anisotropy and asymmetry parameters determined for the different isotropic signals of samples **1**, **1a** and **2** by means of the $R12_5^4$ and $R8_1^2$ recoupling sequences, following the procedure described in section 6.4.2.

		Samples						
R sequence	**CSA parameters**	**1**			**1a**		**2**	
		0 ppm	**39 ppm**	**41 ppm**	**49 ppm**	**52 ppm**	**51 ppm**	**58 ppm**
$R12_5^4$	Δ (ppm)	-185	-220	-215	-210	-205	-220	-235
	η	0.1	0.4	0.5	0.2	0.1	0.4	0.3
$R8_1^2$	Δ (ppm)	-	-	-	-220	-220	-260	-260
	η	-	-	-	1.0	1.0	0.5	0.6

aim was also to test the efficiency of these sequences in measuring very strong CSA interactions, as those characterising ^{19}F in the zirconium phosphonates under investigation ($\Delta \sim 200$ ppm). ^{19}F CSA parameters were determined from analyses of the decoupled patterns, following the procedure described in section 6.4.2. The obtained parameters and the comparisons between the simulated and experimental patterns are reported in Table 7.2 and in Figures 7.4, 7.5 and 7.6. The contour plots of the *rms* of the differences between the experimental and simulated recoupled patterns are reported in Figures C.1, C.2, and C.3 in Appendix C. As far as $R12_5^4$ is concerned, for all the samples and isotropic peaks there is a good match between the simulated and experimental patterns. The results shown for sample **1** in Figure 7.4 were obtained by setting the rf frequency offset at 20 ppm, intermediate between the two groups of signals at 0 and 39-40 ppm in the ^{19}F MAS spectrum, and accordingly the simulations were carried out using relative offsets of +20 and -20 ppm for the signals at 0 and 39-40 ppm, respectively. Indeed an offset of the order of 20 ppm with respect to the observed signal can significantly affect the shape of the recoupled pattern. In order to improve the efficiency of the recoupling sequence for the two groups of isotropic signals in sample **1**, we also performed two experiments with the rf frequency centred at about 0 and 40 ppm. However, these experiments did not give good results and are not reported in this thesis.

$R8_1^2$ was applied only to the samples **1a** and **2**, in which, from the analysis of the

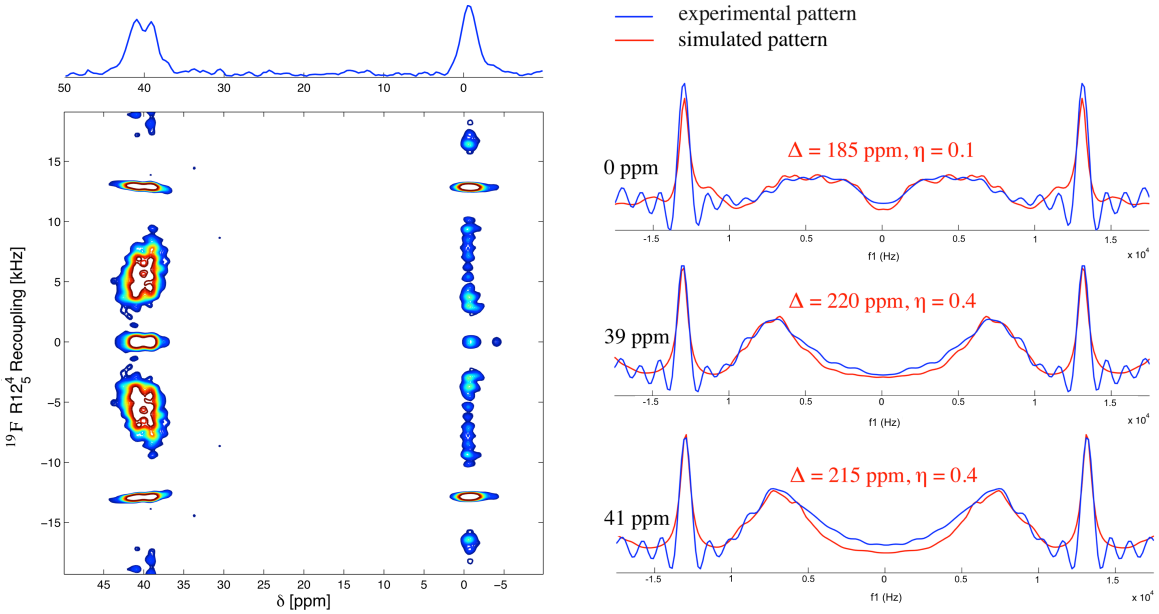

Figure 7.4: Left: experimental ^{19}F 2D recoupling spectra obtained for sample **1** using the R12$^{4}_{5}$ sequence. In the first dimension the ^{19}F MAS spectrum is reported, while in the second dimension the recoupled patterns for each isotropic peak are shown. Right: comparison between the experimental recoupled patterns obtained for the isotropic peaks of sample **1** at 0, 39 and 41 ppm, and the patterns simulated by using the best-fitting CSA parameters determined as described in the text. In the experiments the rf frequency was set at about 20 ppm. The simulations were performed by using a Lorentzian line-broadening of 1200 Hz and an offset of +20 and -20 ppm respect to the peaks at 0 and 39-41 ppm, respectively.

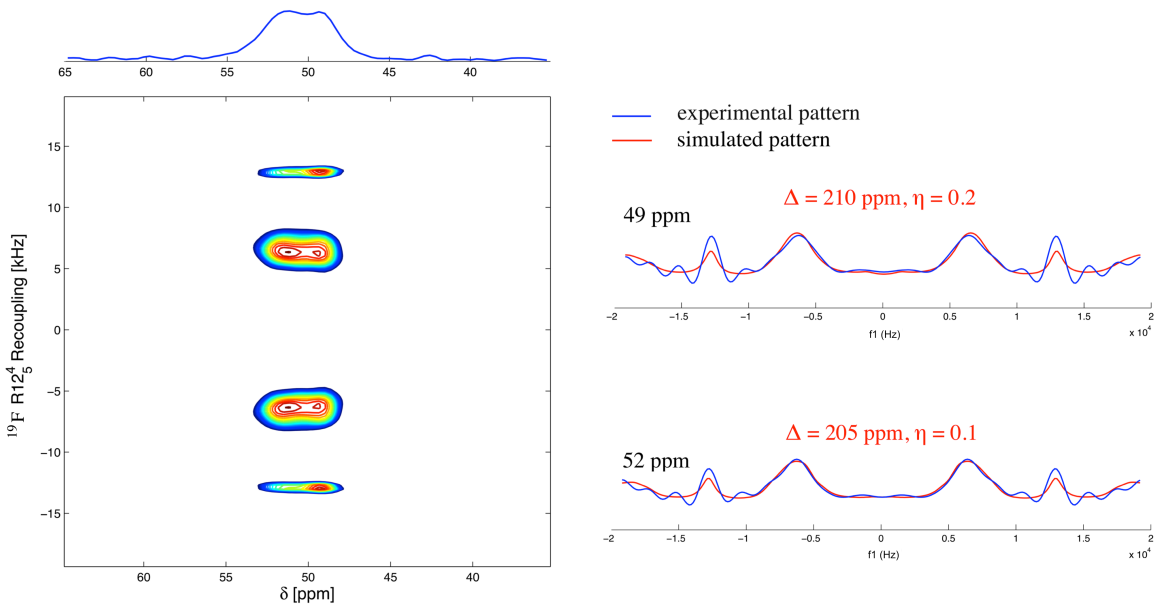

(a)

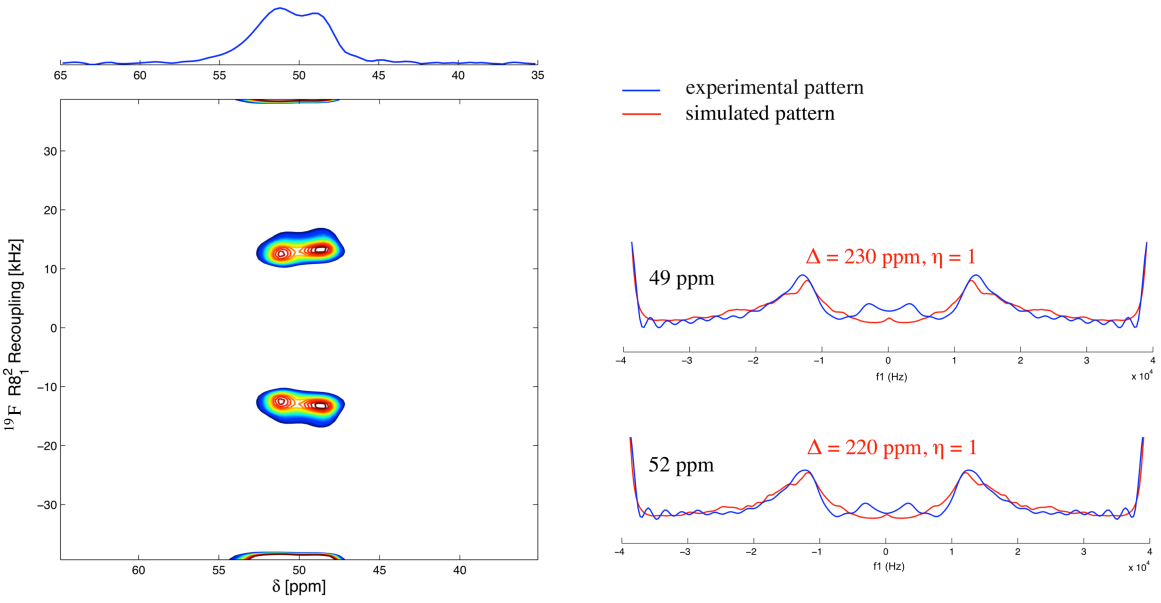

(b)

Figure 7.5: Left: experimental ^{19}F 2D recoupling spectra obtained for sample **1a** using the R12$^4_5$ (a) and R8$^2_1$ (b) sequences. In the first dimension the ^{19}F MAS spectrum is reported, while in the second dimension the recoupled patterns for each isotropic peak are shown. Right: comparison between the experimental recoupled patterns obtained for sample **1a** isotropic peaks at 49 and 51 ppm and the patterns simulated by using the best-fitting CSA parameters determined as described in the text. In the experiments the rf frequency was set at about 40 ppm. The simulations were performed by using a Lorentzian line-broadening of 1200 Hz and an offset of 0 ppm respect to both the isotropic peaks.

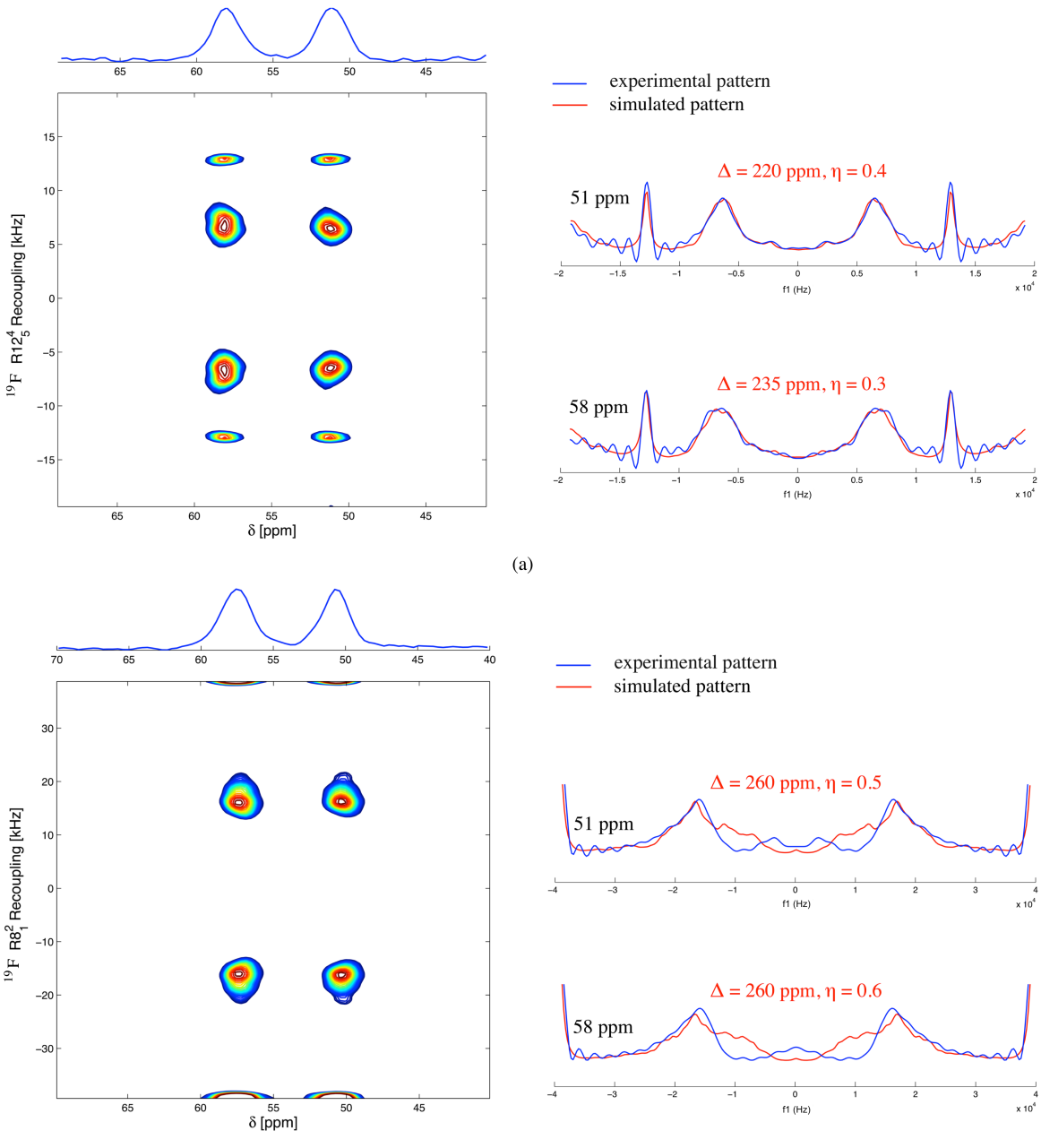

Figure 7.6: Left: experimental ^{19}F 2D recoupling spectra obtained for sample **2** using the R12$^4_5$ (a) and R8$^2_1$ (b) sequences. In the first dimension the ^{19}F MAS spectrum is reported, while in the second dimension the recoupled patterns for each isotropic peak are shown. Right: comparisons between the experimental recoupled patterns obtained for the sample **1** isotropic peaks at 51 and 58 ppm and the patterns simulated by using the best-fitting CSA parameters determined as described in the text. In the experiments the rf frequency was set at 55 ppm. The simulations were performed by using a Lorentzian line-broadening of 1200 Hz and an offset of 0 ppm respect to both the isotropic peaks.

spinning sidebands profile, the fluorine atoms resulted to have the strongest CSA interactions. For both the samples, and especially for sample **2**, the values of Δ (ppm) and η obtained using this sequence are quite bigger than those obtained using $R12_5^4$, and the match between the simulated and the experimental patterns is much less satisfactory (Figures 7.5 and 7.6). It could be that for these samples the contribution of the ^{19}F-^{19}F homonuclear dipolar coupling to the pattern recoupled under $R8_1^2$ is not negligible, or that the experimental set-up was not suitable to completely recouple such strong CSA interactions.

7.3.3 ^{1}H MAS spectra

In Figure 7.7, the ^{1}H *ultrafast* MAS spectra, acquired at the MAS frequency of 65 kHz, of samples **1**, **1a**, and **2** are shown, along with the assignment of the different isotropic signals. As we can see, the increase of MAS frequency determines a significant improvement of the spectral resolution with respect to the ^{1}H MAS spectra reported in [178], acquired at the MAS frequency of 22 kHz. In the spectrum of **1**, the signal at about 12.5 ppm can be ascribed to the proton of the carboxylic group involved in the H$\cdots$F hydrogen bond. This signal is not present in the spectrum of **1a**, in agreement with the loss of a HF molecule following heating of sample **1**. Moreover, it is interesting to notice that in passing from sample **1** to sample **1a**, the features of the ^{1}H MAS spectrum significantly change. In particular, splittings of the signals in both the aromatic and the aliphatic regions can be clearly observed in the spectrum of **1a**, which probably reflect conformational changes concerning the phosphonic ligand. Indeed, the presence of different conformations in the sample can be ruled out on the basis of PXRD data [178]. On the other hand, PXRD structures showed that the plane defined by the NCH2(10)CH2(11) group moves from an orientation perpendicular to the plane of the aromatic ring to a more equatorial one in passing from **1** to **1a**. The equatorial orientation in sample **1a** might determine the chemical inequivalence of the two protons of CH2(11), and it could explain the splitting of the corresponding signal from a peak at about 2.5 ppm in **1** to two peaks at about 2.4 and 3.8 ppm in **1a**. As far as the aromatic region is concerned, from the PXRD structure of **1a** an effect of π-stacking can be hypothesized, such that

one of the protons CH(6) and CH(2) is more de-shielded than the other under the effect of the adjacent aromatic rings. This qualitative consideration could explain the shift of one isotropic signal by about 1.5 ppm, from 9 ppm to 7.5 ppm, but DFT calculation would be necessary to validate this interpretation from a quantitative standpoint. The other two signals at about 8.8 and 9.7 ppm can be assigned to the protons of the CH groups bonded to the nitrogen atom, CH(5) and CH(3), and to the proton CH(2) (or CH(6)), respectively. The differences in chemical shifts with respect to sample **1** are reasonably due to conformational effects.

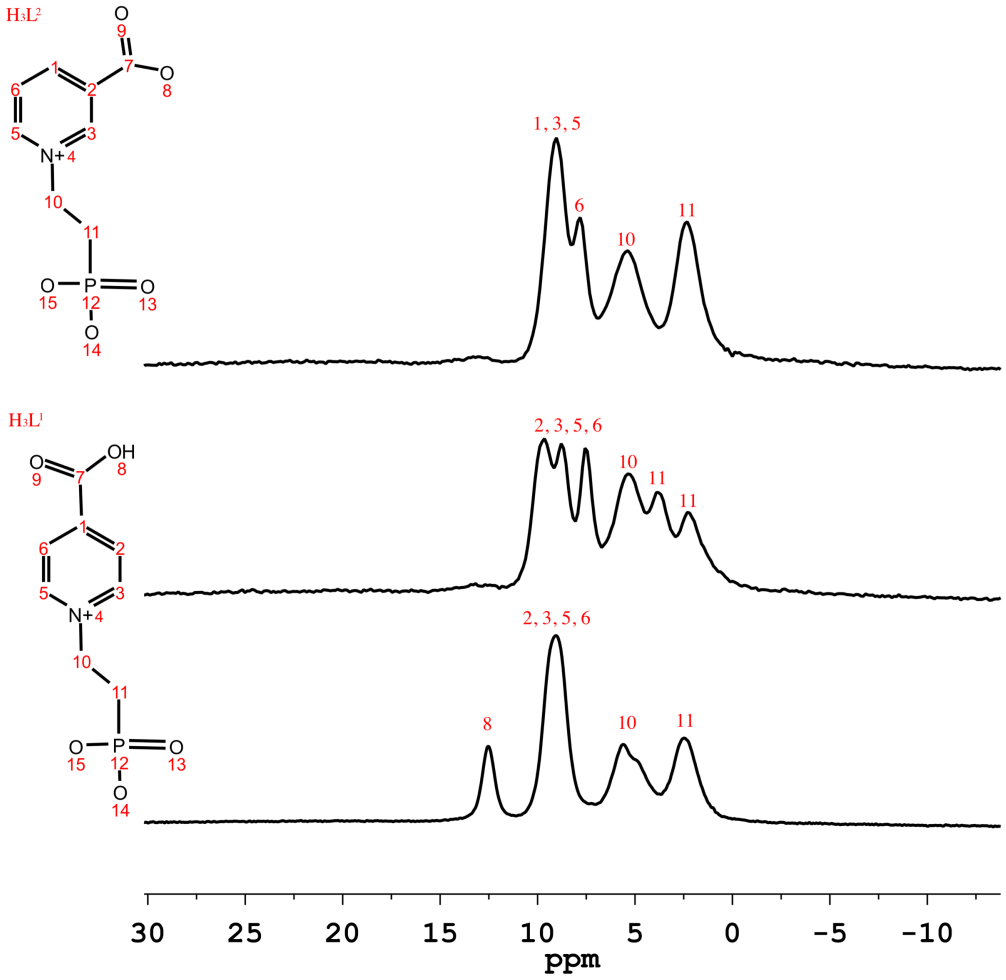

Figure 7.7: ^{1}H MAS spectra, recorded at a MAS frequency of 65 kHz, of, from bottom to top, samples **1**, **1a**, and **2**. The signal assignment is also reported, along with the structures of the ligands H3L1, for samples **1** and **1a**, and H3L2, for sample **2**.

7.3.4 Determination of ^{1}H-^{19}F hydrogen bond length

Jeremy Titman and coworkers recently demonstrated that the sequence R16$_3^2$ can be used to reintroduce ^{1}H CSA interaction under high resolution conditions, that are magnetic high fields and *ultrafast* MAS rotation [160]. In this work this sequence was employed to measure ^{1}H CSA of the hydrogen-bonded proton in sample **1**. In order to get a good resolution in the first dimension a MAS frequency of 62.5 kHz was used. It is worth noticing that, since CSA and heteronuclear dipolar coupling tensors have the same rotational ranks, the experimental decoupled pattern will be affected by both these interactions. In Figure 7.8, the 2D recoupling spectrum obtained for sample **1** is shown, along with the recoupled pattern relative to the hydrogen-bonded proton resonating at 12.5 ppm. As we can see, the shape of the recoupled pattern is characterized by a

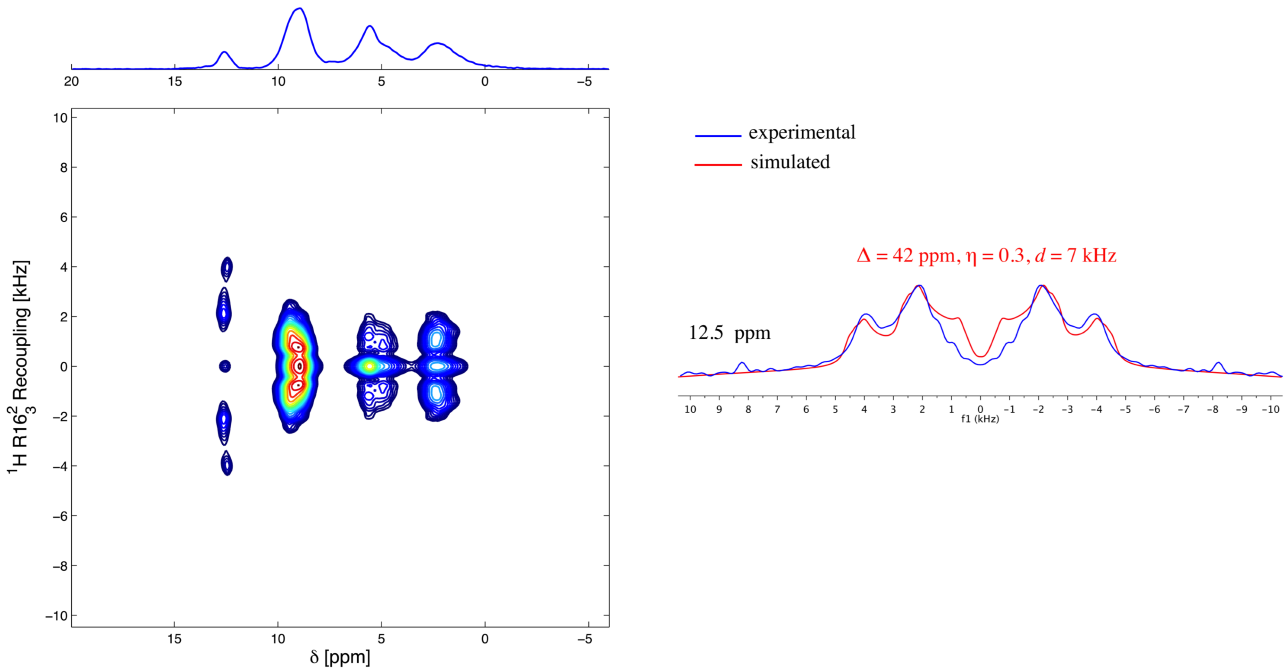

Figure 7.8: Left: experimental ^{1}H 2D recoupling spectra obtained for sample **1** using the R16$_3^2$ sequences. In the first dimension the ^{1}H MAS spectrum is reported, while in the second dimension the recoupled patterns for each isotropic peak are shown. Right: comparison between the experimental recoupled pattern obtained for the peak at about 12.5 ppm and the pattern simulated by using the best-fitting CSA Δ (ppm) and η and the ^{1}H-^{19}F dipolar coupling constant d parameters, determined as described in the text. The simulations were performed by using a Lorentzian line-broadening of 300 Hz and an offset of 0 ppm respect to the isotropic peak.

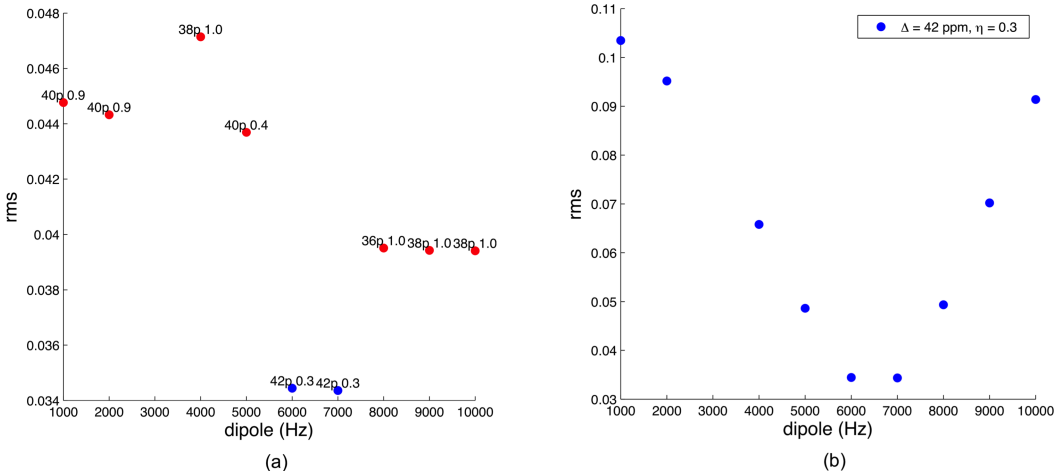

Figure 7.9: (a) Minima of *rms* of the differences between the simulated and the experimental patterns recoupled under $R16_3^2$ for the ^{1}H signal at 12.5 ppm of sample **1**, obtained at different values of the ^{1}H-^{19}F dipolar coupling constant (d). The reported *rms* are obtained by its contour plots as a function of the CSA parameters Δ and η, at a fixed value of d. On the top of each point in the graph the values of Δ (in ppm, indicated as 'p') and η at the minimum are reported. (b) Values of *rms* of the differences between the experimental patterns recoupled under $R16_3^2$ and the patterns simulated with Δ and η of 42 ppm and 0.3, obtained for the hydrogen-bonded proton in sample **1**, as a function of the ^{1}H-^{19}F dipolar coupling constant d (Hz).

splitting, which is reasonably due to the superimposition of the contributions of the ^{1}H CSA and the ^{1}H-^{19}F dipolar coupling interactions. In order to determine both the ^{1}H CSA parameters and the ^{1}H-^{19}F dipolar coupling constant (d), we performed Simpson simulations for different values of Δ, η, and d [163], calculating for each value of d the contour plot of the *rms* of the differences between the simulated and the experimental pattern as a function of Δ and η. In Figure 7.9a we plotted the minimum value of rms in each contour plot as a function of d. It is worth noticing that the values of Δ and η at the minimum, reported in Figure 7.9a on the top of each point, vary with d. The plot shows that the best fitting of the experimental recoupled pattern is obtained for a combination of Δ, η, and d parameters of 42 ppm, 0.3, and 7 kHz, respectively, and in Figure 7.8 the comparison between the corresponding simulated and experimental patterns is shown. The contour plot corresponding to the minimum of rms is reported in Figure C.4. The high value of Δ (42 ppm) is typical of a proton involved in a strong hydrogen bond interaction, as also suggested by the estimated value of d. In order to determine more precisely the best value for d, we plotted the rms at $\Delta = 42$ ppm and η

= 0.3 for different values of d (Figure 7.9b). As expected, a minimum of rms at d values of about 6-7 kHz is present, corresponding to a H$\cdots$F internuclear distance of about 2.5-2.7 Å.

7.4 Discussion

The work described in this chapter had a double aim, one more methodological and the other more applicative. The former concerned the use of the methods described in chapter 6 for measuring ^{19}F CSA in zirconium phosphonates, characterized by larger values of Δ ($\sim$ 200 ppm) compared to those measured for the tests samples PTFE and PVDF ($\sim$ 100 ppm). The latter concerned the study of the structural properties of samples **1**, **1a**, and **2** by determining some SSNMR nuclear properties of nuclei ^{19}F and ^{1}H. To this regard, one of the aim was to relate the measured ^{19}F CSA parameters to specific crystallographic features of the samples.

From a methodological standpoint, ^{19}F CSA parameters were determined for zirconium phosphonates **1**, **1a**, and **2**, by the analysis of both the spinning sideband profiles acquired at different MAS frequencies, and the patterns recoupled under $R12_5^4$ and $R8_1^2$ sequences.

The method of spinning sideband analysis allowed a good reproduction of the experimental MAS spectra (Figures 7.3). Moreover, also thanks to the very large CSA values, i.e. large number of spinning sidebands even at the relatively high MAS frequencies of 15 and 25 kHz, CSA parameters were determined with good precisions on both Δ (uncertainties of about $\pm$ 2-3%) and η (uncertainties of about $\pm$ 0.1) (Figures 7.1).

As far as recoupling sequences are concerned, different results were obtained for $R12_5^4$ and $R8_1^2$. In particular, the fitting of the patterns recoupled under $R12_5^4$ gave a much more satisfactory reproduction of the experimental data compared to $R8_1^2$. Moreover, there is a good match between the values of Δ and η determined by using $R12_5^4$ and the method of spinning sideband analysis (Tables 7.1 and 7.2). Indeed, the differences can always be considered within the uncertainties on the parameters determined under

$R12_5^4$ (Figures C.1, C.2, C.3). To this regard, it is worth noticing that in the range of $\Delta \sim 200$ ppm, $R12_5^4$ is not very sensitive to differences of Δ and η of the order of 10-20 ppm and 0.2, respectively, which, on the contrary, are clearly detectable with the method of spinning sideband analysis. As far as $R8_1^2$ is concerned, the match with the parameters determined by spinning sideband analysis is much less satisfactory, indicating that, experimentally, this sequence was not very efficient in recoupling such large CSA interactions.

In order to make some observations about the sensitivity of ^{19}F chemical shift tensors toward the crystallographic features of zirconium phosphonates, it is reasonable to assume the CSA parameters determined by spinning sideband analysis sufficiently reliable within the uncertainties reported in Table 7.1. As we can see, both the isotropic chemical shift and the CSA parameters Δ and η significantly change among the samples, reflecting differences in their chemical and/or structural and/or conformational properties.

^{19}F isotropic chemical shift was found to be very sensitive to conformational properties around the zirconium centre, as well as to hydrogen bonds directly or indirectly involving the nucleus under observation. In sample **1**, hydrogen bonding with the carboxylic group of H_3L^1 ligand determines a strong shielding of the equatorial ^{19}F directly involved in the interaction (Figure 7.2). The presence of H$\cdots$F hydrogen bonds seems also to affect the chemical shift tensors of the axial fluorine atoms, which resonate at isotropic chemical shifts (39 and 41 ppm) much lower than those determined for the fluorine atoms in **1a** (49 and 52 ppm) and **2** (51 and 59 ppm). In both **1** and **1a**, the differences between the isotropic chemical shifts of the two axial fluorines reflect distortion from the octahedral geometry around the Zr centre. As far as sample **2** is concerned, this is characterized by two Zr centres in the unit cell, each characterized by the presence of two fluorines atoms in "ortho" position with respect to each other, i.e. one in axial and the other in equatorial position. The equatorial-axial, instead of axial-axial, distribution of ^{19}F around the Zr centre could explain the higher values of ^{19}F isotropic chemical shift compared to **1a** (Figure 7.2). In particular, the two signals at 51 and 59 ppm observable in the ^{19}F MAS spectrum of **2** could be ascribed either to two fluorine atoms bonded to

the same Zr centre, or to fluorine atoms belonging to the two different sites in the unit cells. Considering the difference in chemical shift, which is significantly larger than that between the axial ^{19}F in **1** and **1a**, and the differences in the conformational properties of the two Zr centres (Supplementary information to [178]), the latter hypothesis seems more likely. However, the certain assignment of the two signals would need the support of calculations.

As far as ^{19}F anisotropy parameters are concerned, Δ significantly changes among the different fluorine sites. Similarly to the isotropic chemical shift, Δ was found to be sensitive to the presence of hydrogen bonds, which determine a decrease, in absolute value, of Δ. Indeed, the absolute value of Δ measured for the hydrogen-bonded ^{19}F in sample **1** (175 ppm) is much smaller than those obtained for the other two axial fluorines in the same sample (217 and 196 ppm). In turn, the latter result to be smaller than those measured for ^{19}F in **1a** and **2** (Table 7.1), probably due to an indirect effect of the H$\cdots$F hydrogen bond involving the equatorial ^{19}F. Moreover, a sensitivity of Δ towards distortions form the octahedral symmetry around Zr centre can also be observed. Indeed, different values of Δ were measured for the two axial ^{19}F in both **1** and **1a**. It is worth noticing that, if the assigment of the isotropic signals of **2** is correct, this will mean that when the fluorines atoms are in "ortho" position with respect to each other both isotropic chemical shift and Δ will be less sensitive to the conformational properties around the Zr centre. Indeed, the same isotropic chemical shift and CSA parameters are measured for fluorine atoms belonging to the same zirconium centre. Finally, the asymmetry parameter η was found to slightly change among the different fluorine atoms, the average values varying between 0.1 to 0.4 with uncertainties of about 0.1. Values of η greater than 0 indicate that the chemical shift tensors do not show an axial symmetry ($\delta_{xx} \neq \delta_{yy}$), and this could reflect distortions from the octahedral symmetry around the Zr centre.

7.5 Experimental

All the ^{19}F and ^{1}H MAS, as well as the $R12_5^4$, $R8_1^2$ and $R16_3^2$ recoupling experiments were performed on a Bruker Avance 600 MHz spectrometer, available at the University of Nottingham, UK, corresponding to ^{1}H and ^{19}F Larmor frequencies of 600 and 564 MHz, respectively, equipped with a 1.3 mm probe.

The ^{19}F MAS and ^{1}H MAS spectra were recorded accumulating 8 scans and 4 scans with recycle delays of 200 and 20 s, respectively, using a $\frac{\pi}{2}$ pulse duration of 1.5 μs for both the nuclei.

As far as the recoupling experiments are concerned, due to the long ^{19}F and ^{1}H T_1 relaxation times, a train of saturation pulses followed by a recovery delay was introduced before the RN_n^ν sequence (Figure 6.3), that allowed a short recycle delay of 1 s to be used. Recovery delays of 20 and 60 s were used for ^{1}H and ^{19}F, respectively, accumulating 16 (^{1}H) and 32 (^{19}F) scans in the first dimension. $R12_5^4$ and $R8_1^2$ were performed on the nucleus ^{19}F at MAS frequencies of 65 and 39 kHz, corresponding to π pulse durations of 6.4 and 3.2 μs, respectively. In order to have spectral widths in the second dimension sufficiently wide to include the whole ^{19}F recoupled pattern, oversampling was used, by sampling the ^{19}F signal every four π pulses of the $R12_5^4$, or $R8_1^2$, sequence. $R16_3^2$ was performed on the nucleus ^{1}H, at the MAS frequency of 62.5 kHz, corresponding to π pulse duration of 3 μs. The processing of the 2D spectra was performed as described in section 6.6.

The ^{1}H-decoupled ^{19}F MAS spectra were recorded using the Bruker 850 MHz SSNMR spectrometer, corresponding to ^{1}H and ^{19}F Larmor frequencies of about 850 and 800 MHz, available at the University of Warwick, UK, equipped with a HFX 2.5 mm probe. A $\frac{\pi}{2}$ degree pulse duration of 2.5 μs was used, accumulating 32 scans with a recycle delay of 150 s. For ^{1}H-decoupling the SPINAL-64 sequence was used [6].

All the simulations and fittings were performed by using SIMPSON 3.1.0 [163]. The simulated ^{19}F and ^{1}H FID recoupled by RN_n^ν sequences were processed as described in section 6.6. For the fittings of the ^{19}F MAS spectra the SIMPSON Opt package was used [166].

7.6 Conclusions

$R12_5^4$ and $R8_1^2$ recoupling experiments, previously developed and tested on PTFE and PVDF (chapter 6), were used to reintroduce the large ^{19}F CSA interactions in zirconium phosphonates **1**, **1a**, and **2**. Contrary to what expected on the basis of simulations (paragraph 6.4.1), experimentally $R8_1^2$ did not give good results in recoupling CSA with $\Delta \sim 200$ ppm. Indeed neither the fitting of the experimental data, nor the comparison with the CSA parameters determined by spinning sideband analyses were satisfactory. On the contrary, promising results were obtained under $R12_5^4$, which was found to efficiently recouple such strong CSA interactions. The main drawback of using $R12_5^4$ with respect to the method of spinning sideband analysis is that the measured CSA parameters are affected by larger uncertainties, so that it is not possible to detect differences in $\Delta \leq 20$ ppm ($\sim 10\%$).

The method of spinning sideband analysis was found to be the best approach to measure ^{19}F CSA interactions in zirconium phosphonates **1**, **1a**, and **2**, allowing to determine the parameters Δ and η with very good precision. For this reason, ^{19}F CSA parameters obtained with this method were used to make observations about the dependence of these parameters on the crystallographic features of the different zirconium phosphonates. ^{19}F isotropic chemical shift and chemical shift anisotropy were found to be very sensitive to the presence of H$\cdots$F hydrogen bonds, as well as to distortion from octahedral geometry around the zirconium centre. In particular, both ^{19}F isotropic chemical shift and Δ significantly decrease in absolute value when hydrogen bonds directly or indirectly affecting the nucleus under observation are present.

The observation of nucleus ^1H was also very useful to obtain structural information on zirconium phosphonates. Indeed, ^1H isotropic chemical shift was found to be very sensitive to both structural and conformational properties of the phosphonic ligands. Finally, one of the most interesting results was the determination of the H$\cdots$F hydrogen bond length in sample **1**, unknown on the basis of PXRD data, which was found to be within 2.5-2.7 Å. The latter was remarkably determined from the ^1H-^{19}F dipolar coupling interaction measured by analysing the ^1H pattern recoupled under the $R16_3^2$

sequence, which was recently developed by J. Titman and coworkers for recoupling ^{1}H CSA interactions under *ultrafast* MAS conditions [160].

Conclusions

In this thesis, the application of solid-state NMR to the study of the structural and dynamic properties on a molecular and supramolecular level of different classes of functional materials demonstrated the important contribution that this spectroscopy can give to the comprehension of these materials and of the complex relationships between their "microscopic" properties and their functions.

In particular, materials belonging to the classes of ion exchange membranes, polymeric photoactive blends, chromogenic polymeric materials, and, finally, zirconium phosphonates were studied. Depending on the kind of material and on the researched structural or dynamic information, different combination of SSNMR techniques were employed, allowing in each case the determination of the most useful nuclear properties.

High- or low-resolution techniques to determine isotropic and/or anisotropic contributions of internal Hamitionians, and in particular of isotropic chemical shifts, chemical shift anisotropies, heteronuclear and homonuclear dipolar couplings, allowed us to obtain information on different chemical, structural and dynamic properties of both organic and inorganic components. As examples of determination of chemical and structural features, the measurement of the ^{19}F-^{1}H dipolar interaction allowed the internuclear distance between hydrogen-bonded ^{19}F and ^{1}H nuclei in zirconium phosphonates to be determined. Moreover, in the study of LDPE-VBC-Dabco the observation of ^{13}C isotropic chemical shifts allowed the functionalization of LDPE to be confirmed, and the degree of cross-liking of Dabco to be determined. The determination and analysis of ^{13}C spectral features also provided information on the phase and conformational properties of polymeric domains. For example, from the observation of different isotropic chemical shifts it was possible to distinguish crystalline from amorphous domains of LDPE and

PLA in the LDPE-VBC-Dabco membrane and the PLA85PBS15 luminescent indicator, respectively. In other cases, morphological features, such as phase composition and degree of mixing between different phases or components, were investigated, exploiting the analysis of on resonance ^{1}H FIDs or the observation of proton spin diffusion. For example, in PLA85PBS15 luminescent indicators ^{1}H FID analyses allowed the amounts of crystalline and amorphous fractions, distinguished on the basis of the corresponding ^{1}H T_2's, to be quantitatively determined. Moreover, by performing variable temperature measurements, the phase transitions occurring in the PLA/PBS blend under heating were successfully investigated. In more than one study, the effect of spin diffusion on the values of ^{1}H T_1 and $T_{1\rho}$ relaxation times was observed in order to obtain information on the degree of homogeneity of composite systems on the spatial scales of 100-200 Å and 10-20 Å. For example, in P3HT/PCBM photoactive blends the increased difference between the values of ^{1}H T_1 measured for P3HT and PCBM in passing from the pristine to the annealed system indicated a corresponding phase separation between the two components. Finally, measurements of different relaxation times were exploited to investigate dynamic properties on different motional frequency regimes. ^{1}H T_2's were measured to obtain information on dynamic properties in the kHz regime. For example, in PLA85PBS15 the determination of ^{1}H T_2 as a function of temperature allowed the increase of mobility of viscous PLA under heating to be clearly observed. Faster reorientational motions with characteristic frequencies of the order of MHz were investigated by means of ^{1}H and ^{13}C T_1 relaxation times. In P3HT/PCBM photoactive blends the dynamic properties of P3HT in the MHz regime were characterized in details by the simultaneous fitting to suitable theoretical models of ^{13}C and ^{1}H T_1 curves as functions of temperature.

Attempts of correlating the determined molecular and supramolecular features to the specific functional behaviour of the investigated materials were also made, and in some cases interesting relationships were identified. For example, in LDPE-VBC-Dabco anion exchange membrane the onset of a motion in the kHz regime involving crystalline LDPE domains could play a role in the increase of ion conductivity observed at high operating temperatures. Furthermore, the extensive characterization of the phase behaviour of

PLA/PBS blends, in terms of both dynamic and structural properties, allowed a picture of the processes inducing BBS aggregation under heating to be hypothesised, so shedding light on the origins of the luminescent behaviour of the BBS containing PLA85PBS15 film. Finally, the increase of phase separation between P3HT and PCBM observed after thermal annealing can be correlated to the corresponding increase of power conversion efficiency measured for the final solar cell.

Concluding, we can state that the application of SSNMR to the study of functional materials can be a very powerful approach to get detailed insights into the molecular and supramolecular features and processes at the origin of their functional behaviour. Indeed, a wide variety of nuclear properties can be investigated to achieve a very complete picture of the structural and dynamic properties of the system. Nevertheless, the clear identification of specific correlations between "microscopic" and macroscopic properties is not straightforward, due to the complex interplay of many different factors, as well as to the intrinsic complexity of the materials under investigation. To this regard, all the materials investigated in this thesis were polymeric systems, most of which constituted by more than one organic and/or inorganic components, as well as characterized by complex polyphasic morphologies, in which the interaction between the different components played a fundamental role in determining the NMR features, and, in particular, the final macroscopic properties. The obtainment of a complete and detailed characterization of these systems often required the application of multiple SSNMR experiments on different sets of samples, and the use of complex theoretical models for the analysis of the experimental data. A meaningful example of this is the study carried out on P3HT/PCBM photoactive blends, in which the detailed characterization of motional processes involving P3HT side and main chains required the simultaneous fitting of multiple ^{13}C and ^{1}H T_1 vs temperature curves, also obtained at different Larmor frequencies, to complex theoretical models. In some cases, the combination of SSNMR results with those obtained by other complementary techniques was also useful. An example is the study carried out on PLA85PBS15 luminescent indicators, in which the results coming from DSC and SSNMR studies were successfully combined to shed light on the mechanisms at the origin of the smart behaviour of these systems.

Appendix A

Supplementary information to Chapter 3

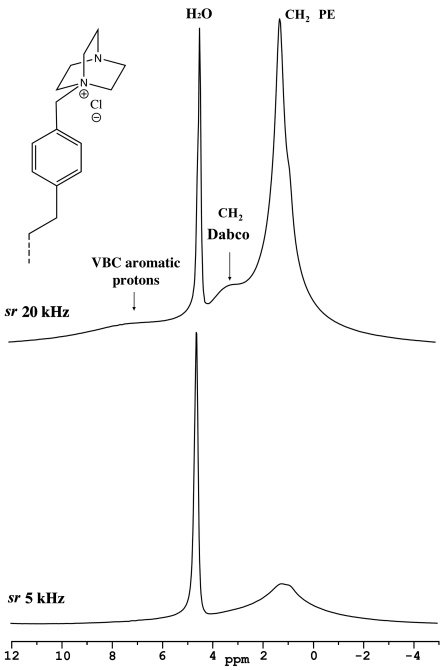

Figure A.1: Comparison between the ^{1}H MAS spectra of LDPE-g-VBC-Dabco recorded at the spinning rates (sr) of 5 (bottom) and 20 (top) kHz. The signals arising from Dabco and VBC protons, distinguishable in the spectrum acquired at the MAS frequency of 20 KHz, cannot be resolved in that recorded at the MAS frequency of 5 kHz, indicating that the system is substantially rigid.

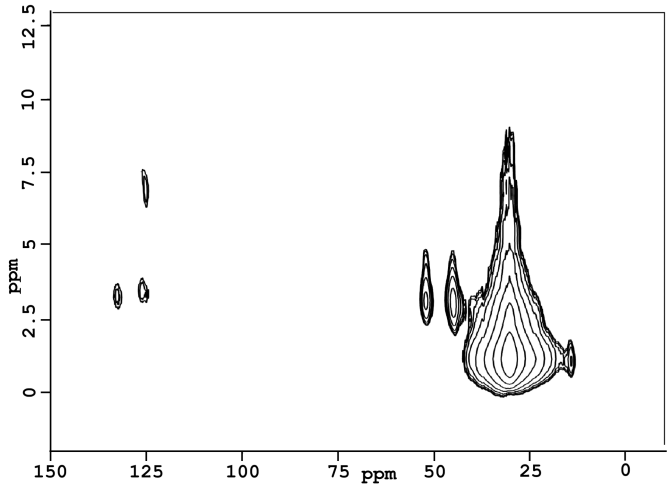

Figure A.2: ^{1}H-^{13}C FSLG-HETCOR spectrum of LDPE-g-VBC-Dabco, recorded at a spinning rate of 5 kHz. This kind of experiment allows correlation peaks between dipolarly coupled (i.e. close in space) ^{13}C-^{1}H pairs to be observed. In the figure, the horizontal and vertical axes report the ^{13}C and ^{1}H chemical shifts, respectively; in order to have a clearer visualization of the correlation peaks, the floor (lowest displayed level) of the 0-100 ppm ^{13}C spectral region is two times higher than that of the 100-150 ppm spectral region. The main correlation peaks are between LDPE carbons ($\sim$ 31-33 ppm) and the corresponding protons ($\sim$ 1.2 ppm) and between Dabco carbons (45.6 and 52.8 ppm) and the corresponding protons ($\sim$ 3 ppm). Less intense correlation peaks between the VBC aromatic carbons resonating at 125.4 ppm and VBC aromatic protons ($\sim$ 6.8 ppm), as well as between the VBC aromatic carbons resonating at 125.4 and 132.9 ppm and Dabco protons can also be observed.

Appendix B

Supplementary information to Chapter 6

Table B.1: CSA parameters, Δ and η, determined for PTFE and PVDF by the fitting of their ^{19}F MAS spectra at different MAS frequencies.

MAS frequency (kHz)	CSA parameters	PTFE	PVDF	
		-123 ppm	-97 ppm	-82 ppm
65	Δ (ppm)	80 ± 40	90 ± 40	100 ± 30
	η	1 ± 0	1 ± 0	1 ± 0
55	Δ (ppm)	70 ± 30	-	-
	η	1 ± 0	-	-
45	Δ (ppm)	80 ± 40	100 ± 20	100 ± 20
	η	0.8 ± 4	0.63 ± 2	0.61 ± 2
35	Δ (ppm)	70 ± 20	100 ± 12	100 ± 10
	η	0.6 ± 2	0.36 ± 0.7	0.41 ± 0.6
25	Δ (ppm)	74 ± 8	103 ± 6	104 ± 6
	η	0.3 ± 0.6	0.52 ±0.3	0.45 ± 0.3
15	Δ (ppm)	68 ±3	-	-
	η	0.2 ± 0.2	-	-
5	Δ (ppm)	70 ± 3	-	-
	η	0.6 ± 0.1	-	-

Appendix C

Supplementary information to Chapter 7

Table C.1: CSA parameters, Δ and η, determined for samples **1**, **1a** and **2** by the fitting of their ^{19}F MAS spectra at different MAS frequencies, acquired with and without ^{1}H-decoupling at the ^{19}F Larmor frequencies of 564 and 800 MHz, respectively.

MAS frequency (kHz)	CSA parameters	@ 600 MHz						
		1			1a		2	
		0 ppm	39 ppm	41 ppm	49 ppm	52 ppm	51 ppm	58 ppm
65	Δ (ppm)	-187 ± 18	-217 ± 18	-201 ± 18	-227 ± 23	-197 ± 22	-232 ± 18	-223 ± 17
	η	0.0 ± 0.7	0.5 ± 0.5	0.0 ± 0.5	0.2 ± 0.4	0.5 ± 0.6	0.3 ± 0.4	0.0 ± 0.4
55	Δ (ppm)	-179 ± 17	-217 ± 16	-195 ± 16	-226 ± 17	-203 ± 17	-230 ± 17	-221 ± 16
	η	0.4 ± 0.5	0.3 ± 0.3	0.0 ± 0.4	0.3 ± 0.2	0.4 ± 0.3	0.3 ± 0.2	0.0 ± 0.2
45	Δ (ppm)	-179 ± 24	-220 ± 18	-197 ± 22	-223 ± 18	-197 ± 22	-229 ± 13	-224 ± 13
	η	0.3 ± 0.2	0.2 ± 0.1	0.3 ± 0.2	0.4 ± 0.1	0.3 ± 0.2	0.3 ± 0.1	0.0 ± 0.1
35	Δ (ppm)	-176 ± 20	-215 ± 14	-197 ± 16	-230 ± 13	-204 ± 16	-232 ± 13	-221 ± 14
	η	0.2 ± 0.2	0.4 ± 0.1	0.3 ± 0.1	0.4 ± 0.1	0.2 ± 0.1	0.3 ± 0.1	0.1 ± 0.1
25	Δ (ppm)	-179 ± 17	-222 ± 10	-192 ± 14	-226 ± 10	-208 ± 11	-226 ± 10	-223 ± 10
	η	0.4 ± 0.1	0.4 ± 0.1	0.4 ± 0.1	0.3 ± 0.1	0.3 ± 0.1	0.3 ± 0.1	0.2 ± 0.1
15	Δ (ppm)	-173 ± 6	-	-	-	-	-230 ± 10	-228 ± 10
	η	0.3 ± 0.1	-	-	-	-	0.3 ± 0.1	0.2 ± 0.1
		@ 850 MHz with ^{1}H decoupling						
MAS frequency (kHz)	CSA parameters	1			1a		2	
		0 ppm	39 ppm	41 ppm	49 ppm	52 ppm	51 ppm	58 ppm
32 (25 kHz for 1)	Δ (ppm)	-173 ± 13	-215 ± 10	-196 ± 12	-225 ± 10	-198 ± 9	-230 ± 11	-223 ± 10
	η	0.2 ± 0.1	0.3 ± 0.1	0.2 ± 0.1	0.2 ± 0.1	0.2 ± 0.1	0.2 ± 0.1	0.1 ± 0.1
20 (15 kHz for 1)	Δ (ppm)	-173 ± 12	-213 ± 11	-197 ± 9	-223 ± 10	-197 ± 9	-231 ± 11	-226 ± 10
	η	0.2 ± 0.1	0.3 ± 0.1	0.1 ± 0.1	0.2- ± 0.1	0.1 ± 0.1	0.2 ± 0.1	0.1 ± 0.1

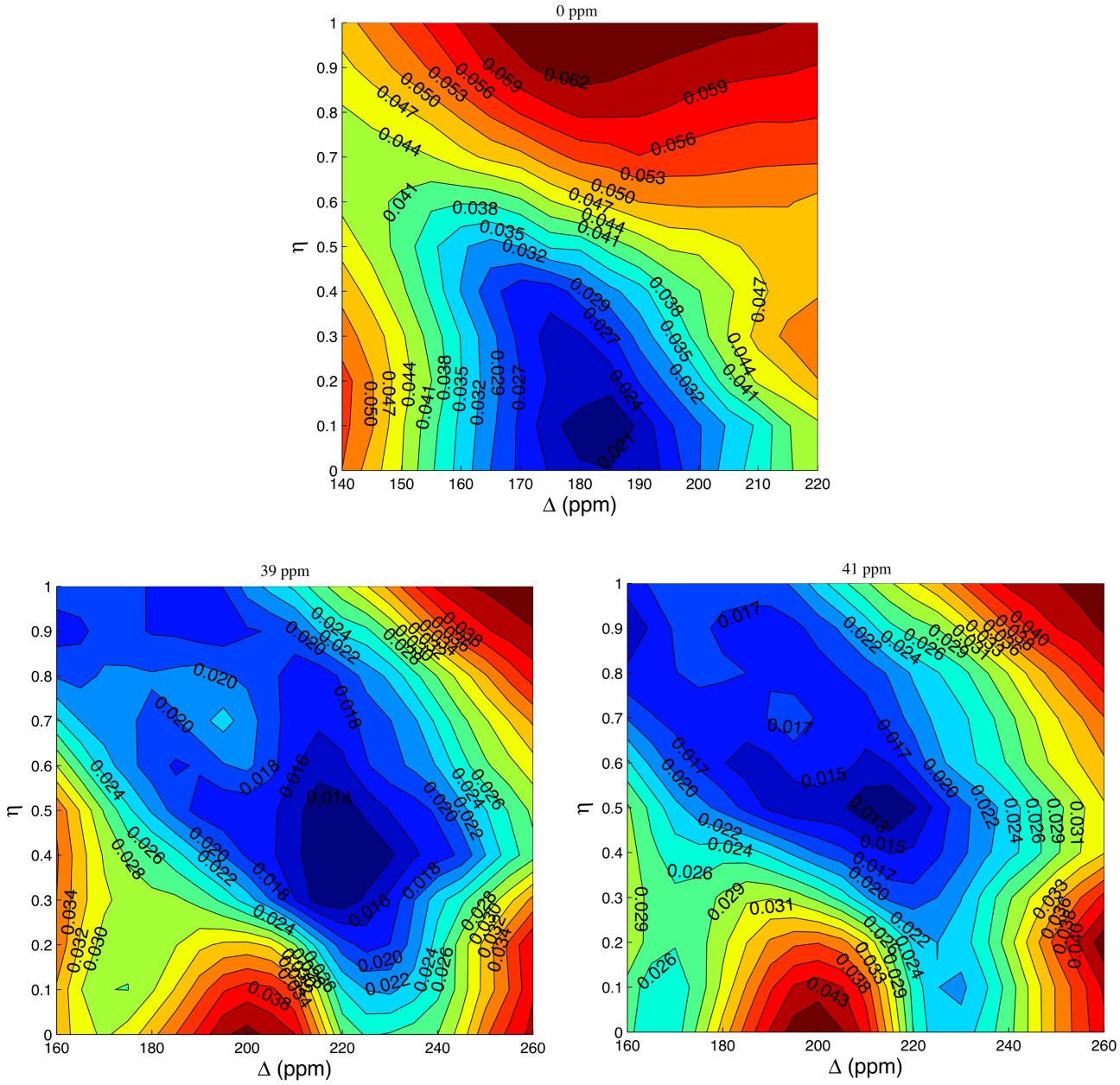

Figure C.1: Contour plots of the normalized root mean square of the differences between the experimental and simulated patterns recoupled by the $R12_5^4$ sequence, as a function of the CSA parameters Δ (ppm) and η, obtained for the ^{19}F isotropic signals at 0, 39, and 41 ppm of sample **1**.

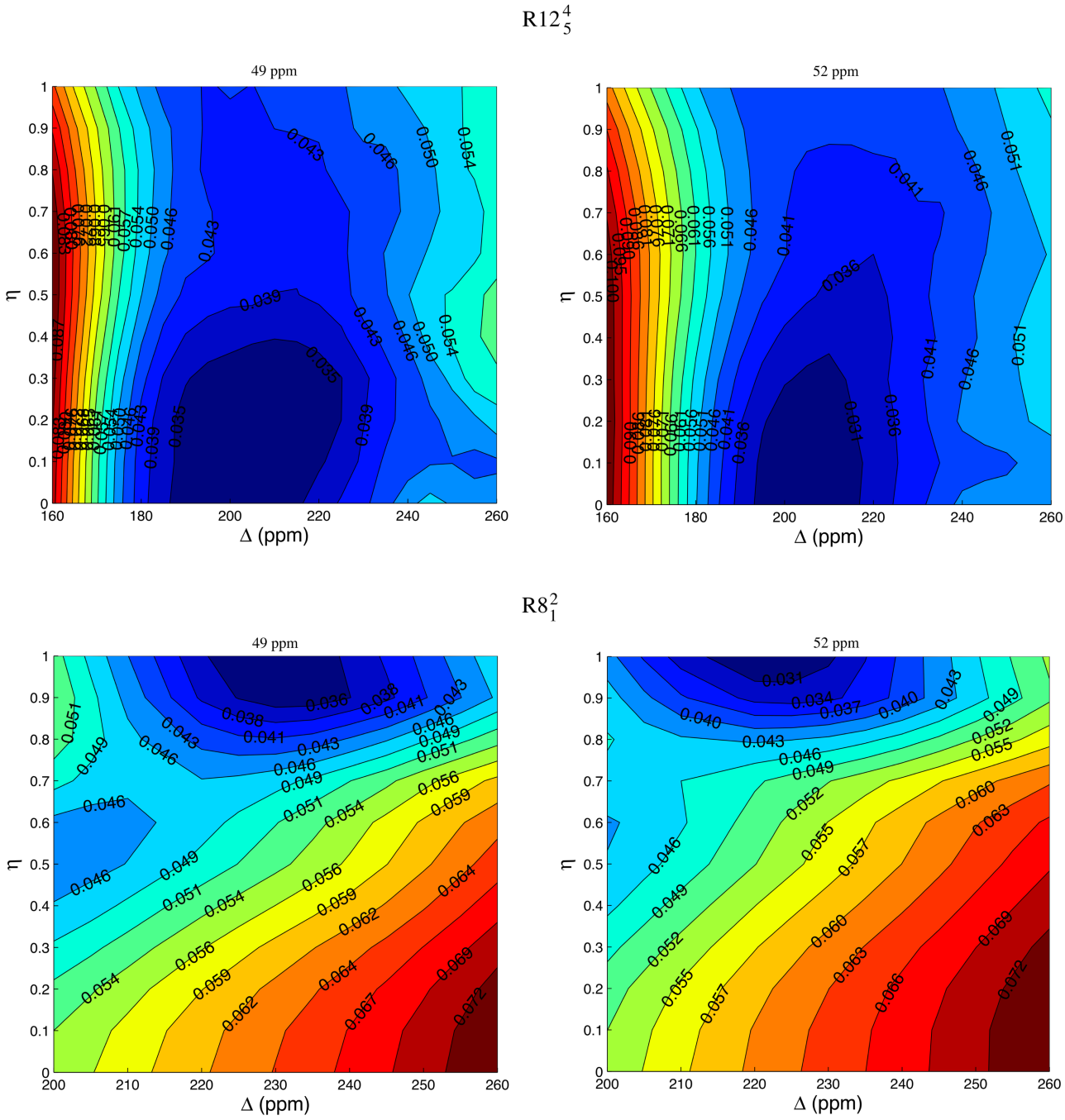

Figure C.2: Contour plots of the normalized root mean square of the differences between the experimental and simulated patterns recoupled by the $R12^4_5$ (top) and $R8^2_1$ (bottom) sequences, as a function of the CSA parameters Δ (ppm) and η, obtained for the ^{19}F isotropic signals at 49 and 52 ppm of sample **1a**.

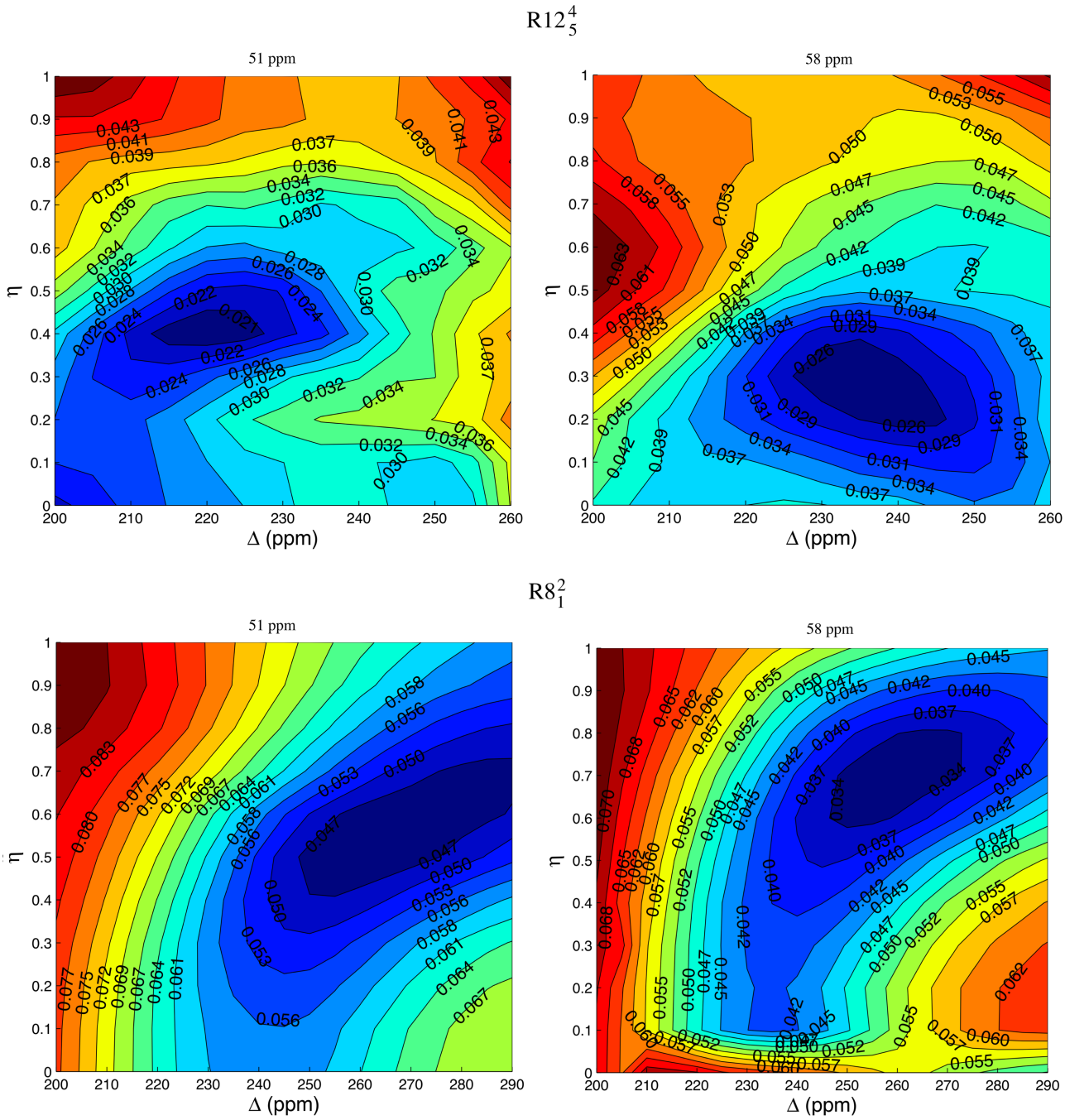

Figure C.3: Contour plots of the normalized root mean square of the differences between the experimental and simulated patterns recoupled by the $R12^4_5$ (top) and $R8^2_1$ (bottom) sequences, as a function of the CSA parameters Δ (ppm) and η, obtained for the ^{19}F isotropic signals at 51 and 58 ppm of sample **2**.

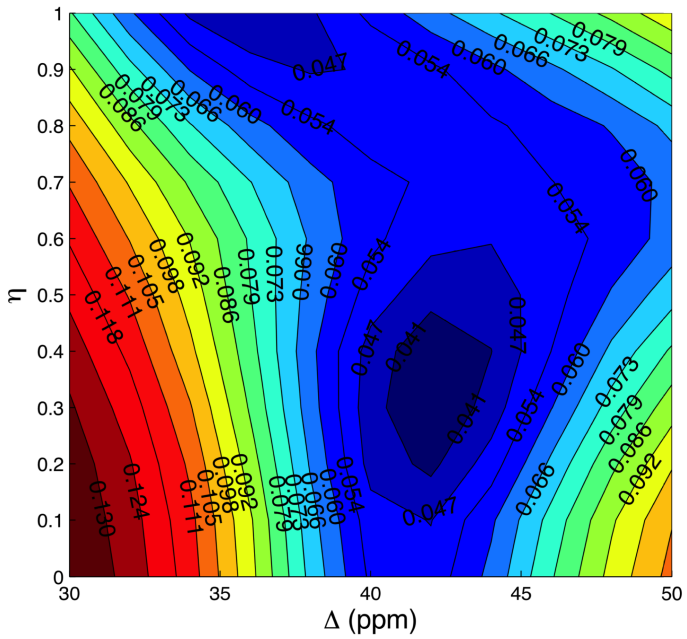

Figure C.4: Contour plot of the normalized root mean square of the differences between the experimental and simulated pattern recoupled by the $R16_3^2$ sequences, as a function of the CSA parameters Δ (ppm) and η, obtained for the ^{1}H isotropic signals at 12.5 ppm of sample **1**, by setting the ^{19}F-^{1}H dipolar coupling constant at the value of 7 kHz.

Bibliography

[1] A. Abragram, *Principles of Nuclear Magnetism*, Oxford University Press, London, **1961**.

[2] M. Duer, *NMR spectroscopy pronciples and applications*, Blackwell Science Ltd, Oxford, **2002**.

[3] M. H. Levitt, *Spin dynamics*, John Wiley & Sons, Chichester, **2001**.

[4] R. Ernst; G. Bodenhausen, *Principles of Nuclear Magnetic Resonance in One and Two Dimensions*, Oxford University Press, **1987**.

[5] A. E. Bennett; C. M. Rienstra; M. Auger; K. V. Lakshmi; R. G. Griffin, *Journal of Chemical Physics* **1995**, *103*, 6951–6958.

[6] B. M. Fung; A. K. Khitrin; K. Ermolaev, *Journal of Magnetic Resonance* **2000**, *142*, 97–101.

[7] B. C. Gerstein; R. G. Pembleton; R. D. Wilson; L. J. Ryan, *Journal of Chemical Physics* **1977**, *66*, 361–362.

[8] G. E. Maciel; C. E. Bronnimann; B. L. Hawkins, *Advances in Magnetic and Optical Resonance* **1990**, *14*, 125–150.

[9] N. Bloembergen; E. M. Purcell; R. V. Pound, *Physical Reviews* **1948**, *73*, 679–712.

[10] N. Bloembergen, *Nuclear Magnetic Relaxation*, Benjamin, New York, **1961**.

[11] N. Bloembergen, *Physica* **1949**, *15*, 386–426.

[12] http://onlinelibrary.wiley.com/journal/10.1002/(issn)1616-3028.

[13] Z. L. Wang; Z. C. Kang, *Functional and Smart Materials Structural Evolution and Structure Analysis*, Plenum Publishing Corp., 233 Spring Street, New York, NY 10013-1578, **1998**.

[14] D. Roy; J. N. Cambre; B. S. Sumerlin, *Progress in Polymer Science* **2010**, *35*, 278.

[15] M. M. Caruso; D. A. Davis; Q. Shen; S. A. Odom; Nancy R. Sottos; S. R. White; J. S. Moore, *Chemical Reviews* **2009**, *109*, 5755.

[16] X. Yan; F. Wang; F. Huang, *Chemical Society Reviews* **2012**, *41*, 6042.

[17] F. Ciardelli; G. Ruggeri; A. Pucci, *Chemical Society Reviews* **2013**, *42*, 857.

[18] A. Pucci; R. Bizzarri; G. Ruggeri, *Soft Matter* **2011**, *7*, 3689.

[19] S. J. Chen; Q. Cao; B. Jing; Y. L. Cai; P. S. Liu; J. L. Hu, *Journal of Applied Polymer Science* **2006**, *102*, 5224.

[20] P. Brochu; Q. Pei, *Macromolecular Rapid Communications* **2009**, *31*, 10.

[21] J. Madden, *IEEE Journal of Oceanic Engineering* **2004**, *29*, 706.

[22] F. Carpi; E. Smela, *Biomedical applications of electroactive polymer actuators*, Wiley, **2009**.

[23] T. Mirfakhrai; J. D. W. Madden; R. H. Baughman, *Materials Today* **2007**, *10*, 30.

[24] S. J. Chen; Q. Cao; P. S. Liu, *ACTA Polymer Sinposium* **2006**, *1*.

[25] M. Behl; M. Y. Razzaq; A. Lendlein, *Advanced Materials* **2010**, *22*, 3388.

[26] S. J. Chen; J. L. Hu; C. W. Yuen; L. K. Chan, *Materials Letters* **2009**, *63*, 1462.

[27] K. Paderni; S. Pandini; S. Passera; F. Pilati; M. Toselli; M. Messori, *Journal of Materials Science* **2012**, *47*, 4354.

[28] M. Messori; M. Degli Esposti; K. Paderni; S. Pandini; S. Passera; T. Riccò; M. Toselli, *Journal of Materials Science* **2013**, *48*, 424.

[29] S. J. Chen; J. L. Hu; H. T. Zhuo; Y. Zhu, *Materials Letters* **2008**, *62*, 4088.

[30] T. Chung; A. Romo-Uribe; P. T. Mather, *Macromolecules* **2008**, *41*, 184.

[31] C. Liu; H. Qin; P. T. Mather, *Journal of Materials Chemistry* **2007**, *17*, 1543.

[32] M. Behl; A. Lendlein, *Materials Today* **2007**, *10*, 20.

[33] S. Mondal, *Mini-Reviews in Organic Chemistry* **2009**, *6*, 114.

[34] S. Chen; J. Hu; Y. Liu; H. Liem; Y. Zhu; Q. Meng, *Polymer International* **2007**, *56*, 1128.

[35] H. M. Jeong; S. Y. Lee; B. K. Kim, *Journal of Materials Science* **2000**, *35*, 1579.

[36] B. K. Kim; J. S. Lee; Y. M. Lee; J. H. Shin; S. H. Park, *Journal of Macromolecular Science, Part B Physics* **2001**, *B40*, 1179.

[37] P. Ping; W. S. Wang; X. S. Chen; X. B. Jing, *Biomacromolecules* **2005**, *6*, 587.

[38] B. S. Lee; B. C. Chun; Y. C. Chung; K. I. Sul; J. W. Cho, *Macromolecules* **2001**, *34*, 6431.

[39] S. Neuss; I. Blomenkamp; R. Stainforth; D. Boltersdorf; M. Jansen; N. Butz; A. Perez-Bouza; R. Knuchel, *Biomaterials* **2009**, *30*, 1697.

[40] Y. Wang; K. S. Chen; J. Mishler; S. C. Cho; X. C. Adroher, *Applied Energy* **2011**, *88*, 981.

[41] S. Bose; T. Kuila; T. X. H. Nguyen; N. H. Kim; K. Lau; J. H. Lee, *Progress in Polymer Science* **2011**, *36*, 813.

[42] A. Bykoğlu, *International Journal of Hydrogen Energy* **2005**, *30*, 1181.

[43] G. Couture; A. Alaaeddine; F. Boschet; B. Ameduri, *Progress in Polymer Science* **2011**, *36*, 1521.

[44] G. Merle; M. Wessling; K. Nijmeijer, *Journal of Membrane Science* **2011**, *377*, 1.

[45] M. A. Hickner; B. S. Pivovar, *Fuel Cells* **2005**, *5*, 213.

[46] Y. S. Kim; M. A. Hickner; L. Dong; B. S. Pivovar; J. E. McGrath, *Journal of Membrane Science* **2004**, *243*, 317.

[47] G. Ye; N. Janzen; G. R. Goward, *Macromolecules* **2006**, *39*, 3283.

[48] S. Günes; H. Neugebauer; N. S. Sariciftci, *Chemical Reviews* **2007**, *107*, 1324.

[49] G. Li; R. Zhu; Y. Yang, *Nature Photonics* **2012**, *6*, 153.

[50] H. Hoppe; M. Niggemann; C. Winder; J. Kraut; R. Hiesgen; A. Hinsch; D. Meissner; N. S. Sariciftci, *Advanced Functional Materials* **2004**, *14*, 1005.

[51] R. Po; M. Maggini; N. Camaioni, *The Journal of Physical Chemistry C* **2010**, *114*, 695.

[52] F. C. Krebs, *Solar Energy Materials and Solar Cells* **2009**, *93*, 394.

[53] H. Hoppe; N. S. Sariciftci, *Journal of Materials Chemistry* **2006**, *16*, 45.

[54] X. Yang; J. Loos; S. C. Veenstra; W. J. H. Verhees; M. M. Wienk; J. M. Kroon; M. A. J. Michels; R. A. J. Janssen, *Nano Letters* **2005**, *5*, 579.

[55] W. Ma; C. Yang; X. Gong; K. Lee; A. J. Heeger, *Advanced Functional Materials* **2005**, *15*, 1617.

[56] X. Yang; J. Loos, *Macromolecules* **2007**, *40*, 1353.

[57] M. Geppi; S. Borsacchi; G. Mollica ; C. A. Veracini, *Applied Spectroscopy Review* **2009**, *44*, 1.

[58] R. Kitamaru; F. Horii; K. Murayama, *Macromolecules* **1986**, *19*, 636.

[59] F. Martini; S. Borsacchi; M. Geppi; Francesco Pilati; M. Toselli, *Polymer* **2011**, *52*, 4536.

[60] S. Borsacchi; F. Martini; M. Geppi; F. Pilati; M. Toselli, *Polymer* **2011**, *52*, 4545.

[61] M. H. Levitt, *Encyclopedia of Nuclear Magnetic Resonance* **2002**, *9*, 165.

[62] T. Chen; J. Fu, *Nanotechnology* **2012**, *23*, 235605.

[63] A. L. Cholli; D. J. Sandman, *Journal of Macromolecular Science, Part A: Pure and Applied Chemistry* **2009**, *46*, 1223.

[64] S. P. Scoville; W. M. Shirley, *Journal of Applied Polymer Science* **2011**, *120*, 2809.

[65] H. Menge; S. Hotopf; Steffen Ponitzsch; S. Richter; K.-F. Arndt; H. Schneider; U. Heuert, *Polymer* **1999**, 5303.

[66] M. Bertmer; A. Buda; I. Blomenkamp-Höfges; S. Kelch; A. Lendlein, *Macromolecules* **2005**, *38*, 3793.

[67] D. S. Powers; R. A. Vaia; H. Koerner; J. Serres; P. A. Mirau, *Macromolecules* **2008**, *41*, 4290.

[68] S. D'hollander; C. J. Gommes; R. Mens; P. Adriaensens; B. Goderis; F. Du Prez, *Journal of Materials Chemistry* **2010**, *20*, 3475.

[69] G. Ye; C. A. Hayden; G. R. Goward, *Macromolecules* **2007**, *40*, 1529.

[70] G. Ye; C. M. Mills; G. R. Goward, *Journal of Membrane Science* **2008**, *319*, 238.

[71] G. Zhong; Z. Liu; Tao Li; H. Cheng; S. Yu; R. Fu; Y. Yang, *Journal of Membrane Science* **2013**, *428*, 212.

[72] Ü. Akbey; R. Graf; Y. G. Peng; P. P. Chu; H. W. Spiess, *Journal of Polymer Science: Part B: Polymer Physics* **2009**, *47*, 138.

[73] D. K. Lee; T. Saito; A. J. Benesi; M. A. Hickner; H. R. Allcock, *The Journal of Physical Chemistry B* **2011**, *115*, 776.

[74] G. Brunklaus; S. Schauff; D. Markova; M. Klapper; K. Müllen; H.-W. Spiess, *The Journal of Physical Chemistry B* **2009**, *113*, 6674.

[75] C. Filipoi; D. E. Demco; X. Zhu; R. Vinokur; O. Conradi; a, R.M.M., *Chemical Physics Letters* **2011**, *513*, 251.

[76] L. Ghassemzadeh; M. Marrony; R. Barrera; K. D. Kreuer; J. Maier; K. Müller, *Journal of Power Sources* **2009**, *186*, 334.

[77] L. Ghassemzadeh; K.D. Kreuer; J. Maier; K. Müller, *Journal of Power Sources* **2011**, *196*, 2490.

[78] L. Ghassemzadeh; K.-D. Kreuer; J. Maier; K. Müller, *The Journal of Physical Chemistry C* **2010**, *114*, 14635.

[79] H. Zhang; P. K. Shen, *Chemical Reviews* **2012**, *112*, 2780.

[80] R. Graf, *Solid State Nuclear Magnetic Resonance* **2011**, *40*, 127.

[81] J. W. Traer; G. R. Goward, *Magnetic Resonance in Chemistry* **2007**, *45*, S135.

[82] V. Sabarinathan; Z. Wu; R.-H. Cheng; S. Ding, *The Journal of Physical Chemistry B* **2013**, *117*, 6558.

[83] T. Yamamoto; D. Komarudin; M. Arai; B. Lee; H. Suganuma; N. Asakawa; Y. Inoue; K. Kubota; S. Sasaki; T. Fukuda; H. Matsuda, *Journal of American Chemical Society* **1998**, *120*, 2047.

[84] T. Chen; X. Wu; R. D. Rieke, *Journal of American Chemical Society* **1995**, *117*, 233.

[85] R. D. McCullough; R. D. Lowe; M. Jayaraman; D. L. Anderson, *Journal of Organic Chemistry* **1993**, *58*, 904.

[86] O. F. Pascui; R. Lohwasser; M. Sommer; M. Thelakkat; T. Thurn-Albrecht; K. Saalwächter, *Macromolecules* **2010**, *43*, 9401.

[87] K. Yazawa; Y. Inoue; T. Shimizu; M. Tansho; N. Asakawa, *The Journal of Physical Chemistry B* **2010**, *114*, 1241.

[88] A. C. Kolbert; N. S. Sariciftci; K.-U. Gaudl; P. Bauerle; M. Mehring, *Journal of American Chemical Society* **1991**, *113*, 8243.

[89] R. Mens; S. Chambon; S. Bertho; G. Reggers; B. Ruttens; J. D'Haen; J. Manca; R. Carleer; D. Vanderzande; P. Adriaensens, *Magnetic Resonance in Chemistry* **2011**, *49*, 242.

[90] F. Piersimoni; S. Chambon; K. Vandewal; R. Mens; T. Boonen; A. Gadisa; M. Izquierdo; S. Filippone; J. D'Haen, B.; N. Martin; L. Lutzen; D. Vardenzande; P. Adriaensens; J. V. Manca, *The Journal of Physical Chemistry C* **2011**, *115*, 10873.

[91] T. Fukushima; H. Kimura; Y. Shimahara; H. Kaji, *Applied Physics Letters* **2011**, *99*, 223301.

[92] R. Mens; S. Bertho; S. Chambon; J. D'Haen; L. Lutzen; J. Manca; J. Gelan; D. Vanderzande; P. Adriaensens, *Journal of Polymer Science-Part A-1* **2011**, *49*, 1699.

[93] R. Mens; F. Demir; G. Van Assche; B. Van Mel; D. Vanderzande; P. Adriaensens, *Journal of Polymer Science-Part A-1* **2012**, *50*, 1037.

[94] S. Chambon; R. Mens; K. Vandewal; E. Clodic; M. Scharber; L. Laurence; J. Gelan; J. Manca; D. Vanderzande; P. Adriaensens, *Solar Energy Materials and Solar Cells* **2012**, *22*, 1255.

[95] R. C. Nieuwendaal; H. W. Ro; D. S. Germack; R. J. Kline; M. F. Toney; C. K. Chan; A. Agrawal; D. Gundlach; D. L. VanderHart; D. M. Delongchamp, *Advanced Functional Materials* **2012**, *22*, 1255.

[96] C. Yang; J. G. Hu; A. J. Heeger, *Journal of American Chemical Society* **2006**, *128*, 12007.

[97] R. C. Nieuwendaal; C. R. Snyder; R. J. Kline; E. K. Lin; D. L. VanderHart; D. M. DeLongchamp, *Chemistry of Materials* **2010**, *22*, 2930.

[98] D. Pletcher; X. Li, *International Journal of Hydrogen Energy* **2011**, *36*, 15089.

[99] Y-C Cao; X. Wu; K. Scott, *International Journal of Hydrogen Energy* **2012**, *37*, 9524.

[100] M. Faraj; M. Boccia; H. Miller; F. Martini; S. Borsacchi; M. Geppi; A. Pucci, *International Journal of Hydrogen Energy* **2012**, *37*, 14992.

[101] M. Zhang; H. K. Kim; E. Chalkova; F. Mark; S. N. Lvov; T. C. M. Chung, *Macromolecules* **2011**, *44*, 5937.

[102] M. Faraj; E. Elia; M. Boccia; A. Filpi; A. Pucci; F. Ciardelli, *Journal of Polymer Science, Part A: Polymer Chemistry* **2011**, *49*, 3437.

[103] V. J. McBrierty; K. J. Packer, *Nuclear magnetic resonance in solid polymers*, Cambridge University Press, Cambridge, **1993**.

[104] M. E. A. Cudby; R. K. Harris; K. Metcalfe; K. J. Packer; P. W. R. Smith; A. Bunn, *Polymer* **1985**, *26*, 169.

[105] J. Schaefer; E. O. Stejskal; R. Buchdahl, *Macromolecules* **1977**, *10*, 384.

[106] R. V. Law; D. C. Sherrington; C. E. Snape, *Industrial and Engineering Chemistry Research* **1995**, *34*, 2940.

[107] T. Takewaki; L. W. Beck; M. E. Davis, *Microporous and Mesoporous Materials* **1999**, *33*, 197.

[108] H. A. Khonakdarand; S. H. Jafari; R. Hässler, *Journal of Applied Polymer Science* **2007**, *104*, 1654–1660.

[109] F. Horii; H. Kaji; H. Ishida; K. Kuwabara; K. Masuda; T. Tai, *Journal of Molecular Structure* **1998**, *441*, 303.

[110] B. J. Van Rossum; H. Förster; H. J. M. De Groot, *Journal of Magnetic Resonance* **1997**, *124*, 516.

[111] B. R. Crenshaw; C. Weder, *Chemistry of Materials* **2003**, *15*, 4717.

[112] M. Kinami; B. R. Crenshaw; C. Weder, *Chemistry of Materials* **2006**, *18*, 946.

[113] B. R. Crenshaw; J. Kunzelman; C. E. Sing; C. Ander; C. Weder, *Macromolecular Chemistry and Physics* **2007**, *208*, 572.

[114] J. Kunzelman; T. Chung; P. T. Mather; C. Weder, *Journal of Materials Chemistry* **2008**, *18*, 1082.

[115] F. Donati; A. Pucci; C. Cappelli; B. Mennucci; G. Ruggeri, *The Journal of Physical Chemistry B* **2008**, *112*, 3668.

[116] F. Donati; A. Pucci; L. Boggioni; I. Tritto; G. Ruggeri, *Macromolecular Chemistry and Physics* **2009**, *210*, 728.

[117] A. Pucci; F. Signori; R. Bizzarri; S. Bronco; G. Rugger; F. Ciardelli, *Journal of Materials Chemistry* **2010**, *20*, 5843.

[118] J. R. Dorgan; B. Braun; J. R. Wegner; D. M. Knauss, *ACS Symposium Series* **2006**, *939*, 102.

[119] S. Pomfrey, *Journal of applied packaging research* **2007**, *1*, 235.

[120] A. Sorrentino; G. Gorrasi; V. Vittoria, *Trends in food science technology* **2007**, *18*, 84.

[121] Y. H. Na; Y. He; X. Shuai; Y. Kikkawa; Y. Doi; Y. Inoue, *Biomacromolecules* **2002**, *3*, 1179.

[122] T. Furukawa; H. Sato; H. Shinzawa; I. Noda; S. Ochiai, *Analytical Science* **2007**, *23*, 871.

[123] T. Furukawa; H. Sato; R. Murakami; J. Zhang; I. Noda; S. Ochiai; Y. Ozaki, *Polymer* **2007**, *48*, 1749.

[124] T. Yokohara; M. Yamaguchi, *European Polymer Journal* **2008**, *44*, 677.

[125] M. B. Coltelli; I. Della Maggiore; M. Bertoldo; F. Signori; S. Bronco; F. Ciardelli, *Journal of Applied Polymer Science* **2008**, *110*, 1250.

[126] F. Signori; M. B. Coltelli; S. Bronco, *Polymer degradation and stability* **2009**, *94*, 74.

[127] F. D. Kopinke; M. Remmler; K. Mackenzie; M. Möder; O. Wachsen, *Polymer degradation and stability* **1996**, *53*, 329.

[128] D. A. Jervis, *Plastic, Additives and Compounding* **2003**, *5*, 42.

[129] A. Pucci; M. Bertoldo; S. Bronco, *Macromolecular Rapid Communications* **2005**, *26*, 1043.

[130] A. Pucci; C. Cappelli; S. Bronco; G. Ruggeri, *The Journal of Physical Chemistry B* **2006**, *110*, 3127.

[131] M. T. Shaw; W. J. MacKnight, *Introduction to Polymer Viscoelasticity*, John Wiley & Sons, Hoboken, New Jersey, 3rd edition, **2005**.

[132] F. Signori; M. Pelagaggi; S. Bronco; M. C. Righetti, *Thermochimica Acta* **2012**, *543*, 74.

[133] E. W. Hansen; P. E. Kristiansen; B. R. Pedersen, *The Journal of Physical Chemistry B* **1998**, *102*, 5444.

[134] H. Tsuji; S. Kamo; F. Horii, *Polymer* **2010**, *51*, 2215.

[135] H. Tsuji; F. Horii; M. Nakagawa; Y. Ikada; H. Odani; R. Kitamaru, *Macromolecules* **1992**, *25*, 4114.

[136] C. Howe; N. Vasanthan; C. MacClamrock; S. Sankar; I. D. Shin; I. K. Simonsen; A. E. Tonelli, *Macromolecules* **1994**, *27*, 7433.

[137] G. Kister; G. Cassanas; M. Vert, *Polymer* **1998**, *39*, 267.

[138] A. Swinnen; I. Haeldermans; M. vande Ven; J. D'Haen; G. Vanhoyland; S. Aresu; M. D'Olieslaeger; J. Manca, *Advanced Functional Materials* **2006**, *16*, 760.

[139] B. A. Collins; J. R. Tumbleston; H. Ade, *Journal of Phisical Chemistry Letters* **2011**, *2*, 3135.

[140] C. Forte; M. Geppi; M. Malvaldi; V. Mattoli, *The Journal of Physical Chemistry B* **2004**, *108*, 10832.

[141] G. Mollica; C. Forte; M. Malvaldi; M. Geppi, *The Journal of Physical Chemistry B* **2011**, *115*, 1978.

[142] E. Carignani; S. Borsacchi; M. Geppi, *ChemPhysChem* **2011**, *12*, 974.

[143] E. Carignani; S. Borsacchi; M. Geppi, *The Journal of Physical Chemistry A* **2011**, *115*, 8783.

[144] F. Martini; S. Borsacchi; S. Spera; C. Carbonera; A. Cominetti; M. Geppi, *The Journal of Physical Chemistry C* **2013**, *117*, 131.

[145] D. A. Torchia, *Journal of Magnetic Resonance* **1978**, *30*, 613.

[146] A. M. Kenwright; B. J. Say, *Solid State Nuclear Magnetic Resonance* **1996**, *7*, 85.

[147] M. Geppi; R. K. Harris; A. M. Kenwright; B. J. Say, *Solid State Nuclear Magnetic Resonance* **1998**, *12*, 15.

[148] M. Geppi; C. Forte, *Journal of Magnetic Resonance* **1999**, *137*, 177.

[149] K. Yazawa; Y. Inoue; T. Yamamoto; N. Asakawa, *Physical Reviews B* **2006**, *74*, 094204.

[150] M. M. Maricq; J. S. Waugh, *Journal of Chemical Physics* **1979**, *70*, 3300.

[151] J. Herzfeld; A. E. Berger, *Journal of Chemical Physics* **1980**, *73*, 6021.

[152] O. N. Antzutkin; S. C. Shekar; M. H. Levitt, *Journal of Magnetic Resonance, Series A* **1995**, *115*, 7.

[153] O. N. Antzutkin; Y. K. Lee; M. H. Levitt, *Journal of Magnetic Resonance* **1998**, *135*, 144.

[154] R. Tycko; G. Dabbagh, *Chemical Physics Letters* **1990**, *173*, 461.

[155] T. Gullion; J. Shaefer, *Journal of Magnetic Resonance* **1989**, *81*, 196.

[156] L. Frydman; J.S. Harwood, *Journal of American Chemical Society* **1995**, *117*, 5367.

[157] G. Hou; I.-J. L. Byeon; J. Ahn; A. M. Gronenborn; T. Polenova, *Journal of American Chemical Society* **2011**, *133*, 18646.

[158] G. Hou; I.-J. L. Byeon; J. Ahn; A. M. Gronenborn; T. Polenova, *The Journal of Chemical Physics* **2012**, *137*, 134201.

[159] G. Hou; S. Paramasivam; S. Yan; T. Polenova; A. J. Vega, *Journal of American Chemical Society* **2013**, *135*, 1358.

[160] H. K. Miah; D. A. Bennett; D. Iuga; J. J. Titman, *Journal of Magnetic Resonance* **2013**, *235*, 1.

[161] D. H. Brouwer; J. A. Ripmeester, *Journal of Magnetic Resonance* **2007**, *185*, 173.

[162] L. Duma; D. Abergel; P. Tekely; G. Bodenhausen, *Chemical Communications* **2008**, 2361.

[163] M. Bak; J. T. Rasmussen; N. C. Nielsen, *Journal of Magnetic Resonance* **2000**, *147*, 296.

[164] P. Holstein; U. Scheler; R. K. Harris, *Polymer* **1998**, *39*, 4937.

[165] Y. Koseki; K. Aimi; S. Ando, *Polymer Journal* **2012**, *44*, 757.

[166] http://bionmr.chem.au.dk/download/tv/opt/.

[167] R. K. Harris, *Solid State Sciences* **2004**, *6*, 1025.

[168] S. P. Brown, *Hydrogen Bonding in Crystalline Organic Solids*, Encyclopedia of Magnetic Resonance, John Wiley & Sons, **2008**.

[169] Potrzebowski, M.J., *Crystallography and NMR: Applications to Organic and Pharmaceutical Chemistry*, Encyclopedia of Magnetic Resonance, John Wiley & Sons, **2008**.

[170] J. K. Harper, *Shift Anisotropy and Asymmetry: Relationships to Crystal Structure*, Encyclopedia of Magnetic Resonance, Wiley and Sons, **2008**.

[171] J. K. Harper; D. M. Grant, *Crystal Growth & Design* **2006**, *6*, 2315.

[172] F. Taulelle, *Solid State Science* **2004**, *6*, 1053.

[173] Z. Gu; R. Zambrano; A. McDermott, *Journal of American Chemical Society* **1994**, *116*, 6368.

[174] G. A. Jeffrey; Y. Yeon, *Acta Crystallographica Section B* **1986**, *42*, 410.

[175] G. Wu; C. J. Freure; E. Verdurand, *Journal of American Chemical Society* **1998**, *120*, 13187.

[176] M. Kibalchenko; D. Lee; L. Shao; M. C. Payne; J. J. Titman; J. R. Yates, *Chemical Physics Letters* **2010**, *498*, 270.

[177] M. Geppi; G. Mollica; S. Borsacchi; C. A. Veracini, *Applied Spectroscopy Reviews* **2008**, *43*, 202.

[178] F. Costantino; P. Sassi; M. Geppi; M. Taddei, *Crystal Growth & Design* **2012**, *12*, 5462.

[179] A. Rawal; B. J. Smith; G. L. Athens; C. L. Edwards; L. Roberts; V. Gupta; B. F. Chmelka, *Journal of American Chemical Society* **2010**, *132*, 7321.

[180] U. Costantino; M. Nocchetti; R. Vivani, *Journal of American Chemical Society* **2002**, *124*, 8428.

[181] R. Vivani; F. Costantino; M. Nocchetti; G. D. Gatta, *Journal of Solid State Chemistry* **2004**, *177*, 4013.

[182] R. Vivani; U. Costantino; M. Nocchetti, *Journal of Materials Chemistry* **2002**, *12*, 3254.

[183] M. Taddei; R. Vivani; F. Costantino, *Dalton Transactions* **2013**, *42*, 9671.

[184] H. Alhendawi; E. Brunet; E. Rodríguez Payán; N. Shurrab; O. Juanes; S. Idhair; M. Al-Asqalany, *Journal of Porous Materials* **2013**, *20*, 1189.

[185] G. Alberti; U. Costantino; M. Casciola; R. Vivani; A. Peraio, *Solid State Ionics* **1991**, *46*, 61.

[186] G. Alberti; M. Casciola; U. Costantino; A. Peraio; E. Montoneri, *Solid State Ionics* **1992**, *50*, 315.

[187] M. Casciola; D. Capitani; A. Donnadio; V. Frittella; M. Pica; M. Sganappa, *Fuel Cells* **2009**, *9*, 381.

[188] R. K. Nagarale; W. Shin; P. K. Singh, *Polymer Chemistry* **2010**, *1*, 388.

[189] X. Wu; X. Ma; Y. Ji; Q. Wang; X. Jia; X. Fu, *Journal of Molecular Catalysis A: Chemical* **2007**, *265*, 316.

[190] S. Calogero; D. Lanari; M. Orrù; O. Piermatti; F. Pizzo; L. Vaccaro, *Journal of Catalysis* **2011**, *282*, 112.

[191] D. Lanari; F. Montanari; F. Marmottini; O. Piermatti; M. Orrù; L. Vaccaro, *Journal of Catalysis* **2011**, *277*, 80.

[192] X.-Z. Lin; Z.-Y. Yuan, *European Journal of Inorganic Chemistry* **2012**, 2661.

[193] C. Liu; J. Ma; X. Gan; R. Li; J. Wang, *Composites Science and Technology* **2012**, *72*, 915.

[194] M. Pica; A. Donnadio; E. Troni; D. Capitani; M. Casciola, *Inorganic Chemistry* **2013**, *52*, 7680.

[195] Y. Tang; Y. Ren; X. Shi, *Inorganic Chemistry* **2013**, *52*, 1388.

[196] K. Segawa; N. Kihara; H. Yamamoto, *Journal of Molecular Catalysis* **1992**, *74*, 213.

[197] P. Kohli; G. J. Blanchard, *Langmuir* **2000**, *16*, 695.

[198] H. L. Ngo; A. Hu; W. Lin, *Journal of Molecular Catalysis A: Chemical* **2004**, *215*, 177.

Aknowledgments

.... so this is THE END! Nothing left but to say THANKS to all the people who, in many different ways, contributed to this thesis, making the last three years so special to me.

The first and immeasurable thanks are for Marco, for having introduced me to SS-NMR, for the enthusiasm with which he always followed my research, and for his brilliant ideas without which this thesis would have not been the same. Special thanks are for Silvia, for her constant presence, for the support and the always precious advices. Thanks to both of them for the trust that they always showed to me, and for the beautiful persons who they are! I wish to thank all the SSNMR group in Pisa, the people who sadly left, those who recently joined us, and those who have always been there. Thank you, "Elis-e", Uma, Lucia, Claudia, Sara, Elionai, Marco M. for the nice moments we spent together... it was and it is a pleasure working with all of you! Especially, many thanks to Elisa(ina), who has been my special companion during all these years in Pisa... thanks for her helpfulness and friendships, and for the special and positive person who she is!

Special and grateful thanks to Prof. Jeremy Titman for the six months I could spend in his laboratories in Nottingham, and to all the SSNMR group in Nottingham, Habeeba Miah, Lyndsey Knight, David Bennett, and Gregory Martin. Thanks to them also for the nice time spent together, making the experience in Nottingham so special and unforgettable. Especially, thanks to Habeeba for the help and the support given to my research (it wasn't easy, I know!), to Lyndsey for her enthusiasm and cheerfulness, and to both of them for being so good and special friends!

Many thanks to all the people I had the chance of working with. Especially, I wish to thank Prof. Giacomo Ruggeri, Dr. Andrea Pucci, Dr. Silvia Spera, Prof. Ferdinando

Costantino and their coworkers... without them most of the previous two hundreds and eleven pages could not have been written!

Last but not least thanks to my family. To Mom and Dad, without whom nothing of this would have been possible. And to you, Emiliano, for believing in me and supporting me unconditionally, being always at my side.